Mechanisms of Intestinal Phosphate Absorption

Dissertation

zur

Erlangung der naturwissenschaftlichen Doktorwürde

(Dr. sc. nat.)

vorgelegt der

Mathematisch-naturwissenschaftlichen Fakultät der

Universität Zürich

Von

Thomas Knöpfel

aus

Teufen AR

Promotionskomitee

Prof. Dr. Carsten A. Wagner (Vorsitz)
Prof. Dr. Jürg Biber
Prof. Dr. Bruno Stieger
Prof. Dr. Gerhard Burckhardt
Dr. Nati Hernando

Zürich, 2017

Table of Contents

Zusammenfassung

Anorganisches Phosphat (inorganic phosphate, Pi) ist essentiel für viele metabolische Prozesse, der Pi Spiegel ist reguliert durch das Zusammenspiel von intestinaler Absorption und renaler Resorption. Mitglieder der Na^+-abhängigen Pi-Transporterfamilien SLC20 (PiT) und SLC34 (NaPi) sind verantwortlich für die apikale Aufnahme von Pi in Epithelzellen im Dünndarm und im proximalen Tubulus der Niere.

NaPi-IIb (SLC34A2) ist verantwortlich für den Grossteil des aktiven Transportes im Darmepithel. In Mäusen ohne funktionellem NaPi-IIb (KO) ist die Aufnahme von Pi in Enterozyten stark vermindert, was jedoch nur zu moderat erhöhter Pi Ausscheidung im Stuhl führt, welche durch eine erhöhte renale Resorption kompensiert wird. Desweiteren führen Mutationen in NaPi-IIb beim Menschen zu pulmonaler alveolärer Mikrolithiasis. Es sind jedoch keine Beeinträchtigungen der Pi Homöostase bekannt. Dies weisst auf einen alternativen Mechanismus der intestinalen Pi Absorption hin, in welchem der parazelluläre Weg eine entscheidende Rolle einnehmen könnte. Unter normalen Ernährungsbedingungen scheint der Pi Gradient ausreichend zu sein um eine passive Absorption im Darm zu ermöglichen und NaPi-IIb KO Mäuse mit ausreichend Pi zu versorgen. NaPi-IIb ist ein Transporter mit hoher Pi-Affinität und ist stark reguliert durch den Pi Gehalt in der Nahrung. Deshalb könnte die Rolle von NaPi-IIb vorallem wichtig sein, sobald der Pi Anteil in der Nahrung limitiert ist. Das Ziel dieser Studie ist die Rolle von NaPi-IIb in der intestinalen Pi Absorption zu untersuchen. Dazu adaptierten wir KO Mäuse an eine Diät mit tiefem Pi Gehalt. Nach unserer Hypothese wäre unter solchen Bedingungen NaPi-IIb der dominante Transportmechanismus für Pi. Um weitere regulatorische Mechanismen zu untersuchen, welche das Fehlen von NaPi-IIb kompensieren, wurden KO und Wildtyp (WT) Mäuse an eine Diät mit hohem (HPD) oder tiefen (LPD) Pi-Gehalt adaptiert.

Wie in WT Tieren führt die HPD auch bei KO Mäusen zu einer erhöhten Pi Ausscheidung in Kot und Urin, was darauf hindeutet, dass auch ohne transzellulären Transport eine erhöhte Aufnahme von Pi erfolgt. Jedoch war unter HPD Bedingungen bei KO Mäusen die fäkale Pi Ausscheidung höher und die Menge an Pi im Urin geringer als bei WT Tieren. Umgekehrt führte LPD in beiden Genotypen zu reduzierter Pi Ausscheidung in Kot und Urin, diese kompensatorischen Mechanismen

erlaubte es WT Mäusen die Pi Homöostase aufrecht zu erhalten. In KO Mäusen war die reduzierte renale Exkretion nicht ausreichend um die beeinträchtigte intestinale Absorption zu kompensieren. Dies führte zu einer transienten Erniedrigung der Plasma Pi Konzentration. Trotz dieser transienten Hypophosphatämie war die zirkulierende Konzentration von Vitamin D_3, Parathormon (PTH) und des Fibroblast Growth Factorsr 23 (FGF23) vergleichbar mit den Werten der WT Tiere. Jedoch erhöhte die LPD in KO Mäusen die renale Ausscheidung von Ca^{2+}, Desoxypyridionlin, einem Marker für Osteoklastenaktivität im Knochen, und Kortikosteron im Urin und führte zu einer verringerten Knochendichte im Vergleich zum WT. Diese Beobachtungen deuten darauf hin, dass KO Mäuse beginnen Knochen zu resorbieren um die Konzentration von Pi im Blut aufrecht zu erhalten sobald der Pi Gehalt in der Nahrung knapp wird.

In Experimenten in Ussing-Kammern wurde die parazelluläre Durchlässigkeit für Pi sowie Na^+ und Cl^- in intestinalen Zellkulturmodellen sowie Darmsegmenten von Maus und Ratte gemessen. Messungen der Diffusionspotentiale in Zellkultur zeigten, dass die Tight Junctions (TJ) durchlässig sind für Pi, wobei monovalentes Pi ($H_2PO_4^-$) die höhere Permeabilität aufwies als divalentes Pi (HPO_4^{2-}). Dies konnte bestätigt werden in Messungen von verschiedenen Darmabschnitten von Ratte und Maus. Unsere ex vivo Experimente deuten darauf hin, dass alle Darmabschnitte vom Duodenum bis zum Kolon einen parazellulären Weg für Pi aufweisen. Intressanterweise war die Permeabilität der TJ für Na^+, Cl^- und Pi unverändert in NaPi-IIb KO Mäusen.

Zusammengefasst implizieren unsere Beobachtungen, dass der parazelluläre Weg ausreicht unter normalen Bedingungen um KO Mäuse (und wahrscheinlich Patienten mit NaPi-IIb Mutationen) mit ausreichend Pi zu versorgen. Sobald jedoch der Pi Gehalt in der Nahrung limitiert ist, könnte der Pi Gradient nicht genügend sein, um die passive Absorption anzutreiben, und die Niere kann nicht mehr für die beeinträchtigte Pi Absorption im Darm aufkommen. Daraus erschliesst sich, das die Hauptrolle von NaPi-IIb im Darm darin besteht Pi aufzufangen, wenn der Organismus mit niedriger Verfügbarkeit von Pi zu kämpfen hat. Knochen dienen als endliche alternative Pi Quelle für den Organismus in der Abwesenheit von NaPi-IIb.

Da Pi in vielen biochemischen Prozessen involviert ist, ist es nicht weiter erstaunlich, dass Änderungen im Pi Gehalt der Nahrung nicht nur Konsequenzen für die Pi

Homöostase hat, sondern weitreichende systemische Auswirkunen hat. Eine renale Trasnkriptomsanalyse von Mäusen adaptiert auf HPD und LPD zeigte, dass Slc16a14 (MCT14) stark heraufreguliert ist unter HPD Bedingungen. MCT14 ist ein nicht charakterisiertes Mitglied der Familie von Monokarboxylattransportern. Die Niere zeigt die höchste Expression von MCT14 mRNA in Mäusen. Ein Antikörper wurde entwickelt und dessen Spezifität bestätigt, um mRNA Änderungen auf Proteinebene zu untersuchen und MCT14 in der Niere zu lokalisieren. Mit Hilfe dieses Antikörpers wurde MCT14 in der luminalen Membrane des dicken aufsteigenden Schenkels der Henle'schen Schleife (TAL) der Niere lokalisiert. Desweiteren konnte bestätigt werden, dass auch die MCT14 Proteinmenge erhöht ist, wie auf mRNA Ebene bei erhöhter Pi Zufuhr über die Nahrung. Um Transportsubstrat(e) zu identifizieren wurde MCT14 in Oozyten von Xenopus laevis exprimiert, wo der Transporter nachweislich in die Membran integriert wurde. Es konnte jedoch kein Transport von Pi oder den klassischen Substraten der SLC16 Familie gemessen werden. Zusammengefasst ist die Expression von MCT14 reguliert über den Pi Gehalt der Nahrung und angereichert in der Niere, wo er spezifisch im TAL lokalisiert ist.

Summary

Phosphate (Pi) is essential for many metabolic processes, and its levels are regulated by integrating intestinal absorption and renal reabsorption. Luminal uptake of Pi into epithelial cells of the small intestine and kidney proximal tubule is mediated by members of the Na^+-dependent Pi transporter families SLC20 (PiT) and SLC34 (NaPi).

NaPi-IIb (SLC34A2) accounts for most of the active transport of Pi into intestinal epithelial cells. Ablation of NaPi-IIb in mice abolishes Pi uptake into enterocytes but leads to only a moderate increase in fecal excretion of Pi, which is compensated by higher renal reabsorption. Additionally, patients with mutations in NaPi-IIb develop pulmonary alveolar microlithiasis, but no alterations in Pi homeostasis have been reported. This suggests another way for Pi absorption, and the paracellular pathway might be a crucial mechanism. As long as the luminal Pi concentration is high enough to provide a diffusion gradient, intestinal passive absorption seems to be sufficient to provide NaPi-IIb deficient mice with Pi under normal dietary conditions. However since NaPi-IIb is a high affinity transporter and is regulated by dietary Pi, its role may become more important once dietary Pi availability is restricted. In this study we aimed to explore the role of NaPi-IIb in intestinal Pi absorption by challenging NaPi-Iib deficient mice with a low Pi diet, as we hypothesized that under low Pi conditions NaPi-IIb would be the predominant transport pathway for Pi. Moreover, we explored the regulatory mechanisms that help to compensate for the loss of NaPi-Iib. To this end, wild type (WT) and NaPi-IIb deficient mice were challenged with high (HPD) or low (LPD) dietary Pi.

As in WT animals, HPD lead to increased fecal and urinary excretion of Pi in NaPi-IIb deficient mice, indicating a high delivery of Pi from the intestinal lumen into the circulation even in the absence of transcellular transport. Moreover, fecal Pi was higher and urinary Pi lower in knockout than in wild type mice fed HPD, whereas hormonal levels and plasma Pi were similar in both genotypes. In contrast, LPD decreased fecal and urinary Pi excretion in both genotypes. These compensatory changes allowed WT mice to remain normophosphatemic. However, the reduction in renal excretion was not sufficient to compensate the impaired intestinal Pi absorption in NaPi-IIb depleted animals, and plasma Pi levels declined transiently in these mice.

Despite this transient hypophosphatemia, NaPi-IIb deficient mice fed low Pi still showed levels of vitamin D_3, PTH and FGF23 that were comparable to the values of their WT littermates. Instead, upon feeding low Pi, NaPi-IIb deficient animals had higher urinary excretion of Ca^{2+}, deoxypyridionline, a marker of osteoclast activity in bone, and chorticosterone, and lower bone mineral density than WT mice. These data suggests that NaPi-IIb deficient mice start to resorb bone, in order to maintain circulating levels of Pi upon dietary Pi restriction.

We set up Ussing chamber experiments with rodent intestinal segments as well as with intestinal cell cultures lines to assess paracellular permeabilities for major cat- and anions including Pi. Dilution potential measurements in intestinal cell culture models indicated that the tight junction (TJ) is permeable to Pi, with monovalent Pi ($H_2PO_4^-$) having a higher permeability than divalent Pi (HPO_4^{2-}). These findings could be confirmed in measurements in various intestinal segments from rat and mouse. Moreover, our *ex vivo* experiments indicated that all intestinal segments from duodenum to colon may have a paracellular pathway for Pi. Of interest, no differences in the permeabilities for Na^+, Cl^- and Pi of intestinal TJs was observed between WT and NaPi-IIb deficient mice.

Together, our observations suggests that the paracellular pathway is sufficient to provide NaPi-IIb deficient animals (and potentially also to patients with mutations in NaPi-IIb) with enough Pi as long as dietary Pi is not limited. However, as soon as dietary Pi is restricted, the gradient across the intestinal epithelia might not be enough to support this function, and the kidney cannot compensate for the impaired intestinal absorption in NaPi-IIb depleted mice. Thus, the main role of NaPi-IIb in intestine is to scavenge Pi from diet when the organism is challenged with low Pi availability. Under conditions, when NaPi-IIb is absent, bone may provide an alternative but finite source of Pi for the organism.

Since Pi is involved in many biochemical processes, it is not surprising that the dietary content of Pi does not only alter Pi homeostasis, but has broader systemic impact. A renal transcriptome analysis on mice adapted to high or low dietary Pi was performed to identify renal and intestinal transcripts regulated by changes in dietary Pi intake. Transcriptome analysis revealed that Slc16a14 (MCT14) is strongly upregulated upon HPD. MCT14 is an orphan member of the monocarboxylate transporter family. In mouse, MCT14 mRNA abundance is highest in kidney. To analyze its tissue distribution and regulation on protein level an antibody was developed and validated. Using this antibody, MCT14 was localized to the luminal membrane of the thick ascending limb of the loop of Henle (TAL). Further, the increased mRNA abundance induced by HPD could be confirmed on protein level. In order to identify the transport substrate(s), we expressed MCT14 in *Xenopus laevis* oocytes where MCT14 was integrated into the plasma membrane. However, no transport was detected for the classical substrates of the SLC16 family or for Pi. In summary, MCT14 is an orphan transporter regulated by phosphate and highly enriched in kidney localizing to the luminal membrane of the TAL.

Chapter 1

1. Introduction

1.1 Inorganic phosphate

Inorganic Phosphate (Pi) is among the most abundant intracellular anion and essential for many biochemical processes. Due to its nature as a titratable acid, it acts as a buffer in plasma and urine, where it is present in its monovalent ($H_2PO_4^-$) and divalent (HPO_4^{2-}) forms under physiological conditions. But beyond buffering Pi serves in energy storage and transfer when bound and released from ATP, it builds part of the backbone of DNA and RNA, and defines the polarity of phospholipids of the cell membrane. Intracellular signaling often involves phosphorylation and dephosphorylation of target proteins by kinases and phosphatases, respectively. Moreover, in higher organisms Pi is part of the skeleton in form of hydroxyapatite for physical support of structure. Hence Pi has a variety of important functions in life and its homeostasis is of vital importance, mainly maintained by the coordinated interplay of intestinal absorption and renal reabsorption. We ingest between 700 and 1200 mg of Pi per day; urinary and fecal excretion reflect ingested and absorbed Pi under normal conditions. Pi can be stored in bones complexed with calcium and released upon Pi depletion; under normal condition bone resorption and bone formation are in balance, with a daily exchange of around 300 mg of Pi. Around 700 g of Pi or 85% of total body Pi is stored in bones and teeth, 14% resides intracellularly in soft tissue and only 1% of total Pi content is found in the extracellular fluid, of which 15% is bound to protein. Serum Pi concentration is maintained between 0.8 to 1.45 mM under normal conditions. Since a vast majority of Pi in the body is present as hydroxyapatite, it is no surprise that many factors impacting Pi homeostasis ultimately alter also calcium balance.

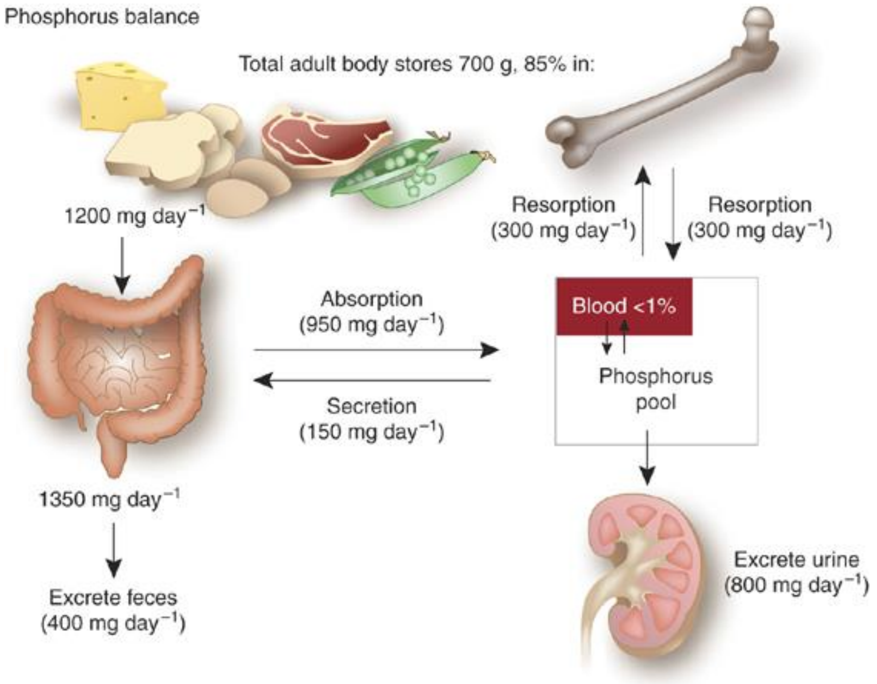

Figure 1: Quantitative Pi balance. The intestine and the kidney are the main organs to (re) absorb and maintain Pi balance. Bones serve as an exchangeable pool of Pi. Taken from Hruska et al*.* (2008) [1].

The interaction of organs involved in Pi homeostais is coordinated by a complex hormonal network and dysregulation of Pi homeostasis has severe adverse effects, as hypophosphatemia can lead to skeletal malformation and muscle weakness and an excess of Pi is associated with an increased cardiovascular mortality. Hyperphosphatemia occurring in patients with chronic kidney disease leads to vascular calcification and secondary hyperparathyroidism.

1.2 Phosphate transport

1.2.1 Sodium dependent phosphate transporters

Transepithelial Pi transport is an important component to maintain Pi homeostasis, since the small intestine absorbs Pi from the diet and the kidney reabsorbs Pi from the glomerular filtrate. Pi transport across the membrane of epithelial cells occurs in a secondary active fashion, as Pi has to be imported into cells against its concentration gradient. The energy is provided by the Na^+ concentration gradient generated by the Na^+/K^+-ATPase located at the basolateral site of epithelial cells [2].The SLC34 family of Na^+ dependent Pi transporters plays a major role in intestinal uptake and renal reabsorption. The family consists of three members NaPi-IIa (SLC34A1), NaPi-IIb (SLC34A2) and NaPi-IIc (SLC34A3). Members of the SLC34 family favor transport of divalent Pi [3,4]. NaPi-IIa and NaPi-IIb transport three Na^+ along with one Pi, which leads to a net import of a positive charge, thus their transport is electrogenic [3]. In contrast NaPi-IIc translocates only two Na^+ with Pi resulting in electroneutral transport [5]. Tough only two Na^+ are translocated, NaPi-IIc requires the interaction of three Na^+ to initiate the transport cycle [6]. Pi transport of SLC34 isoforms shows a pH dependency, which is not solely explained by the titration of divalent Pi, since protons might also compete with Na^+ for binding [7]. NaPi-IIa and NaPi-IIc are localized to the brush border membrane (BBM) of proximal tubular cells in the kidney, where they reabsorb Pi [8,9]. Of interest, in mice NaPi-IIa seems to account for the majority of phosphate transport, since ablation of NaPi-IIa leads to severe Pi wasting in urine and decreased Pi uptake [10]. Inducible deletion of NaPi-IIc in kidney has no impact on urinary Pi excretion in mice [11], whereas in humans genetics demonstrated that the contribution of NaPi-IIa and NaPi-IIc appears to be more similar [12]. NaPi-IIa and NaPi-IIc are mainly expressed in kidney whereas NaPi-IIb is localized to the luminal membrane in the small intestine [13,14] and is also expressed in testis, lungs and lactating mammary glands [13]. NaPi-IIa and NaPi-IIc show a similar affinity for Pi with an apparent K_m <100 µM and around 40 mM for Na^+ at pH 7.4 [15,16], which is below the range of concentration typically found in the renal proximal tubule; therefore they probably transport Pi close to their maximal capacity. NaPi-IIb displays a lower affinity for Pi of about 10 µM, which might be due to the more acidic environment of the small intestine and the consequently lower availability of divalent Pi [16]. The primary structure of the SLC34 transporters ranges from 599 to about 689 amino acids, with sequence differences mainly in the C- and N-termini [2]. All members are predicted to have twelve transmembrane domains, C- and N-terminus intracellular and a big extracellular loop between the fourth and fifth transmembrane domain [17]. SLC34 members harbor a PDZ binding domain in their C-terminus, which is of importance for apical expression and regulatory mechanisms [18,19]. The 3D structure for SLC34 members is unknown, but a computational approach using the structure of VcINDY (bacterial Na^+ dependent dicarboxylate transporter) as a template predicted a structure of NaPi-IIa revealing important residues for substrate binding, which were experimentally confirmed in Xenopus laevis oocytes heterologously expressing the corresponding NaPi-IIa mutants [20,21].

The other known Pi transporters, Pit-1 and Pit-2, belong to the SLC20 family. In contrast to the SLC34 family they favor monovalent Pi and transport Pi together with Na^+ in a 1:2 ratio, hence they are electrogenic [22,23]. Up to date they have been granted little contribution in transpepithelial Pi transport. They have a much wider tissue distribution than the SLC34 isoforms. Pit-1 might play a role in bone Pi handling, parathyroid function, as well as in vascular calcification observed in hyperphosphatemic conditions. Pit-2 mutations have been identified in patients suffering from basal ganglia calcification [24], and knock-out mice show increased Pi levels in the cerebral spinal fluid, decreased body length and bone mineral density [25]. These observations might suggest an important role of SLC20 isoforms apart from intestinal and renal Pi re-/absorption; even though Pit-2 expression was shown in the BBM of renal proximal tubules, its exact role in Pi homeostasis needs further investigation.

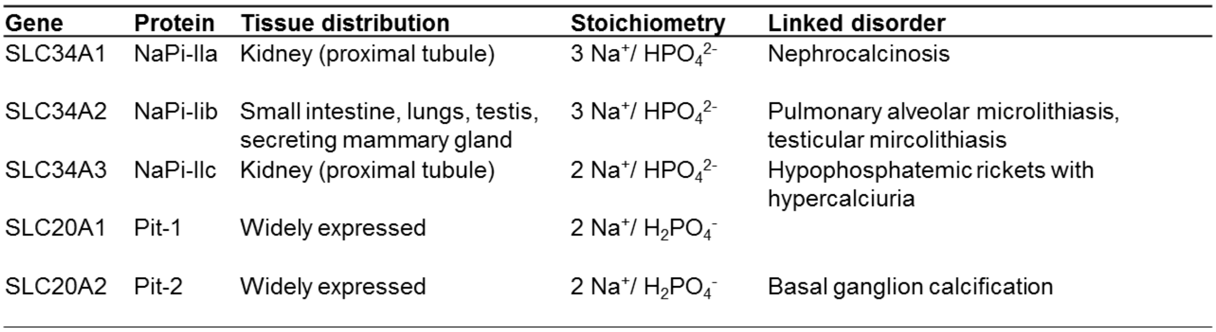

Gene	Protein	Tissue distribution	Stoichiometry	Linked disorder
SLC34A1	NaPi-IIa	Kidney (proximal tubule)	$3\ Na^+/\ HPO_4^{2-}$	Nephrocalcinosis
SLC34A2	NaPi-Iib	Small intestine, lungs, testis, secreting mammary gland	$3\ Na^+/\ HPO_4^{2-}$	Pulmonary alveolar microlithiasis, testicular mircolithiasis
SLC34A3	NaPi-IIc	Kidney (proximal tubule)	$2\ Na^+/\ HPO_4^{2-}$	Hypophosphatemic rickets with hypercalciuria
SLC20A1	Pit-1	Widely expressed	$2\ Na^+/\ H_2PO_4^-$	
SLC20A2	Pit-2	Widely expressed	$2\ Na^+/\ H_2PO_4^-$	Basal ganglion calcification

Table 1: Na^+-dependent Pi transporters of the SLC34 and SLC20 families

Apical entry of Pi into epithelial cells of kidney and intestine has been studied extensively, but only little is known about the basolateral efflux mechanism in those cells. It has been reported that xenotropic and polytropic virus receptor XPR1 can mediate the efflux of Pi in cultured cells [26]. Transport studies in Xenopus laevis oocytes failed to proof Pi efflux activity mediated by XPR1, including our own unpublished observation. Nevertheless, XPR1 seems to be one of the few proteins in mammals that contains the SPX domain, which is a domain shared by many proteins involved in plant and fungal Pi sensing and transport. XPR1 shares sequence homologies with the plant phosphate PHO1 and the yeast SYG1. Both proteins seem to be involved in phosphate transport or sensing. Recently, it was reported that the SPX domain might offer a binding site for inositol poly phosphate [27], the concentration of which change upon Pi availability. The authors suggest that this inositol poly phosphate concentration might be part of the Pi sensing mechanism, to trigger response to Pi starvation [27]. Indeed a protein named Pi uptake stimulator (PiUS) identified in uptake experiments performed in Xenopus laevis oocytes turned out to be a hexakisphosphate kinase [28], able to convert inositol-6-phosphate into inositol-7-phosphate. This might suggest that XPR1 has a role in Pi sensing, and that the observed mediation of Pi efflux in cell culture could be through regulatory or accessory action of XPR1. Inducible renal specific ablation of Xpr1 in mice leads to hypophosphatemia accompanied hyperphosphaturia and impaired bone mineralization [29]. Pi efflux in isolated proximal tubular cells is impaired upon Xpr1 deletion. Despite this Pi related effects, those mice excrete massive amounts of glucose, amino acids and albumin [29] indicating severe renal damage. This severe phenotype might suggest that Xpr1 might be involved in more than just the suggested Pi efflux.

1.2.2 Intestinal Pi absorption

Dietary Pi is mainly absorbed in the small intestine with a possible contribution of the colon. Though experiments using radiolabeled Pi [30] or enemas with very high Pi concentrations [31] highlight that the colon has the ability to absorb Pi, the physiological relevance of this transport remains elusive, since many studies point out the higher absorptive capacity for Pi in the small intestine. Additionally, solidity of colon content might make Pi less available for absorption in the large intestine. Several studies propose two different mechanisms by which Pi is absorbed in the intestine: passive diffusion along the paracellular route and secondary active transport across the apical membrane of intestinal cells. Early reports indicated that an intragastric bolus of Pi in rats increased plasma Pi levels linearly with increasing Pi concentration of the bolus [32], indicating a passive diffusion mechanism since no saturation was observed. However everted gut sac experiments showed Na^+ dependency of Pi transport in rachitic chick ileum [33]. Further experiments in Ussing chambers, using rat jejunum, suggested a two component transport, with a linear relationship of transport at luminal Pi concentrations above 1 mM, whereas below 1 mM Pi transport appeared more complex and an active transport system seemed more likely, since a passive system alone would cause a Pi flux from blood to the intestinal lumen following the chemical gradient [34]. These observations were confirmed in intestinal transport studies in humans [35,36], confirming the existence of both transport mechanisms for Pi in the gastrointestinal tract. Since then the active transcellular transport was extensively studied and cloning of NaPi-IIb [13] revealed at least a part of the molecular mechanism behind.

Transcellular Pi transport in mice occurs mostly in ileum. In contrast rats show higher transport in duodenum and jejunum, which seems also to be the case for humans [14,37]. This difference in Pi transport between rats and mice is also reflected in the expression pattern of NaPi-IIb, since NaPi-IIb is expressed in enterocytes of the corresponding segments (Figure 2) [14]. The transporter is expressed along the whole intestinal villi, whereas no expression is observed in crypt cells [38]. NaPi-IIb appears to be the major transporter for Pi in the small intestine with possible (but untested) contribution of Pit-1 and Pit-2 [39]. Though both Pit-transporters have been detected in BBM preparations of small intestine [37,40], their subcellular distribution has not been fully characterized by immunohistochemistry; Pit-1 mRNA has been localized throughout the whole epithelum including crypts in intestine [41]. The relative contribution of Pit-1 and Pit-2 in intestinal Pi transport remains elusive, but knock out animal models suggest a dominant role of NaPi-IIb in intestinal Na^+/Pi cotransport [42,43]. Constitutive deletion of NaPi-IIb has proven to be embryonically lethal, likely due to impaired Pi absorption from the maternal circulation [42]. In humans mutations in NaPi-IIb manifest with pulmonary and testicular microlithiasis, deposits of Pi and calcium in lungs, but no changes in serum Pi levels are observed [44]. No information about any possible compensatory mechanism or hormonal changes in these patients is available. These data indicate that there is another transport mechanism, most likely passive diffusion across the paracellular route, which provides patients and NaPi-IIb deficient mice sufficiently with Pi. The abundance of NaPi-IIb in intestine is regulated by several factors like glucocorticoids [45] and estrogen, but the two major stimulators are vitamin D_3 and low dietary Pi content [46]. Animals fed a low Pi diet show increased uptake of Pi into intestinal BBMV and NaPi-IIb protein abundance compared to animals fed high Pi diet [38]. Similar effects were observed in animals injected with vitamin D_3 [47]. Co-immunoprecipitation and Förster resonance energy transfer (FRET) experiments show a physical interaction between NaPi-IIb and NHERF1, likely through the PDZ domain in the C-terminal tail of NaPi-IIb [48]. Adaptation of NaPi-IIb to dietary Pi was impaired in NHERF1 deficient mice [48], suggesting an important role of NHERF1 in the regulation of NaPi-IIb in a similar fashion to NaPi-IIa in kidney (see 1.2.3) [49]. Up to date no other major Pi transporter in the intestine is known, though there are reports for a pH dependent mechanism in goat duodenum, where NaPi-IIb is absent [50], and in the intestinal Caco2BBE cell line [51], but the molecular mechanism behind remains elusive.

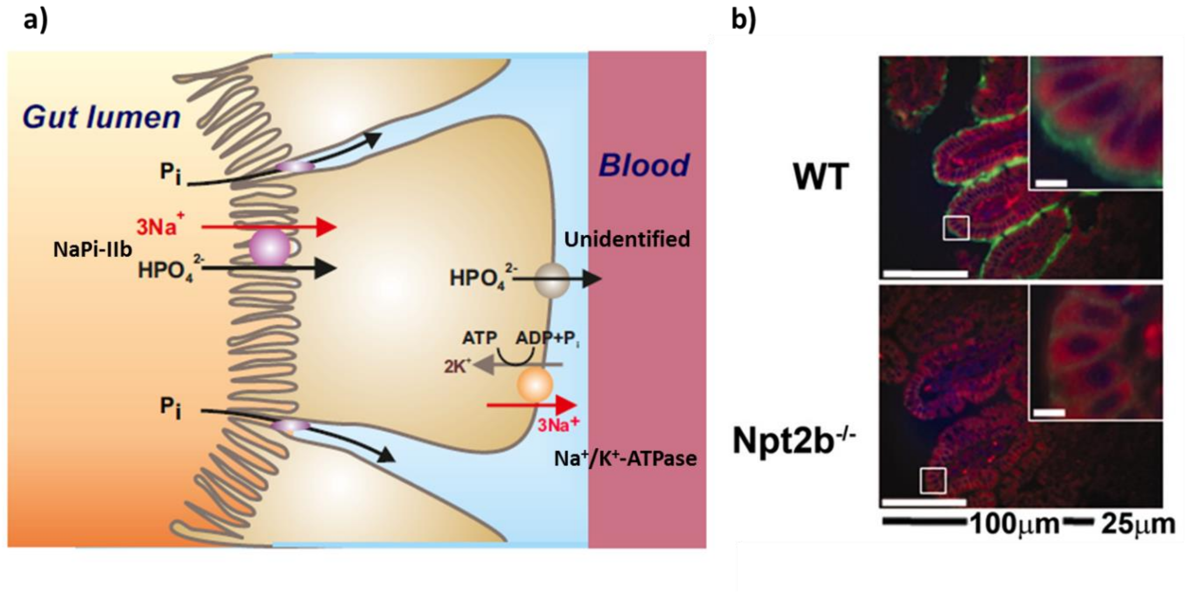

Figure 2: a) Representation of intestinal Pi transport mechanisms mediated by NaPi-IIb which is driven by the basolateral Na^+/K^+-ATPase. Mechanisms for Pi export or paracellular diffusion remain to be identified. The subcellular localization of Pit-1/2 has not been determined. Adapted from Forster Ian unpublished. **b)** NaPi-IIb expression in enterocytes in WT and NaPi-IIb deficient mice. Adapted from Sabbagh et al. (2009) [52]

Compared to transcellular transport of Pi, only little is known about paracellular Pi fluxes across the intestinal epithelium. Passive diffusion through the tight junctions requires a chemical gradient for Pi from the lumen of the intestine to the blood. It has been reported that under normal dietary conditions luminal Pi concentrations exceed the levels in serum [53] consistent with our own observation, providing a gradient for passive absorption of Pi across the intestinal epithelium. Epithelia form physical and chemical barriers between two body cavities and tight junctions seal the space between adjacent cells, by interaction of junctional proteins from each neighboring cell, preventing free passage of ions, other molecules, and cells [54]. Thus passive diffusion along the paracellular pathway requires the presence of pore forming complexes in the tight junction, which are rather substrate specific and help to maintain barrier function of the epithelium. The claudins are a family of tight junction proteins, which form strands along the tight junction that interact with the strands of claudins of adjacent cells and contribute to transepithelial resistance [55-57]. Freeze fracture images indicated that increasing the number of tight junction strands correlates with increasing transepithelial resistance and paracellular transport [54,58]. Diffusion potential measurements and flux studies suggested that the conductance of tight junctions is charge and size selective [59,60]. Claudin-2 was then the first claudin to be identified as a paracellular cation channel (Figure 3) [61]. Nowadays, there are 27 claudin genes, though not all of them are expressed in every species, where some have barrier and some conductive properties [54]. Several of them have been characterized as anion or cation selective, but up to date there has been no association of a particular claudin with Pi permeability across epithelia; furthermore whether claudins participate in Pi uptake in the intestine is still to be determined. However, the linear correlation between Pi fluxes and luminal Pi concentrations at high luminal Pi [32,35], strongly indicates a paracellular contribution. Additionally the relatively mild phenotype in mice with deletion of NaPi-IIb, despite the absence of transport of Pi into ileal BBMV [43] supports this hypothesis. One might also consider the reduction of NaPi-IIb expression and the lower uptakes observed in animals fed a high Pi diet [47]. Moreover, one may take also into account that NaPi-IIb might be already saturated at normal dietary conditions with the given luminal Pi concentration [53]. Still there is a higher delivery of Pi from the intestine, despite lower NaPi-IIb, possibly driven by the higher chemical gradient provided by the diet, since those mice excrete much higher levels of Pi in urine. In the study presented here, we attempt to get a better understanding of overall mechanisms of intestinal Pi absorption with the possible contribution of the paracellular pathway.

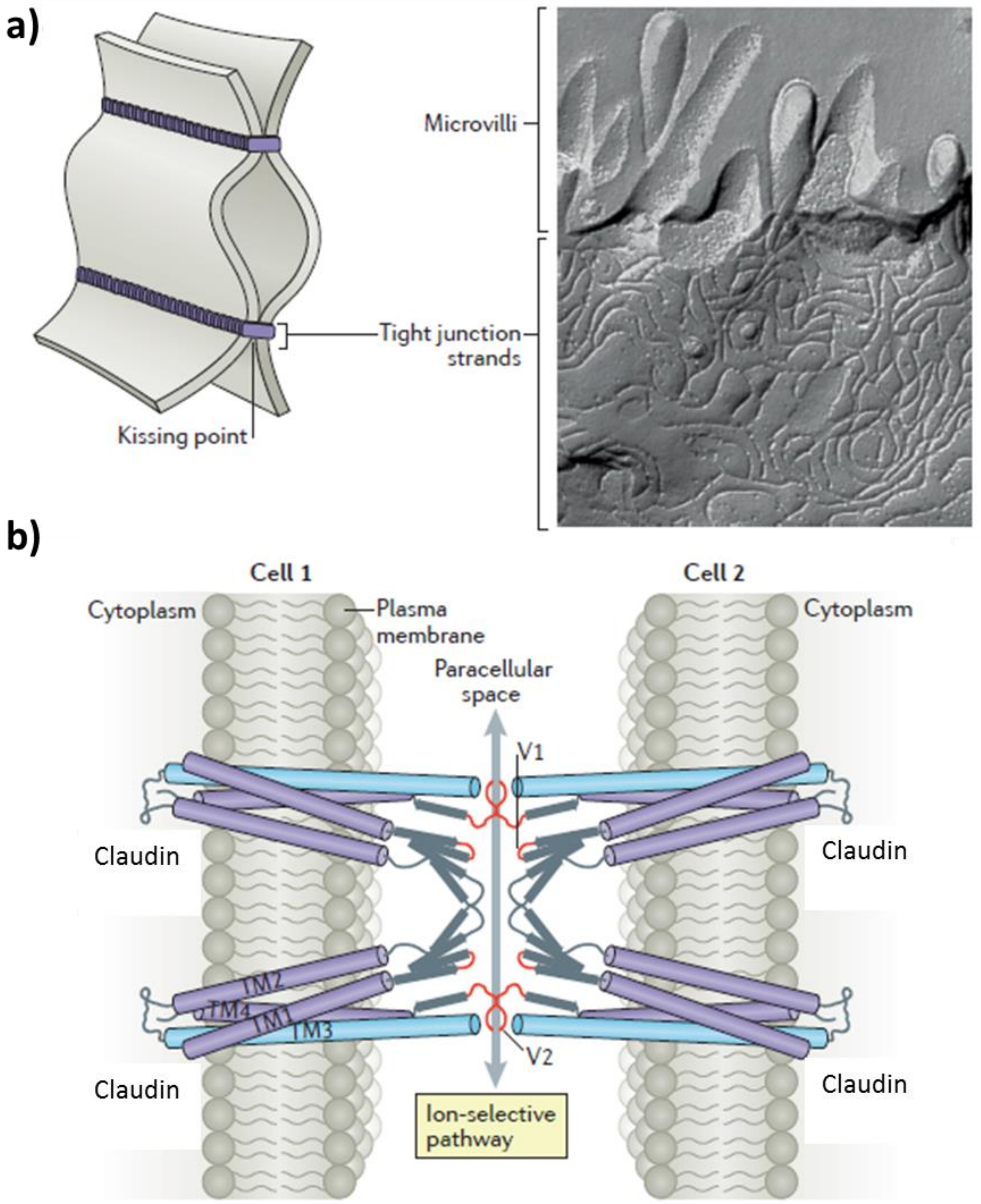

Figure 3: a) Schematic representation of tight junction strands connecting two adjacent cells and a corresponding freeze fracture electron microscopy picture of microvilli and the tight junction strands beneath. **b)** Intracellular space between two adjacent cells. In each membrane are shown two claudins interacting in trans, and the cis interaction between claudins of neighboring cells, which are thought to represent the strands observed in the freeze fracture image. The interacting claudins form a selective pore for the paracellular pathway, in which selectivity depends on the expressed claudin. Modified from Zihni et al. (2016) [62].

1.2.3 Renal phosphate reabsorption

The glomerulus in the kidney freely filters Pi, and consecutive nephron segments reabsorb Pi form the primary filtrate to prevent its loss. Approximately 90% of the filtered Pi is reabsorbed [63]. The proximal tubule is the main segment involved in renal Pi reabsorption, and the contribution of later segments to overall Pi reabsorption is not entirely clear [64,65]. Under normal conditions the initial proximal tubule (S1) is the segment contributing the most to Pi reabsorption, reflecting the expression of NaPi-IIa, NaPi-IIc and Pit-2 (Figure 4) [9,66,67]. The amount of Pi excreted in the urine is proportional to the amount of Na^+/Pi cotransporters expressed in the BBM of the proximal tubule [63]. Under dietary Pi restriction the abundance of NaPi-IIa, NaPi-IIc and Pit-2 is enhanced and expression of NaPi-IIa extends to S2 and S3 segments of the proximal tubule [68], resulting in reduced Pi excretion in urine. Different time courses in adaptation to low dietary Pi for the three transporters are observed, where NaPi-IIa regulation appears to be the fastest [69]. There are several factors involved in modulating Pi excretion, the most prominent phosphaturic hormones are parathyroid hormone (PTH) [70] and fibroblast growth factor 23 (FGF23) [71], that act by decreasing the amount of Na^+/Pi cotransporters expressed in the kidney. As already discussed, NaPi-IIa has a major role in renal Pi handling, and its expression and hormonal regulation seems to depend on the interaction with NHERF1 (NHE3 regulatory factor 1) through its C-terminal PDZ-binding domain [72,73]. Physical interaction between the two proteins is important for stable retention of NaPi-IIa in the BBM [74]. NHERF1 indirectly associates with actin [75], and thereby anchors NaPi-IIa in the membrane. Phosphaturic factors as PTH [76,77] and FGF23 [71,78] lead to a phosphorylation at the interaction domain of NHERF1 and hence reduce binding to NaPi-IIa, further leading to the retraction of NaPi-IIa from the membrane and targeting to lysosomes for degradation [79]. Additionally, deletion of Nherf1 in mice results in lower NaPi-IIa abundance and hyperphoshaturia [49]. Mutations of NHERF1 in humans have been reported to cause hypophosphatemia supporting the findings in mice [80]. Similarly, the ablation of Nherf3 (Pdzk1) in mice impairs the regulation of NaPi-IIc, though a direct physical interaction has not been demonstrated. Nherf3 ablation has no effect on NaPi-IIa or renal Pi excretion [81].

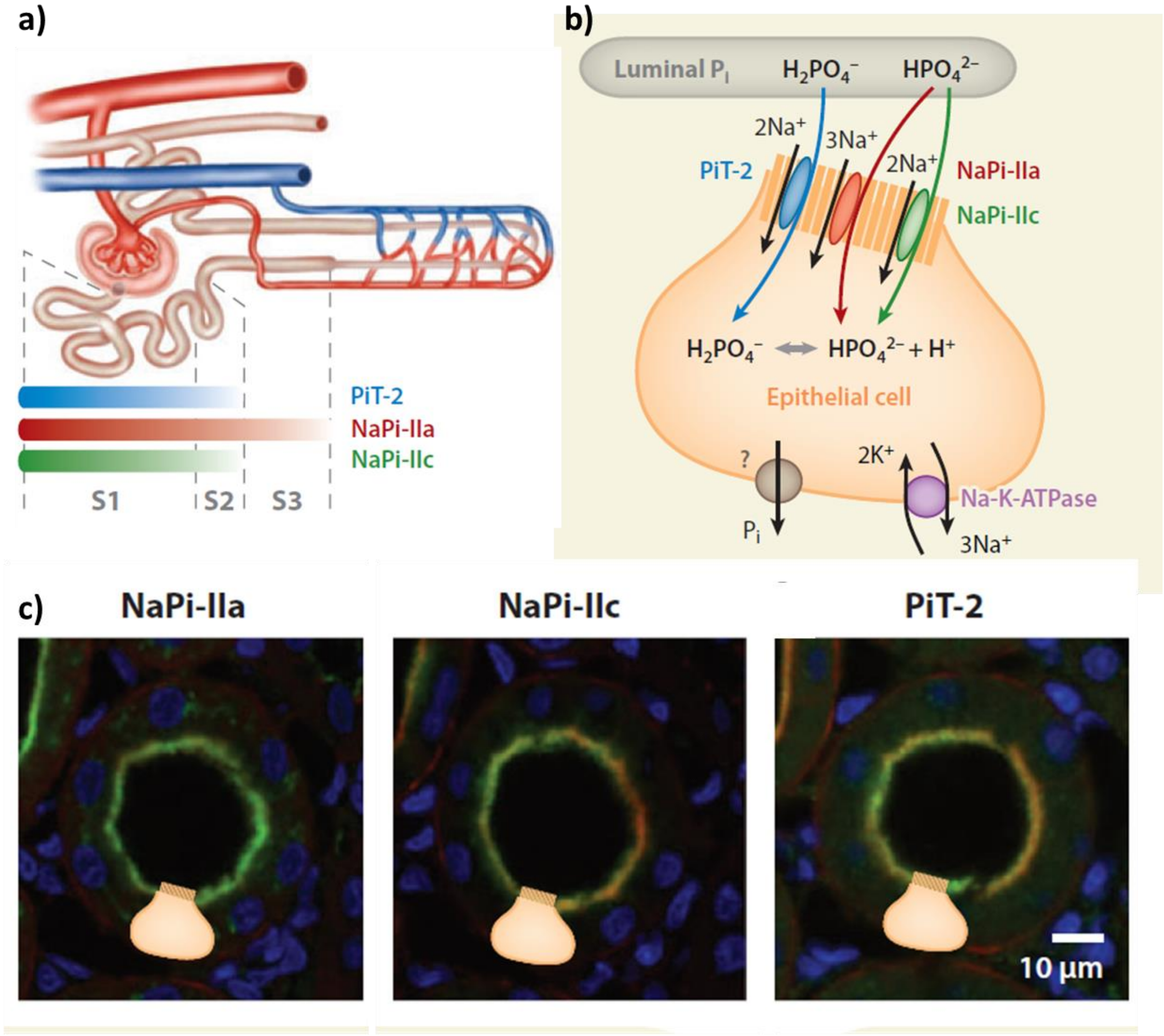

Figure 4: a) Renal distribution of Na$^+$-dependent Pi transporters. **b)** Representation of Na$^+$-dependent Pi transport across a proximal tubular cell. NaPi-IIa and NaPI-IIc are expressed apically and favor transport of divalent Pi, whereas Pit-2, also expressed in the apical membrane, prefers monovalent Pi. Transport is energized by the basolateral Na$^+$/K$^+$-ATPase. Basolateral efflux mechanism remains to be identified. **c)** Immunofluorescence staining of NaPi-IIa, NaPi-IIc and Pit-2 in the apical membrane of a cell in S1 of proximal tubules, where transporters are shown in green, red represents β-actin (phalloidin) and blue represents nuclear (DAPI) staining. Adapted from Biber et al. (2013) [2].

1.3 Hormonal Regulation

The total amount of Pi transporters in BBM of intestine and kidney are tightly regulated by a hormonal network including PTH, FGF23, and vitamin D_3. Vitamin D_3 increases Pi absorption in the gut, whereas PTH and FGF23 both act as phosphaturic factors to decrease plasma levels of Pi (Figure 5). Furthermore, vitamin D_3 and PTH are major regulators of Ca^{2+} homeostasis, where both hormones promote an increase in circulating Ca^{2+}. These hormones do not only exert effects on Pi and Ca^{2+} transport but also regulate each other in a cross talk between organs.

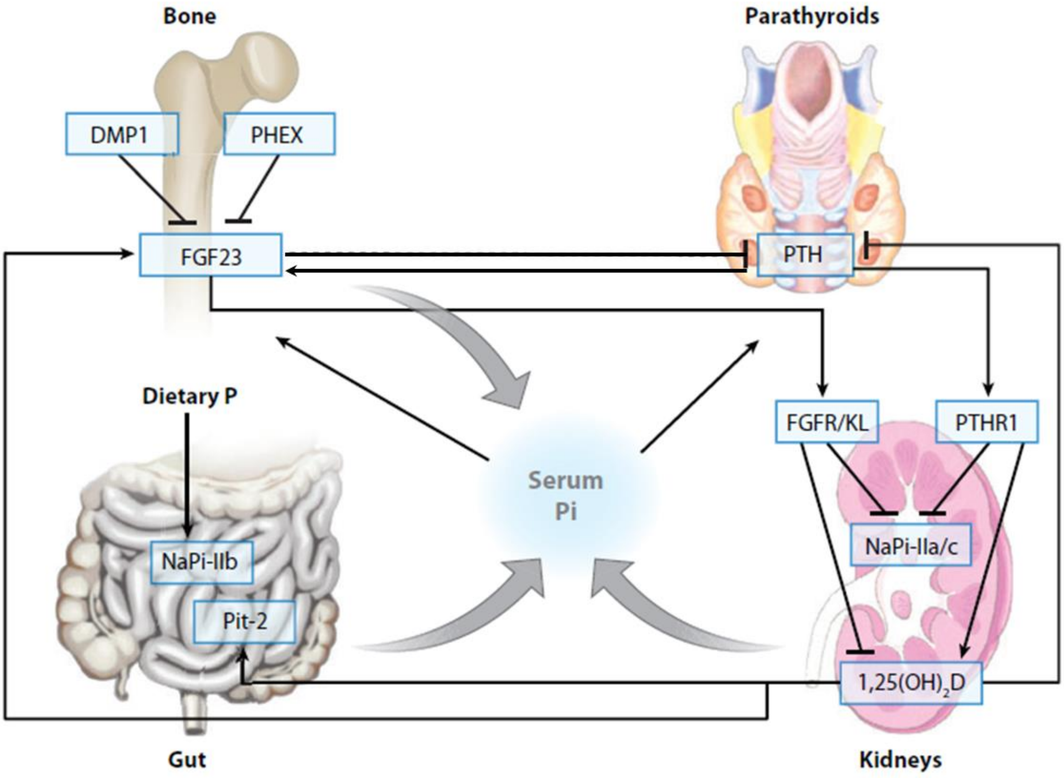

Figure 5: Pi homeostasis is maintained by intestinal absorption, renal reabsorption and bone formation/reabsorption. Vitamin D_3 stimulates intestinal absorption and the expression of FGF23, whereas PTH synthesis is inhibited. PTH inhibits renal reabsorption and promotes vitamin D_3 and FGF23 production. FGF23 suppresses renal reabsorption as well as PTH and vitamin D_3 synthesis. Modified from Bergwitz et al. (2010) [82].

1.3.1 Vitamin D_3

The production and activation of vitamin D_3 involves several organs starting in the skin, where 7-dehydrocholesterol and ergosterol are converted into cholecalciferol due to the exposure to ultraviolet light. Cholecalciferol is then hydroxylated by CYP2R1 in liver to 25-hydroxycholecalciferol [83,84], which upon another hydroxylation in the renal proximal tubule by the 1α-hydroxylase (CYP27B1) is turned into the active form 1,25-dihydroxycholecalciferol [85]. Another enzyme in the proximal tubule CYP24A1 is responsible for the inactivation of vitamin D_3 through 24-hydroxylation [86,87]. The 1α-hydroxylase is induced by hypophosphatemia, hypocalcemia and PTH [82], hence these conditions enhance vitamin D_3 production. FGF23 and vitamin D_3 itself increase the expression of renal CYP24A1 to inactivate vitamin D_3 [88].

Vitamin D_3 acts on target organs by binding the vitamin D receptor (VDR). VDR is a cytosolic protein and acts as a nuclear receptor. Upon binding its ligand, VDR dimerizes with retinoid-X-receptor [89,90], translocates to the nucleus and modulates expression of genes with a VDR responsive element [91], though there have been also non-transcriptional effects reported [92]. VDR deficient mice show low levels of serum Pi and FGF23, impaired bone formation, and have a shorter life span [93].

In the intestine vitamin D_3 induces the expression of the TRPV6 (transient receptor potential cation channel subfamily V member 6) Ca^{2+} channel and the plasma membrane Ca^{2+}-ATPase leading to increased Ca^{2+} absorption [94]. In addition, the renal expression of TRPV5 and calbindin-$D28_K$ is enhanced and thereby renal Ca^{2+} reabsorption also increases [95]. In enterocytes vitamin D_3 also enhances the RNA and protein expression of NaPi-IIb [38] and Pit-2 [96]. Consistently, VDR knock out mice show a decreased amount of NaPi-IIb mRNA and develop hypophosphatemia and hypocalcemia [97] similar to the phenotype of Cyp27b1 knock out mice [98]. In contrast animals injected with vitamin D_3 had no increase in NaPi-IIb mRNA but protein abundance of the cotransporter was upregulated [38], indicating that there are also transcription independent effects. In addition to vitamin D_3, a major stimulator of intestinal Pi transport is dietary Pi depletion that was initially assumed to act through vitamin D_3 to enhance transcription of NaPi-IIb. However when VDR knock out animals were challenged with a low Pi diet, intestinal abundance of NaPi-IIb was increased as in the wild type animals, suggesting that dietary restriction can induce NaPi-IIb independently of vitamin D_3 [47]. In bone, vitamin D_3 stimulates osteoclasts [99], in order to increase bone resorption and hence promotes the release of Pi and Ca^{2+}. In osteoblasts and osteocytes vitamin D_3 enhances the production and release of FGF23. The promotor region of FGF23 harbors a vitamin D_3 responsive element [100], and as indicated above VDR deficient mice have hypophosphatemia, hyperparathyroidism, and low levels of plasma FGF23. A high Pi and Ca^{2+} diet corrects these alterations, suggesting that Pi can regulate FGF23 in a vitamin D_3 independent manner. Activation of VDR in the parathyroid gland suppresses the transcription of PTH-gene harboring an VDR-responsive element [101].

1.3.2 Parathyroid hormone

PTH is synthesized as a prepro-peptide consisting of a 25-amino acid signal sequence, a 6-amino acid prosequence and a 84-amino acid sequence exerting the hormonal activity. The signal- and prosequence are cleaved in the endoplasmic reticulum and Golgi, and the active (1-84) PTH is stored in secretory vesicles [82]. The release of PTH is stimulated by low serum Ca^{2+} and high Pi. Plasma levels of Ca^{2+} are sensed by the parathyroid glands through the calcium sensing receptor (CaSR). The CaSR is G-protein coupled receptor; upon binding of Ca^{2+} to the receptor, G_q associated phospholipase C catalyzes the hydrolysis of PIP_2 into IP_3 and diacylglycerol (DAG) [102]. IP_3 leads to a release of Ca^{2+} from the endoplasmic reticulum to activate Ca^{2+}-sensitive proteases to cleave PTH in secretory vesicles and inactivate it [82]. High intracellular Ca^{2+} as well as DAG-activated PKC also inhibits PTH expression and release. On the contrary, inactivation of the CaSR in situations of low plasma Ca^{2+} stimulates the synthesis and release of PTH [103]. Hyperphosphatemia is also a strong stimulator for PTH synthesis and secretion; though the mechanism by which Pi levels are sensed by the parathyroid gland are not known, high Pi leads to increased PTH mRNA stability, through protein binding at the 3'-UTR [104]. Hyperphosphatemia induces PTH independent of Ca^{2+}, since cell culture experiments showed and increased secretion of PTH despite high levels of Ca^{2+} [105]. Oral application of Pi in humans leads to an increase of circulating PTH after 45 minutes [106], similarly rats show an increase in PTH after intravenous and intragastric Pi administration [107]. Intravenous administration led to a massive phosphaturia and a drop in serum Ca^{2+} within 10 minutes, whereas intragastric Pi application caused a delayed phosphaturia without altering Ca^{2+}. Phosphaturia was blunted in parathyroidectomized rats, which show a higher creatinine clearance without alteration of renal Pi transporter expression.

PTH exerts its effect on target cells through the PTH-receptor (PTHR1). PTHR1 is a G-protein coupled receptor that activates PKC signaling by coupling to G_q and PKA signaling by coupling to G_s and therefore cAMP production by adenylyl cyclases; both pathways were shown to activate MAPK signaling. In renal proximal tubules PTH reduces the membrane abundance of NaPi-IIa, NaPi-IIc and Pit-2 and thereby promotes phosphaturia [9,108]. PTHR1 is expressed on apical and basolateral sites of these cells, where apical binding of PTH is associated with G_q-signaling and basolateral with G_s and consequently PKA signaling [109].

Inhibition of either PKA or PKC dependent action suggests both to be involved in the regulation of renal Pi transport [109]. PKA phosphorylates NHERF1 in the PDZ domain that interacts with the PDZ-binding domain of NaPi-IIa, lowering the interaction affinity. As already indicated (1.2.3) the reduced binding to NHERF1 allows NaPi-IIa to be retrieved from the membrane and consecutively to be routed for lysosomal degradation [76,77]. Mice expressing a PTHR1 deficient in G_q-dependent activation of PKC do not develop hypophosphatemia when hyperparathyroidism is induced by Ca^{2+} free diet [110]. This suggests that PTH induced phosphaturia is at least partially dependent on G_q and PKC signaling. The mechanism behind PTH induced downregulation of NaPi-IIc and Pit-2 remains elusive, but NaPi-IIc seems to undergo degradation in a different compartment than NaPi-IIa (i.e. lysosomes) upon PTH signaling.

PTH also enhances Ca^{2+} reabsorption in the distal convoluted tubule in the kidney, by stimulating the transport activity of TRPV5 as well as the expression of calbindin $D28_K$ and the Na^+/Ca^{2+}-exchanger NCX [111]. Additionally it increases expression of CYP27B1, resulting in an increased production of active vitamin D_3 [112], in order to stimulate intestinal absorption of Ca^{2+}.

In bone, PTH induces resorption mediated by osteoclasts. This activation is indirect, since osteoclasts do not express PTHR1. Continuous administration of PTH results in reduced expression of osteoprotegrin a member of the TNF-receptor family and increased abundance of RANKL (itself a TNF ligand). These changes trigger osteoclast precursors to mature and resorb bone [113]. Additionally PTH increases the expression of FGF23 in osteoblasts and osteocytes. The increased expression of FGF23 seems to be dependent on PKA activity upon PTHR1 activation, which promotes FGF23 mRNA synthesis possibly through the transcription factor Nurr1 [114]. Consequently FGF23 concentration is reduced after parathyroidectomy [115]. PTH ablation in mice leads to a renal loss of Ca^{2+}, high Pi levels due to Pi retention, decreased circulating vitamin D_3 and FGF23 concentrations and abnormal bone formation [82,116,117].

1.3.3 FGF23

The fibroblast growth factors are a family of 22 peptides involved among other processes in organogenesis, development, and wound healing. Most FGFs have a heparin binding domain with high affinity for heparan sulfates, which is critical for their receptor binding and signaling function [118]. The binding to heparan sulfate in the extracellular matrix restricts FGF action locally, thus most of them act in a paracrine and autocrine fashion [119]. However the FGF19 subfamily lacks the domain for heparan sulfate binding, facilitating their release and enables them to act as endocrine factors [120]. FGFs act through FGF receptors (FGFR1-4), which consist of three extracellular immunoglobulin like domains, a transmembrane domain and an intracellular tyrosine kinase [118,120]. Heparan sulfate is essential for formation of the FGF-FGFR complex [119]; the lack of the heparin binding domain in endocrine FGFs is compensated by Klotho as a cofactor to bind the receptor [121]. The Klotho family of single transmembrane domain proteins consists of three members α, β and γKlotho. FGFRs dimerize upon binding of FGFs, followed by an autophosphorylation.

FGF23 belongs to the endocrine FGFs, it binds to FGFR1, 3 and 4 in complex with αKlotho [122]. Though recently it has been shown that FGF23 can induce cardiac hypertrophy through FGFR4 in absence of αKlotho [123]. FGF23 is a 251 amino acid glycoprotein [124] and is mainly expressed in osteoblasts [125] and osteocytes [126] in bone, tough expression in other tissues like heart, parathyroid gland, small intestine, thymus and brain [118,127]. FGF23 expression has also been detected in renal cysts in a mouse model for polycystic kidney disease (PKD1) [128], and elevated FGF23 levels is a common feature in patients suffering from CKD. The protein consists of an N-terminal hydrophobic signaling sequence, an N-terminal FGF-like domain and a C-terminal sequence containing binding sites for the FGFR

(Figure 6) [118]. The N- and C-terminal domains are separated by a proteolytic cleavage site (RXXR) [129]. Proteolytic cleavage leads to inactivation of FGF23 [130], and the C-terminal fragment probably competes for binding to the receptor with the intact FGF23, potentially further decreasing the action of FGF23 [131]. There are four O-glycosylation sites around the RXXR site [118,127], and glycosylation through the N-acetylgalactos aminyltransferase 3 (GALNT3) prevents cleavage at the RXXR site [132]. Consequently Galnt3 deficient mice have lower levels of circulating FGF23, even though FGF23 gene expression is dramatically increased. The production of FGF23 is stimulated by high serum levels of Pi, vitamin D_3 and PTH [133,134]. There is also evidence that Ca^{2+} might reduce FGF23 levels [135]. Additionally in vitro experiments using HEK293 cells showed an increased expression when stimulated with high concentrations of Pi [136]. The increase in GALNT3 might just match increased expression of FGF23 or further stabilize circulating FGF23 levels.

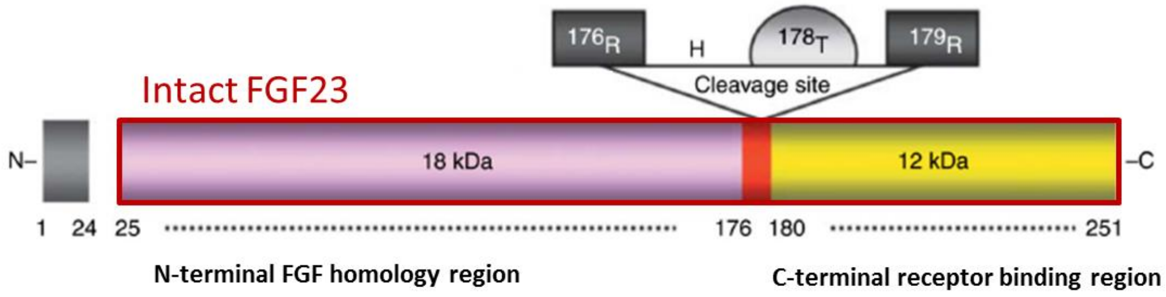

Figure 6: Structure of the full length intact fibroblast growth factor 23 (framed in red) after removal of the N-terminal signal peptide. The RXXR motive between position ^{176}R and ^{179}R is the site for proteolytic cleavage and inactivation of FGF23. ^{178}T represents one of the glycosylation sites, which prevent FGF23 from being cleaved upon glycosylation. Modified from Razzaque et al. (2007) [137].

In kidney FGF23 inhibits Pi reabsorption as well as vitamin D_3 synthesis. The effect on renal Pi transport is likely to be mediated by FGFR1, since administration of FGF23 to FGFR3 and FGFR4 ablated mice leads to a reduction of serum Pi levels, whereas in FGFR1 deficient mice the FGF23-dependent serum Pi decline is absent [138]. Receptor binding increases extracellular signaling regulated kinase (ERK1/2) phosphorylation, which phosphorylates the SGK1 [71]. SGK1 acts on the same phosphorylation site in the PDZ domain of NHERF1 which is targeted by PTH signaling (see 1.3.2) [71,76,78]. Consequently, NaPi-IIa is internalized and targeted for lysosomal degradation. This effect is absent in Klotho deficient mice and similarly in mice with FGF23 ablation [71] these mice have hyperphosphatemia, high levels of vitamin D_3 and suffer from tissue calcification, highlighting the importance of Klotho in FGF23 function. Furthermore, FGF23 reduces plasma vitamin D_3 levels, since it decreases the expression of CYP27B1 and upregulates mRNA and protein abundance of CYP24A1 in a MAPK dependent fashion [139,140]. Inhibition of the MAPK pathway blunts this effect [141]. It was also reported that FGF23 leads to a downregulation of intestinal NaPi-IIb [142], but this might be a secondary effect due to decreased plasma vitamin D_3 levels. There is also evidence that FGF23 stimulates Ca^{2+} reabsorption in the kidney through activation of TRPV5 in the distal convoluted tubule [143].

Parathyroid glands are equipped with FGFR1 and 3 as well as with Klotho [144]; administration of FGF23 was shown to downregulate PTH mRNA levels in parathyroid glands and decreases serum PTH [144]. The effect of FGF23 is ERK1/2 dependent, since its inhibition prevents the effect of FGF23 on PTH [144]. Furthermore FGF23 increases expression of CaSR and VDR, sensitizing the parathyroid gland for PTH repressive signals [145].

1.3.4 Glucocorticoids

Glucocorticoids (GCs) are steroid hormones synthetized by the cortex of the adrenal gland from cholesterol. Their effects are mediated by a cytoplasmic receptor, which once it is bound to its ligand translocates to the nucleus and regulates the expression of target genes containing GC-response elements. While cortisol is the main GC in humans, corticosterone (17-deoxycortisol) is the main counterpart in several other species including rodents.

Although their role is not entirely clear, there is evidence that GCs alter Pi homeostasis. GCs administration to several experimental animals models lowered serum levels of Pi and induced phosphaturia [146-149]. The site of action was assumed to be in the renal proximal tubule, where GC receptors are expressed. Indeed the GC dexamethasone decreased Na^+-dependent uptake of Pi into renal BBMV in rats [150] and reduced NaPi-IIa mRNA and protein abundance [151]. Further it has been demonstrated that GC administration also results in a downregulation of intestinal NaPi-IIb mRNA and protein [152]. However, the molecular mechanisms by which GC modulate Na$^+$-dependent Pi cotransporters has not been resolved yet.

GCs also alter bone remodeling through an increase in bone resorption and decreased bone formation [153,154]. Long term treatment with GCs has been shown to decrease bone mineral density and induces osteoporosis [155,156]. Osteoblast specific ablation of the GC receptor in mice prevents these effects [157], indicating that GCs directly act on osteoblasts to inhibit bone formation. Additionally, GCs inhibit differentiation and induce apoptosis of osteoblasts and osteocytes [158,159], further decreasing bone formation rate. GCs also increase osteoclast number through RANKL-RANK and osteoprotegrin dependent differentiation (see 1.3.2), resulting in an increase in bone resorption [160,161]. Ca^{2+} absorption is also decreased by GCs whereas renal excretion is increased [162], indirectly modulating other factor acting on Ca^{2+} homeostasis and thereby bone resorption/formation. Possible bone mediated effects on Pi homeostasis through GCs still need to be determined.

Hormone	Pi homeostasis	Cotransporter	Ca^{2+} homeostasis	Hormonal Feedback
Vitamin D	↑ intestinal Pi absorption	↑ NaPi-Iib	↑ intestinal Ca^{2+} absorption ↑ renal Ca^{2+} reabsorption	↑ FGF23 ↓ PTH
PTH	↓ renal Pi reabsorption	↓ NaPi-IIa, NaPi-IIc, Pit-2	↑ renal Ca^{2+} reabsorption	↑ FGF23 ↑ Vitamin D
FGF23	↓ renal Pi reabsorption	↓ NaPi-IIa, NaPi-IIc	(↑ renal Ca^{2+} reabsorption)	↓ Vitamin D ↓ PTH
Gucocorticoids	↓ renal Pi reabsorption ↓ intestinal Pi absorption	↓ NaPi-IIa ↓ NaPi-Iib	↓ intestinal Ca^{2+} absorption ↑ renal Ca^{2+} reabsorption	

Table 2: Hormonal effect on Pi and Ca^{2+} homeostasis and regulatory feedback

1.4 Hereditary phosphate disorders

As indicated above, Pi homeostasis is maintained through a complex system of hormones that coordinate the expression of renal and intestinal Na^+/Pi-transporters. A defect in any of the mediators of Pi balance can have large systemic effects. There are several pathological states, where patients suffer from hyperphosphaturia often accompanied by impaired skeletal integrity and hereditary hypophosphatemic rickets [163]. Pi depletion is not always reflected in plasma Pi concentrations, since only a minority of total body Pi is present in extracellular fluid [164]. Major causes of renal Pi wasting are mutations impairing Pi transporters or their regulators. Several mutations have been identified within the SLC34A1 (NaPi-IIa) gene that result in different clinical outcomes. The first report identified heterozygous mutations in hypophosphatemic patients suffering from nephrolithiasis and osteoporosis [165]. Although co-injection of Xenopus laevis oocytes with wild type and mutant NaPi-IIa cRNA indicated altered function of the mutant [165], these findings could not be confirmed independently [166]. A homozygous in-frame duplication of 21 base pairs was later identified in two siblings, suffering from Fanconi syndrome [167]. Fanconi syndrome is characterized by renal wasting of metabolites including severe hyperphosphaturia. Renal Pi wasting resulted in hypophosphatemic rickets and stunted growth. The siblings had elevated levels of vitamin D_3 [168], normal PTH and hypercalciuria. High vitamin D_3 might be the cause of hypercalciuria, by increasing intestinal Ca^{2+} absorption. Since the siblings also suffered from hypophosphatemic rickets, decreased bone formation might increase the hypercalciuria. In vitro studies confirmed the dysfunction of mutated NaPi-IIa. Several additional studies reported homozygous mutations of NaPi-IIa in infants with idiopathic hypercalcemia and nephrocalcinosis [169,170]. In these patients, high vitamin D_3 levels triggered by hypophosphatemia are suspected to lead to kidney stones. In most cases, the mutation impairs the trafficking and/or stability of the transporter in the apical membrane. Interestingly hereditary hypophosphatemic rickets with hypercalciuria (HHRH) is caused by several mutations in the SLC34A3 (NaPi-IIc) gene [171,172], which was rather surprising since animal models suggested a minimal role of NaPi-IIc in renal reabsorption [10,11]. HHRH is characterized by reduced renal Pi absorption, hence hypophosphatemia, elevated vitamin D_3, causing a suppression of PTH, leading to increased Ca^{2+} absorption and renal excretion [163]. Patients suffer from rickets, short growth, bone pain and muscle weakness. Commonly patients also develop tubular calcification due to high urinary excretion of Pi and Ca^{2+}. Mutations in SLC34A2 (NaPi-IIb) are considered as the main cause of pulmonary alveolar microlithiasis (PAM) and probably also of testicular microlithiasis [44]. In the lung, NaPi-IIb is expressed in the apical membrane of type II alveolar cells [173]; these are the cells responsible for the production of surfactant, which is rich in phospholipids particularly dipalmitoylphosphatidylcholine. In contrast to other epithelia, alveolar NaPi-IIb has been proposed to mediate the extrusion of intracellular Pi produced by the metabolism of phospholipids. Therefore, its absence it expected to result in intracellular accumulation of Pi, that would favor the formation of mineral deposits (Pi complex with Ca^{2+}) in the airways. However, in the few cases for which data is available, mutations in NaPi-IIb do not alter the plasma levels of Pi. This is in agreement with data obtained with NaPi-IIb deficient mice, in which the lack of the transporter in the intestine is compensated by the kidney.

Autosomal dominant hypophosphatemic rickets is a disorder caused by a mutation affecting one of the arginine residues in the RXXR motive in FGF23 [174], resulting in a cleavage resistant hormone. Degradation-resistant FGF23 decreases renal Pi absorption and vitamin D_3 synthesis. Thus patients develop hypophosphatemia along with rickets. X-linked dominant hypophophatemic rickets and autosomal recessive hypophosphatemic rickets are also due to inappropriately high levels of FGF23, caused by mutations in either the PHEX [175] or DMP-1 genes, respectively [176]. In vitro studies suggest that both genes are involved in the regulation of FGF23 in bone, but the exact mechanism behind is not fully resolved. Mouse models deficient for Phex [177,178] and Dmp-1 [176] replicate the phenotype associated with increased FGF23 expression, and show increased renal Pi excretion and impaired bone mineralization. Double ablation of Dmp-1 and Phex has no additive effect and the common phenotype of both models suggests that FGF23 regulation by both proteins involves the same pathway [179], whereas the function of Dmp-1 appears Phex dependent [180].

1.5 Monocarboxylate transporters

1.5.1 The monocarboxylate transporter family

The SLC16 gene family of solute carriers consists of 14 members (see Figure 7). The first four members (MCT1-4) were characterized as transporters for mononcarboxylates such as lactate, pyruvate, and ketone bodies in a H^+-dependent manner, leading to name the family as MCTs (monocarboxylate transporter) [181]. MCT7 is the only other member to be associated with transport of monocarboxylates in a H^+-dependent manner [182]. Characterization of other members of the MCT family revealed that the substrate spectrum exceeds monocarboxylates, thus, the name might be misleading. MCT8 was characterized as a transporter for the thyroid hormones triiodothyronine and tetraiodothyronine [183,184]. MCT10 was identified as a transporter for aromatic amino acids and is also known as TAT1 (T-type amino acid transporter 1) [185]. It shares the highest sequence homology with MCT8 and it also has the capacity to transport thyroid hormones. MCT12 is associated with juvenile cataract and has recently been identified as creatine transporter [186]. MCT9 is associated with elevated carnitine levels and subsequent transport studies confirmed transport [187]. The other members of the family remain orphans. Tough they do not share substrates, all MCTs are predicted to contain twelve transmembrane domains with intracellular N- and C-termini as well as a big intracellular loop between transmembrane domain six and seven [181]. Proteolytic cleavage experiments of MCT1 in red blood cells confirmed the predicted topology, since the intracellular N- and C-termini as well as the intracellular loop were not accessible for proteolytic cleavage in intact blood cells but in leaky ghosts [188].

1.5.2 Classical monocarboxylate transporters

MCT1 is expressed in tissues relying on oxidative phosphorylation like heart, providing those cells with lactate as respiratory fuel [181,189]. In liver it provides lactate to perform gluconeogenesis or lipogenesis [190]. In contrast MCT4 is expressed in glycolytic tissues to export the lactate produced during glycolysis [191]. MCT1, 3 and 4 interact with CD147 (basignin), an immunoglobulin-like protein that acts as an accessory protein to increase MCT abundance in the membrane [192,193]. It has been shown that the sorting of MCT1 to the right pole of an epithelial cell relies on CD147 [192]. Tissue specific expression of different isoforms reflects the activity of the tissue: MCT4 is expressed in white muscle fibers to export lactate produced during glycolysis, MCT1 on the other hand is expressed in the red muscle fibers to fuel β-oxidation [194]. The low affinity of MCT4 for lactate restricts glycolysis in white muscle fibers due to raising levels of lactate in the cell, causing muscle fatigue, MCT1 with a higher affinity imports lactate then into red muscle fibers [194]. This mechanism might prevent an excess of lactate and thus acidic load released to the system. A similar mechanism is present in the nervous system, where astrocytes express MCT4 and MCT2 is localized in the postsynaptic density in neurons [195,196], containing a lot of mitochondria reflecting the oxidative capacity.

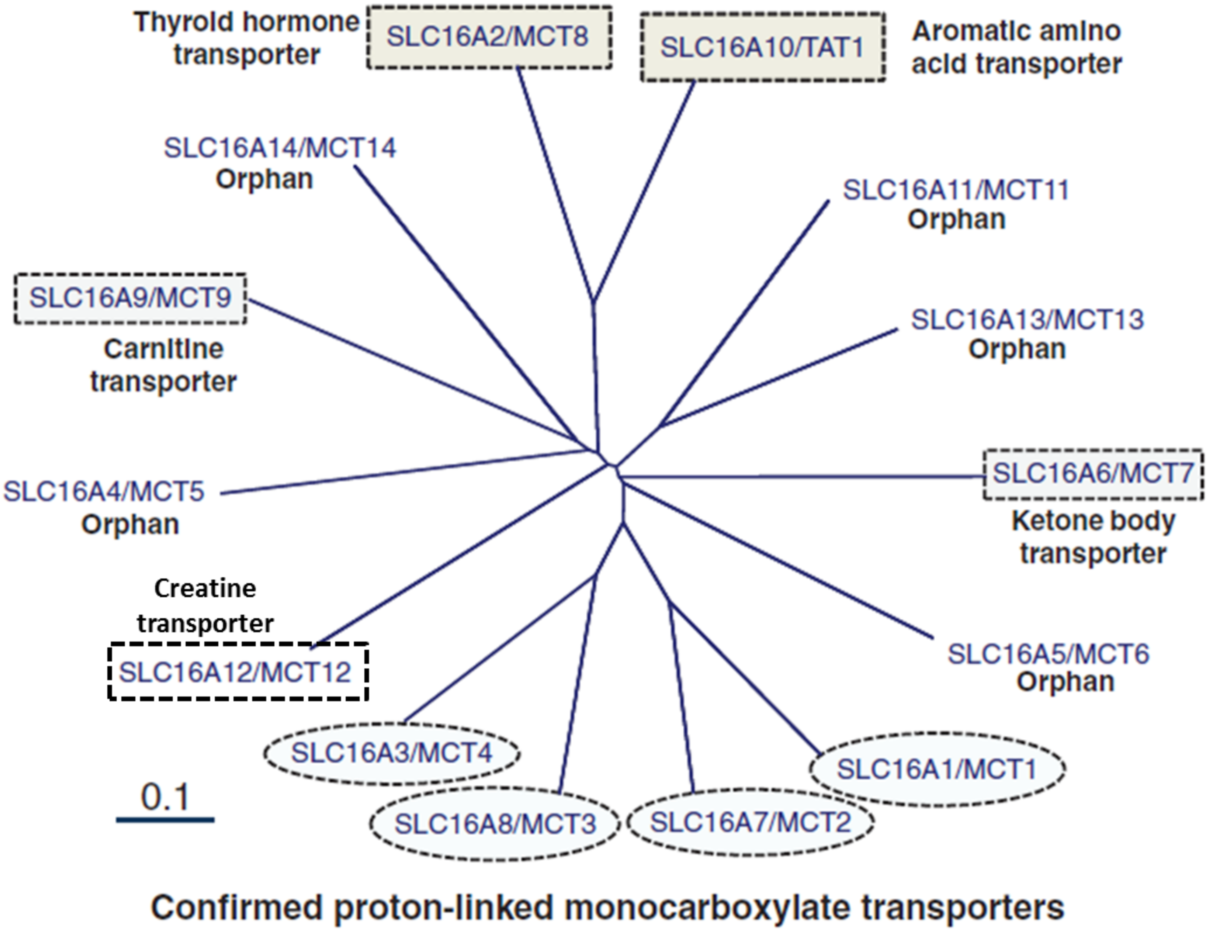

Figure 7: Phylogenetic tree of the MCT/SLC16 family. Both SLC and MCT numbers are given since MCT numbering was done based on the order of characterization, whereas SLC16 numbers were introduced once cDNA sequences were available. Only MCT1-4 are confirmed monocarboxylate transporters, with MCT7 been the only other member likely to transport monocarboxylates in H^+-dependent manner. Adapted from Halestrap (2013) [190].

1.5.3 Monocarboxylate transporters in the kidney

A renal transcriptome analysis on murine kidneys detected mRNA of several classical and orphan MCTs, including MCT1, MCT2, MCT5, MCT6, MCT7, MCT8, MCT9, MCT10 (TAT1), MCT13 and MCT14 [197]. Luminal uptake of monocarboxylates from urine is mediated by two members of the SLC5 family, namely SMCT1 (SLC5A8) and SMCT2 (SLC5A12), both localized in the proximal tubule [198,199]. MCT1 resides in the basolateral membrane of those tubules [200] facilitating the efflux of reabsorbed monocarboxylates. MCT2 is localized to the basolateral side of cells of the thick ascending limb of the loop of Henle and the distal convoluted tubule [200]. Both transporters can mediate import and efflux lactate depending on the cellular environment. The renal proximal tubule is involved in gluconeogenesis and uses β-oxidation for energy metabolism [201]; MCT1 might also provide tubules with lactate from blood as a substrate for those processes.

MCT8 [200], MCT10 [185] and MCT12 [202] (though no mRNA was detected by the transcriptomic screen) are all expressed at the basolateral membrane of proximal tubules. Consistently with the expression of MCT8, those cells express the type I iodotyronine 5’-deiodinase, which converts tetraiodothyronine to triiodothyronine [203]. Thyroid hormones regulate the function and maturation of proximal tubules; however, the possible role of MCT8 in this process remains to be determined. MCT10 exports aromatic amino acids that were reabsorbed from the glomerular filtrate [185]. Mutations of MCT12 are associated with increased amounts of guanidinoacetate in urine [202]. However, functional studies showed that MCT12 transports creatine but not its precursor guanidinoacetate [186,202].

1.5.4 MCT14

Only little is known about MCT14. First reports indicated that this orphan transporter is expressed at mRNA level in the mammary gland of lactating cows and along the whole bovine intestinal tract [204,205]. Recently, its expression was also characterized in the central nervous system of mouse, where it is located in excitatory and inhibitory neurons as well as epithelial cells in the brain [206]. This study also provided the analysis of the relative expression of MCT14 in several tissues; MCT14 was highly expressed in the kidney, but also in testis, uterus and liver [206]. MCT14 was detected in a renal transcriptome analysis of mice adapted to high Pi or low Pi diet respectively (unpublished data). The function of this protein and its contribution in the adaptation to dietary Pi content is still unknown. Phylogenetic analysis indicates that MCT14 is closer related the MCT8, 9 and 10 than to the classical members of the family [206], which might suggest that its role involves transport of other solutes than monocarboxylates.

Chapter 2

2. Aims

The general aim of this study was to explore the mechanisms underlying intestinal Pi absorption. Active transcellular transport mediated by the Na^+-dependent Pi transporter NaPi-IIb is well characterized, but little is known about the rleative importance of this transport pathway and a possible passive absorption of Pi along the paracellular pathway. Current pharmacological approaches to treat hyperphosphatemia in CKD patients involve the use of Pi binders and the development of NaPi-IIb inhibitors is considered as a potential alternative or complementary method. Thus, it is important to understand the nature of different pathways for intestinal Pi absorption and their relative contribution. NaPi-IIb is a high affinity transporter strongly upregulated upon dietary Pi restriction. Furthermore patients with mutations in NaPi-IIb suffer from pulmonary alveolar microlithiasis, but no adverse effect on Pi homeostasis is reported. Therefore we postulate that Pi is mainly absorbed passively through the paracellular pathway as long as dietary Pi supply is sufficient to drive passive diffusion, whereas once dietary Pi is restricted the presence of NaPi-IIb may be crucial.

Based on the considerations above, the aims of this study were:

1. To examine the role of NaPi-IIb in intestinal absorption of Pi under normal Pi dietary conditions (generation of a NaPi-IIb deficient mouse model)
2. To investigate the role of NaPi-IIb under high and low dietary Pi conditions (using the NaPi-IIb deficient model)
3. To test the permeability of intestinal tight junctions to Pi (in Ussing chamber experiments)

Furthermore we aimed to characterize the orphan Slc16a14/ MCT14 transporter, whose transcript was found to be highly regulated by dietary Pi in the kidneys of mice. For that, we investigated:

1. Its pattern of expression along the renal tubule
2. Its substrate specificity (transport experiments in *Xenopus laevis* oocytes heterologously expressing MCT14)

Chapter 3

3. Experimental Studies

3.1 Intestinal Depletion of NaPi-IIb/Slc34a2 in Mice: Renal and Hormonal Adaptation

Nati Hernando, Komuraiah Myakala, Fabia Simona, Thomas Knöpfel, Linto Thomas, Heini Murer, Carsten A Wagner, and Jürg Biber

Institute of Physiology and Zurich Center for Integrative Human Physiology (ZIHP). University of Zurich, Zurich, Switzerland

Published in: Journal of Bone and Mineral Research, Vol. 30, No. 10, October 2015, pp 1925–1937 DOI: 10.1002/jbmr.2523

Own contribution:

Thomas Knöpfel contributed to the animal experiments, the design of primers and probes for mRNA analysis as well as mRNA data analysis

ORIGINAL ARTICLE

JBMR®

Intestinal Depletion of NaPi-IIb/*Slc34*a2 in Mice: Renal and Hormonal Adaptation

Nati Hernando, Komuraiah Myakala, Fabia Simona, Thomas Knöpfel, Linto Thomas, Heini Murer, Carsten A Wagner, and Jürg Biber

Institute of Physiology and Zurich Center for Integrative Human Physiology (ZIHP). University of Zurich, Zurich, Switzerland

ABSTRACT

The Na^+-dependent phosphate-cotransporter NaPi-IIb (SLC34A2) is widely expressed, with intestine, lung, and testis among the organs with highest levels of mRNA abundance. In mice, the intestinal expression of NaPi-IIb is restricted to the ileum, where the cotransporter localizes specifically at the brush border membrane (BBM) and mediates the active transport of inorganic phosphate (Pi). Constitutive full ablation of NaPi-IIb is embryonically lethal whereas the global but inducible removal of the transporter in young mice leads to intestinal loss of Pi and lung calcifications. Here we report the generation of a constitutive but intestinal-specific NaPi-IIb/*Slc34a2*–deficient mouse model. Constitutive intestinal ablation of NaPi-IIb results in viable pups with normal growth. Homozygous mice are characterized by fecal wasting of Pi and complete absence of Na/Pi cotransport activity in BBM vesicles (BBMVs) isolated from ileum. In contrast, the urinary excretion of Pi is reduced in these animals. The plasma levels of Pi are similar in wild-type and NaPi-IIb–deficient mice. In females, the reduced phosphaturia associates with higher expression of NaPi-IIa and higher Na/Pi cotransport activity in renal BBMVs, as well as with reduced plasma levels of intact FGF-23. A similar trend is found in males. Thus, NaPi-IIb is the only luminal Na^+-dependent Pi transporter in the murine ileum and its absence is fully compensated for in adult females by a mechanism involving the bone-kidney axis. The contribution of this mechanism to the adaptive response is less apparent in adult males. © 2015 American Society for Bone and Mineral Research.

KEY WORDS: PHOSPHATE HOMEOSTASIS; SLC34A1; PTH; VITAMIN D3; FGF-23

Introduction

Homeostasis of inorganic phosphate (Pi) is a multiorgan process that ensures relatively constant levels of Pi in plasma (for review see Bergwitz and Jüppner(1) and Hu and colleagues(2)). The improper control of plasma Pi concentration results in a wide range of pathological states, with hypophosphatemia resulting in abnormal skeletal growth and rickets, whereas hyperphosphatemia is currently considered as a major risk factor for vascular calcification and mortality (for review see Alizadeh Naderi and Reilly(3) and Paloian and Giachelli(4)). The concentration of Pi in plasma is controlled by the coordinated action of intestine, kidneys, and bones (for review see Bergwitz and Jüppner(1) and Hu and colleagues(2)). The epithelial cells of intestine and kidney are equipped with apically located Na/Pi-cotransporters belonging to the SLC34 and SLC20 families. The intestine expresses NaPi-IIb/SLC34A2 and PiT2/SLC20A2 whereas the renal proximal tubule expresses NaPi-IIa/SLC34A1, NaPi-IIc/SLC34A3, and PiT2/SLC20A2 (for review see Biber and colleagues,(5) Forster and colleagues,(6) and Wagner and colleagues(7)).

The pattern of expression of NaPi-IIb along the intestinal tract is species-dependent. Thus, the cotransporter is expressed in the duodenum and jejunum of rats, whereas it is not detectable in the ileum.(8) Higher expression of the cotransporter mRNA in the duodenum than the ileum has also been reported in human mRNA samples.(9) Instead, the ileum is the only intestinal segment expressing significant levels of NaPi-IIb in mice.(10) In the intestinal epithelia, the cotransporter is specifically located at the brush border membrane (BBM) of enterocytes, along the entire axis of the villi.(8,11) In addition to intestine, NaPi-IIb is expressed in other organs, including lung and testis. Genetic studies have shown a clear association of mutations in the transporter with pulmonary alveolar microlithiasis (PAM) and probably with testicular microlithiasis.(12) There are also some indications for overexpression of NaPi-IIb in breast and epithelial ovarian cancers.(13,14)

Absorption of dietary Pi occurs through a combination of passive and active transport processes across the intestinal epithelia(15) (for review see Lee and Marks(16) and Marks and colleagues(17)). The intrinsic properties of NaPi-IIb parallel the kinetic and regulatory features of the active component: its expression is regulated by the dietary content of Pi as well as by the circulating levels of the steroid hormone 1,25-dihydroxyvitamin D_3 ($1,25(OH)_2D_3$), whereas its activity is reduced by high luminal pH.(11,18) In mice, the intestinal abundance of NaPi-IIb adapts to changes in dietary Pi, increasing in response to diets with low content of Pi and decreasing upon high dietary Pi.

Received in original form September 16, 2014; revised form March 26, 2015; accepted March 27, 2015. Accepted manuscript online March 31, 2015.
Address correspondence to: Nati Hernando, PhD, Winterthurerstrasse 190, 8057 Zurich, Switzerland. E-mail: hernando@physiol.uzh.ch

Journal of Bone and Mineral Research, Vol. 30, No. 10, October 2015, pp 1925–1937
DOI: 10.1002/jbmr.2523

Although chronic changes in Pi intake regulate the levels of 1,25 $(OH)_2D_3$, the dietary adaptation of the cotransporter seems to be independent from the vitamin D_3 levels, because it is preserved in animal models in which either the signaling or the expression of $1,25(OH)_2D_3$ is abolished.(19,20) Still, $1,25(OH)_2D_3$ is per se a main regulator of Pi homeostasis by promoting the expression of NaPi-IIb in the intestinal microvilli.(18,21) It remains unclear whether the effect of $1,25(OH)_2D_3$ on NaPi-IIb abundance is dependent or independent from changes in gene expression. Thus, mice injected with cholecalciferol have higher levels of NaPi-IIb protein in the absence of changes in mRNA expression(18) and the levels of the transcript are normal in vitamin D receptor (VDR) knockouts,(20) whereas injection of $1,25(OH)_2D_3$ in young rats results in upregulation of the cotransporter at the mRNA and protein level and the activity of the human promoter increases after $1,25(OH)_2D_3$ treatment.(21) Under steady-state conditions, the intestinal absorption of Pi in healthy adults is matched by an equivalent urinary excretion. In mice, renal reabsorption of Pi is mediated to a major extent by NaPi-IIa, with some minor contribution of NaPi-IIc and PiT2.(22–24) The expression of these cotransporters in the BBM of proximal tubules is under tight hormonal control, with parathyroid hormone (PTH) and fibroblast grown factor 23 (FGF-23) playing a major role (for review see Biber and colleagues(5) and Wagner and colleagues(7)).

Full ablation of NaPi-IIb is embryonically lethal,(25) whereas the global but inducible removal of the transporter leads to increased fecal excretion of Pi and reduced phosphaturia.(15) In order to decipher the specific contribution of intestinal NaPi-IIb to Pi homeostasis, we created a constitutive but intestinal-specific NaPi-IIb knockout mouse model and characterized its phenotype in terms of intestinal, renal, and hormonal adaptation, in both females and males.

Materials and Methods

Generation of intestinal-specific NaPi-IIb/*Slc34a2* knockout mice

The features of the targeting vector engineered to generate floxed transgenic mice is shown in Fig. 1*A*. This vector consisted of a 2.5-kb fragment of the *Slc34a2* gene that encodes the last 350 amino acids of the transporter, flanked by loxP sites. The 5′

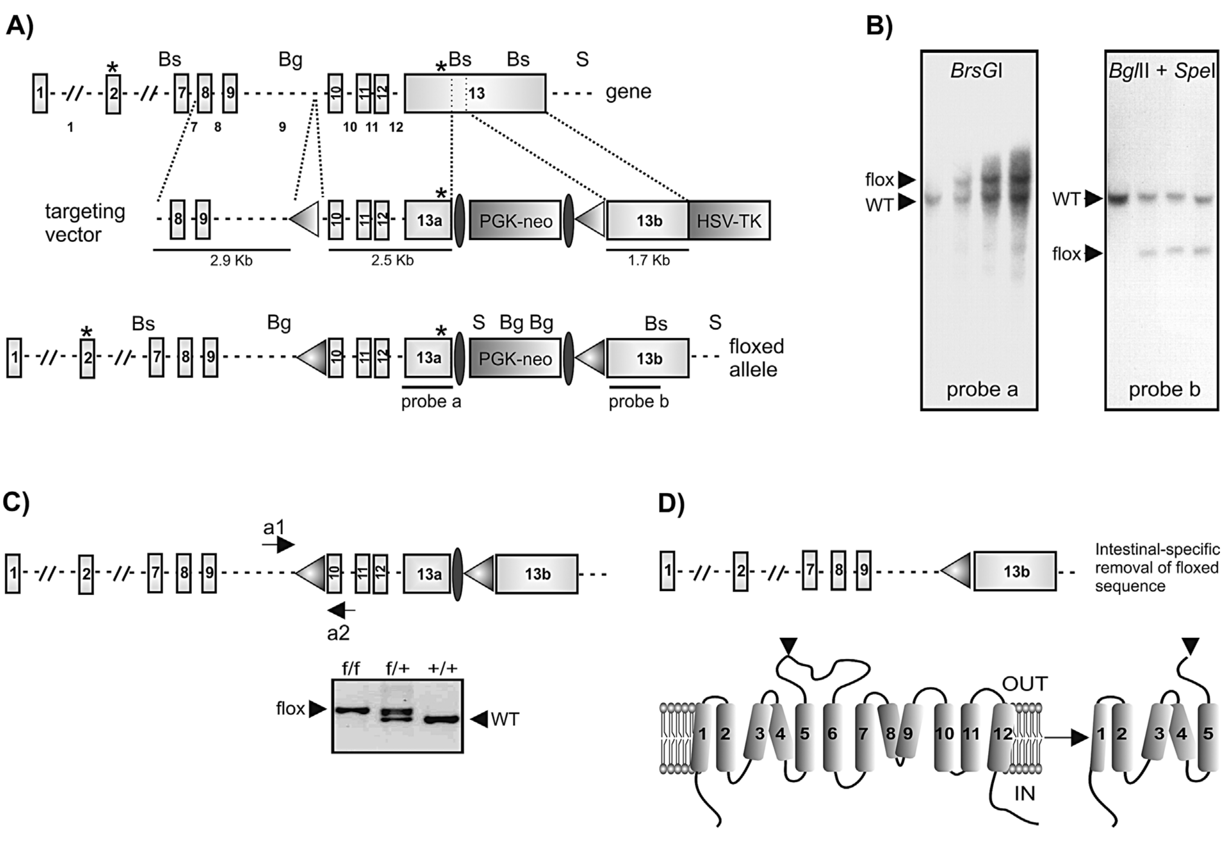

Fig. 1. Generation of intestinal-specific NaPi-IIb/*Slc34a2* knockout mice. (*A*) Schematic representation of the *Slc34a2* gene (top), targeting vector (middle), and floxed allele (bottom). The gene consists of 13 exons (E), with the starting codon in E2 and the stop codon in E13 (both indicated by asterisks). The targeting vector contains 5′ and 3′ homology arms of 2.9 and 1.7 kb, respectively, 2 LoxP sites (shaded triangles) flanking a 2.5 kb genomic fragment, a neo cassette (PGK-neo) flanked by FRT sites (black ellipses), and the herpes simplex virus thymidine kinase (HSV-TK). (*B*) Southern blot of genomic DNA isolated from untransfected ES cells and from three selected clones. DNA samples were digested with the restriction enzymes whose sites are indicated above the floxed allele (Bs = *BsrG*I, *Bg* = *Bgl*II, S = *Spe*I) and incubated with the ^{32}P-labelled probes whose location is shown below the floxed allele. (*C*) Structure of the conditional allele upon removal of the neo cassette by cross-breeding with 64FlpeB6 mice. Genotyping was done by PCR on genomic DNA, using the a1 and a2 primers. An example of the genotyping is shown below. (*D*) Structure of the allele upon Cre-mediated removal of the floxed-sequence (top). Topology of NaPi-IIb (bottom): recombination results in a truncated cotransporter.

and 3′ homologous arms consisted of genomic fragments of 2.9 kb and 1.7 kb, respectively. The neomycin resistance gene driven by the phosphoglycerate kinase (PGK) promoter was flanked by Flp recombinase target (frt) sites and inserted between the 2.5-kb floxed fragment and the 3′ loxP site. The thymidine kinase from the herpes simplex virus (HSV-TK) was cloned downstream of the 3′ homologous arm. Upon electroporation of the vector into 129SV embryonic stem (ES) cells, the PGK-neo and HSV-TK elements were used for positive and negative selection of clones, respectively. Selected clones were tested for homologous recombination by Southern blot using two different probes (Fig. 1*A*, *B*). For that, genomic DNA isolated from three selected clones as well as from untransfected ES cells was digested with either *BsrG*I or *Bgl*II/*Spe*I and hybridized with the ^{32}P-labeled probe according to standard procedures. Hybridization of the probe "a" to DNA digested with *BsrG*I should label a single fragment of 6.3 kb corresponding to the wild-type allele in untransfected cells; an additional 8.8-kb fragment representing the floxed allele is expected in electroporated cells upon homologous recombination of the targeting vector. Hybridization of the probe "b" to DNA digested with *Bgl*II and *Spe*I should label fragments of 5.7 kb and 2.3 kb corresponding to the wild-type and recombined allele, respectively. One recombinant clone was used to produce floxed-*Slc34a2* mice. Electroporation of ES cell as well as generation of floxed animals was done in collaboration with Dr. E Hummler from the Transgenic Animal Facility of the University of Lausanne (TAF UNIL) as described.(26) The neo-cassette was removed from the transgene by crossing heterozygous floxed-*Slc34a2* pups with 64FlpeB6 mice purchased from The Jackson Laboratory (Bar Harbor, MN, USA) (Fig. 1*C*). Ablation of *Slc34a2* in intestinal cells was then achieved by breeding floxed-*Slc34a2*, devoid of neo, with villin-Cre mice (a kind gift from Dr. Gerhard Rogler, Department of Gastroenterology and Hepatology, University of Zurich, Zurich, Switzerland). A PCR genotyping protocol was set up to identify wild-type (*Slc34a2*$^{+/+}$), conditional heterozygous (*Slc34a2*$^{f/+}$), and homozygous (*Slc34a2*$^{f/f}$) pups positive for Cre. Genotyping was done with a pair of forward (CCTTCTCCGCGTCTAAGG) and reverse (GCCTTGACACACTGTTG) primers flanking the 5′ loxP site, using genomic DNA isolated from ear punches as a template. The size of the generated amplicons is 550 bp for the wild-type allele and 600 bp for the floxed allele (Fig. 1*C*). The sequence of the primers used to detect the presence of Cre-recombinase was TCGCTGCATTACCGGTCGATGC and CCATGAGTGAACGAACCTGGTCG for the forward and reverse oligonucleotides, respectively, with an amplicon size of about 400 bp.

Animal handling and collection of samples

Experiments were performed with 3-month-old males and females. Animals were fed with standard diet (KLIBA, SA) containing 0.8% Pi, 1% Ca^{++}, and 800 u/kg vitamin D3. Three days prior to collection of biological samples, mice were placed individually in metabolic cages (Tecniplast). Stool and urine (under mineral oil) were collected during the last 24 hours. On the last day, mice were anaesthetized with ketamine/xylazine i.p. prior to the collection of blood and organs. Heparinized blood was immediately centrifuged and plasma was aliquotted into several tubes, whereas dissected ileum was rinsed with cold PBS and inverted prior to collection of the mucosa by scraping. Plasma and organs were immediately frozen in liquid nitrogen until further use. Animal experiments were approved by the local veterinary authority (Kantonales Veterinäramt Zürich) and animal handling complied with the Swiss Animal Welfare laws.

Quantification of mRNA expression by real-time PCR

Total RNA was extracted from ileum mucosa, lung, testis, and femurs (upon removal of bone marrow) and reverse-transcribed to cDNA by standard methods (RNAeasy Minikit from Qiagen; Hombrechtikon, Switzerland; TaqMan Reverse Transcription Kit from Applied Biosystems; Zug, Switzerland). The cDNA was amplified by PCR with the TaqMan Universal PCR Master Mix in the presence of specific pairs of forward (Fw) and reverse (Rv) primers and FAM/TAMRA-labeled probes (Pb). To quantify the expression of NaPi-IIb/*Slc34a2* mRNA, we designed a set of primers and labeled-probe annealing within the sequence contained between both loxP sites (Fig. 1*A*): the forward and reverse primers anneal to exons 10 and 12, respectively, whereas the probe anneals to exon 11. The sequences of the primers and probes are shown in Table 1. The expressions of the genes of interest were normalized to the expression of either hypoxanthine phosphoribosyltransferase (HPRT) or 18S according to the formula $R = 2^{[Ct(control) - Ct(test\ gene)]}$, where R is the relative ratio and Ct indicates the cycle number at a given threshold.

Uptakes of ^{32}P and ^{3}H-D-glucose into intestinal and renal BBM vesicles

Frozen ileum mucosa as well as frozen decapsulated kidneys were homogenized with a buffer containing 300 mM mannitol, 5 mM EGTA, and 12 mM Tris-HCl, pH 7.1, supplemented with protease and phosphatase inhibitors. BBM vesicles (BBMVs) were then isolated by the Mg^{++}-precipitation technique as reported,(27) and finally resuspended in a buffer containing 300 mM mannitol and 20 mM HEPES-Tris, pH 7.4. Uptakes were performed according to the filtration technique as described,(28) by incubating BBMVs in three different solutions: 0 mM Na^{+},

Table 1. Sequences of the Forward and Reverse Primers as Well as the Probes Used for Quantification of mRNA Expressions

	Gene	Primer
Fw	NaPi-IIb	5′-GAAGACCCTGAATACTGATTTCC-3′
Rv	NaPi-IIb	5′-GATATGCCCTCTCAATGCTG-3′
Pb	NaPi-IIb	5′-AGGCATGACCTTCATCGTGCAAAGC-3′
Fw	FGF-23	5′-GTATGGATCTCCACGGCAAC-3′
Rv	FGF-23	5′-AGTGATGCTTCTGCGACAAGT-3′
Pb	FGF-23	5′-TTTTTGGATCGCTTCACTTCAGCCC-3′
Fw	GALNT3	5′-GAGAAAGAGCGAGGGGAAAC-3′
Rv	GALNT3	5′-GTGGACCATGCTTCATTGTG-3′
Pb	GALNT3	5′-ACACCCGACCACCTGAATGTATTGAAC-3′
Fw	VDR	5′-AGGCCCACACTCAGCTTCT-3′
Rv	VDR	5′-ACAGGTCCAGGGTCACAGAG-3′
Pb	VDR	5′-TACACCCCCTCACTGGACATGATGG-3′
Fw	PHEX	5′-GCTGCCAGAGAACAAGTGC-3′
Rv	PHEX	5′-TCCTCAGCTATGCCAGGAAG-3′
Pb	PHEX	5′-CAGTCCTCCACAATTTAGGGTCAATGGTG-3′
Fw	BMP1	5′-ACAGCAAACAGCCCGAAG-3′
Rv	BMP1	5′-TCCAATCACAAACGGGATG-3′
Pb	BMP1	5′-CCATCCATCAAAGCTGCAGGAAACTC-3′
Fw	DMP1	5′-TCTCCCAGTTGCCAGATACC-3′
Rv	DMP1	5′-TCTCCAGATTCACTGCTGTCC-3′
Pb	DMP1	5′-CTCTGAAGAGAGGACGGGTGATTTGG-3′

Fw = forward; Rv = reverse; Pb = probe.

100 mM Na^+, and 100 mM Na^+ plus 6 mM phosphonoformic acid (PFA). All reactions were done in the presence of 0.1 mM KH_2PO_4 and 0.1 mM D-glucose, together with ^{32}P and ^3H-D-glucose as tracer. Uptakes into intestinal BBMVs were done in a single set of experiments, whereas uptakes into renal BBMVs were done independently in three sets of mice, each containing at least 7 animals per gender and genotype. Because there is a certain degree of interexperiment variability (see Results), values within each of the three sets of experiments have been normalized as percentage of the uptakes in the presence of Na^+ (total uptakes) in the corresponding wild-types (*Slc34a2*$^{+/+}$). Similar normalization was done for the intestinal uptakes. The protein concentration of the BBMVs and homogenates was quantified with a protein determination kit (Bio-Rad, Cressier, Switzerland).

Western blots

Samples of BBM or homogenates containing 20 or 40 μg of proteins were electrophoresed in 9% SDS-PAGE gels and transferred to polyvinylidene fluoride (PVDF) membranes (Millipore, Schaffhausen, Switzerland). Upon blocking with 5% milk powder in Tris-buffered saline (TBS), membranes were incubated overnight with primary antibodies against NaPi-IIa,(29) NaPi-IIb,(11) NaPi-IIc,(30) klotho (TransGenic Inc, Kobe, Japan), and β-actin (Sigma-Aldrich, Buchs, Switzerland), followed by 2 hours of incubation with the corresponding secondary antibody (GE Healthcare, Glattbrugg, Switzerland). After addition of the appropriated substrate (Millipore), chemiluminescence signals were detected with the LAS-4000 luminescent image analyzer (Fujifilm) and further quantified (ImageJ). Quantifications are shown as ratios to actin.

Immunofluorescence

Animals were perfused with 3% paraformaldehyde in 0.1 M sodium-cacodylate and tissues were then fixed as reported.(31) Ileum cryosections were processed for antigen retrieval with 1% SDS in PBS at room temperature for 5 min. Upon overnight incubation with the NaPi-IIb antibody, samples were exposed for 1 hour to the Alexa-594 secondary antibody (Invitrogen, Dietikon, Switzerland) together with Alexa 488-coupled phalloidin (Invitrogen) and 4,6-diamidino-2-phenylindole (DAPI; Sigma-Aldrich). Immunofluorescence signals were detected with an epifluorescence microscope (Leica).

Quantification of Pi and Ca^{++} in stool, urine, and plasma

Stool was processed as reported(15) by reconstituting dried stool pellets during 3 days in 0.6 M HCl, followed by a short centrifugation to remove undissolved material. The content of Pi in stool, urine, and plasma was determined according to the Fiske Subarow method (Sigma-Aldrich) and the concentration of Ca^{++} was assessed with the QuantiChrom Calcium assay kit (BioAssay Systems, Hayward, CA, USA). Pi determination was done in several rounds of quantification, each containing a mixture of genders and genotypes, whereas the concentration of Ca^{++} was quantified simultaneously in all groups. Urinary excretions were normalized to the concentration of creatinine that was quantified according to the Jaffe method (Wako Chemicals, Neuss, Germany).

Quantification of PTH, FGF-23, and $1,25(OH)_2D_3$ in plasma

The concentrations of intact PTH and FGF-23 (intact and C-terminal fragments) were quantified by ELISA (Immunotopics International, San Clemente, CA, USA and KAINOS, Sissach, Switzerland), whereas the levels of $1,25(OH)_2D_3$ were determined by radioimmunoassay (Immunodiagnostic System, Frankfurt am Main, Germany). We strictly followed the manufacturers' protocols. PTH, intact FGF-23, and $1,25(OH)_2D_3$ were measured independently in two sets of experiments. The first set consisted of animals of both genders and three genotypes, whereas only wild-type and homozygous males and females were analyzed in the second set of experiments. The C-terminal fragment of FGF-23 was measured only in samples from the first batch of animals. Within each experiment, samples from all mice were quantified simultaneously. Hormonal measurements in each of the two batches of animals resulted in very different mean values (see Results), thus preventing the pooling of raw date. Therefore, all values were normalized as a percentage of the concentration in the corresponding wild-type (*Slc34a2*$^{+/+}$) females.

Statistical analysis

Differences between groups were analyzed by *t* test or ANOVA/Bonferroni test, as indicated. Values of $p < 0.05$ were considered significant. All data are shown as mean ± SE.

Results

Generation and validation of an intestinal-specific NaPi-IIb/*Slc34a2* knockout mice

The first step to generate intestinal-specific NaPi-IIb/*Slc34a2* knockouts was to produce floxed-*Slc34a2* transgenic mice by homologous recombination between the genomic DNA of 129SV-ES cells and the targeting vector show in Fig. 1*A*. Homologous recombination was confirmed by Southern blot using two different probes (Fig. 1*A*, *B*). Hybridization of both probes to genomic DNA isolated from three selected ES cell clones labeled DNA fragments of the expected size (Fig. 1*B*). A single clone was microinjected into blastocysts derived from C57BL/6 mice that were then implanted into NMRI pseudopregnant females. The neo-cassette was removed from the floxed offspring by breeding them with 64FlpeB6 mice in which the Flp recombinase is under control of the human beta-actin promoter. Upon excision of the neo-cassette, floxed animals were mated with villin-Cre mice in which the expression of Cre recombinase is driven by the villin promoter. Further crossbreeding produced wild-type (*Slc34a2*$^{+/+}$), conditional heterozygous (*Slc34a2*$^{f/+}$), and homozygous mice (*Slc34a2*$^{f/f}$) positive for Cre recombinase (Fig. 1*C*). Removal of the loxP-flanked sequence by Cre recombinase should result in a truncated transcript lacking the last 350 codons (Fig. 1*D*).

The abundance of *Slc34a2* mRNA was measured by real-time PCR using primers and probe annealing within the floxed fragment. This analysis indicated a reduced mRNA expression in the ileum of *Slc34a2*$^{f/+}$ mice compared with *Slc34a2*$^{+/+}$ littermates, whereas the transcript was hardly detected in *Slc34a2*$^{f/f}$ animals (Fig. 2*A*). The mRNA expression of the cotransporter in lung (Fig. 2*B*) and testis (Fig. 2*C*) was similar in *Slc34a2*$^{+/+}$ and *Slc34a2*$^{f/f}$ mice.

Western blot analysis using a NaPi-IIb antibody(11) indicated that the abundance of the cotransporter is reduced in BBM isolated from ileum of *Slc34a2*$^{f/+}$ mice as compared with *Slc34a2*$^{+/+}$ littermates, whereas the cotransporter is undetectable in samples from *Slc34a2*$^{f/f}$ animals. Similar effects were detected in females (Fig. 2*D*) and males (Fig. 2*E*). As reported recently for *Slc34a3* knockout mice,(23) there is high heterogeneity in the abundance of NaPi-IIb within the wild-type and

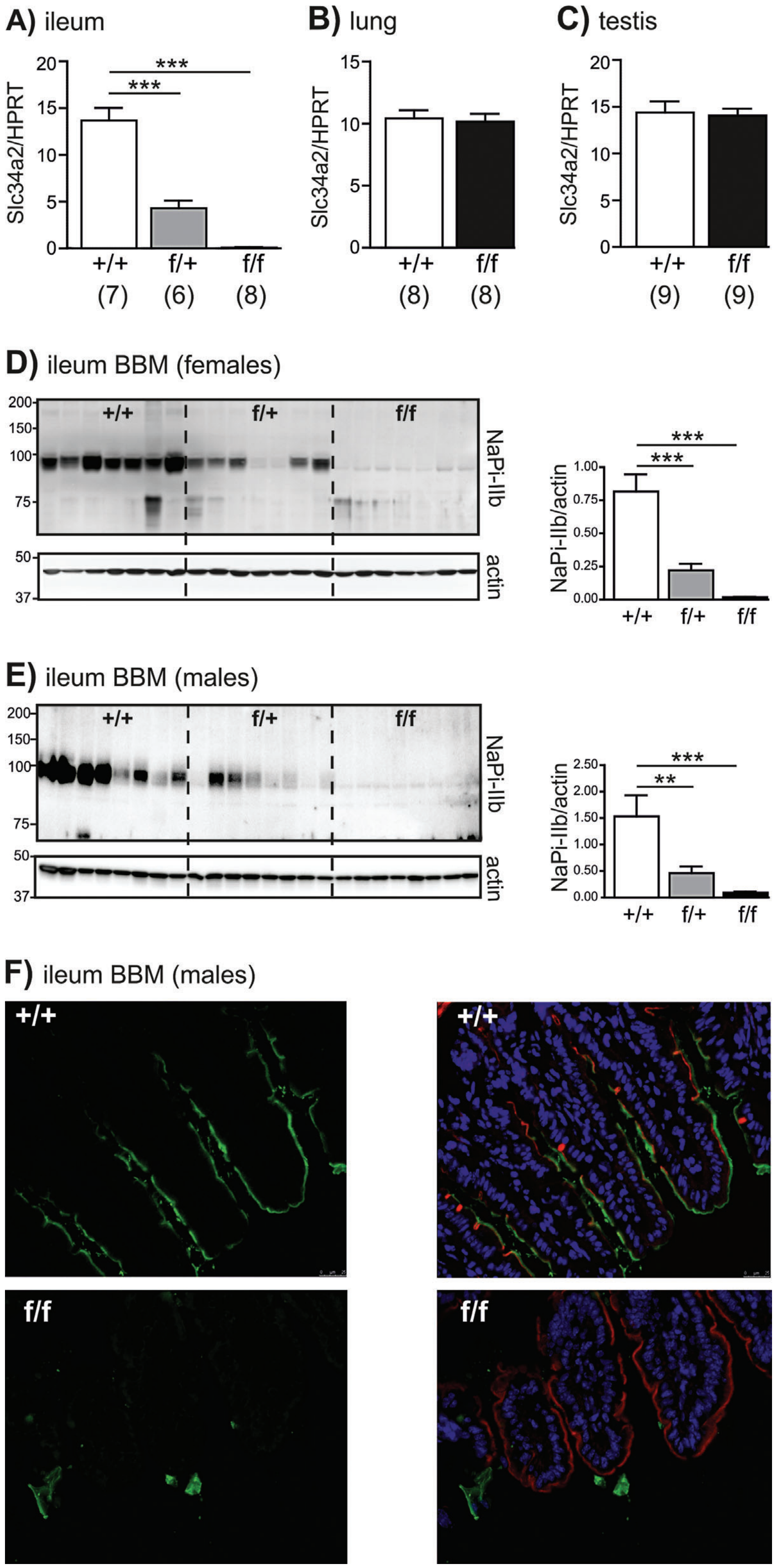

Fig. 2. Expression of *Slc34a2* mRNA and protein. The mRNA expression was quantified by real time PCR in total RNA samples extracted from (*A*) ileum, (*B*) lungs, and (*C*) testis of *Slc*34a2$^{+/+}$ (+/+), *Slc*34a2$^{f/+}$ (f/+), and/or *Slc34a2*$^{f/f}$ (f/f) males. The expression of the cotransporter was normalized to the one of HPRT. Data are given as mean ± SE. The number of mice per group is indicated in parentheses. $^{***}p \leq 0.001$ versus wild-type, ANOVA test. NaPi-IIb protein abundance was analyzed by Western blot (*D*, *E*) and immunofluorescence (*F*). Western blots were performed with BBM isolated from ileum of (*D*) female and (*E*) male mice. Actin was used as loading control. Data are given as mean ± SE and statistical significances were calculated with ANOVA test. $^{**}p \leq 0.01$ and $^{***}p \leq 0.001$, versus wild-types. Immunofluorescence was performed on ileum samples from males. The cotransporter signal is shown in green, the actin staining in red, and the nuclear fluorescence in blue.

heterozygous groups, which may be due to different feeding behaviors of individual animals. Immunostaining of ileum samples with the same NaPi-IIb antibody revealed an apical signal in tissue collected from *Slc34a2*$^{+/+}$ but not from *Slc34a2*$^{f/f}$ mice, confirming the absence of NaPi-IIb in ileum of homozygous animals (Fig. 2*F*).

Effect of NaPi-IIb/*Slc34a2* knockdown on the uptake of Pi into ileal BBMVs

Uptakes of ^{32}P into BBMVs isolated from ileum were carried out in the presence/absence of Na^{+} (to determine the total uptake as well as the Na^{+}-dependent and independent components), with or without PFA in the Na^{+} media (to discriminate between Slc34-dependent and independent mechanisms of the Na^{+}-dependent component). (32) Absolute values for the total uptakes (column a) in wild-type animals (*Slc34a2*$^{+/+}$) were (in pmol ^{32}P/μg protein/min) 0.32 ± 0.03 for females and 0.41 ± 0.06 for males. As shown in Fig. 3*A* and *B*, in both genders the Na^{+}-dependent uptake (columns labeled “c”) represented around 95% of the total uptake of Pi (columns labeled “a”), with a very small contribution of Na^{+}-independent processes (columns labeled “b”). With the exception of this Na^{+}-independent component that remained unaffected, uptakes of ^{32}P into ileal BBMVs were reduced by around 40% in *Slc34a2*$^{f/+}$ animals and were almost fully abolished in *Slc34a2*$^{f/f}$ mice. The reduction in the PFA-insensitive uptake detected in *Slc34a2*$^{f/f}$ females (columns labeled “d”) probably reflects the inability of PFA, at the used concentration, to fully inhibit the Slc34-dependent component (columns labeled “e”). For every given genotype, the incorporation of ^{32}Pi was comparable in BBMVs from females and males. The uptake of ^{3}H-D-glucose was similar in *Slc34a2*$^{+/+}$, *Slc34a2*$^{f/+}$, and *Slc34a2*$^{f/f}$ mice and was insensitive to PFA (Fig. 3*C*, *D*).

Effect of NaPi-IIb/*Slc34a2* knockdown on fecal, urinary, and plasma concentrations of Pi and Ca^{++}

The absence of NaPi-IIb from the BBM of ileum resulted in a higher fecal excretion of Pi in *Slc34a2*$^{f/f}$ mice as compared with their corresponding *Slc34a2*$^{+/+}$ littermates (Fig. 4*A*). The excretion in *Slc34a2*$^{f/+}$ mice was unaffected (Fig. 4*A*), despite the clear reduction in NaPi-IIb protein abundance and in the ileal uptake of Pi. The urinary excretion of Pi was reduced in *Slc34a2*$^{f/f}$

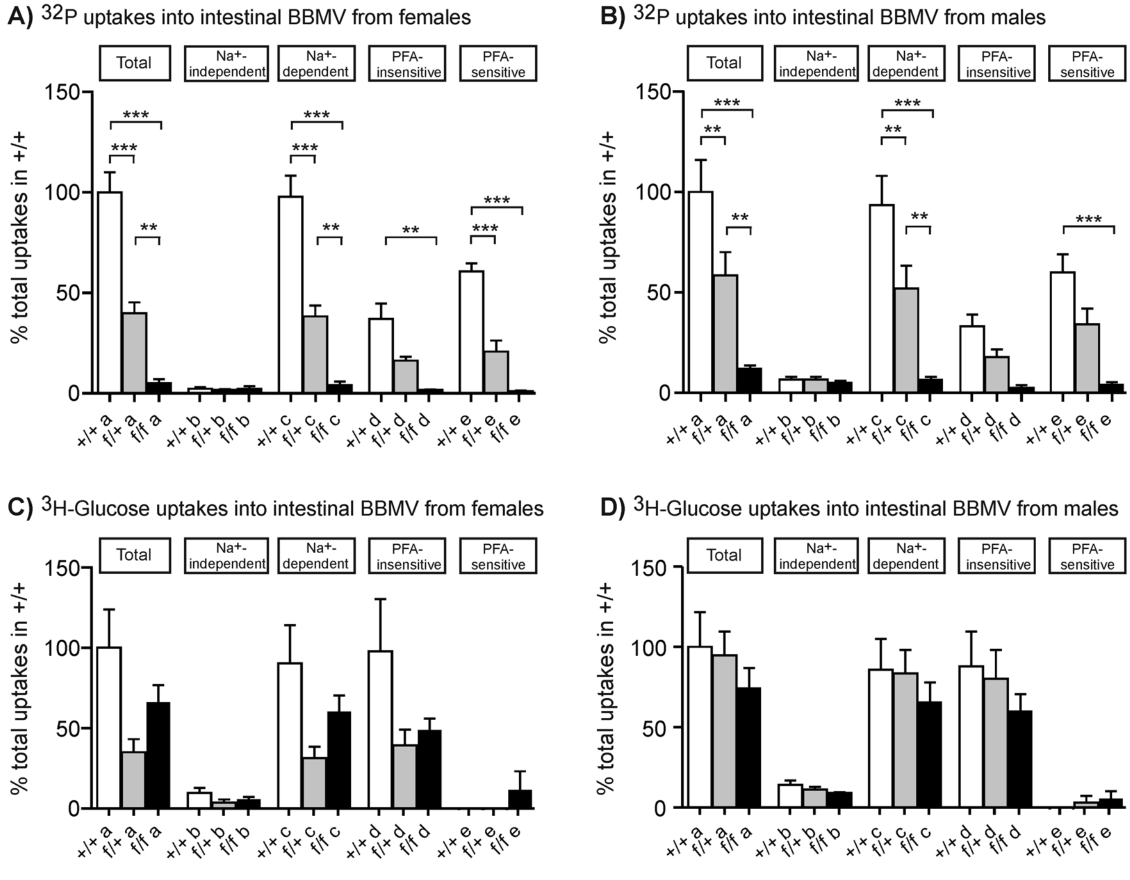

Fig. 3. Effect of *Slc34a2* knockdown on the uptake of Pi into intestinal BBMVs. Uptakes were performed with BBMVs isolated from ileum of (*A*, *C*) female and (*B*, *D*) male *Slc34a2*$^{+/+}$ (+/+, white columns), *Slc34a2*$^{f/+}$ (f/+, gray columns), and *Slc34a2*$^{f/f}$ (f/f, black columns). For each experimental group, the components of the uptakes are indicated as follows: (a) total uptake, corresponding to the uptake measured in the presence of Na^{+}; (b) Na^{+}-independent uptake, the incorporation obtained in the absence of Na^{+}; (c) Na^{+}-dependent uptake, calculated by subtracting the value obtained in the absence of Na^{+} from that in the presence of Na^{+}; (d) PFA-insensitive uptake: calculated by subtracting the Na^{+}-independent uptake from that measured in the presence of Na^{+} plus PFA; (e) PFA-sensitive uptake: calculated by subtracting the PFA-insensitive component from the Na^{+}-dependent uptake. Data are presented as mean ± SE. The number of females per group was 9 *Slc34a2*$^{+/+}$, 7 *Slc34a2*$^{f/+}$, and 7 *Slc34a2*$^{f/f}$, whereas the size of the male groups was 8 *Slc34a2*$^{+/+}$, 7 *Slc34a2*$^{f/+}$, and 8 *Slc34a2*$^{f/f}$. Statistical significances between groups were calculated with ANOVA/Bonferroni test: $^{**}p \leq 0.01$; $^{***}p \leq 0.001$.

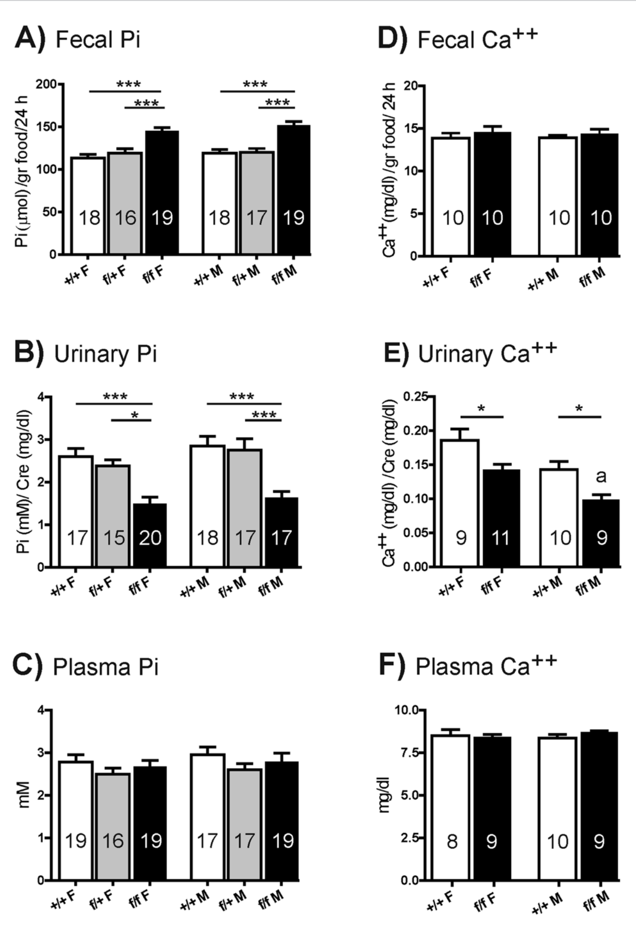

Fig. 4. Effect of *Slc34a2* knockdown on Pi and Ca^{++} levels. The concentrations of (*A–C*) Pi and (*D–F*) Ca^{++} were measured in (*A*, *D*) stool, (*B*, *E*) urine, and (*C*, *F*) plasma. Samples were collected from *Slc34a2*$^{+/+}$ (+/+, white columns), *Slc34a2*$^{f/+}$ (f/+, gray columns), and/or *Slc34a2*$^{f/f}$ (f/f, black columns), both females (F) and males (M). Data are given as mean ± SE. The number of mice analyzed per group is indicated within the bars. Statistical significances between groups were calculated with ANOVA/Bonferroni test: $*p \leq 0.05$; $***p \leq 0.001$; (a) $*p \leq 0.05$ between genders.

mice, whereas no changes were detected in *Slc34a2*$^{f/+}$ littermates (Fig. 4*B*). The concentration of Pi in plasma was similar in all groups regardless of the presence or absence of the cotransporter (Fig. 4*C*). For all genotypes, the concentration of Pi in stool, urine, and plasma was similar in females and males. The fecal excretion (Fig. 4*D*) and the plasma levels of Ca^{++} (Fig. 4*F*) were not affected by the absence of intestinal NaPi-IIb. However, the urinary excretion of Ca^{++} was reduced *Slc34a2*$^{f/f}$ compared with their corresponding *Slc34a2*$^{+/+}$ littermates (Fig. 4*E*). The urinary concentrations of Na^{+} and K^{+} were similar in all genotypes (data not shown).

Effect of NaPi-IIb/*Slc34a2* knockdown on the uptake of Pi into renal BBMVs and on the expression of renal Pi transporters

Uptake of ^{32}P into renal BBMVs isolated from *Slc34a2*$^{+/+}$ and *Slc34a2*$^{f/f}$ animals were performed in the same conditions as reported for the intestinal experiments. Absolute values for the total uptake (Fig. 5*A*, *B*, column "a") in wild-type mice (*Slc34a2*$^{+/+}$) ranged between 1 and 5 pmol ^{32}P/µg protein/min in three independent experiments. When measured in parallel, similar total uptake was detected in wild-type females and males (3.46 ± 0.41 versus 4.97 ± 0.71 and 1.25 ± 0.18 versus 1.00 ± 0.10, in two independent experiments). As shown in Fig. 5*A*, the total uptake (column "a") and the Na^{+}-dependent component (column "c") were significantly upregulated in BBMVs from females *Slc34a2*$^{f/f}$ as compared with *Slc34a2*$^{+/+}$ littermates. Similar tendency for higher uptake values was also detected in male *Slc34a2*$^{f/f}$, though it did not reach statistical significance (Fig. 5*B*).

The expression of NaPi-IIa was increased in renal BBM from female *Slc34a2*$^{f/f}$ compared with their *Slc34a2*$^{+/+}$ littermates (Fig. 5*C*). A similar trend was observed in males, though it did not reach statistical significance (Fig. 5*D*). In males and females, the abundance of NaPi-IIc was similar in both genotypes (Fig. 5*C*, *D*).

Effect of NaPi-IIb/*Slc34a2* knockdown on Pi-regulating factors

The plasma concentrations of 1,25(OH)$_2$D$_3$, intact PTH, and intact FGF-23 were measured in two independent sets of experiments, whereas the levels of the C-terminal fragment of FGF-23 were quantified only in the first set of experiments. In all cases, concentrations were normalized to the levels in the corresponding *Slc34a2*$^{+/+}$ females. The absolute hormonal values in *Slc34a2*$^{+/+}$ females in two experiments were (in pg/mL): 119 ± 8.0 and 58 ± 9.1 for 1,25(OH)$_2$D$_3$, 165 ± 44 and 90 ± 32 for PTH, and 76 ± 8.8 and 201 ± 10.9 for the intact FGF-23. The concentration of the C-terminal FGF-23 fragment in *Slc34a2*$^{+/+}$ females was 307 ± 20 pg/mL. The plasma levels of 1,25(OH)$_2$D$_3$ were similar in *Slc34a2*$^{f/f}$ and *Slc34a2*$^{+/+}$ littermates, both in females and in males (Fig. 6*A*). The concentrations of PTH (Fig. 6*B*) as well as of the C-terminal FGF-23 fragment (Fig. 6*C*) were comparable in *Slc34a2*$^{f/f}$, *Slc34a2*$^{f/+}$, and *Slc34a2*$^{+/+}$ mice, in both females and males. In contrast, the levels of intact FGF-23 were significantly lower in homozygous females compared with their wild-type littermates (Fig. 6*D*). A similar trend for reduced intact FGF-23 in *Slc34a2*$^{f/f}$ was observed in males, but it did not reach statistical significance (Fig. 6*D*).

The abundance of klotho in renal homogenates was comparable in *Slc34a2*$^{f/f}$ and *Slc34a2*$^{+/+}$ mice, both in females (Fig. 6*E*, left panel) and in males (Fig. 6*E*, right panel).

Effect of NaPi-IIb/*Slc34a2* knockdown on FGF-23 regulators

The impact of NaPi-IIb depletion on the mRNA expression of several bone factors proposed to regulate FGF-23 (Fig. 7*A*) was analyzed. Although the expression of N-acetylgalactosaminyltransferase (GALNT3; Fig. 7*B*) as well as FGF-23 (Fig. 7*C*) and VDR transcripts (Fig. 7*D*) tended to be reduced in bones from *Slc34a2*$^{f/f}$ females compared with the corresponding *Slc34a2*$^{+/+}$ littermates, only the changes on VDR were statistically significant. The expressions of the phosphate-regulating gene with homology to endopeptidases on the X-chromosome (PHEX; Fig. 7*E*), bone morphogenetic protein 1 (BMP1; Fig. 7*F*), and dentin matrix protein-1 (DMP1; Fig. 7*G*) were similar in all groups of animals.

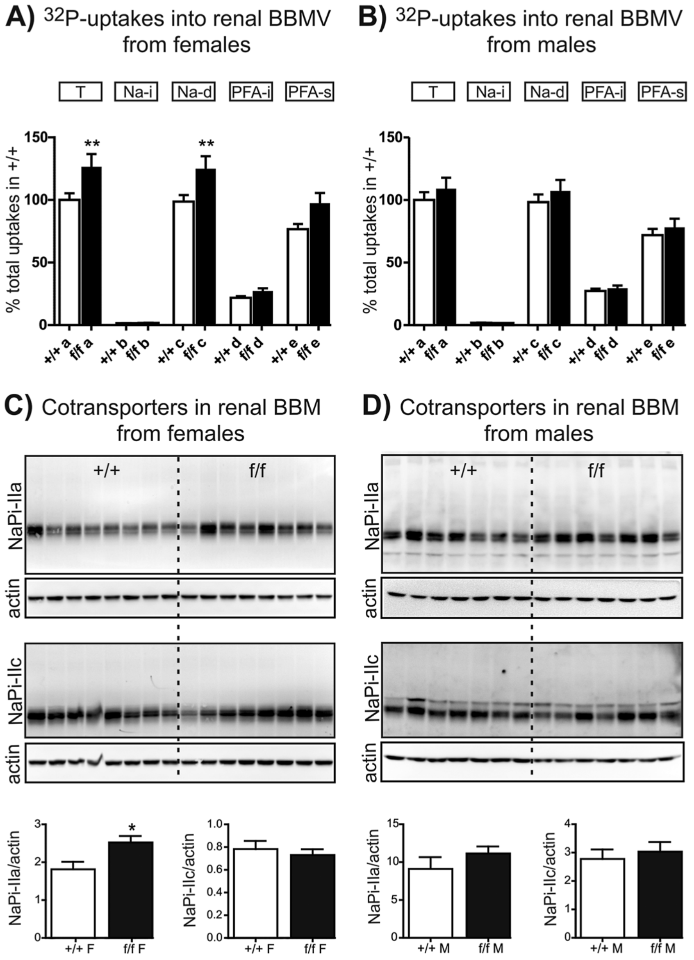

A) ^{32}P-uptakes into renal BBMV from females

B) ^{32}P-uptakes into renal BBMV from males

C) Cotransporters in renal BBM from females

D) Cotransporters in renal BBM from males

Fig. 5. Effect of *Slc34a2* knockdown on the uptake of Pi into renal BBMVs and on the expression of renal cotransporters. The incorporation of ^{32}P in renal BBMVs was measured in three independent sets of experiments in samples from (*A*) female and (*B*) male *Slc34a2*$^{+/+}$ (+/+, white columns) and *Slc34a2*$^{f/f}$ (f/f, black columns). The components of the uptakes are indicated as follows: (a) total uptake, (b) Na^{+}-independent uptake, (c) Na^{+}-dependent uptake, (d) PFA-insensitive uptake, and (e) PFA-sensitive uptake. Data are presented as mean ± SE. The number of females per group was 24 *Slc34a2*$^{+/+}$ and 24 *Slc34a2*$^{f/f}$; the size of the male groups was 23 *Slc34a2*$^{+/+}$ and 25 *Slc34a2*$^{f/f}$. Statistical significances versus the corresponding wild-type values were calculated with ANOVA/Bonferroni test: $^{**}p \leq 0.01$. Western blots with NaPi-IIa and NaPi-IIc antibodies in renal BBM from (*C*) female and (*D*) male *Slc34a2*$^{+/+}$ (+/+) and *Slc34a2*$^{f/f}$ (f/f). Actin was used as loading control. Statistical significances were calculated with t test: $^{*}p \leq 0.05$.

Discussion

To study the specific contribution of intestinal NaPi-IIb/*Slc34a2* to Pi homeostasis, we generated a constitutive but tissue-specific knockout mouse model in which ablation of the cotransporter is achieved by villin-driven Cre recombinase. Constitutive depletion of intestinal *Slc34a2* results in viable and fertile pups. Adult homozygous mice show fecal wasting of Pi that correlates with almost complete absence of Na/Pi cotransport activity in ileal BBMVs. The urinary excretion of Pi is reduced in homozygous animals whereas the plasma levels of Pi are similar in wild-type and knockout animals. In females, the reduced phosphaturia associates with increased Na/Pi cotransport activity in renal BBMVs, increased expression of NaPi-IIa, and reduced circulating levels of intact FGF-23.

As indicated, the expression of the Cre recombinase was driven by the promoter of villin, a Ca^{++}-regulated actin-binding protein detected in several epithelia.(33) *Slc34a2* mRNA is widely expressed and, in addition to intestine, two of the tissues with higher mRNA levels are the lungs and testis.(34) In humans, mutations of *SLC34A2* associate with PAM, an autosomal-recessive disease characterized by intra-alveolar accumulation of Pi-containing microliths.(12) This PAM phenotype was reproduced in mice with global and inducible depletion of the cotransporter.(15) There are also some indications suggesting a correlation between mutations of *SLC34A2* and testicular microlithiasis.(12) The expression of the cotransporter mRNA remains unchanged in lungs and testis of *Slc34a2*$^{f/f}$ mice (Fig. 2*B*, *C*), suggesting that the villin-driven Cre system efficiently ablates the *Slc34a2* gene in ileum, without affecting its expression in other organs in which the cotransporter is known to play a critical role.

Shibasaki and colleagues(25) reported that the constitutive and global knockout of *Slc34a2* results in intrauterine death of homozygous pups, probably due to impaired absorption of Pi from the maternal circulation. This is consistent with the high expression of the cotransporter mRNA detected in placenta.(35)

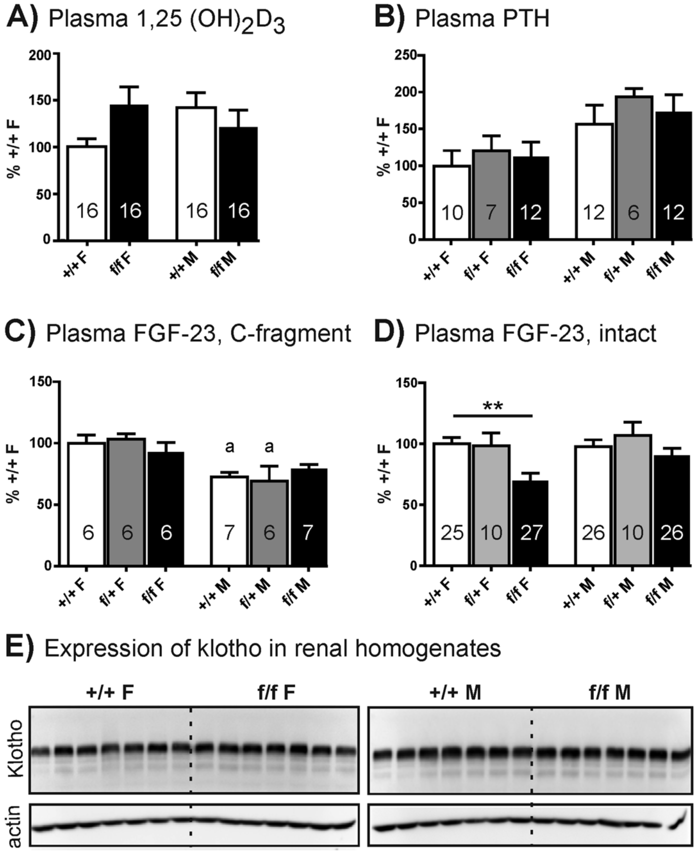

Fig. 6. Effect of *Slc34a2* knockdown on regulators of Pi homeostasis. Plasma concentrations of (*A*) 1,25$(OH)_2D3$, (*B*) PTH, (*C*) C-terminal fragment of FGF-23, and (*D*) intact FGF-23 were measured either in two or one independent sets of experiments (see Materials and Methods). Measurements were done in samples from *Slc34a2*$^{+/+}$ (+/+, white columns), *Slc34a2*$^{f/+}$ (f/+, gray columns), and/or *Slc34a2*$^{f/f}$ (f/f, black columns), both females (F) and males (M). Within each experiment, samples from all groups of mice were processed simultaneously. Data are given as mean ± SE. The number of mice analyzed per group is indicated within the bars. Statistical significances were calculated with ANOVA/Bonferroni test: $^{**}p \leq 0.01$ versus the corresponding wild-type; (a) $p \leq 0.05$ between genders. (*E*) Western blot with a klotho antibody of renal homogenates from *Slc34a2*$^{+/+}$ (+/+) and *Slc34a2*$^{f/f}$ (f/f) females (left panel) and males (right panel).

Unlike the global model, breeding of intestinal-specific heterozygous produced the expected Mendelian ratio of wild-type/heterozygous/homozygous pups (data not shown). Therefore, the constitutive intestinal depletion of the cotransporter does not seem to have any deleterious effects and produces viable pups.

Our data demonstrates that NaPi-IIb is responsible for up to 95% of the Na^+-dependent uptake of Pi in the ileum and that its absence results in fecal wasting of Pi, in both males and females (Figs. 3 and 4). In both genders, the intestinal loss is at least partially compensated by reduced urinary output, allowing *Slc34a2*$^{f/f}$ mice to remain normophosphatemic (Fig. 4). These findings are in agreement with a previous report from Sabbagh and colleagues(15) showing that the Na^+-dependent incorporation of ^{32}P into everted sacs is hardly detectable in the ileum of mice with global and inducible removal of the transporter. Normophosphatemia, increased fecal output, and reduced phosphaturia were also reported in this inducible model.

Alterations in the urinary excretion of Pi usually reflect changes in the capacity of the renal proximal tubule to reabsorb Pi from the primary urine. Our transport studies in renal BBM indicate that the reduced phosphaturia exhibited by homozygous females correlates with increased total and Na^+-dependent uptake of Pi (Fig. 5*A*). The expression of the Na^+/Pi cotransporters NaPi-IIa/*Slc34a1* and NaPi-IIc/*Slc34a3* in the BBM of renal proximal tubules is regulated by many of the factors that control the renal reabsorption of Pi. In mice, NaPi-IIa plays a major quantitative role because its absence results in massively reduced renal uptake of Pi, hyperphosphaturia, and hypophosphatemia,(22) whereas depletion of NaPi-IIc has no effect on Pi homeostasis.(23,24) Consistent with the renal uptake data, we found that the expression of NaPi-IIa is upregulated in female *Slc34a2*$^{f/f}$ mice (Fig. 5).

The expression of NaPi-IIb is under the control of 1,25$(OH)_2D_3$, which via posttranscriptional and perhaps also transcriptional mechanisms increases the abundance of the cotransporter, thereby enhancing the absorption of dietary Pi. The plasma levels of 1,25$(OH)_2D_3$ depend on the intrarenal activation of 25(OH)D_3 by the Cyp27b1/1α-hydroxylase as well as on its catabolism by the Cyp24a1/24α-hydroxylase.(36) The concentration of 1,25$(OH)_2D_3$ increases upon dietary restriction of Pi, due to higher synthesis and reduced catabolism.(36) However, in adult mice the intestinal loss of Pi caused by the absence of NaPi-IIb does not trigger a similar upregulation of 1,25$(OH)_2D_3$ (Fig. 6*A*). This finding is compatible with the report from Sabbagh and

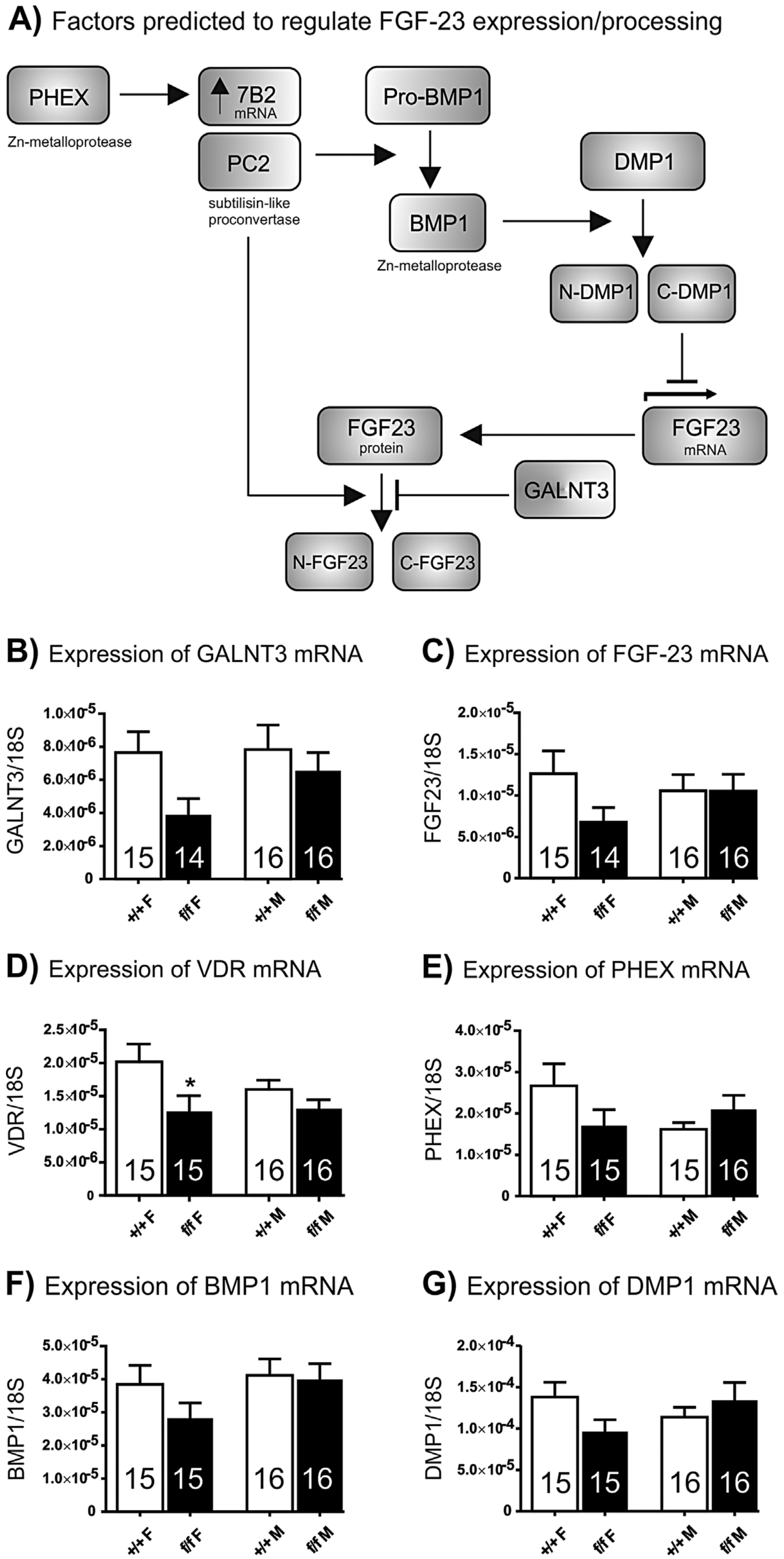

Fig. 7. Effect of *Slc34a2* knockdown on regulators of FGF-23. (*A*) Proposed working model showing some of the factors involved in transcriptional and posttranscriptional regulation of FGF-23 (adapted from Feng and colleagues(49)). The expression of (*B*) GALNT3, (*C*) FGF-23, (*D*) VDR, (*E*) PHEX, (*F*) BMP1, and (*G*) DMP1 mRNAs in bones was analyzed by real-time PCR in samples from *Slc34a2*$^{+/+}$ (+/+,white columns) and *Slc34a2*$^{f/f}$ (f/f, black columns) mice, both male (M) and female (F). The expression of the genes was normalized to the expression of 18S. Each gene was simultaneously analyzed in all groups of mice. Data are given as mean ± SE. The number of mice analyzed per group is indicated within the bars. Statistical significances were calculated using ANOVA/Bonferroni test: $^*p \leq 0.05$.

colleagues(15) showing that the plasma concentration of 1,25 $(OH)_2D_3$ was increased 4 weeks after deletion of the cotransporter, but normalized thereafter. Regarding the renal expression of both hydroxylases, the mRNA abundance of Cyp27b1 was similar in *Slc34a2*$^{f/f}$ and *Slc34a2*$^{+/+}$ littermates of both genders, whereas the expression of Cyp24a1 was reduced in male *Slc34a2*$^{f/f}$ as compared with *Slc34a2*$^{+/+}$ mice (data not shown).

As indicated, the reduced phosphaturia caused by depletion of *Slc34a2* correlates in females with increased uptake of Pi into renal BBM and increased expression of NaPi-IIa. The urinary excretion of Pi as well as the abundance of NaPi-IIa in the proximal BBM are regulated by several hormones, with PTH and FGF-23 playing a major role (for review see Bergwitz and Jüppner(1)). Both hormones are involved in feedback loops with each other as well as with $1,25(OH)_2D_3$ and they both reduce the expression of NaPi-IIa in the proximal tubule triggering a phosphaturic response.(31,37–40) Therefore, their levels may decrease when Pi reabsorption is stimulated. However, our data suggests that the reduced phosphaturia observed in *Slc34a2*$^{f/f}$ mice cannot be explained on the basis of lower PTH levels (Fig. 6*B*).

FGF-23 is a 251–amino acid peptide hormone mostly produced by osteocytes. The active form secreted into the circulation consists of amino acids 25 to 251 and acts on its target tissue by simultaneously binding to FGF receptors and klotho (for review see Hu and colleagues(2)). Active FGF-23 is proteolytically processed at a subtilisin-like site, resulting in inactive N-terminal and C-terminal fragments.(41) Similar to PTH, FGF-23 induces a phosphaturic effect by promoting the endocytosis of NaPi-IIa and NaPi-IIc from the proximal BBM.(39,42) Furthermore, both hormones have been proposed to share similar mechanisms to induce the retrieval of NaPi-IIa from the apical microvilli.(40) We measured the concentration of FGF-23 using two different ELISA kits: one kit detects the C-terminal fragment and therefore can measure, in principle, both the non-cleaved (active) and cleaved (inactive) forms, whereas the second kit detects only the non-cleaved peptide. The reduction in intact FGF-23 observed in of *Slc34a2*$^{f/f}$ females (Fig. 6*D*) supports the observations of increased NaPi-IIa abundance and higher Pi uptake in renal BBM of the female homozygous. The reduction in intact FGF-23 without significant changes in $1,25(OH)_2D_3$ is interesting, considering the key role of $1,25(OH)_2D_3$ in maintaining Pi homeostasis and FGF-23 expression, and the fact that its levels are increased in mice with constitutive ablation of either NaPi-IIa(22) or NaPi-IIc.(24) However, and as indicated above, only a transient increase of $1,25(OH)_2D_3$ has been reported in NaPi-IIb–inducible knockouts.(15) In addition to the role as co-receptor, klotho has also been shown to control the membrane expression of NaPi-IIa independently of FGF-23, by a mechanism that involves its glucuronidase activity. Thus, in vivo administration of klotho leads to hypophosphatemia, hyperphosphaturia, and reduced expression of NaPi-IIa both in wild-type and FGF23-deficient mice.(43) Moreover, klotho inhibits the transport of Pi in renal proximal cells prior to any measurable reduction in the abundance of NaPi-IIa. The abundance of klotho was not influenced by the absence of intestinal NaPi-IIb (Fig. 6*E*).

The hormonal data reported here are in agreement with the data from Sabbagh and colleagues,(15) describing only a transient upregulation of $1,25(OH)_2D_3$, lack of changes of PTH, and persistent downregulation of intact FGF-23 upon inducible and global removal of *Slc34a2*.

FGF-23 is O-glycosylated at a threonine residue that overlaps with the subtilisin-like cleavage site. Glycosylation is mediated by GALNT3, and protects the modified peptide from proteolytic cleavage and inactivation(44) (Fig. 7*A*). Consequently, mutations of FGF-23 that prevent its cleavage result in higher levels of intact FGF-23, causing autosomal dominant hypophosphatemic rickets,(45,46) whereas mutations in GALNT3 result in low concentrations of intact FGF-23 and hyperphosphatemic familial tumoral calcinosis (for review see Bergwitz and Jüppner(1) and Strom and Jüppner(46)). The lack of changes in the levels of the FGF-23 C-terminal fragment together with the reduction in the intact form (Fig. 6*C*, *D*) may suggest that *Slc34a2*$^{f/f}$ females adapt to the absence of NaPi-IIb by increasing the proteolytic processing of FGF-23. Although the expression of GALNT3 mRNA tended to be reduced in bones from female *Slc34a2*$^{f/f}$ (Fig. 7*B*), the change did not reach statistical significance. The transcription of the FGF-23 gene is activated by $1,25(OH)_2D_3$ in a VDR-dependent manner and administration of $1,25(OH)_2D_3$ results in a dose-dependent increase of FGF-23 in wild-type mice; instead, VDR-deficient mice have low basal levels of FGF-23 and do not respond to $1,25(OH)_2D_3$.(47,48) Although the plasma levels of $1,25(OH)_2D_3$ remained unchanged in *Slc34a2*-depleted animals (Fig. 6*A*), the expression of the VDR was reduced in bones from *Slc34a2*$^{f/f}$ females (Fig. 7*D*). The lower levels of VDR in homozygous females could potentially blunt the transcriptional effect of $1,25(OH)_2D_3$ in FGF-23 expression. However, the reduction in the mRNA expression of FGF-23 was below statistical significance.

In addition to GALNT3 and $1,25(OH)_2D_3$, the expression and stability of FGF-23 is regulated, among other factors, by a cascade of proteins that includes PHEX, the proprotein convertase 2/7B2 complex (7B2.PC2), BMP1, and DMP1 (Fig. 7*A*). (49) PHEX is a Zn-metalloprotease recently shown to promote the expression of 7B2, a cofactor required for activation of the subtilisin-like proprotein convertase PC2.(50) The 7B2.PC2 complex seems to directly induce the proteolytic inactivation of FGF-23 and indirectly inhibit FGF-23 mRNA transcription.(50) The effect on transcription involves proteolytic activation of BMP1, itself a Zn-metalloprotease that in turn targets DMP1. The C-terminal fragment of DMP1 inhibits the transcription of FGF-23.(51) In consequence, activation of this protein cascade reduces the active FGF-23 by promoting its proteolytic processing while preventing its transcription. Consistently, mutations in PHEX(52) and DMP1(53) result in higher FGF-23 levels and hypophosphatemia (for review see Bergwitz and Jüppner(1) and Strom and Jüppner(46)). With the exception of the 7B2.PC2 complex, the expression of the other components of this pathway was detected in mRNA from bone. However, the mRNA expression of PHEX, BMP1, and DMP1 were not modified in *Slc34a2*-depleted mice.

In homozygous males, the compensatory changes on Pi renal transport, NaPi-IIa abundance, and FGF-23 plasma concentration were less evident than in females. Further studies should address whether the reduction in the urinary output of Pi in males correlates with changes in other renal parameters such as glomerular filtration rate or the distal tubular handling of Pi. The possibility that females and males have different thresholds for triggering compensatory changes, and therefore that the adaptive response could be similar in younger (or older) mice of both genders, cannot be ruled out. For some parameters, the normalization of results from two independent sets of mice may have contributed to mask real differences in the pooled results.

In summary, we have shown that specific removal of the Na^+/Pi cotransporter NaPi-IIb/*Slc34a2* from the intestinal epithelia results in almost complete loss of active transport of Pi in ileal

BBMVs, leading to increased fecal excretion and a compensatory reduction of the renal output of Pi. All these changes are comparable in females and males. In females, the adaptation to the absence of the intestinal cotransporter seems to involve the bone-kidney axis, with lower levels of FGF-23. Lower FGF-23 in turn allows stimulation of renal Pi reabsorption due to higher expression of NaPi-IIa and therefore increased uptake of Pi into renal BBM. These changes are less apparent in males. The cause for the gender differences remain to be elucidated.

Disclosures

The authors state that they have no conflicts of interest

Acknowledgments

This study was supported by a grant from the Swiss National Science Foundation (31003A-127288 to JB and NH). We gratefully acknowledge Nicole Kampik for helping with the tissue fixation, as well as the technical support of Udo Schnitzbauer, Nicole Gehring, and Eva Maria Pastor-Arroyo. The use of the ZIRP Core Facility for Rodent Phenotyping is also acknowledged.

Authors' roles: Study design: NH, HM, CAW, and JB. Study conduct: NH, KM, FS, TK, and LT. Data collection: NH, KM, FS, TK, and LT. Data analysis: NH, KM, FS, TK, LT, HM, CAW, and JB. Data interpretation: NH, KM, FS, TK, LT, HM, CAW, and JB. Drafting manuscript: NH. Revising manuscript content: NH, KM, FS, TK, LT, HM, CAW, and JB. Approving final version manuscript: NH, KM, FS, TK, LT, HM, CAW, and JB. NH, KM, FS, TK, LT, HM, CAW, and JB take responsibility for the integrity of the data analysis.

References

1. Bergwitz C, Jüppner H. Regulation of phosphate homeostasis by PTH, vitamin D, and FGF23. Annu Rev Med. 2010;61:91–104.
2. Hu MC, Shiizaki K, Kuro-o M, Moe OW. Fibroblast growth factor 23 and Klotho: physiology and pathophysiology of an endocrine network of mineral metabolism. Annu Rev Physiol. 2013;75: 503–33.
3. Alizadeh Naderi AS, Reilly RF. Hereditary disorders of renal phosphate wasting. Nat Rev Nephrol. 2010 Nov;6(11):657–65.
4. Paloian NJ, Giachelli CM. A current understanding of vascular calcification in CKD. Am J Physiol Renal Physiol. 2014 Oct 15;307(8): F891–900.
5. Biber J, Hernando N, Forster I. Phosphate transporters and their function. Annu Rev Physiol. 2013;75:535–50.
6. Forster IC, Hernando N, Biber J, Murer H. Phosphate transporters of the SLC20 and SLC34 families. Mol Aspects Med. 2013;34(2-3): 386–95.
7. Wagner CA, Hernando N, Forster IC, Biber J. The SLC34 family of sodium-dependent phosphate transporters. Pflugers Archiv. 2014;466(1):139–53.
8. Giral H, Caldas Y, Sutherland E, et al. Regulation of rat intestinal Na-dependent phosphate transporters by dietary phosphate. Am J Physiol Renal Physiol. 2009;297(5):F1466–75.
9. Xu H, Bai L, Collins JF, Ghishan FK. Molecular cloning, functional characterization, tissue distribution, and chromosomal localization of a human, small intestinal sodium-phosphate (Na+-Pi) transporter (SLC34A2). Genomics. 1999;62(2):281–4.
10. Radanovic T, Wagner CA, Murer H, Biber J. Regulation of intestinal phosphate transport. I. Segmental expression and adaptation to low-P(i) diet of the type IIb Na(+)-P(i) cotransporter in mouse small intestine. Am J Physiol Gastrointest Liver Physiol. 2005;288(3): G496–500.
11. Hilfiker H, Hattenhauer O, Traebert M, Forster I, Murer H, Biber J. Characterization of a murine type II sodium-phosphate cotransporter expressed in mammalian small intestine. Proc Natl Acad Sci U S A. 1998;95(24):14564–9.
12. Corut A, Senyigit A, Ugur SA, et al. Mutations in SLC34A2 cause pulmonary alveolar microlithiasis and are possibly associated with testicular microlithiasis. Am J Hum Genet. 2006;79(4):650–6.
13. Chen DR, Chien SY, Kuo SJ, et al. SLC34A2 as a novel marker for diagnosis and targeted therapy of breast cancer. Anticancer Res. 2010;30(10):4135–40.
14. Shyian M, Gryshkova V, Kostianets O, et al. Quantitative analysis of SLC34A2 expression in different types of ovarian tumors. Exp Oncol. 2011;33(2):94–8.
15. Sabbagh Y, O'Brien SP, Song W, et al. Intestinal npt2b plays a major role in phosphate absorption and homeostasis. J Am Soc Nephrol. 2009;20(11):2348–58.
16. Lee GJ, Marks J. Intestinal phosphate transport: a therapeutic target in chronic kidney disease and beyond? Pediatr Nephrol. 2015 Mar;30(3):363–71.
17. Marks J, Debnam ES, Unwin RJ. Phosphate homeostasis and the renal-gastrointestinal axis. Am J Physiol Renal Physiol. 2010;299(2): F285–296.
18. Hattenhauer O, Traebert M, Murer H, Biber J. Regulation of small intestinal Na-P(i) type IIb cotransporter by dietary phosphate intake. Am J Physiol. 1999;277(4 Pt 1):G756–762.
19. Capuano P, Radanovic T, Wagner CA, et al. Intestinal and renal adaptation to a low-Pi diet of type II NaPi cotransporters in vitamin D receptor- and 1alphaOHase-deficient mice. Am J Physiol Cell Physiol. 2005;288(2):C429–434.
20. Segawa H, Kaneko I, Yamanaka S, et al. Intestinal Na-P(i) cotransporter adaptation to dietary P(i) content in vitamin D receptor null mice. Am J Physiol Renal Physiol. 2004;287(1):F39–47.
21. Xu H, Bai L, Collins JF, Ghishan FK. Age-dependent regulation of rat intestinal type IIb sodium-phosphate cotransporter by 1,25-(OH)(2) vitamin D(3). Am J Physiol Cell Physiol. 2002;282(3):C487–93.
22. Beck L, et al. Targeted inactivation of Npt2 in mice leads to severe renal phosphate wasting, hypercalciuria, and skeletal abnormalities. Proc Natl Acad Sci U S.A. 1998;95(9):5372–7.
23. Myakala K, Motta S, Murer H, et al. Renal-specific and inducible depletion of NaPi-IIc/Slc34a3, the cotransporter mutated in HHRH, does not affect phosphate or calcium homeostasis in mice. Am J Physiol Renal Physiol. 2014 Apr 15;306(8):F833–43.
24. Segawa H, Onitsuka A, Kuwahata M, et al. Type IIc sodium-dependent phosphate transporter regulates calcium metabolism. J Am Soc Nephrol. 2009;20(1):104–13.
25. Shibasaki Y, Etoh N, Hayasaka M, et al. Targeted deletion of the tybe IIb Na(+)-dependent Pi-co-transporter, NaPi-IIb, results in early embryonic lethality. Biochem Biophys Res Commun. 2009;381-(4):482–6.
26. Porret A, Merillat AM, Guichard S, Beermann F, Hummler E. Tissue-specific transgenic and knockout mice. Methods Mol Biol. 2006;337:185–205.
27. Biber J, Stieger B, Stange G, Murer H. Isolation of renal proximal tubular brush-border membranes. Nat Protoc. 2007;2(6):1356–9.
28. Stoll R, Kinne R, Murer H. Effect of dietary phosphate intake on phosphate transport by isolated rat renal brush-border vesicles. Biochem J. 1979;180(3):465–70.
29. Custer M, Lotscher M, Biber J, Murer H, Kaissling B. Expression of Na-P(i) cotransport in rat kidney: localization by RT-PCR and immunohistochemistry. Am J Physiol. 1994;266(5 Pt 2):F767–74.
30. Nowik M, Picard N, Stange G, et al. Renal phosphaturia during metabolic acidosis revisited: molecular mechanisms for decreased renal phosphate reabsorption. Pflugers Arch. 2008;457(2): 539–49.
31. Lotscher M, Kaissling B, Biber J, Murer H, Kempson SA, Levi M. Regulation of rat renal Na/Pi-cotransporter by parathyroid hormone: immunohistochemistry. Kidney Int. 1996;49(4):1010–11.
32. Villa-Bellosta R, Sorribas V. Role of rat sodium/phosphate cotransporters in the cell membrane transport of arsenate. Toxicol Appl Pharmacol. 2008;232(1):125–34.

33. Khurana S, George SP. Regulation of cell structure and function by actin-binding proteins: villin's perspective. FEBS Lett. 2008;582(14): 2128–39.

34. Nishimura M, Naito S. Tissue-specific mRNA expression profiles of human solute carrier transporter superfamilies. Drug Metab Pharmacokinet. 2008;23(1):22–44.

35. Ma Y, Samaraweera M, Cooke-Hubley S, et al. Neither absence nor excess of FGF23 disturbs murine fetal-placental phosphorus homeostasis or prenatal skeletal development and mineralization. Endocrinology. 2014;155(5):1596–605.

36. Perwad F, Portale AA. Vitamin D metabolism in the kidney: regulation by phosphorus and fibroblast growth factor 23. Mol Cell Endocrinol. 2011;347(1-2):17–24.

37. Deliot N, Hernando N, Horst-Liu Z, et al. Parathyroid hormone treatment induces dissociation of type IIa Na+-P(i) cotransporter-Na+/H+ exchanger regulatory factor-1 complexes. Am J Physiol Cell Physiol. 2005;289(1):C159–67.

38. Gattineni J, Bates C, Twombley K, et al. FGF23 decreases renal NaPi-2a and NaPi-2c expression and induces hypophosphatemia in vivo predominantly via FGF receptor 1. Am J Physiol Renal Physiol. 2009;297(2):F282–91.

39. Segawa H, Kawakami E, Kaneko I, et al. Effect of hydrolysis-resistant FGF23-R179Q on dietary phosphate regulation of the renal type-II Na/Pi transporter. Pflugers Archiv. 2003;446(5):585–92.

40. Weinman EJ, Steplock D, Shenolikar S, Biswas R. Fibroblast growth factor-23-mediated inhibition of renal phosphate transport in mice requires sodium-hydrogen exchanger regulatory factor-1 (NHERF-1) and synergizes with parathyroid hormone. J Biol Chem. 2011;286(43): 37216–21.

41. Shimada T, Muto T, Urakawa I, et al. Mutant FGF-23 responsible for autosomal dominant hypophosphatemic, rickets is resistant to proteolytic cleavage and causes hypophosphatemia in vivo. Endocrinology. 2002;143(8):3179–82.

42. Saito H, Kusano K, Kinosaki M, et al. Human fibroblast growth factor-23 mutants suppress Na+-dependent phosphate co-transport activity and 1alpha,25-dihydroxyvitamin D3 production. J Biol Chem. 2003;278(4):2206–11.

43. Hu MC, Shi M, Zhang J, et al. Klotho: a novel phosphaturic substance acting as an autocrine enzyme in the renal proximal tubule. FASEB J. 2010;24(9):3438–50.

44. Kato K, Jeanneau C, Tarp MA, et al. Polypeptide GalNAc-transferase T3 and familial tumoral calcinosis. Secretion of fibroblast growth factor 23 requires O-glycosylation. J Biol Chem. 2006;281(27): 18370–7.

45. White KE, Evans WE, O'Riordan JLH, et al. ADHR Consortium. Autosomal dominant hypophosphataemic rickets is associated with mutations in FGF23. Nat Genet. 2000;26(3):345–8.

46. Strom TM, Jüppner H. PHEX, FGF23, DMP1 and beyond. Curr Opin Nephrol Hypertens. 2008;17(4):357–62.

47. Kolek OI, Hines ER, Jones MD, et al. 1 alpha, 25-Dihydroxyvitamin D3 upregulates FGF23 gene expression in bone: the final link in a renal-gastrointestinal-skeletal axis that controls phosphate transport. Am J Physiol Gastrointest Liver Physiol. 2005;289(6):G1036–42.

48. Saito H, Maeda A, Ohtomo S, et al. Circulating FGF-23 is regulated by 1alpha, 25-dihydroxyvitamin D3 and phosphorus in vivo. J Biol Chem. 2005;280(4):2543–9.

49. Feng JQ, Clinkenbeard EL, Yuan B, White KE, Drezner MK. Osteocyte regulation of phosphate homeostasis and bone mineralization underlies the pathophysiology of the heritable disorders of rickets and osteomalacia. Bone. 2013;54(2):213–21.

50. Yuan B, Feng JQ, Bowman S, et al. Hexa-D-arginine treatment increases 7B2*PC2 activity in hyp-mouse osteoblasts and rescues the HYP phenotype. J Bone Miner Res. 2013;28(1):56–72.

51. Martin A, David V, Li H, Dai B, Feng JQ, Quarles LD. Overexpression of the DMP1 C-terminal fragment stimulates FGF23 and exacerbates the hypophosphatemic rickets phenotype in Hyp mice. Mol Endocrinol. 2012;26(11):1883–95.

52. Holm IA, Huang X, Kunkel LM. Mutational analysis of the PEX gene in patients with X-linked hypophosphatemic rickets. Am J Hum Genet. 1997;60(4):790–7.

53. Lorenz-Depiereux B, Bastepe M, Benet-Pagès A, et al. DMP1 mutations in autosomal recessive hypophosphatemia implicate a bone matrix protein in the regulation of phosphate homeostasis. Nat Genet. 2006;38(11):1248–50.

3.2 The intestinal phosphate transporter NaPi-IIb (Slc34a2) is required to protect bone during dietary phosphate restriction

Thomas Knöpfel[1], Eva M. Pastor[1], Udo Schnitzbauer[1], Denise Kratschmar[2], Alex Odermatt[2], Nati Hernando[1]*, Carsten A. Wagner[1]*

[1]Institute of Physiology, University of Zurich, Switzerland, [2]Division of Molecular and Systems Toxicology, Department of Pharmaceutical Sciences, University of Basel

*N. Hernando and C.A. Wagner contributed equally and share last authorship

Own contribution:

Thomas Knöpfel (TK) contributed to the experimental design of the study and the animal experiments. TK performed western blots, quantitative real time PCR, urine analysis and microcomputer tomography of bones. The manuscript including figures was drafted by TK.

Abstract

NaPi-IIb (Slc34a1) is a Na^+-dependent phosphate (Pi) transporter that accounts for the majority of the active transport of phosphate into epithelial cells of the small intestine. Its abundance in the intestinal brush border membrane is regulated by dietary phosphate, being high during dietary Pi restriction. Intestinal ablation of NaPi-IIb in mice leads to increased fecal excretion of phosphate, which is compensated by enhanced renal Pi reabsorption to maintain phosphate homeostasis. Here we report the response of NaPi-IIb deficient mice to alterations in dietary phosphate content. As in wild type animals, high phosphate load increases fecal and urinary excretion of phosphate in NaPi-IIb deficient mice, whereas phosphate restriction decreases intestinal and urinary phosphate excretion. However under dietary phosphate restriction, plasma phosphate levels decline more rapidly in NaPi-IIb deficient mice. Despite hypophosphatemia, NaPi-IIb deficient mice fed low phosphate show comparable levels of vitamin D_3, parathyroid hormone and fibroblast growth factor 23 to wild type littermates. Furthermore, the expression of renal cotransporters is also similar in both groups of mice. Instead, upon feeding low phosphate, NaPi-IIb deficient animals show a more pronounced increase in urinary excretion of calcium, cortiscosterone and the bone resorption marker deoxypyridionline, as well as lower bone mineral density than wild type mice. These data suggests that NaPi-IIb mediated phosphate absorption during dietary phosphate restriction prevents excessive demineralization of bone as an alternative source of phosphate.

Introduction

Phosphate (Pi) is a vital compound for many biological functions including energy metabolism, intracellular signaling, structural composition of cellular membranes, and bone mineralization. Hence Pi homeostasis is regulated by the coordinated interplay of different organs and endocrine networks. The intestine absorbs Pi from the diet and kidneys reabsorb Pi from the primary filtrate. Additionally, the bones serve as a reservoir for Pi, where it can be deposited as hydroxyapatite or released, in case Pi supply gets low (1, 2). Under normal conditions bone formation through osteoblasts is in balance with bone resorption mediated by osteoclasts. Several hormones such as parathyroid hormone (PTH) or glucocorticoids can stimulate osteoclast activity and thereby increase bone mineral release and promote demineralization (3, 4).

The Slc34 family of Na^+-dependent Pi transporters plays an essential role in Pi homeostasis. In the intestine of mice, transcellular transport of Pi occurs mainly in the ileum, where NaPi-IIb (Slc34a2) is localized (5, 6). Indeed, NaPi-IIb appears to be the major murine intestinal Pi transporter, as its depletion results in abrogation of Na^+-dependent transport of Pi and fecal loss of Pi (7, 8). Although mutations in NaPi-IIb have been described as a main cause of pulmonary alveolar microlithiasis in humans (9), Pi metabolism of these patients has not been investigated. NaPi-IIa (Slc34a1) and NaPi-IIc (Slc34a3) are responsible for the renal reabsorption of Pi. Both transporters are localized in the brush border membrane (BBM) of the renal proximal tubular cells (10, 11). NaPi-IIa accounts for the majority of Pi reabsorption, since its ablation in mice leads to severe renal Pi wasting and hypophosphatemia, resulting in underdeveloped bone trabeculae, impaired bone formation and nephrocalcinosis (12, 13). Hypophosphatemia and nephrocalcinosis have been also reported in patients with mutations in NaPi-IIa (14, 15), and gene wide association studies indicate a strong correlation between NaPi-IIa and plasma levels of Pi (16). In contrast, deletion of NaPi-IIc does not impair Pi homeostasis in mice (17, 18); however, many studies have reported mutations in NaPi-IIc in patients with hereditary hypophosphatemic rickets with hypercalciuria (for review see (19, 20)). The Slc20 family of Na^+-dependent Pi transporters consists of Pit1 and Pit2, both showing broad tissue distribution including the epithelia of intestine and the renal proximal tubule (21). Their contribution to intestinal and renal transport of Pi remains to be tested, though the renal expression of Pit2 is regulated by factors controlling Pi homeostasis (22).

The abundance of Slc34 transporters is regulated by a hormonal network consisting of PTH, fibroblast growth factor 23 (FGF23) and vitamin D_3 (for review see (23, 24)). PTH and FGF23 target the kidney to promote phosphaturia by removing NaPi-IIa and NaPi-IIc from the BBM of proximal cells (for review see (25)), whereas vitamin D_3 acts on the intestine to stimulate absorption of Pi by increasing the expression of NaPi-IIb (26). In addition, each of these hormones controls the levels of the other two (for review see (23, 24)). Defects in any of these hormonal regulators of Pi homeostasis have a large impact on mineral homeostasis.

Dietary Pi content influences the levels of Pi-regulating hormones and Pi-transporters. Thus, low dietary Pi as well as hypophosphatemia increase the abundance of NaPi-IIa, NaPi-IIc and NaPi-IIb (22, 27-30) and thereby promote intestinal absorption and renal reabsorption. These changes are at least in part secondary to higher circulating levels of vitamin D_3 and reduced concentrations of FGF23 and PTH (28). However, studies in VDR KO mice indicate that stimulation of NaPi-IIb also occurs in a vitamin D_3 independent fashion (29, 30). The reduced levels of FGF23 and PTH triggered by hypophosphatemia remove the suppression of renal NaPi-IIa and NaPi-IIc and thereby enhance renal Pi reabsorption. In contrast, high levels of dietary Pi as well as hyperphosphatemia stimulate PTH and FGF23 and reduce vitamin D_3 (28, 31, 32). In addition to its phosphaturic effect, high FGF23 also reduces the production of vitamin D_3 and increases its degradation (33), blunting the stimulatory effect on intestinal Pi absorption. Besides their effects on Pi handling, vitamin D_3 and PTH also control the levels of plasma Ca^{2+} by stimulating the expression of intestinal (TPRV6, calbindin D_{9K} and Ca^{2+}-ATPase) and renal (TRPV5, calbindin D_{28K} and NCX1) proteins involved in epithelial Ca^{2+} transport (for review see (34, 35)) as well as by stimulation of osteoclasts and thereby bone resorption (36).

As discussed above, intestinal ablation of NaPi-IIb in mice abolishes Na^+-dependent Pi uptake into intestinal BBM (7, 8). However, under standard dietary condition these mice only show slightly increased fecal Pi losses, which is compensated by reduced urinary excretion, thus preserving normophosphatemia. Since the expression of NaPi-IIb is upregulated by low dietary Pi (37), the role of NaPi-IIb may become more important once dietary Pi is restricted. In this study we compare the effect of the dietary Pi content particularly Pi-restriction, in wild type and intestinal-specific NaPi-

IIb deficient mice and show that under these conditions, NaPi-IIb deficient mice demineralize bone which may help to prevent more severe hypophosphatemia.

Methods

Animal handling

Experiments were performed in two month old floxed-Slc34a2 male mice expressing villin-driven Cre recombinase (NaPi-IIb$^{f/f}$) (8) and their wild type litter mates (WT, NaPi-IIb$^{-/-}$). Mice were initially fed normal diets (0.8 % Pi, 1 % calcium) while housed in metabolic cages (Tecniplast, Buguggiate, Italy) to collect basal urinary (under mineral oil) and stool samples. Then, they were randomized in three groups: two of them received either a low (LPD; 0.1 % Pi, 1 % calcium) or high (HPD; 1.2 % Pi, 1 % calcium) Pi diet (Kliba Promivi AG, Switzerland) for 3 days, whereas the third group was fed the low Pi diet for 14 days. During the whole procedure mice were fed ad libitum with free access to water. Three days before harvesting samples, animals were placed in metabolic cages to collect urine and stool samples. Mice were then anesthetized using ketamine and xylazine. Upon opening the abdominal cavity, blood was collected from the vena cava and centrifuged at 4°C in heparinized tubes for 7 minutes at 7000 rpm; plasma was aliquoted and immediately frozen in liquid nitrogen. Organs were harvested and frozen in liquid nitrogen. Plasma, organs and scrapings from mucosa of ileum were stored at -80°C for further analysis. Urine was centrifuged at 10000 rpm for 10 minutes and stored at -20°C. Experiments were approved by the local veterinary authority (Veterinäramt Zürich) and performed according to Swiss Animal Welfare laws.

Plasma, urine and stool parameters

The levels of Pi in stool, urine and plasma were colorimetrically determined according to the Fiske Subbarow method (38). For determination of fecal Pi content, dried stool samples were first dissolved in 0.6 M HCl for three days, homogenized and centrifuged as reported (7). The Jaffe method was used to measure urinary creatinine (39). Urinary calcium, sodium, potassium, magnesium and chloride as well as plasma calcium and creatinine were measured on a UniCel DxC 800 Synchron Clinical System (Beckman Coulter), a service provided by the Zürich Integrative Rodent Physiology (ZIRP) facility.

FGF23, PTH, vitamin D and DPD measurement

FGF23 (intact) and PTH (intact) levels in plasma were analyzed by ELISA (Immunotopics International, San Clemente, CA, USA). For plasma 1,25 $(OH)_2$-Vitamin D_3 measurements, a radioimmunoassay kit (Immunodiagnostic System, Frankfurt am Main, Germany) was used. Urinary deoxypyridionline (DPD) was assessed with an enzymatic immunoassay kit (MicroVue DPD EIA, Quidel Corporation, Athens, USA). All assays were performed according to the manufacturers' protocol.

Renal brush border membrane vesicle and homogenate preparation

Brush border membrane vesicles (BBMV) were prepared from frozen kidneys as described before (40). A polytron (PT 10-35, Kinematica GmbH, Lucerne) was used to homogenize kidneys in a buffer containing 300 mM mannitol, 5 mM EGTA, 12 mM Tris-HCl (pH 7.1) and complete mini protease inhibitor cocktail (Roche, Switzerland). A small aliquot of the homogenate was frozen and stored at -80°C for western blot analysis. Upon addition of $MgCl_2$ (12 mM final concentration), the remaining homogenate was kept on ice for 15 minutes followed by centrifugation at 4500 rpm for 15 minutes at 4°C. The resulting supernatant was further centrifuged at 17500 rpm for 30 minutes at 4°C to collect BBMV. The pellet, containing BBMV was resuspended in a buffer composed of 300 mM mannitol and 20 mM HEPES-Tris (pH 7.4).

Uptake of ^{32}P-phosphate, ^{3}H-D-glucose and ^{14}C-isoleucine into renal BBMV

Uptakes were done according to the reported filtration technique (41). Freshly prepared BBMV were incubated in solutions containing either 100 mM NaCl or 100 mM KCl, both solutions supplemented with 0.1 mM Pi and ^{32}P labelled tracer. ^{3}H-D-glucose and ^{14}C-leucine uptakes were measured following the same protocol using solutions containing 0.1 mM D-glucose and 0.1 mM isoleucine together with the indicated radiolabeled tracers. Uptakes were left to proceed for either 30 seconds (^{3}H-Glucose and ^{14}C-leucine) or 1 minute (^{32}P). The incorporation of traces into the BBMV was measured with a β-counter (Packard BioScience). Remaining BBMVs were snap-frozen and stored at -80°C for western blot analysis.

Total membrane fractions from ileum

Scrapings from mucosa of ileum were homogenized in a buffer containing 200 mM mannitol, 80 mM HEPES, 41 mM KOH, and protease inhibitors, with pH adjusted to 7.5. Homogenization was performed with MagNa Lyser Green Beads (Roche), in a Precellys 24 Homogenizer. Upon centrifugation at 800 rpm for 20 minutes at 4°C, supernatants were further centrifuged at 41’000 rpm for 30 minutes at 4°C, and pellets containing total membrane proteins were resuspendend in the same buffer used for homogenization.

Western blot

A Bio Rad DC protein assay kit (BioRad, Cressier, Switzerland) was used to measure the protein concentration of renal homogenates and BBMV as well as of total membrane fractions from ileum. Then, 20 µg of proteins were mixed with Laemmli sample buffer (0.38 M Tris base, 8% SDS, 4 mM EDTA, 40% (v/v) glycerol, pH adjusted to 6.8 with HCl, and 40 mg/10 ml of bromphenol blue) and loaded on 9% or 12% acrylamide SDS-PAGE. A standard tank system (Mini Trans-Blot, Bio-Rad) was used to transfer proteins from gels onto polyvinylidene difluoride (PVDF) membranes (Immobilon-P, Millipore, Schaffhausen, Switzerland). Tris buffered saline (TBS) containing 5% fat free powder milk was used to block membranes for 30 minutes at room temperature. Then, PVDF membranes were incubated overnight at 4°C with primary antibodies against NaPi-IIa (10), NaPi-IIb (ref), NaPi-IIc (42), TRPV5 (43), CaSR (Thermofisher Scientific), Calbindin D28k (SWANT, Marly, Switzerland), Cyp24a1 (Protein Tech, Manchester, United Kingdom), and β-actin (Sigma-Aldrich, Buchs, Switzerland). Upon three consecutive washing steps with TBS, membranes were again blocked and incubated for 2 hours at room temperature with the appropriate (anti- mouse or-rabbit) secondary antibody linked to horse radish peroxidase (HRP) (Promega AG, Dübendorf, Switzerland). After three washes with TBS, membranes were exposed to HRP substrate (Western Chemiluminescence HRP Substrate, Millipore, Schaffhausen, Switzerland) for 5 minutes. Chemiluminiscence was detected with a LAS-4000 camera system (Fujifilm). Densitometric analysis was performed using ImagJ and normalized to β-actin.

Semi-quantitative real time RT-PCR

Half a kidney was homogenized in RLT buffer supplemented with β-mercaptoethanol. RNA from homogenates was isolated using the Qiagen RNeasy Mini kit (Qiagen, Hombrechtikon, Switzerland) following the protocol provided by the supplier. TaqMan Reverse Transcription Kit (Applied Biosystems, Zug, Switzerland) was then used for reverse transcription of the isolated RNA according to the manufacturers' protocol.

To quantify relative gene expression, specific sets of primers and FAM/TAMRA-labelled probes for Cyp27b1 (Mm01165918_g1,) and Slc34a2 (Microsynth, Switzerland) were used, and their abundance was normalized to the expression of hypoxanthine-guanine phosphoribosyltransferase (HPRT, Microsynth, Switzerland). KAPA PROBE FAST qPCR Kit Master Mix (KAPA BIOSYSTEMS, Boston USA) containing primers (5 µM) and probe (25 µM) was used to amplify cDNA in a 7500 Fast Real Time PCR System (Applied Biosystems, Zug, Switzerland). The cycle number at a given threshold (Ct) was measured and gene expression relative to the expression of HPRT was calculated according to the formula $R=2^\wedge(Ct_{HPRT}-Ct_{gene\ of\ interest})$.

Micro Computer Tomography

Freshly isolated femurs were scanned in a Quantum GX microCT Imaging System (PerkinElmer) provided by the ZIRP facility. Distal epiphysis and subsequent diaphysis was imaged for 3 minutes using a 5 mm field of view at a tube current of 100 µA and 90 kV tube voltage. Analyze 12.0 program (AnalyzeDirect, Inc., Overland Park, USA) was used to asses bone mineral density (BMD) and bone volume data. Bones were analyzed from the end of the patellar surface of the distal epiphysis and 100 sections into the diaphysis were averaged. Grey scales of the scans were translated into BMD using a calibration curve obtained by scans of a 1200 mg/cm3 hydroxy apatite phantom (Micro-CT HA Phantom, QRM GmbH, Moehrendorf, Germany).

Glucocorticoids

Urinary glucocorticoids (corticosterone, 11-dehydrocorticosterone and 5 alpha-Dihydrocorticosterone was measured by ultra-pressure liquid chromatography-tandem mass spectrometry (UPLC-MS/MS) by our collaborators in Basel (Alex Odermatt and Denise Kratschmar).

Statistical Analysis

Unpaired students t-test or ANOVA with Bonferroni correction for multiple comparisons were used to analyze comparisons. P-values > 0.05 were considered as significant. Data is presented as Mean + SEM.

Results

Intestinal ablation of NaPi-IIb and Pi deprivation causes transient hypophosphatemia and stimulates urinary calcium excretion

Wild type mice and mice lacking intestinal NaPi-IIb expression were analyzed in metabolic cages under standard conditions as well as after 3 days HPD or LPD and 14 days LPD (Figure 1A and Table 1). For both genotypes, the fecal excretion of Pi reflected the dietary Pi content: it was higher in animals fed high Pi and progressively lower in those fed low Pi as compared with mice kept on normal chow. Under all dietary conditions, there was a tendency for increased fecal Pi excretion in KO compared with WT mice, which was only significant during HPD conditions when absolute values were compared. However, the relative differences in fecal Pi excretion between both genotypes increased with decreasing levels of Pi in the diet: NaPi-IIb KO showed around 18% higher excretion than WT mice when fed normal or high Pi diets whereas the increase was 44% and 55% in the groups fed low Pi for 3 and 14 days, respectively (supplementary Figure 1).

Urinary Pi was quantified for the same dietary conditions. In both genotypes, the urinary content of Pi adapted to the dietary Pi content, being higher in mice fed HPD diet and progressively lower in the groups fed LPD as compared with mice receiving standard food (Figure 1B and Table 1). NaPi-IIb KO animals excreted significantly less Pi in urine than the WT littermates after 3 days of LPD adaptation, whereas no differences between genotypes were observed under 3 days of HPD or after 14 days of LPD.

Plasma levels of Pi were measured during dietary adaptations (Figure 1C and Table 1). The different dietary conditions did not result in significant changes in plasma Pi values neither in WT nor in NaPi-IIb deficient mice. However, due to a transient trend for hypophosphatemia in NaPi-IIb KO fed LPD, plasma Pi was lower in mutant mice than in WT upon 3 days LPD. No differences between both genotypes were detected in the other dietary conditions.

Urinary Ca^{2+} excretion was analyzed under normal dietary conditions as well as after 3 days HPD or LPD and 14 days LPD (Figure 1D and Table 1). In both genotypes excretion was comparable in mice fed a normal diet or HPD for 3 days, whereas a drastic increase was observed in animals fed a LPD for either 3 or 14 days. This increase was even stronger (more than 70%) in NaPi-IIb KO animals compared to WT mice.

Additionally a higher volume of urine was excreted in NaPi-IIb KO mice after long term dietary Pi restriction (Table 1), but the creatinine clearance as an indicator for glomerular filtration rate (GFR) was not significantly altered and excretion of other measured ions was comparable to WT animals (Table 2).

Plasma levels of Ca^{2+} progressively increased in the groups fed LPD compared with HPD (Figure 1D and Table 1). However, there were no differences between WT and NaPi-IIb KO animals under any dietary condition.

Hormonal adaptation is similar in both genotypes

WT and NaPi-IIb KO animals fed a LPD showed a transient increase in the levels of plasma 1,25-$(OH)_2$ vitamin D_3 compared to animals fed a HPD (Figure 2A). 1,25-$(OH)_2$ vitamin D_3 levels were comparable in WT and NaPi-IIb KO mice under all conditions. Renal expression of Cyp27b1 mRNA and Cyp24a1 protein was analyzed in animals fed LPD for 14 days. There was no difference between WT and NaPi-IIb KO mice neither on the mRNA levels of the vitamin D_3 activating enzyme Cyp27b1 (Figure 2B), nor on the protein expression of the vitamin D_3 catabolizing enzyme Cyp24a1 (Figure 2C).

The concentration of plasma PTH was significantly lower in animals fed a LPD for 3 days than in animals adapted to HPD (Figure 2D). Long term dietary Pi restriction led to an even further decrease in plasma PTH. However, both WT and NaPi-IIb KO animals showed similar PTH levels after adapting to the different dietary conditions. For intact FGF23 levels, a similar pattern to PTH was observed (Figure 2E), i.e. LPD resulted in a progressive reduction of plasma FGF23. No differences between genotypes were observed under the same conditions.

Phosphate transport into renal BBMVs and expression of NaPi-IIa and NaPi-IIc is not altered

Transport studies were performed in renal BBMVs from mice fed LPD diet for 14 days. Uptakes were done in presence and absence of sodium, to determine sodium dependent and independent components of Pi, leucine and glucose transport. Both WT and NaPi-IIb KO animals showed at least a 97% decrease of Pi uptake into renal BBMVs in the absence of sodium, but the sodium dependent and independent transport rates were similar in both genotypes (Figure 3A). Transport rates of leucine (Figure 3B) and glucose (Figure 3C) also showed a strong dependency on sodium (more than 80%), but intestinal ablation of NaPi-IIb did not affect uptakes.

The protein abundance of NaPi-IIa and NaPi-IIc was assessed in the same BBMV preparations that were used for the uptake experiments (long term dietary Pi restriction). The expression of NaPi-IIa (Figure 3D) and NaPi-IIc (Figure 3E), was not affected by intestinal NaPi-IIb deficiency.

NaPi-IIb protein abundance in ileum was increased after 3 and 14 days of LPD compared to HPD, whereas the cotransporter was not detected in NaPi-IIb deficient animals (Figure 3F)

Pi restriction does not affect expression of proteins involved in renal calcium handling between genotypes

The abundance of proteins involved in renal Ca^{2+} handling was assessed in apical membrane preparations and total kidney homogenates from WT and NaPi-IIb KO animals after 14 days dietary Pi restriction. The expression of the Ca^{2+} channel TRPV5 was analyzed in apical membranes (Figure 4A), whereas the abundance of the Ca^{2+} sensing receptor (CaSR, Figure 4B) and calbindin-D28k (Figure 4C) was quantified in renal homogenates. Similar levels of all three proteins were observed in WT and NaPi-IIb KO animals.

Urinary excretion of deoxypyridionline and corticosterone, as well as bone mineral density are altered in Pi-restricted NaPi-IIb KO mice

Urinary excretion of deoxypyridionline (DPD) was quantified as a marker for bone resorption (Figure 5A). The dietary content of Pi did not influence the urinary concentration of DPD in WT animals; however, LPD triggered a progressive increase in the amount of DPD excreted into urine by intestinal NaPi-IIb KO mice. No difference was observed between WT and NaPi-IIb KO fed a HPD or LPD for three days, whereas after long term Pi restriction the levels of DPD in the urine of NaPi-IIb

KO animals were significantly higher (about 85%) than in the corresponding WT animals.

Urinary corticosterone levels were higher in NaPi-IIb deficient animals than in WT litter mates after 14 days of dietary Pi restriction (Figure 5B). The corticosterone metabolites 11-dehydrocorticosterone and 5-alpha-dihydrocorticosterone were also increased in NaPi-IIb deficient animals (113.2±19.9 and 176.2±14.8, respectively) compared to WT (52.0±10.4 and 109.0±15.5, respectively).

Bone mineral density (BMD) was measured in the femurs of WT and NaPi-II KO mice fed 14 days LPD. BMD significantly decreased in NaPi-IIb KO animals when challenged with a long term dietary Pi restriction, compared with the WT littermates (Figure 5B). The difference was detected both in cortical and trabecular bone tissue of femurs, though the changes were higher in trabecular bone.

Discussion

NaPi-IIb has been considered to be the major apical phosphate transporter in the small intestine since its intestinal ablation in mice abolishes Na^+-dependent uptake of Pi into intestinal sacks and BBMV from ileum (7, 8), indicating the loss of active transcellular transport of Pi in the small intestine. However, under standard feeding conditions the absence of NaPi-IIb only leads to a moderate fecal wasting of Pi, which is compensated by increased renal reabsorption, thus resulting in normal plasma Pi. This mild phenotype suggests an alternative transport pathway across the intestinal epithelium able to supply enough Pi, at least under normal dietary Pi. Passive absorption through the paracellular pathway may contribute to this process when a sufficient gradient of Pi is stablished across the epithelium. However, in response to low dietary Pi the expression of NaPi-IIb increases (27, 28), indicating that the active component may be required to adapt to a reduced oral supply of Pi. Therefore, we investigated whether the contribution of NaPi-IIb becomes higher once dietary Pi is limited.

As observed in WT animals, the fecal excretion of Pi in NaPi-IIb KO also increased with HPD and decreased under LPD. However, under all dietary conditions, the fecal Pi output was higher in NaPi-IIa KO than WT, though the difference between genotypes was significant only in HPD when ANOVA was applied to the absolute values. The large differences in the fecal Pi content between the HPD and LPD groups probably masked the relatively smaller differences between genotypes in the normal and LPD; indeed, significant differences were observed in all feeding protocols when the NaPi-IIb KO values were normalized to the excretion of the dietary-matched WT. Moreover, normalization also indicated that the absence of NaPi-IIb had a larger impact in the Pi-restricted groups than in animals fed high Pi. This may indicate that the contribution of the active transport component (mediated mostly by NaPi-IIb) becomes bigger when dietary Pi is low: dietary restriction could theoretically result in lower Pi levels in the intestinal lumen, thus providing a lower gradient for passive transport of Pi across the epithelium. As expected, vitamin D_3, a major stimulus for intestinal Pi absorption (26), was increased in animals fed the LPD compared to HPD. However, no differences were detected between KO and WT mice. This observation was further supported by the finding that the expression of Cyp27b1 and Cyp24a1 (mRNA and protein respectively) was similar in both groups of mice. These renal enzymes are crucial in controlling the systemic levels of vitamin D_3, since Cyp27b1 converts 25(OH)D_3 into the active 1,25$(OH)_2D_3$, whereas Cyp24a1 catabolizes vitamin D_3 (44). The higher NaPi-IIb abundance triggered by low dietary Pi/high vitamin D_3 might further increase the relative difference in Pi transport between WT and NaPi-IIb KO animals, which is in agreement with the observed trend of bigger relative differences in Pi excretion as dietary Pi is restricted.

Dietary loading with Pi triggers a phosphaturic response whereas urinary Pi is low upon dietary Pi restriction. These changes inversely correlate with the abundance of the renal transporters NaPi-IIa and NaPi-IIc, which in turn are controlled by the plasma levels of PTH, FGF23, and 1,25$(OH)_2D_3$. Thus, dietary supply of Pi increases the abundance of both hormones whereas Pi deficiency reduces their levels (28, 32). As for the fecal output, also the urinary excretion of Pi adapted in a similar fashion in NaPi-IIb KO and WT mice, increasing in response to HDP and decreasing upon dietary Pi restriction. Although the increase in renal Pi excretion triggered by the HPD was lower in NaPi-IIb KO compared to the WT mice, the massive phosphaturia also observed in NaPi-IIb depleted mice indicates that the component responsible for the passive intestinal transport of Pi is able to absorb a considerable amount of Pi which must be later excreted by the kidney. Instead, both genotypes excreted similar low amounts of Pi after adaptation to LPD. Since WT animals fed low Pi already increased renal Pi reabsorption to a point where almost no Pi is excreted with urine (especially after 14 days LPD), it is not surprising that the kidneys of KO mice cannot further compensate for the impaired intestinal absorption. In agreement with urinary Pi excretion, the adaptation of PTH and FGF23 to changes in dietary Pi was also comparable in WT and NaPi-IIb deficient mice, as the levels of both hormones were strongly and similarly reduced in mice fed LPD. Consistently, transport of Pi into renal BBMV and protein expression of NaPi-IIa and NaPi-IIc was similar in WT and NaPi-IIb deficient mice fed LPD during 14 days. The combination of increased fecal loss but similar urinary excretion of Pi detected in NaPi-IIb KO on LPD likely caused the more pronounced reduction in the plasma Pi levels in NaPi-IIb KO animals after 3 days of LPD. In contrast, WT mice were able to maintain normal Pi values though a tendency for reduced plasma Pi was detected after 14 days of LPD. The pronounced and earlier fall in plasma Pi may indicate that NaPi-IIb KO animals need an extra-renal compensatory mechanism when facing longer Pi restriction.

Chronic hypophosphatemia may lead to osteomalacia and hypophosphatemic rickets (45), due to the mobilization of Pi from bone and/or decreased mineralization of newly formed bone. The stronger increase in urinary Ca^{2+} excretion in the NaPi-IIb KO mice during LPD suggested bones as source for Pi: although a drastic increase of urinary Ca^{2+} was observed in both genotypes when fed a LPD (both 3 and 14 days), urinary Ca^{2+} levels were more than 70% higher in NaPi-IIb KO mice than in their WT littermates. Since vitamin D_3 stimulates not only Pi but also Ca^{2+} absorption in the intestine (46), high vitamin D_3 may contribute to the increase in plasma and urinary Ca^{2+} observed in both animal groups with prolonged Pi deprivation. Moreover, intestinal Ca^{2+} absorption may be enhanced by the absence of Pi reacting with free Ca^{2+} in the intestinal lumen. In addition, low PTH may lead to urinary wasting of Ca^{2+}, as a main function of this hormone is to promote Ca^{2+} reabsorption in the kidney (47, 48). However, none of these factors can explain the difference in urinary Ca^{2+} between WT and NaPi-IIb KO mice, since they were equally affected in both genotypes. Also, the renal expression of several proteins involved in Ca^{2+} transport, including TRPV5, calbindin-28K and the CaSR, was similar in WT and NaPi-IIb KO. Thus, in response to hypophosphatemia, bone resorption may be enhanced in NaPi-IIb deficient mice releasing Pi, together with Ca^{2+}, at the cost of bone mass loss. In turn, renal excretion of Ca^{2+} will be higher to remove excessive Ca^{2+}. This interpretation is further supported by the changes in urinary excretion of DPD, a marker for bone resorption (49). DPD excretion was massively elevated in NaPi-IIb KO upon prolonged Pi restriction, whereas no indication for enhanced bone resorption was detected in dietary-matched WT. in agreement with the DPD data, the BMD was decreased in Pi-restricted NaPi-IIb deficient mice.

NaPi-IIb deficient mice fed low Pi also showed higher urinary corticosterone, which is accepted to reflect its circulating levels. Glucocorticoids reduce bone formation rates (50) and increase osteoclast number, promoting bone resorption (51). The observed increase in excreted glucocorticoids might partially explain the reduced bone mineralization observed in NaPi-IIb deficient animals. Together, these observations strongly suggest that the compensation for the loss of active intestinal absorption of Pi requires the mobilization of Pi from bones when the dietary supply is low.

In summary, we found that in response to dietary Pi restriction, renal compensation is not sufficient to maintain plasma Pi levels in mice lacking intestinal NaPi-IIb. Instead, and unlike to WT mice, NaPi-IIb KO develop a transient hypophosphatemia followed by a compensatory mechanism that involves release of Pi from bone. Thus, active intestinal Pi absorption mediated by NaPi-IIb is critical to protect bone during periods of low dietary Pi availability.

Acknowledgments

We would like to gratefully acknowledge the use of the Zurich Integrative Rodent Physiology Core Facility (ZIRP) for animal handling and technical support.

This study was supported by grants from the Wolfermann-Nägeli Stiftung, Zurich and the Hartmann Müller Stiftung, Zurich.

Figure legends

Figure 1: Intestinal ablation of NaPi-IIb and Pi deprivation causes transient hypophosphatemia and stimulates urinary calcium excretion. Fecal (A), urinary (B) and plasma (C) concentrations of Pi as well as urinary (D) and plasma (E) levels of Ca^{2+} were measured in samples collected from wild type (WT) and NaPi-IIb deficient mice (KO). Mice were fed diets containing normal (N) and/or high (H) or low (L) amounts of Pi. The high Pi diet was provided for 3 days (3d) whereas the low Pi diet was provided for 3 (3d) and 14 days (14d). Data is presented as mean + SEM (n=10) and was analyzed by ANOVA-Bonferroni. Significant differences are indicated as: ^{a}/* $p<0.05$, ^{b}/** $p<0.01$ and ^{c}/***$p<0.001$, where letters indicate significant changes versus normal diets (or versus the high Pi diet, if normal diet is not available), and asterisks mark differences between genotypes under the same dietary condition.

Figure 2: Hormonal adaptation is similar in both genotypes. Circulating levels of 1,25-$(OH)_2$ vitamin D_3 (A), PTH (D) and FGF23 (E) were measured in plasma collected from wild type (WT) and NaPi-IIb deficient mice (KO) fed diets containing high (H) or low (L) amounts of Pi. The high Pi diet was provided for 3 days (3d) whereas the low Pi diet was provided for 3 (3d) and 14 days (14d). Renal mRNA levels of Cyp27b1 (B) and renal protein abundance of Cyp24a1 (C) were measured after 14 days of Pi restriction. Data is presented as mean + SEM (n=10), and was

analyzed by ANOVA-Bonferroni. Significant differences are indicated as: ^{a} $p<0.05$, ^{b} $p<0.01$ and ^{c} $p<0.001$, were significances refer to high dietary Pi groups (no differences between genotypes were observed).

Figure 3: Phosphate transport into renal BBMVs and expression of NaPi-IIa and NaPi-IIc is not altered. Uptakes of Pi (A), leucine (B) and glucose (C) were performed with renal BBMVs isolated from wild type (WT) and NaPi-IIb deficient mice (KO) after 14 days of dietary Pi restriction. Experiments were carried out in the presence (Na) and absence (K) of Na^+. The renal expression of NaPi-IIa (D) and NaPi-IIc (E) was quantified by Western blot of the same BBMV used for the uptake experiments; the bar graphs show the corresponding densitometric analysis normalized for the expression of β-actin. Differences between genotypes were analyzed by unpaired t-test. The abundance of NaPi-IIb in ileum (F) was analyzed by Western blot in samples from wild type mice fed 3 days high or low Pi diets as well as 14 days low Pi; one sample of the corresponding dietary-matched NaPi-IIb deficient mice (KO) was also included. Densitometric analysis normalized for the expression of β-actin is shown as mean + SEM. Statistical differences versus the high dietary group were analyze by ANOVA-Bonferroni with * $p<0.05$ and ** $p<0.01$.

Figure 4: Pi restriction does not affect expression of proteins involved in renal calcium handling between genotypes. Renal protein abundance of Cabindin 28_K (A), TRPV5 (B) and calcium sensing receptor (C) was assessed by Western blot in homogenates from kidneys of wild type (WT) and NaPi-IIb deficient animals (KO) after 14 days of Pi restriction. Corresponding densitometric analysis was normalized by the expression level of β-actin and data is shown as mean + SEM. Differences between genotypes were analyzed by unpaired t-test.

Figure 5: Urinary excretion of deoxypyridionline (DPD) and chorticosterone as well as bone mineral density (BMD) are altered in Pi-restricted NaPi-IIb KO mice. Urinary DPD (A) levels were measured in samples from wild type (WT) and NaPi-IIb deficient mice (KO) mice fed 3 days high or low Pi diets as well as 14 days low Pi. Corticosterone levels in urine (B) were determined in both genotypes after 14 days of Pi restriction. Cortical (C) and trabecular (D) BMD were measured in femurs of mice after 14 days Pi restriction. Data is presented as mean + SEM and was analyzed by either ANOVA-Bonferroni (DPD) or unpaired t-test (corticosterone and BMD). Significant differences are indicated as: ^{a}/* $p<0.05$, ** $p<0.01$ and *** $p<0.001$, where

a represents the difference versus the corresponding high dietary group, whereas asterisks mark differences between genotypes under the same dietary conditions.

Table 1: Metabolic data. Parameters were measured in wild type (WT) and NaPi-IIb deficient mice (KO) fed diets containing normal (N), high (H) and low (L) amounts of Pi. The high Pi diet was provided for 3 days (3d) whereas the low Pi diet was provided for 3 (3d) and 14 days (14d). Data is presented as mean + SEM (n≥10) and was analyzed by ANOVA-Bonferroni. Significant differences are indicated as: ^{a}/* $p<0.05$, ^{b}/** $p<0.01$ and ^{c}/***$p<0.001$, where letters indicate significant changes versus normal diets (or versus the high Pi diet, if normal diet is not available), and asterisks mark differences between genotypes under the same dietary condition.

Table 2: Additional urinary parameters measured in samples collected from wild type (WT) and NaPi-IIb deficient mice (KO) after 14 days Pi restriction. Data is presented as mean + SEM (n≥10) and was analyzed by unpaired t-test.

Supplementary figure 1: Fecal Pi excretion in wild type (WT) and NaPi-IIb deficient mice (KO) after normal, 3 days high, 3 days low and 14 days low dietary Pi. Values of the KO mice were normalized to the mean of the dietary-matched WT. Data is presented as mean + SEM (n=10), and was analyzed by ANOVA-Bonferroni, with ***$p<0.001$ versus the dietary-matched WT.

References

1. Bruin WJ, Baylink DJ, Wergedal JE. Acute Inhibition of Mineralization and Stimulation of Bone-Resorption Mediated by Hypophosphatemia. Endocrinology. 1975;96(2):394-9. PubMed PMID: ISI:A1975V450400020. English.
2. Day HG, McCollum EV. Mineral metabolism, growth, and symptomatology of rats on a diet extremely deficient in phosphorus. Journal of Biological Chemistry. 1939 Sep;130(1):269-83. PubMed PMID: ISI:000187899000030. English.
3. Weinstein RS. Glucocorticoid-Induced Bone Disease. New Engl J Med. 2011 Jul 7;365(1):62-70. PubMed PMID: ISI:000292459400010. English.
4. Goltzman D. Studies on the mechanisms of the skeletal anabolic action of endogenous and exogenous parathyroid hormone. Archives of biochemistry and biophysics. 2008 May 15;473(2):218-24. PubMed PMID: 18358824. Epub 2008/03/25. eng.
5. Marks J, Srai SK, Biber J, Murer H, Unwin RJ, Debnam ES. Intestinal phosphate absorption and the effect of vitamin D: a comparison of rats with mice. Experimental physiology. 2006 May;91(3):531-7. PubMed PMID: 16431934.
6. Hilfiker H, Hattenhauer O, Traebert M, Forster I, Murer H, Biber J. Characterization of a murine type II sodium-phosphate cotransporter expressed in mammalian small intestine. Proceedings of the National Academy of Sciences of the United States of America. 1998 Nov 24;95(24):14564-9. PubMed PMID: 9826740. Pubmed Central PMCID: 24413.
7. Sabbagh Y, O'Brien SP, Song W, Boulanger JH, Stockmann A, Arbeeny C, et al. Intestinal npt2b plays a major role in phosphate absorption and homeostasis. Journal of the American Society of Nephrology : JASN. 2009 Nov;20(11):2348-58. PubMed PMID: 19729436. Pubmed Central PMCID: 2799172.
8. Hernando N, Myakala K, Simona F, Knopfel T, Thomas L, Murer H, et al. Intestinal Depletion of NaPi-IIb/Slc34a2 in Mice: Renal and Hormonal Adaptation. Journal of bone and mineral research : the official journal of the American Society for Bone and Mineral Research. 2015 Oct;30(10):1925-37. PubMed PMID: 25827490. Epub 2015/04/02. eng.
9. Castellana G, Castellana G, Gentile M, Castellana R, Resta O. Pulmonary alveolar microlithiasis: review of the 1022 cases reported worldwide. European respiratory review : an official journal of the European Respiratory Society. 2015 Dec;24(138):607-20. PubMed PMID: 26621975.
10. Custer M, Lotscher M, Biber J, Murer H, Kaissling B. Expression of Na-P(i) cotransport in rat kidney: localization by RT-PCR and immunohistochemistry. The American journal of physiology. 1994 May;266(5 Pt 2):F767-74. PubMed PMID: 7515582. Epub 1994/05/01. eng.
11. Segawa H, Kaneko I, Takahashi A, Kuwahata M, Ito M, Ohkido I, et al. Growth-related renal type II Na/Pi cotransporter. The Journal of biological chemistry. 2002 May 31;277(22):19665-72. PubMed PMID: 11880379. Epub 2002/03/07. eng.
12. Beck L, Karaplis AC, Amizuka N, Hewson AS, Ozawa H, Tenenhouse HS. Targeted inactivation of Npt2 in mice leads to severe renal phosphate wasting, hypercalciuria, and skeletal abnormalities. Proceedings of the National Academy of Sciences of the United States of America. 1998 Apr 28;95(9):5372-7. PubMed PMID: 9560283. Pubmed Central PMCID: 20268.
13. Chau H, El-Maadawy S, McKee MD, Tenenhouse HS. Renal calcification in mice homozygous for the disrupted type IIa Na/Pi cotransporter gene Npt2. Journal of bone and mineral research : the official journal of the American Society for Bone and Mineral Research. 2003 Apr;18(4):644-57. PubMed PMID: 12674325.
14. Rajagopal A, Braslavsky D, Lu JT, Kleppe S, Clement F, Cassinelli H, et al. Exome sequencing identifies a novel homozygous mutation in the phosphate transporter SLC34A1 in hypophosphatemia and nephrocalcinosis. The Journal of clinical endocrinology and metabolism. 2014 Nov;99(11):E2451-6. PubMed PMID: 25050900. Pubmed Central PMCID: 4223446.
15. Schlingmann KP, Ruminska J, Kaufmann M, Dursun I, Patti M, Kranz B, et al. Autosomal-Recessive Mutations in SLC34A1 Encoding Sodium-Phosphate Cotransporter 2A Cause Idiopathic

Infantile Hypercalcemia. Journal of the American Society of Nephrology : JASN. 2015 Jun 5. PubMed PMID: 26047794.

16. Kestenbaum B, Glazer NL, Kottgen A, Felix JF, Hwang SJ, Liu Y, et al. Common genetic variants associate with serum phosphorus concentration. Journal of the American Society of Nephrology : JASN. 2010 Jul;21(7):1223-32. PubMed PMID: 20558539. Pubmed Central PMCID: 3152230.

17. Segawa H, Onitsuka A, Kuwahata M, Hanabusa E, Furutani J, Kaneko I, et al. Type IIc sodium-dependent phosphate transporter regulates calcium metabolism. Journal of the American Society of Nephrology : JASN. 2009 Jan;20(1):104-13. PubMed PMID: 19056871. Pubmed Central PMCID: 2615734.

18. Myakala K, Motta S, Murer H, Wagner CA, Koesters R, Biber J, et al. Renal-specific and inducible depletion of NaPi-IIc/Slc34a3, the cotransporter mutated in HHRH, does not affect phosphate or calcium homeostasis in mice. American journal of physiology Renal physiology. 2014 Apr 15;306(8):F833-43. PubMed PMID: 24553430.

19. Bastepe M, Juppner H. Inherited hypophosphatemic disorders in children and the evolving mechanisms of phosphate regulation. Reviews in endocrine & metabolic disorders. 2008 Jun;9(2):171-80. PubMed PMID: 18365315.

20. Wagner CA, Rubio-Aliaga I, Biber J, Hernando N. Genetic diseases of renal phosphate handling. Nephrology, dialysis, transplantation : official publication of the European Dialysis and Transplant Association - European Renal Association. 2014 Sep;29 Suppl 4:iv45-54. PubMed PMID: 25165185.

21. Forster IC, Hernando N, Biber J, Murer H. Phosphate transport kinetics and structure-function relationships of SLC34 and SLC20 proteins. Current topics in membranes. 2012;70:313-56. PubMed PMID: 23177991. Epub 2012/11/28. eng.

22. Villa-Bellosta R, Ravera S, Sorribas V, Stange G, Levi M, Murer H, et al. The Na+-Pi cotransporter PiT-2 (SLC20A2) is expressed in the apical membrane of rat renal proximal tubules and regulated by dietary Pi. American journal of physiology Renal physiology. 2009 Apr;296(4):F691-9. PubMed PMID: 19073637. Pubmed Central PMCID: 2670642.

23. Bergwitz C, Juppner H. Regulation of phosphate homeostasis by PTH, vitamin D, and FGF23. Annual review of medicine. 2010;61:91-104. PubMed PMID: 20059333.

24. Hu MC, Shiizaki K, Kuro-o M, Moe OW. Fibroblast growth factor 23 and Klotho: physiology and pathophysiology of an endocrine network of mineral metabolism. Annual review of physiology. 2013;75:503-33. PubMed PMID: 23398153. Pubmed Central PMCID: 3770142.

25. Biber J, Hernando N, Forster I. Phosphate transporters and their function. Annual review of physiology. 2013;75:535-50. PubMed PMID: 23398154.

26. Hattenhauer O, Traebert M, Murer H, Biber J. Regulation of small intestinal Na-P(i) type IIb cotransporter by dietary phosphate intake. The American journal of physiology. 1999 Oct;277(4 Pt 1):G756-62. PubMed PMID: 10516141.

27. Levi M, Lotscher M, Sorribas V, Custer M, Arar M, Kaissling B, et al. Cellular mechanisms of acute and chronic adaptation of rat renal P(i) transporter to alterations in dietary P(i). The American journal of physiology. 1994 Nov;267(5 Pt 2):F900-8. PubMed PMID: 7977794.

28. Bourgeois S, Capuano P, Stange G, Muhlemann R, Murer H, Biber J, et al. The phosphate transporter NaPi-IIa determines the rapid renal adaptation to dietary phosphate intake in mouse irrespective of persistently high FGF23 levels. Pflugers Archiv : European journal of physiology. 2013 Nov;465(11):1557-72. PubMed PMID: 23708836.

29. Capuano P, Radanovic T, Wagner CA, Bacic D, Kato S, Uchiyama Y, et al. Intestinal and renal adaptation to a low-Pi diet of type II NaPi cotransporters in vitamin D receptor- and 1alphaOHase-deficient mice. American journal of physiology Cell physiology. 2005 Feb;288(2):C429-34. PubMed PMID: 15643054.

30. Segawa H, Kaneko I, Yamanaka S, Ito M, Kuwahata M, Inoue Y, et al. Intestinal Na-P(i) cotransporter adaptation to dietary P(i) content in vitamin D receptor null mice. American journal of physiology Renal physiology. 2004 Jul;287(1):F39-47. PubMed PMID: 14996670.

31. Scanni R, vonRotz M, Jehle S, Hulter HN, Krapf R. The human response to acute enteral and parenteral phosphate loads. Journal of the American Society of Nephrology : JASN. 2014 Dec;25(12):2730-9. PubMed PMID: 24854273. Pubmed Central PMCID: 4243350.

32. Thomas L, Bettoni C, Kno pfel T, Hernando N, Biber J, Wagner CA. Acute Adaption to Oral or Intravenous Phosphate Requires Parathyroid Hormone. Journal of the American Society of Nephrology. 2016.

33. Shimada T, Hasegawa H, Yamazaki Y, Muto T, Hino R, Takeuchi Y, et al. FGF-23 is a potent regulator of vitamin D metabolism and phosphate homeostasis. Journal of Bone and Mineral Research. 2004 Mar;19(3):429-35. PubMed PMID: ISI:000189249000011. English.

34. Moor MB, Bonny O. Ways of calcium reabsorption in the kidney. American journal of physiology Renal physiology. 2016 Jun 1;310(11):F1337-50. PubMed PMID: 27009338.

35. Khanal RC, Nemere I. Regulation of intestinal calcium transport. Annual review of nutrition. 2008;28:179-96. PubMed PMID: 18598134.

36. Manolagas SC. Birth and death of bone cells: basic regulatory mechanisms and implications for the pathogenesis and treatment of osteoporosis. Endocrine reviews. 2000 Apr;21(2):115-37. PubMed PMID: 10782361. Epub 2000/04/27. eng.

37. Radanovic T, Wagner CA, Murer H, Biber J. Regulation of intestinal phosphate transport. I. Segmental expression and adaptation to low-P(i) diet of the type IIb Na(+)-P(i) cotransporter in mouse small intestine. American journal of physiology Gastrointestinal and liver physiology. 2005 Mar;288(3):G496-500. PubMed PMID: 15701623.

38. Fiske CH, Subbarow Y. The colorimetric determination of phosphorus. Journal of Biological Chemistry. 1925 Dec;66(2):375-400. PubMed PMID: ISI:000187538900004. English.

39. Slot C. Plasma Creatinine Determination - a New and Specific Jaffe Reaction Method. Scand J Clin Lab Inv. 1965;17(4):381-&. PubMed PMID: ISI:A19656765100012. English.

40. Biber J, Stieger B, Stange G, Murer H. Isolation of renal proximal tubular brush-border membranes. Nature protocols. 2007;2(6):1356-9. PubMed PMID: 17545973.

41. Stoll R, Kinne R, Murer H. Effect of dietary phosphate intake on phosphate transport by isolated rat renal brush-border vesicles. The Biochemical journal. 1979 Jun 15;180(3):465-70. PubMed PMID: 486124. Pubmed Central PMCID: 1161083.

42. Nowik M, Picard N, Stange G, Capuano P, Tenenhouse HS, Biber J, et al. Renal phosphaturia during metabolic acidosis revisited: molecular mechanisms for decreased renal phosphate reabsorption. Pflugers Archiv : European journal of physiology. 2008 Nov;457(2):539-49. PubMed PMID: 18535837. Epub 2008/06/07. eng.

43. van der Hagen EA, Lavrijsen M, van Zeeland F, Praetorius J, Bonny O, Bindels RJ, et al. Coordinated regulation of TRPV5-mediated Ca(2)(+) transport in primary distal convolution cultures. Pflugers Archiv : European journal of physiology. 2014 Nov;466(11):2077-87. PubMed PMID: 24557712. Epub 2014/02/22. eng.

44. Perwad F, Portale AA. Vitamin D metabolism in the kidney: regulation by phosphorus and fibroblast growth factor 23. Molecular and cellular endocrinology. 2011 Dec 5;347(1-2):17-24. PubMed PMID: 21914460.

45. Alizadeh Naderi AS, Reilly RF. Hereditary disorders of renal phosphate wasting. Nature reviews Nephrology. 2010 Nov;6(11):657-65. PubMed PMID: 20924400. Epub 2010/10/07. eng.

46. Song Y, Peng X, Porta A, Takanaga H, Peng JB, Hediger MA, et al. Calcium transporter 1 and epithelial calcium channel messenger ribonucleic acid are differentially regulated by 1,25 dihydroxyvitamin D3 in the intestine and kidney of mice. Endocrinology. 2003 Sep;144(9):3885-94. PubMed PMID: 12933662. Epub 2003/08/23. eng.

47. Bourdeau JE, Burg MB. Effect of PTH on calcium transport across the cortical thick ascending limb of Henle's loop. The American journal of physiology. 1980 Aug;239(2):F121-6. PubMed PMID: 6250408. Epub 1980/08/01. eng.

48. de Groot T, Lee K, Langeslag M, Xi Q, Jalink K, Bindels RJ, et al. Parathyroid hormone activates TRPV5 via PKA-dependent phosphorylation. Journal of the American Society of Nephrology : JASN.

2009 Aug;20(8):1693-704. PubMed PMID: 19423690. Pubmed Central PMCID: 2723979. Epub 2009/05/09. eng.

49. Seibel MJ, Robins SP, Bilezikian JP. Urinary Pyridinium Cross-Links of Collagen - Specific Markers of Bone-Resorption in Metabolic Bone-Disease. Trends Endocrin Met. 1992 Sep;3(7):263-70. PubMed PMID: ISI:A1992JL49300005. English.

50. Rauch A, Seitz S, Baschant U, Schilling AF, Illing A, Stride B, et al. Glucocorticoids Suppress Bone Formation by Attenuating Osteoblast Differentiation via the Monomeric Glucocorticoid Receptor. Cell Metab. 2010 Jun 9;11(6):517-31. PubMed PMID: ISI:000278747800010. English.

51. Khosla S. Minireview: The OPG/RANKL/RANK system. Endocrinology. 2001 Dec;142(12):5050-5. PubMed PMID: ISI:000172452700002. English.

Figure 1

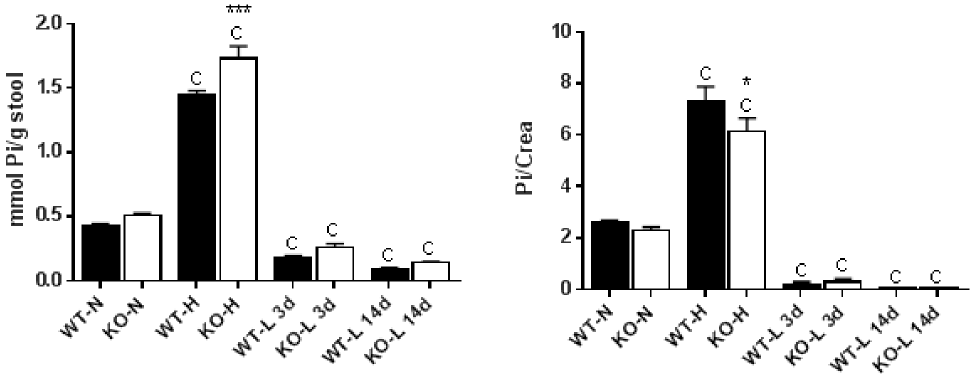
A) Fecal Pi

B) Urinary Pi

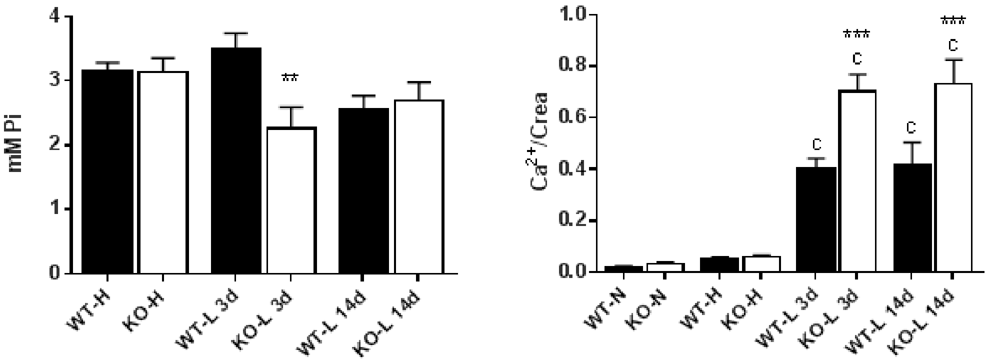
C) Plasma Pi

D) Urinary calcium

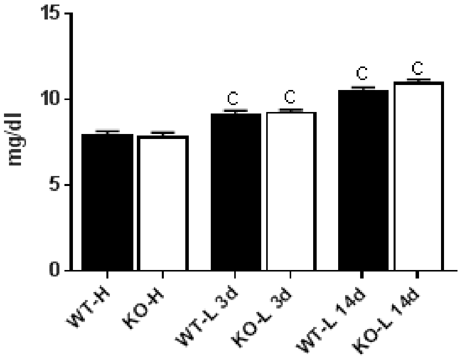
E) Plasma calcium

Figure 2

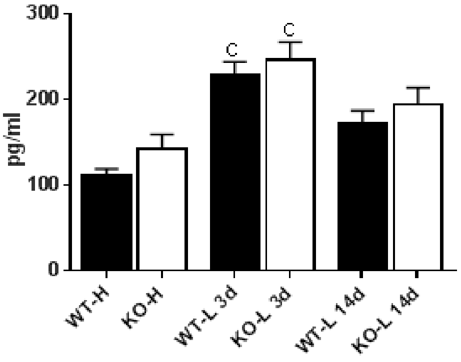
A) Vitamin D_3

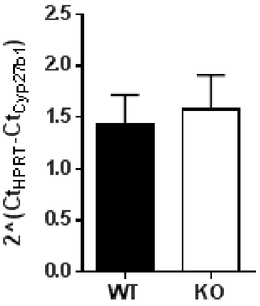
B) Renal Cyp27b1

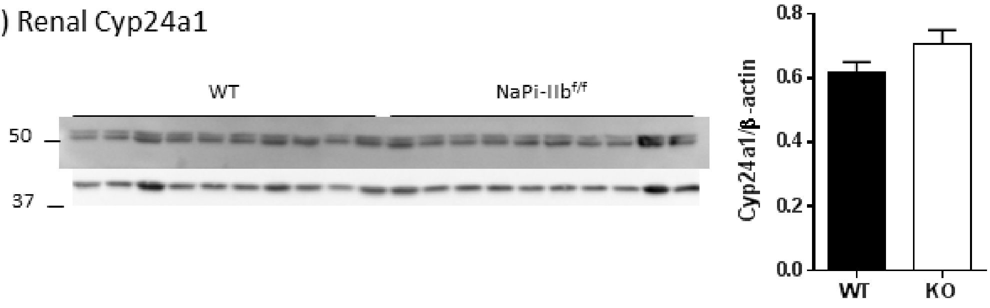
C) Renal Cyp24a1

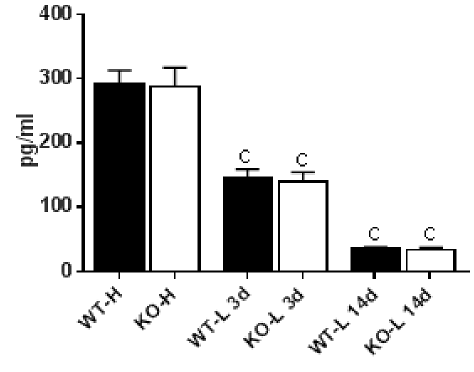
D) PTH

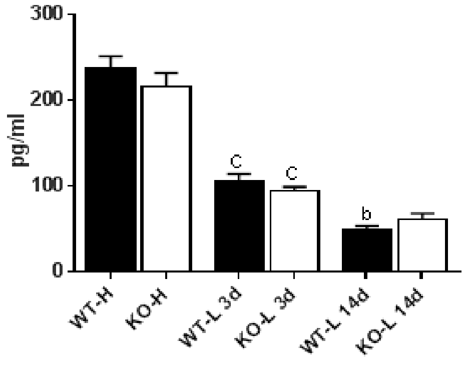
E) FGF23

Figure 3

A) Renal Pi uptake B) Renal leucine uptake C) Renal glucose uptake

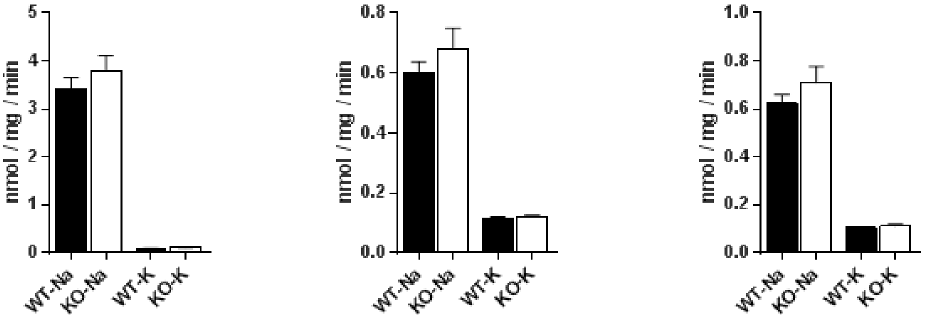

D) Renal NaPi-IIa

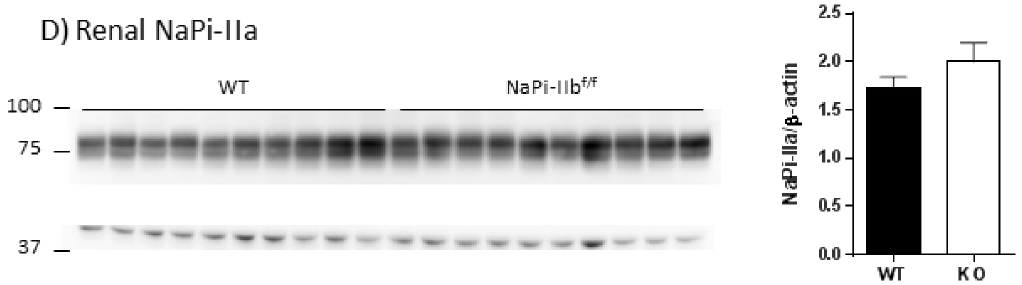

E) Renal NaPi-IIc

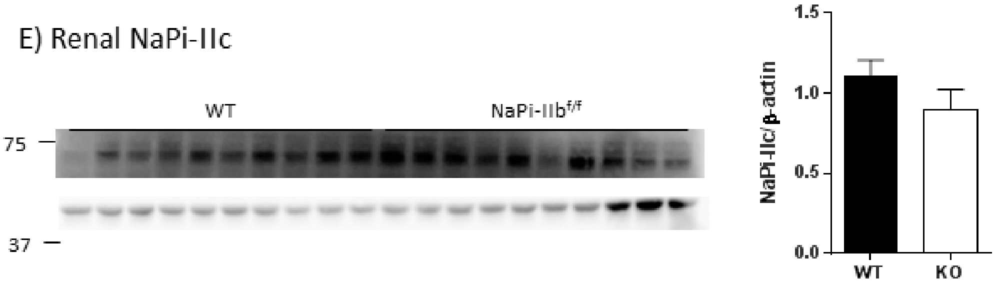

F) Ileal NaPi-IIb

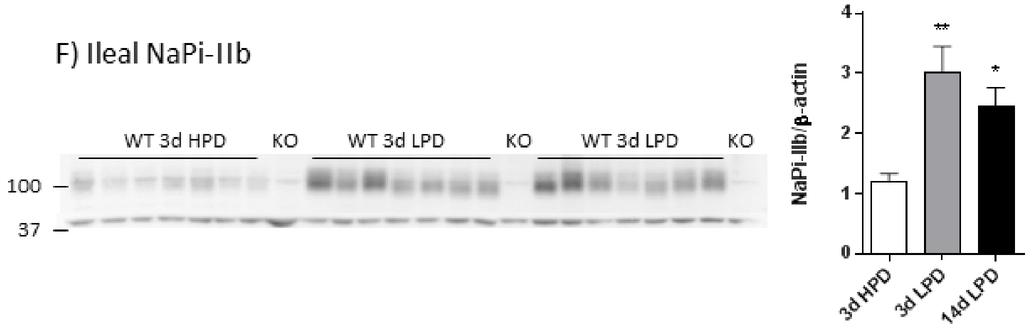

Figure 4

A) Renal Calbindin-28K

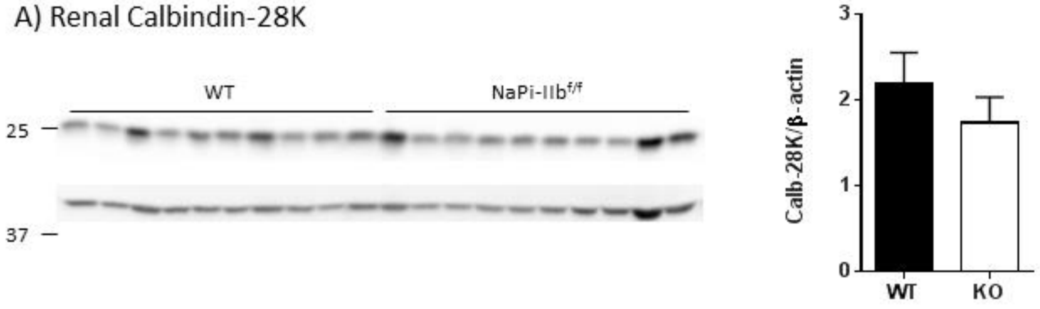

B) Renal TRPV5

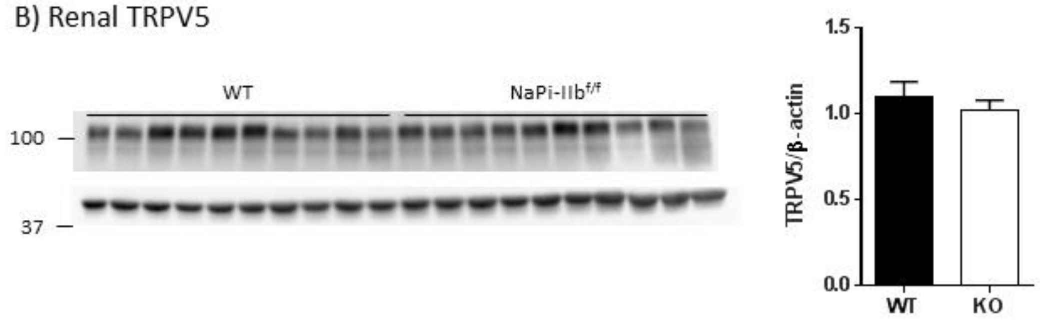

C) Renal Calcium Sensing Receptor

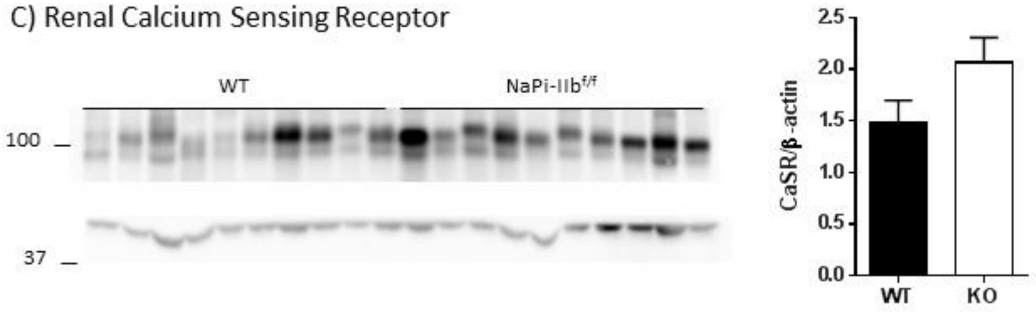

Figure 5

A) Urinary DPD

B) Urinary chorticosterone

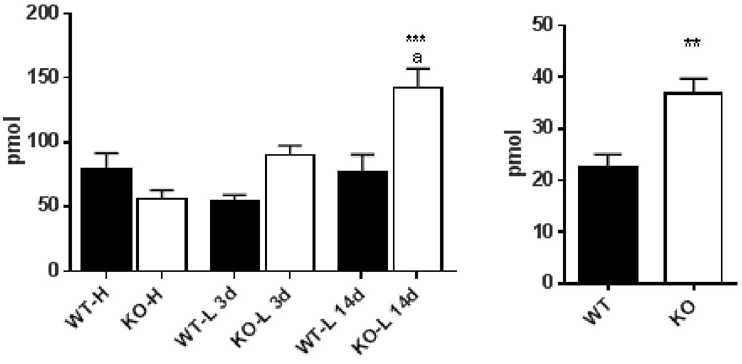

C) Cortical BMD

D) Trabecularl BMD

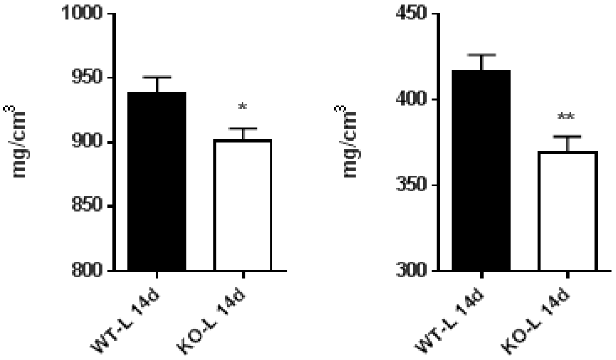

Tables

Table 1: Metabolic data

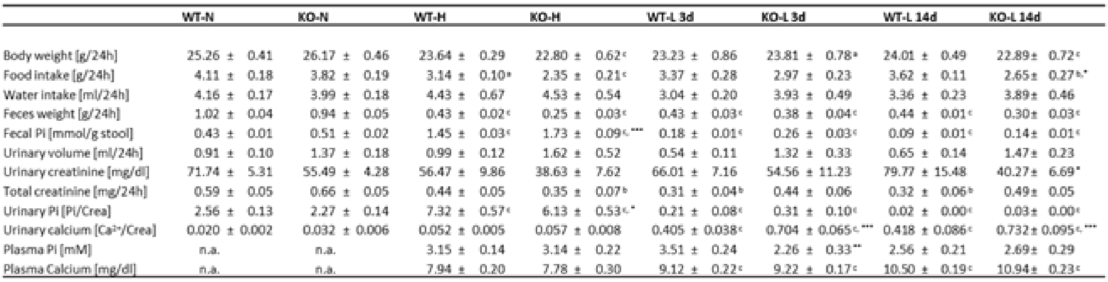

	WT-N	KO-N	WT-H	KO-H	WT-L 3d	KO-L 3d	WT-L 14d	KO-L 14d
Body weight [g/24h]	25.26 ± 0.41	26.17 ± 0.46	23.64 ± 0.29	22.80 ± 0.62^{c}	23.23 ± 0.86	23.81 ± 0.78^{a}	24.01 ± 0.49	22.89± 0.72^{c}
Food intake [g/24h]	4.11 ± 0.18	3.82 ± 0.19	3.14 ± 0.10^{a}	2.35 ± 0.21^{c}	3.37 ± 0.28	2.97 ± 0.23	3.62 ± 0.11	2.65± 0.27^{b,*}
Water intake [ml/24h]	4.16 ± 0.17	3.99 ± 0.18	4.43 ± 0.67	4.53 ± 0.54	3.04 ± 0.20	3.93 ± 0.49	3.36 ± 0.23	3.89± 0.46
Feces weight [g/24h]	1.02 ± 0.04	0.94 ± 0.05	0.43 ± 0.02^{c}	0.25 ± 0.03^{c}	0.43 ± 0.03^{c}	0.38 ± 0.04^{c}	0.44 ± 0.01^{c}	0.30± 0.03^{c}
Fecal Pi [mmol/g stool]	0.43 ± 0.01	0.51 ± 0.02	1.45 ± 0.03^{c}	1.73 ± 0.09^{c,***}	0.18 ± 0.01^{c}	0.26 ± 0.03^{c}	0.09 ± 0.01^{c}	0.14± 0.01^{c}
Urinary volume [ml/24h]	0.91 ± 0.10	1.37 ± 0.18	0.99 ± 0.12	1.62 ± 0.52	0.54 ± 0.11	1.32 ± 0.33	0.65 ± 0.14	1.47± 0.23
Urinary creatinine [mg/dl]	71.74 ± 5.31	55.49 ± 4.28	56.47 ± 9.86	38.63 ± 7.62	66.01 ± 7.16	54.56 ± 11.23	79.77 ± 15.48	40.27± 6.69*
Total creatinine [mg/24h]	0.59 ± 0.05	0.66 ± 0.05	0.44 ± 0.05	0.35 ± 0.07^{b}	0.31 ± 0.04^{b}	0.44 ± 0.06	0.32 ± 0.06^{b}	0.49± 0.05
Urinary Pi [Pi/Crea]	2.56 ± 0.13	2.27 ± 0.14	7.32 ± 0.57^{c}	6.13 ± 0.53^{c,*}	0.21 ± 0.08^{c}	0.31 ± 0.10^{c}	0.02 ± 0.00^{c}	0.03± 0.00^{c}
Urinary calcium [Ca^{2+}/Crea]	0.020 ± 0.002	0.032 ± 0.006	0.052 ± 0.005	0.057 ± 0.008	0.405 ± 0.038^{c}	0.704 ± 0.065^{c,***}	0.418 ± 0.086^{c}	0.732± 0.095^{c,***}
Plasma Pi [mM]	n.a.	n.a.	3.15 ± 0.14	3.14 ± 0.22	3.51 ± 0.24	2.26 ± 0.33**	2.56 ± 0.21	2.69± 0.29
Plasma Calcium [mg/dl]	n.a.	n.a.	7.94 ± 0.20	7.78 ± 0.30	9.12 ± 0.22^{c}	9.22 ± 0.17^{c}	10.50 ± 0.19^{c}	10.94± 0.23^{c}

Table 2: Other urinary parameters after 14 days Pi restriction

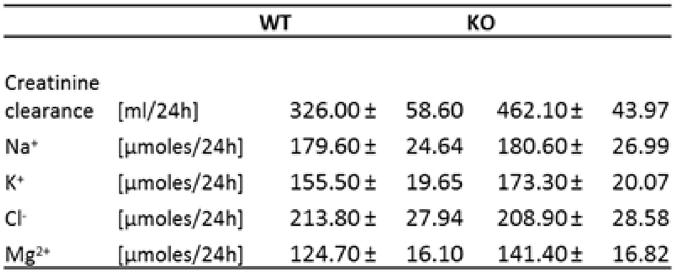

		WT		KO	
Creatinine clearance	[ml/24h]	326.00 ±	58.60	462.10 ±	43.97
Na^{+}	[µmoles/24h]	179.60 ±	24.64	180.60 ±	26.99
K^{+}	[µmoles/24h]	155.50 ±	19.65	173.30 ±	20.07
Cl^{-}	[µmoles/24h]	213.80 ±	27.94	208.90 ±	28.58
Mg^{2+}	[µmoles/24h]	124.70 ±	16.10	141.40 ±	16.82

Supplementary Figure 1

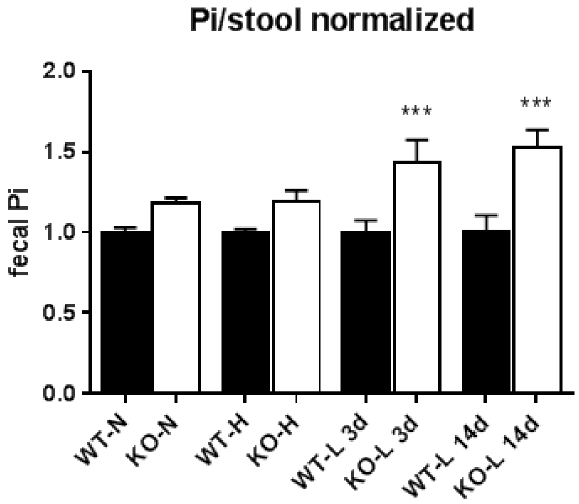

3.3 Preliminary results paracellular Pi permeability

3.3.1 Summary

In order to address the possible role of the paracellular pathway in the intestinal transport of Pi, dilution potential measurements in Ussing chamber were performed. Experiments in intestinal cell culture models and *ex vivo* preparations of intestinal segments of rats and mice showed that the tight junctions are permeable to Pi. Furthermore the paracellular pathway seems to discriminate between monovalent and divalent Pi in favor of the monovalent form. No differences in the paracellular permeabilities were found in NaPi-IIb KO mice suggesting that the existing permeability is either not regulated or sufficient to provide Pi under conditions of normal or high Pi availability.

3.3.2 Methods

Dilution potential measurement in cell culture models and rat intestine

The permeabilities for Na^+ (P_{Na}), Cl^- (P_{Cl}) and Pi (P_{Pi}) of intestinal cell culture models and rat intestinal segments were determined by dilution potential measurements. Determinations were done in Ussing chambers modified for cell culture or tissue inserts, in which the basolateral and apical sides were independently perfused as previously described [207]. Experiments were performed at pH 6 (14 0mM NaCl, 5.4 mM KCl, 1 mM $MgCl_2$, 1.2 mM $CaCl_2$, 10 mM glucose, 10 mM MES, pH 6 adjusted with NaOH) or pH 8.4 (140 mM NaCl, 5.4 mM KCl, 1 mM $MgCl_2$, 1.2 mM $CaCl_2$, 10 mM glucose, 10 mM TAPS, pH 8.4 adjusted with NaOH) in a bubble lift system, gassed with oxygen, that drives the circulation of the bathing solutions (10 ml) on each side. Temperature was maintained at 37°C with a water jacket. To determine Na^+ and Cl^- permeabilities 5 ml on either the basolateral or apical side were replaced by a 5 ml of a solution containing 280 mM mannitol instead of 140 mM NaCl. After equilibrating each side again, Pi permeability was assessed by replacing 5 ml on either side with a solution containing 140 mM NaH_2PO_4 (pH 6) or 70 mM Na_2HPO_4 (pH 8.4, with additional 70 mM mannitol to maintain osmolality) instead of 140 mM NaCl. Differences in transepithelial voltage (V_{te}) upon change of solution were corrected for previously defined liquid junction potentials. The ratios P_{Na}/P_{Cl} and

P_{Na}/P_{Pi} obtained by the Goldman-Hodgkin-Katz equation and the transepithelial resistance (R_{te}) were used to calculate permeabilities.

Dilution potential measurement in mouse intestine

Freshly isolated intestinal segments from mouse were mounted into a modified Ussing chamber, with an exposed area of 0.8 mm^2. The basolateral and apical side were independently perfused with a flow rate of 5-10 ml/min. The basolateral side was perfused with Ringer solution (145 mM NaCl, 0.4 mM KH_2PO_4, 1.6 mM K_2HPO_4, 5 mM glucose, 1 mM $MgCl_2$, 1.3 mM Ca-Gluconate, pH7.4). After equilibration of the mounted tissue the apical side was consecutively perfused with Ringer solution (pH 6), a low NaCl Ringer (30 mM, isotonic with 230 mM Mannitol, pH 6), and a modified Ringer containing 140 mM NaH_2PO_4 (pH 6). Differences in V_{te} upon change of perfusion solution were measured under open-circuit conditions with V_{te} referring to the basolateral side. R_{te} was assessed with short pulses (1s) of 1.41 µA, and the difference in V_{te} upon the pulse was used to calculate the R_{te} according to Ohm’s law ($R_{te}=\Delta V_{te}/I$) after correction for the resistance of the empty chamber. Relative and absolute permeabilities for Na^+, Cl^- and Pi were calculated using the Goldman-Hodgkin-Katz equation and the R_{te}.

3.3.3 Results

Passive absorption of Pi along the paracellular pathway requires a concentration gradient across the epithelium. Thus we measured Pi in the different segments of the gut. Our measurements indicate that luminal Pi concentration of Pi exceeds plasma levels by at least tenfold (Figure 8) providing a gradient to drive passive diffusion of Pi from the lumen to the blood.

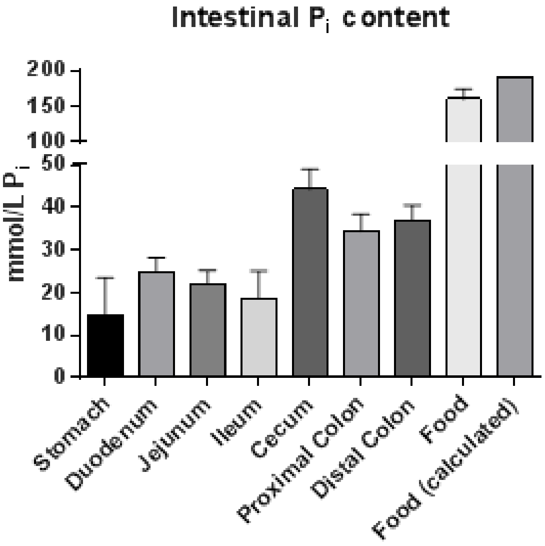

Figure 8: Pi concentration in different compartments of the intestine and in dissolved chow (measurement and theoretical).

IPEC-J2 (swine small intestine), HT-29/B6, Caco2-bbe and T84 cells (the last three of human colon carcinoma origin) grown to confluency were analyzed in Ussing chambers to determine the permeability of the tight junctions to Pi.

As shown in Figure 9, alkaline pH lowers transepithelilal resistance in all models and thereby affects the absolute permeability for all ions. Therefore results are shown as relative permeabilities P_{Na}/P_{Cl} and P_{Pi}/P_{Na}, since the ratio between the permeabilities of Cl^- and Na^+ seems to be unaffected by pH. The cell culture experiments indicate that the tight junctions are permeable to Pi and discriminate between Pi species. Monovalent Pi ($H_2PO_4^-$), the predominant species at pH 6, seems to pass the tight junctions more easily than its divalent form (HPO_4^{2-}). The permeability for Pi observed at pH 6 was about 40-50% of the one of Na^+. The permeability of the tight junctions is mostly dependent on the expression profile of claudins [208]. Claudins form pores that facilitate passive diffusion and thereby their transport characteristics are symmetric, unlike transcellular transport. To test the symmetry of Pi transport, Na^+ and Pi gradients were introduced from either the basolateral or the apical side: as expected, no differences in permeability were observed, confirming that transport was symmetric. Data presented in Figure 9 was obtained by pooling results from apical and basolateral applications.

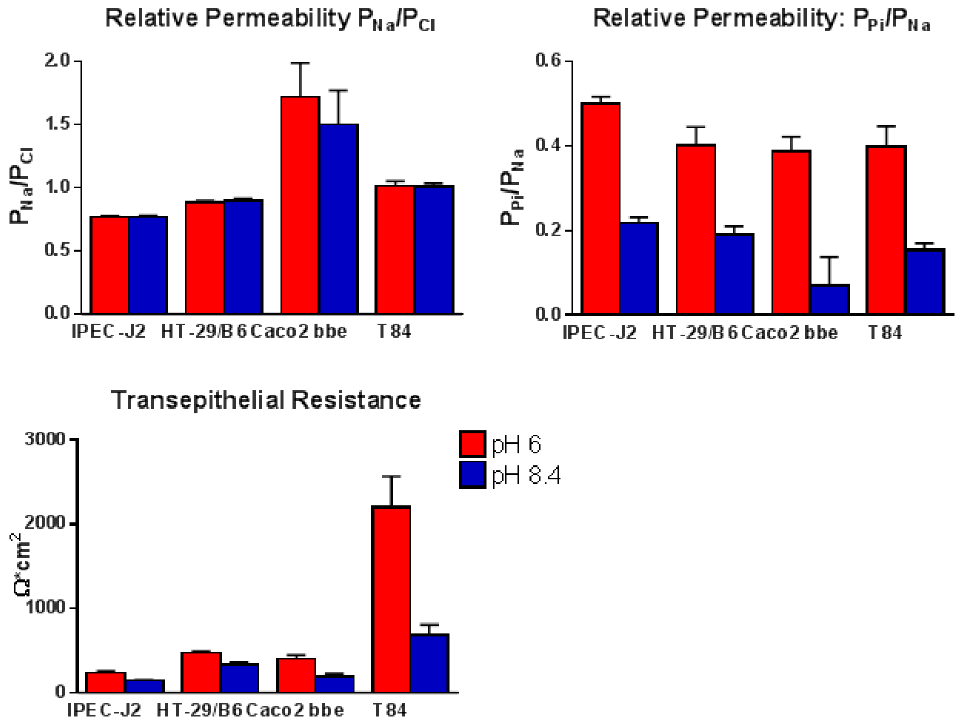

Figure 9: Relative permeabilities P_{Na}/P_{Cl} and P_{Pi}/P_{Na} and transepithelial resistance in different cell culture models under pH 6 (red) and 8.4 (blue).

Introduction of the anion selective claudin17 [209] and tricellulin into renal MDCK cells did not affect P_{Pi} in dilution potential measurements (Figure 10). Introduction of claudin17 shifted the selectivity towards Cl^- (compare decreased P_{Na} and increased P_{Cl}) as expected.

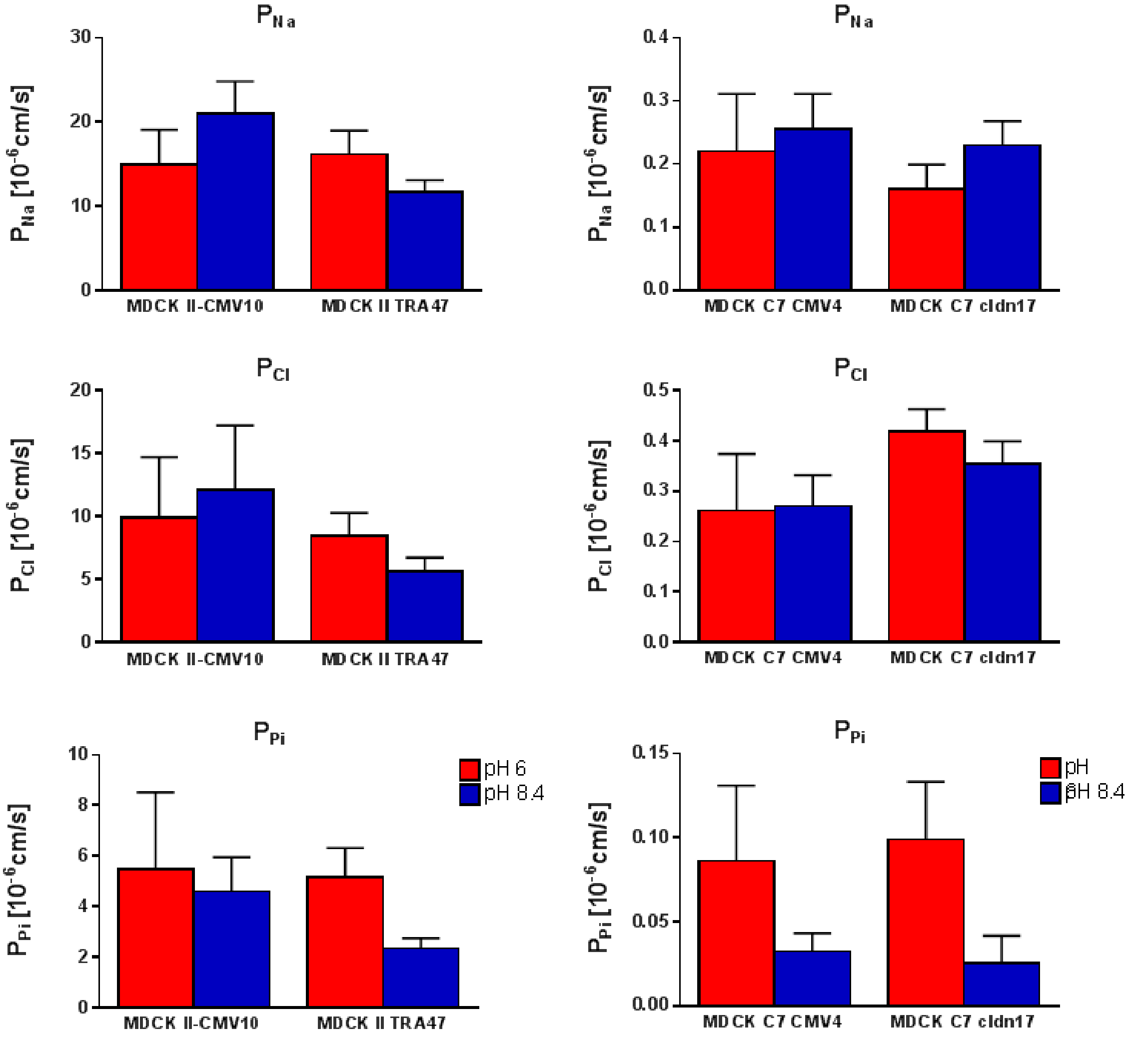

Figure 10: Permeability to Na^+ (P_{Na}), Cl^- (P_{Cl}) and Pi (P_{Pi}) in renal MDCK cells at pH 6 (red) and pH 8.4 (blue). The left panels show MDCK II cells stably transfected with tricellulin (TRA47) and the corresponding control (CMV10). The right panels show MDCK C7 cells expressing claudin 17 (cldn17) and corresponding control (CMV4)

The same experimental procedure was used to measure Pi permeability in different intestinal segments of rats (Figure 11). Dilution potential measurements showed that the rat intestine is also permeable to Pi. Alkaline pH did not affect transepithelial resistance of the tissue, unlike in the cell culture experiments. The permeability to Pi was again higher at pH 6 than pH 8.4, though the difference was not as pronounced as in cultured cells. Instead, the permeabilities to Na^+ and Cl^- were not affected by pH. Monovalent Pi showed about half the permeability of Na^+ or Cl^- in all the segments analyzed. A higher transepithelial resistance was observed in preparations of colon tissue, which leads to an overall lower conductance of the tissue to ions (due to Ohm's law; the higher the resistance the lower the current). This is reflected in the lower permeability to Na^+, Cl^- and Pi all together, but comparatively the ratio between the ions stays the same.

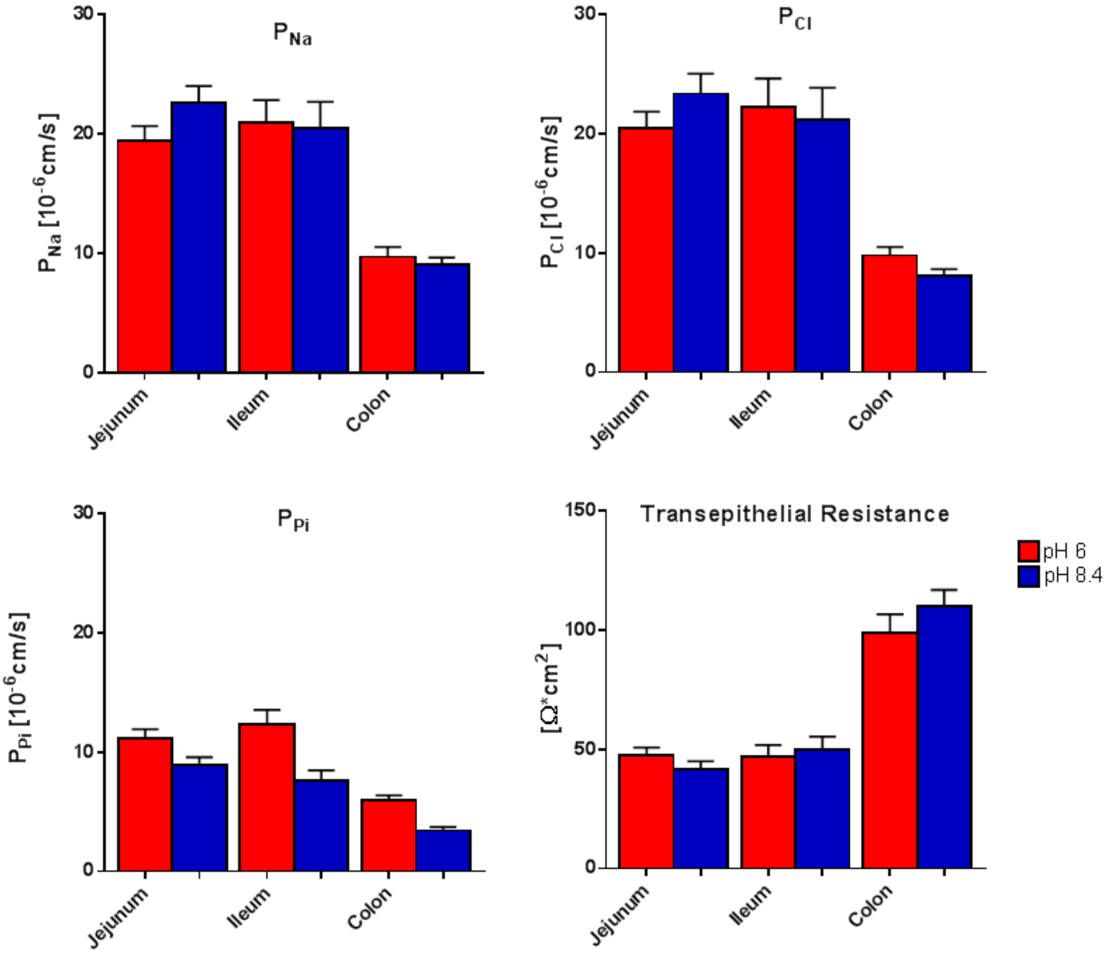

Figure 11: Permeability to Na^+ (P_{Na}), Cl^- (P_{Cl}) and Pi (P_{Pi}) observed in rat jejunum, ileum and colon, with recording of the corresponding transepithelial resistance. Dilution potential measurements were performed at pH 6 (red) and pH 8.4 (blue).

Dilution potential measurements in mouse intestine were performed with a luminal pH of 6 and basolateral pH of 7.4 to achieve a more physiological condition (Figure 12). The pH difference across the epithelium did not alter the measurements (data not shown). Overall it looks like that the mouse intestine has a higher selectivity for Na^+. Otherwise no major differences between species were observed, with P_{Pi} about half of P_{Cl}, and lowest permeability to all ions in the colon, due to high tissue resistance.

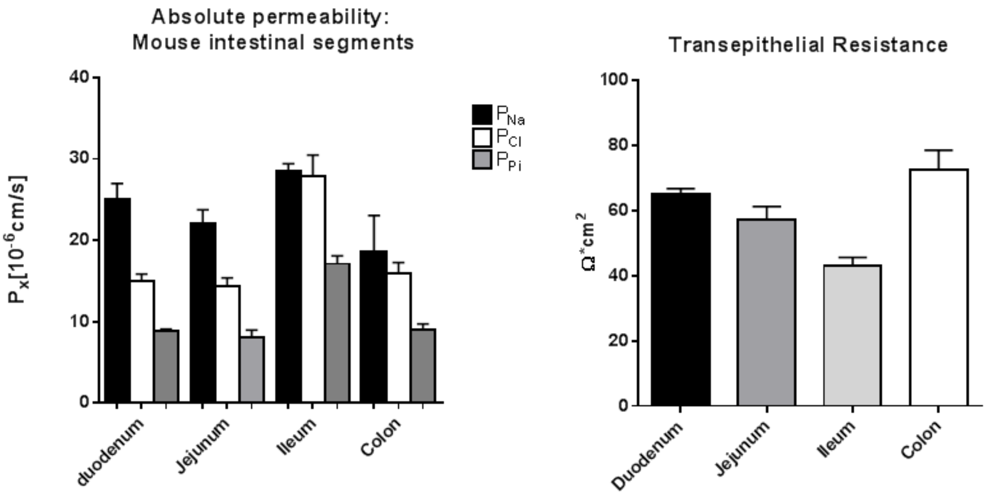

Figure 12: Permeability to Na^+ (P_{Na}), Cl^- (P_{Cl}) and Pi (P_{Pi}) observed in mouse duodenum, jejunum, ileum and colon, with recording of the corresponding transepithelial resistance.

The absence of NaPi-IIb had no effect on the paracellular ion permeability. As shown in Figure 13, NaPi-IIb deficient mice show similar P_{Na}, P_{Cl} and P_{Pi} along the intestine.

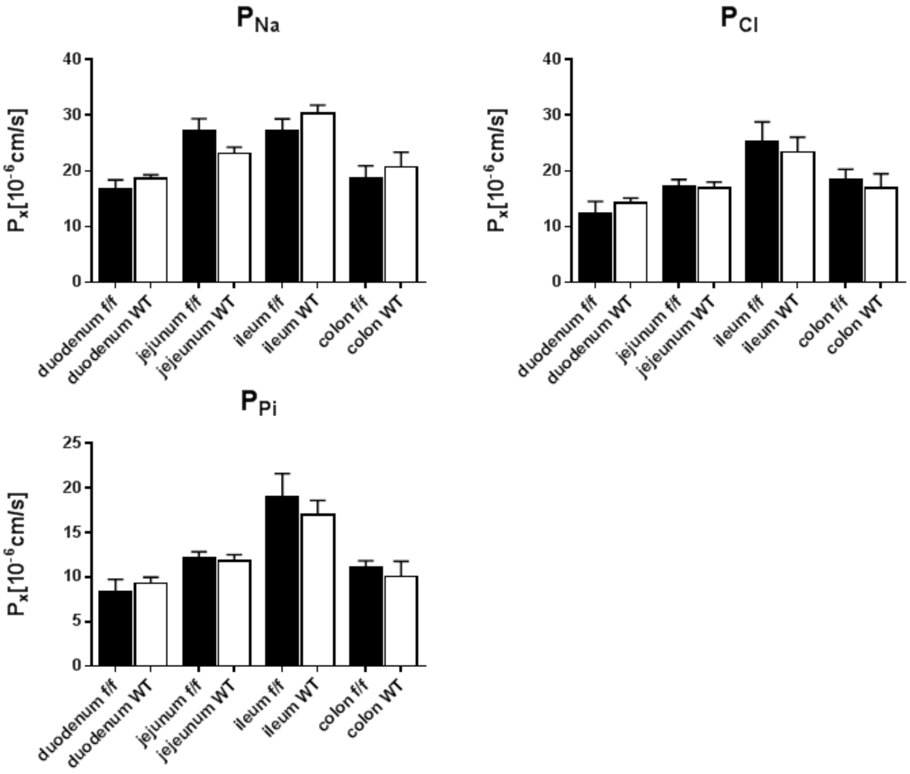

Figure 13: Permeability to Na^+ (P_{Na}), Cl^- (P_{Cl}) and Pi (P_{Pi}) observed in NaPi-IIb deficient (f/f) and corresponding wild type mice (WT).

3.4 Renal localization and regulation by dietary phosphate of the MCT14 orphan transporter

Thomas Knöpfel[#], Alexander Atanassoff[#], Nati Hernando, Jürg Biber*, Carsten A. Wagner*

[#]T. Knöpfel and A. Atanassoff contributed equally and share first autorship

*J. Biber and C.A. Wagner contributed equally and share last authorship

Institute of Physiology, University of Zurich, Zurich, Switzerland

and NCCR Kidney.CH

The manuscript was submitted to PLOS ONE on the 08.11.2016

Own contribution:

Thomas Knöpfel (TK) contributed to the animal experiments, antibody validation, westernblots, performed immunofluorescence experiments for localization and uptake experiments in *Xenopus laevis*. The manuscript including figures was drafted by TK.

Abstract

MCT14 is an orphan transporter belonging to the SLC16 transporter family mediating the transport of monocarboxylates, aromatic amino acids, creatine, and thyroid hormones. The expression, tissue localization, regulation, and function of MCT14 are unknown. In mouse MCT14 mRNA abundance is highest in kidney. Using a newly developed and validated antibody, MCT14 was localized to the luminal membrane of the thick ascending limb of the loop of Henle colocalizing in the same cells with uromodulin and NKCC2. MCT14 mRNA and protein was found to be highly regulated by dietary phosphate intake in mice being increased by high dietary phosphate intake at both mRNA and protein level. In order to identify the transport substrate(s), we expressed MCT14 in Xenopus leavis oocytes where MCT14 was integrated into the plasma membrane. However, no transport was discovered for the classic substrates of the SLC16 family nor for phosphate. In summary, MCT14 is an orphan transporter regulated by phosphate and highly enriched in kidney localizing to the luminal membrane of one specific nephron segment.

Key words: Slc16a14/MCT14, renal expression, dietary regulation

Introduction

Inorganic phosphate (Pi) is a molecule involved in energy metabolism and signaling as well as essential for structural molecules in cells and bone. Phosphate excess triggers ectopic calcifications and is associated with increased cardiovascular mortality. Therefore, the plasma levels of phosphate are kept in a close range; this is achieved by a variety of compensatory and highly regulated mechanisms. Phosphate deficiency leads to increased levels of plasma active vitamin D, which promotes intestinal phosphate absorption at least in part by stimulating the expression of the Na^+-dependent phosphate transporter NaPi-IIb [1]. Additionally, hypophosphatemia blunts the production of parathyroid hormone (PTH) [2] and fibroblast growth factor 23 (FGF23) [3], releasing the inhibitory effect of both hormones on renal phosphate cotransporters (NaPi-IIa, NaPi-IIc and PiT-2), thus enhancing renal reabsorption of phosphate. On the other hand hyperphosphatemia leads to an increased renal excretion of phosphate, an effect mediated at least in part by PTH [2] and FGF23 [4-6] . Both hormones reduce the renal expression of NaPi-IIa NaPi-IIc and PiT-2 in the proximal tubule [2], and FGF23 additionally suppresses the production of vitamin D[7]. But beyond these effects directly linked to phosphate metabolism, alterations in phosphate intake affect, among other effects, glycogenolysis and glucose production [8], indicating broader systemic changes in response to phosphate status.

The SLC16 gene family comprises 14 members collectively called MCTs (monocarboxylate transporter) due to the fact that the first 4 members to be characterized mediate transport of monocarboxylates such as lactate, pyruvate and ketone bodies, in a proton dependent manner [9]. MCT1, 3 and 4 associate with CD147 (basignin) [10], an immunoglobulin-like protein, that acts as a chaperone for these MCTs. The interaction of MCT1 and CD147 has been extensively studied and it was shown that sorting of MCT1 to the right pole of an epithelial cell relies on CD147 [11]. MCT1 and 2 are both expressed in kidney where they are involved in reabsorbing lactate. MCT1 is localized to the basolateral membrane of the renal proximal tubule together with CD147 [12], whereas MCT2 is found in the basolateral membrane of cells in the thick ascending limb of the loop of Henle [13].

The characterization of further members of the SLC16 family revealed that transport by MCTs is not limited to monocarboxylates. MCT8 transports thyroid hormone [14] and mutations of MCT8 associate with elevated levels of triiodothyronine (T_3) and psychomotor retardation [15]. MCT10 is an aromatic amino acid transporter, also known as TAT1 (T-type amino acid transporter 1). Both transporters mediate transport in a proton (and sodium) independent manner [16], unlike the first 4 members. Recently MCT12, associated with juvenile cataract, was characterized as a creatine transporter [17], further widening the substrate spectrum of the MCT family. MCT12 localizes to the basolateral membrane of proximal tubules in kidney, and patients with mutated MCT12 excrete increased amounts of guanidinoacetate, but functional studies did not show transport of the creatine precursor [18]. The other members of the family remain orphan transporters, and although it has been suggested that they might act as drug transporters (as demonstrated with bumetanide transport for MCT6 [19]) their endogenous transport substrates are still elusive. A renal transcriptome study detected mRNA of MCT1, MCT2, MCT5, MCT6, MCT7, MCT8, MCT9, MCT10 (TAT1), MCT13 and MCT14 in kidney [20], and the renal localization of MCT1, 2, 7, 8 and 10 has been described [12,21].

MCT14, encoded by the SLC16A14 gene, is an orphan member of the family that has been shown to be expressed in the bovine intestinal tract [22] and the mammary gland of lactating cows [23]. A recent study also mapped the expression of MCT14 in the mouse brain and provided a relative expression of this transporter in several tissues [24]. Of interest, among all the tissues tested renal mRNA abundance was the highest (by about 20 fold). This report also provides a phylogenetic analysis of the MCTs, which shows that MCT14 is closest related to MCT8, 9 and 10 [24], the non-classical members of the family.

Here we report that the renal expression of MCT14 is regulated by the dietary content of phosphate, the generation and validation of a polyclonal antibody to analyze its segmental distribution in kidney as well as our attempts to identify substrates.

Experimental procedures

Animals

All experiments with animals were performed according to Swiss Animal Welfare laws and were approved by the local veterinary authority (Veterinäramt Zürich). Male mice (C57BL/6) 10 to 13 weeks old were fed for 14 hours or 5 days with either high (1.2%) or low (0.1%) phosphate diet (Kliba Promivi AG, Switzerland). Food was provided ad libitum and animals had free access to water. After the adaptation, mice were anesthetized with a mixture of ketamine and xylazine. Venous blood was collected from the vena cava and centrifuged (8 min at 8'000rpm at 4°C) in tubes containing heparin. After centrifugation the plasma was aliquoted and snap frozen in liquid nitrogen. Organs were extracted and snap frozen. All samples were stored at -80°C until further use.

RNA isolation and semi-quantitative real-time PCR (RT-qPCR)

Snap frozen kidneys were homogenized in RLT buffer (Qiagen, Germany) containing 1% β-mercaptoethanol. Total RNA was purified from these homogenates using the Qiagen RNeasy Mini Kit following the manufacturer's protocol. Isolated RNA was reverse transcribed to cDNA with the TaqMan Reverse Transcription Kit (Applied Biosystems), following the manufacturers protocol.

Specific primers for Slc16a14/MCT14 and Cyp27b1 and the corresponding probe labeled with FAM/TAMRA (Mm01272722_m1, Mm01165918_g1; Applied Biosystems) as well as for β-actin (Microsynth, Switzerland) used as a control gene were purchased. TaqMan universal PCR master mix (Applied Biosystems) containing primers and probes in concentrations of 5 μM and 25 μM, respectively, was used to amplify cDNA. Relative mRNA expression levels were measured on a 7500 Fast Real Time PCR System (Applied Biosystems). The cycle number at a given threshold (Ct) was determined, and the relative expression (R) was calculated according to the formula R=2^((CT– β-actin) – (CT-MCT14), where R represents the expression of MCT14 relative to the housekeeping gene (β-actin).

Western blot analysis

Frozen kidneys were homogenized in homogenization buffer (300 mM Mannitol, 5 mM EGTA, 12 mM Tris/HCl, pH 7.1) for 2 min on ice using a Polytron homogenizer (PT 10-35, Kinematica GmbH, Lucerne). The homogenates were then centrifuged for 5 min at 2’000 rpm at 4°C. Supernatants were collected and protein concentrations were determined with the BioRad DC protein assay, based on the Lowry method (44). Aliquots of 50 µg of renal homogenates were mixed with Laemmli sample buffer (0.38 M Tris base, 8% SDS, 4 mM EDTA, 40% (v/v) glycerol, pH 6.8 with HCl, 4 mg/ml of Bromphenol Blue) and loaded on a 10 % acrylamide SDS gel for SDS-PAGE. Proteins were transferred from gel onto polyvinylidene difluoride membranes (PVDF; Immobilon-P, Millipore) in a standard tank system (Mini Trans- Blot, Bio-Rad). PVDF membranes were blocked with TBS containing 5 % fat-free powder milk at room temperature and incubated with primary antibodies over night at 4°C. Membranes were then washed with TBS and blocked again before incubation with secondary antibodies for 2 hours at room temperature. Horseradish peroxidase-coupled secondary antibodies (GE Healthcare, United Kingdom) were used to detect primary antibody binding. Chemiluminescence was detected upon incubation with HRP substrate (Western Chemiluminescence HRP Substrate, Millipore) for 5 minutes, using a LAS-4000 camera system (Fujifilm).

An antibody targeting a predicted extracellular loop (Uniprot) of MCT14 was raised by immunizing rabbits with an antigenic peptide (NH_2-KSGGPLGMAEEQDRRPGNEEMVC-COOH) linked to KLH (Pineda, Berlin, Germany). The anti-serum was affinity purified using protein A/G chromatography.

Immunofluorescence

Animals were perfused through the left cardiac ventricle with a pre-fixative solution (1000 U/ml Heparin, 0.2 % procain-HCl, 3.2 % $CaCl_2$ and 0.18 % NaCl) followed by the fixative (3 % Paraformaldehyde (PFA)/PBS). After incubation in PFA for one hour, kidneys were placed overnight in 32 % sucrose/PBS and subsequently embedded in OCT embedding Matrix (Cell Path, Newtown, Wales, United Kingdom) and frozen in liquid propane. Cryosections of 5 µm were mounted on slides (Superfrost Plus, Thermo Scientific) and blocked with 3 % bovine serum albumin/PBS; the primary antibodies against MCT14 (1/1000), NKCC2 [25] (1/1000), Uromodulin [26] (1/400), NCC [27] (1/500) or NaPi-IIa [28] (1/400) were diluted in PBS and added to the cryosections for incubation over night at 4°C. Then, samples were washed twice with hypertonic PBS (18g NaCl/PBS), once with PBS and incubated with the secondary antibodies donkey anti-rabbit Alexa594, donkey anti-sheep Alexa 488 and goat anti-guinea-pig Alexa 488 (1/1000, Invitrogen) during 2 hours at room temperature. After two consecutive washing steps with hypertonic PBS and once with PBS, cover slips were mounted with Glycergel (DakoCytomation, Baar, Switzerland). Fluorescence was detected with a Leica fluorescence microscope (Leica CTR600). Leica AF lite and Image J freeware programs were used to process the pictures.

Expression of MCT14 in *Xenopus laevis* oocytes

An *Escherichia coli* clone containing the cDNA of murine Slc16a14 inserted into the pCMV-Sport6 expression vector downstream of the SP6 promotor (IRAVp968E0963D) was purchased from imaGenes (Berlin, Germany). Bacterial clones were selected and expanded using standard procedures. The expression vector was isolated using the QIAprep Spin Miniprep Kit (QIagen) and was linearized with the restriction enzyme NotI. The restriction product was purified with the QIAquick gel extraction kit (Qiagen) following the manufactures protocol. Linearized plasmid was used as template to synthesize cRNA using the mMessage mMachine SP6 kit (Ambion) with addition of a 5’-cap analogue (m7G(5')ppp(5')G RNA Cap Structure Analog (New England BioLabs inc., Allschwil, Switzerland). Upon purification, 10 ng of MCT14 cRNA were injected into oocytes isolated from female *Xenopus laevis.* Three days after cRNA injection, oocytes were used for experiments. Non-injected oocytes served as control.

Oocyte preparation for immunodetection of MCT14

Xenopus laevis oocytes were placed in 20 µl lysis buffer (100 mM NaCl, 20 mM Tris HCl (pH 7.6) and 1% Igepal CA 630 (Sigma Aldrich, Buchs, CH)) and lysed by pipetting up and down. Lysates were then centrifuged for 3 minutes at 16000g at 22°C. Yolk-free supernatants were collected avoiding contamination with floating lipids and mixed with Laemmli sample buffer. A volume corresponding to 1/3 of an oocyte/lane was loaded on an acrylamide SDS gel and protein expression was tested following the Western blot protocol described above.

To prepare *Xenopus laevis* oocytes for immunohistological detection, cells were incubated in 3% PFA in PBS for 4 hours at 4°C. After washing with PBS, oocytes were placed in 30 % sucrose/PBS over night at 4°C for cryoprotection. Oocytes were then transferred to cryomolds (Cryomold Biopsy, Sakura Finetek Germany GmbH, Staufen, Germany) containing embedding medium (OCT embedding Matrix, Cell Path, Newtown, Wales, United Kingdom) and were immediately frozen in liquid propane. Frozen oocytes were stored at -80°C and processed for immunofluorescence experiments as described above.

Transport studies in *Xenopus laevis* oocytes expressing MCT14

Ten oocytes were transferred into plastic vials containing ice cold ND96 (96 mM NaCl, 2 mM KCl, 1.8 mM $CaCl_2$, 1 mM $MgCl_2$, 5 mM Hepes, pH 7.4 adjusted with Tris). ND96 was replaced with ND96 containing the desired uptake substrate in 100 µM concentration and traces of radioactively labelled substrate (5 µCi/ml). Upon 10 minutes incubation at room temperature, substrate solution was removed and oocytes were subsequently washed 4 times with ice cold ND96. Single oocytes were transferred to a scintillation vial containing 200 µl of 2% SDS and lysed by shaking. Upon addition of Emulsifier-Safe (PerkinElmer), radioactivity accumulated in each oocyte was measured in a β-counter (Packard BioScience) and total uptake was calculated.

Statistical Analysis

Unpaired students t-test was used to analyze expression level comparisons. P-values > 0.05 were considered as significant. Data is presented as Mean + SEM.

Results

Dietary phosphate content regulates Slc16a14 mRNA

A transcriptome analysis using a GeneChip Mouse Genome 430 2.0 arrays (Affymetrix, Santa Clara, CA) was performed on kidneys from mice adapted to high (1.2 % Pi, HPD) or low (0.1 % Pi, LPD) dietary phosphate for either 14 hours or 5 days, conditions that are considered as acute or chronic adaptation, respectively. Adaptation to the diets was validated by quantifying the renal protein expression of the Na^+/phosphate cotransporter NaPi-IIa [29]. As expected, acute (Figure 1A) and chronic (Figure 1B) LPD diets increased the abundance of NaPi-IIa protein compared to HPD. The microarray detected more than 12’000 protein coding transcripts. Only transcripts with at least 1.5 fold change and p-values <0.05 were considered for further analysis. Under LPD conditions 50 transcripts were found to be upregulated acutely and 1259 under chronic adaptation. LPD further decreased the expression of 93 transcripts acutely and 631 chronically (detailed data to be reported elsewhere). The mRNA expression of Cyp27b1 was used as a marker to validate data obtained by the microarray by RT-PCR. Cyp27b1 did not show any different expression after acute changes in dietary Pi (Figure 1C), but chronic adaptation led to a 10 fold increase of Cyp27b1 under LPD conditions compared to HPD (Figure 1D).

In both, acute and chronic adaptation experiments, transcriptome analysis revealed that the mRNA of Slc16a14 (the gene encoding the monocarboxylate transporter MCT14) was strongly regulated. SLC16a14 mRNA appeared among the SLC transporter transcripts to be the most highly affected transcript. In fact Slc16a14 mRNA abundance was decreased by a factor of 4.3 in mice acutely fed a LPD as compared with mice fed a HPD, whereas the reduction was by a factor of 5.0 in chronically adapted mice. The microarray data was confirmed by semi-quantitative real time RT-PCR with renal mRNA extracted from the same group of mice as well as from an independent group of animals. Already 14 hours after the start of the dietary adaptation renal Slc16a14 mRNA expression was drastically decreased in animals under LPD condition compared with HPD (Figure 1E). This effect was further enhanced after chronic adaptation for 5 days (Figure 1F).

Antibody generation and validation of specificity

To investigate if the changes in mRNA expression were paralleled by altered protein levels, a polyclonal antibody was raised in rabbits against a peptide located in a predicted extracellular loop of MCT14. Western blot analysis with renal homogenates was performed in the presence and absence of the antigenic peptide to confirm specific binding of the antibody to its epitope. The anti-MCT14 antibody detected several bands in renal homogenates at approximately 40 and 50 kDa (Figure 2A). Preincubation with the antigenic peptide abolished detection of these bands. The expected size of the MCT14 transporter is estimated to be around 50 kDa (510 amino acids). The MCT14 antigenic peptide did not affect the binding of the NaPi-IIa [28] antibody in the same homogenates (Figure 2B). Further proof of binding specificity was achieved by western blots of lysates from *Xenopus laevis* oocytes injected with Slc16a14/MCT14 cRNA or left non-injected. In lysates of oocytes injected with Slc16a14/MCT14 cRNA, the antibody detected two bands with molecular sizes of about 40 and 50 kDa corresponding to the major bands protected by the antigenic peptide in renal homogenates. These bands were absent from non-injected oocytes (Figure 1C).

Renal localization of MCT14

Real time PCR on mRNA samples extracted from several mouse tissues indicated that the kidney expresses the highest levels of Slc16a14/MCT14 mRNA, folpancreas and testis where the mRNA expression levels are about ten times lower than in kidney (data not shown) confirming a previous report [24]. In immunofluorescence experiments on murine kidney cryosections using the newly generated MCT14 antibody, staining was observed mainly in the luminal membrane of nephron segments located in the outer renal medulla and to a lesser extent in the cortex (Figure 2D). Upon co-incubation of the antigenic peptide with the anti-MCT14 antibody, tubular staining was abolished (figure 2D). These findings indicate specific staining of MCT14 in kidney sections using a standard immunofluorescence protocol.

In order to further characterize the segmental distribution of MCT14 in the murine kidney, (co)immunostainings were performed in single or consecutive renal sections using the MCT14 antibody as well as antibodies against proteins with well-established patterns of renal expression. Incubation of consecutive sections with antibodies against MCT14 and NaPi-IIa, a marker for the proximal tubule [28], showed that both proteins labelled different nephron segments, with the MCT14 related signal mostly detected in the outer medulla whereas NaPi-IIa showed the expected cortical expression (Figure 3A), thus indicating that MCT14 is not expressed in proximal tubule. Instead, immunostainings on consecutive sections with antibodies against MCT14 and NKCC2, a marker for the thick ascending limb of the loop of Henle, showed that both proteins are present in the same cells, in cortex and outer medulla (Figure3B and 3C). Moreover, coincubation of renal slices with antibodies against MCT14 and uromodulin, all cells positive for MCT14 stained also for uromodulin (Figure 3D). Uromodulin staining was present within the whole cell as well as on the luminal membrane of those cells, whereas MCT14 signal was restricted to the apical membrane. Costainings with antibodies against MCT14 and NCC, exclusively expressed in distal convoluted tubules [27] resulted in labeling of different tubular segments (Figure 3E).

Dietary Pi content regulates renal MCT14 protein abundance

Western blot analysis of renal homogenates from animals used previously for transcriptome analysis showed that MCT14 protein abundance followed the regulation of mRNA by dietary Pi. Reduced amounts of MCT14 protein was detected after 14 hours and 5 days LPD compared to HPD (Figures 4A and 4B). Immunostainings on renal cryosections of mice chronically adapted to HPD and LPD did not show a change of expression pattern as already observed in the initial localization experiments (Figure 4C).

Functional studies in *Xenopus laevis* oocytes

We used Xenopus oocytes to search for transport substrates of MCT14. Western blot analysis confirmed that the protein was produced by the oocytes (see Figure 2C). For transport studies in oocytes it is required that the expressed protein is incorporated into the cell membrane. Trafficking of MCT14 to the membrane was ascertained by immunostaining experiments. Oocytes injected with Slc16a14/MCT14 cRNA showed a signal framing the cell body, which was absent from non-expressing cells (Figure 2E), indicating insertion of MCT14 into the oocyte cell membrane.

Next, oocytes expressing MCT14 and non-injected oocytes were incubated with several substrates previously shown to be transported by different members of the MCT family. However, oocytes injected with Slc16a14/MCT14 mRNA did not show any significant transport activity for lactate compared to non-injected oocytes, neither at substrate concentrations of 3 mM (Figure 5A) or at 100 µM (Table 1). Coexpression of MCT14 with CD147 also failed to induce lactate transport. Similarly, inorganic phosphate was not accumulated in oocytes expressing MCT14 (Table 1). Also creatine was not transported by oocytes injected with MCT14, whereas this substrate was incorporated by MCT12 expressing oocytes (Figure 5B). Introduction of CD147 had again no effect in Slc16a14/MCT14 expressing oocytes regarding their failure to transport creatine. Further uptake experiments were performed in which oocytes were incubated with different amino acids (alanine, glutamine, cysteine, asparagine, serine, methionine, tyrosine and glutamate) in 100 µM concentrations. No significant differences were observed comparing oocytes expressing MCT14 and the corresponding non-expressing cells (Figure 5C, Table 1). Similarly, MCT14 failed to induce transport of tryptophan, phenylalanine, valine, leucine and isoleucine, with substrates present at 3 mM concentrations (Table 1).

Discussion

Phosphate plays an essential role in a large variety of vital functions ranging from cell signaling and energy metabolism to structural purposes. Hence, it is not surprising that changes in phosphate status, as those induced by alterations in dietary phosphate intake, have a broader impact on systemic homeostasis than just adjusting intestinal and renal (re)absorption of phosphate. Thus, dietary alterations in phosphate supply cause a fast response in PTH and later on in vitamin D and FGF23 [4,5], but also promote changes in other metabolic pathways such as gluconeogenesis, or altered insulin sensitivity [8], indicating the importance of phosphate in energy metabolism.

By performing a transcriptome-wide analysis on kidneys from mice fed on diets with high or low phosphate content we identified Slc16a14/MCT14 as one of the transcripts more strongly down-regulated under acute and chronic dietary phosphate restriction. Altered expression of NaPi-IIa protein and Cyp27b1 mRNA confirmed the adaptation of the mice to the dietary content of Pi, where NaPi-IIa is regulated acutely and chronically as described before [30]. Cyp27b1 on the other hand was only regulated after chronic adaptation, in agreement with previous observations, indicating that the activation of vitamin D_3 is not affected acutely by Pi restriction [31]. It was recently reported that MCT14 mRNA shows the highest abundance in the kidney [24], which is in agreement with our own observations (data not shown). The fact that MCT14 abundance decreases drastically in kidney after only 14 hours of LPD might suggest that this transporter is directly involved in an immediate metabolic response to phosphate deprivation, but without identification of its substrate it is impossible to draw conclusions as to its functional relevance.

MCT14 consist of 510 amino acids and, as for other members of this family, hydropathy plots predict 12 transmembane domains with cytoplasmic N and C-termini [32]. The predicted topology of MCT1 was experimentally confirmed in proteolytic cleavage experiments in red blood cells, where the big intracellular loop and the N- and C-termini were only accessible for cleavage in leaky ghosts [33]. In order to analyze MCT14 at the protein level and to localize its expression in kidney, a polyclonal antibody was raised against a predicted extracellular loop. We provide a careful validation of the specificity of this antibody by showing peptide protection of antibody binding to renal samples (western blot and immunofluorescence) as well as specific antibody binding to cell lysates overexpressing MCT14 (western blot in *X. laevis* oocytes). On Western blots, the antibody detected one band of about 50 kDa that is in good agreement with the expected size of the full length protein as well as smaller bands at about 40 kDa that may represent either degradation products or unglycosylated proteins, since they were mostly detected in boiled samples, whereas in unboiled samples they became fainter with and a stronger representation of the full length MCT14. A similar pattern of bands was reported in a recent publication using a commercial antibody [24].

Initial immunofluorescence experiments on renal sections indicated that the expression of MCT14 is restricted to apical membrane of renal tubules, with higher levels in the outer medulla than the cortex. To identify its precise segmental distribution, we compared the pattern of expression of MCT14 with that of several other proteins with well characterized renal location. Expression in proximal tubules was ruled out based on the observation that MCT14 did not colocalize with NaPi-IIa, the major Na^+-dependent phosphate transporter expressed in the apical membrane of the renal proximal tubule [29]. NKCC2 was used as a marker for the thick ascending limb of the loop of Henle (TAL) [34]. Immunostaining of consecutive sections with both antibodies suggest that MCT14 and NKCC2 are present in the same cells. TAL expression of MCT14 was further supported by co-staining of MCT14 and uromodulin (Tamm-Horsfall protein). Uromodulin is exclusively expressed in cells of the TAL and excreted into the urine [35]. On renal slices all cells positive for MCT14 did also show a signal for uromodulin. Uromodulin staining was present within the whole cell as well as on the luminal membrane of those cells, whereas the MCT14 signal was restricted to the apical membrane of TAL cells. In order to investigate if MCT14 is exclusively expressed in the TAL or its expression extends into the adjacent distal convoluted tubule (DCT), further co-stainings were performed with a marker of the DCT, namely the Na^+/Cl^- cotransporter NCC [36]. As no coexpression of MCT14 with NCC was detected, we conclude that expression of MCT14 is restricted to the apical membrane of the TAL. Of note, despite the strong regulation of RNA/protein abundance caused by dietary phosphate, no changes were detected in the distribution pattern of MCT14 in renal sections from mice fed high or low phosphate.

The physiological role of the classical monocarboxylate transporters MCT1-4 is the import and export of lactate as a substrate of oxidation or end product of glycolysis. MCT1, 3 and 4 interact with the accessory protein CD147 and for MCT1 it is well documented that association with CD147 is required for proper targeting to the basolateral membrane of the proximal tubule [11]. We could demonstrate that transport of lactate is not facilitated by MCT14, and introduction of CD147 did not show any effect. In fact expression and incorporation of MCT14 into the *Xenopus laevis* oocyte membrane in the absence of CD147 was confirmed by western blot and immunofluorescence experiments. Expression of MCT14 in *Xenopus laevis* oocytes did not support either transport of phosphate, suggesting that that MCT14 is not directly involved in renal Pi transport. Previous experiments detected CD147 at the basolateral membrane of TAL cells [12] whereas MCT14 appears to be restricted to the apical membrane of these cells making a relevant direct interaction between these two proteins in vivo rather unlikely.

Phylogenetically MCT14 is closer related to MCT8 and MCT10, than to the classical monocarboxylate transporters. MCT8 and MCT10 transport thyroid hormone [14] and aromatic amino acids [16] respectively. A recent study suggested that MCT14 might be involved in transport of amino acids, rather than in the shuttling of monocarboxylates [24]. However, our transport studies do not support this hypothesis since they failed to show any significant transport of any of the tested amino acids. There might be a tendency of slightly higher import of serine and glutamate, which could be due to structural homologies to endogenous substrate. However, the rate of induction was very small and may represent rather the stimulation of an endogenous Xenopus transport system than transport by MCT14 itself. Since most amino acids are already absorbed in the proximal tubule, very low concentrations are reaching the TAL; therefore, amino acid transporters located in the TAL must have the properties of a high affinity transporter. Another member of the MCT family, which has been recently characterized, is MCT12. MCT12 has been shown to be a creatine transporter [17]. However, compared to MCT12, MCT14 did not show any transport for creatine. Interestingly MCT7, which is another orphan member of the family, is expressed at the basolateral membrane of the TAL [12]; thus we can speculate that MCT7 might work in tandem with MCT14 for vectorial shuttling of metabolites across the epithelium.

In summary, we showed that the renal abundance of MCT14 is highly regulated by the dietary content of phosphate and that its expression in kidney is restricted to the luminal side of the TAL. However, MCT14 seems to transport neither phosphate nor several other substrates of different members of the MCT family.

Acknowledgments

This study was supported by National Center for Excellence in Research NCCR Kidney.CH financed by the Swiss National Science Foundation. We would like to gratefully acknowledge Nicole Kampik for helping with tissue fixation, Eva Hänsenberger for handling *Xenopus laevis* and providing oocytes as well as Dr. Johannes Loffing (University of Zurich) and Dr. Olivier Devuyst (University of Zurich) for providing us with antibodies.

Figure legend

Figure 1: Renal adaptation to low (LPD) and high (HPD) dietary phosphate. Adaptation was confirmed by the expression of NaPi-IIa protein abundance in kidneys of mice fed 14 hours (A) and 5 days (B) with both diets. β-actin was used as a loading control. Renal mRNA expression of Cyp27b1 and MCT14 after either 14 hours (C and E) or 5 days (D and F) of LPD respectively HPD, n = 5-6 animals/group. Statistical differences were calculated with t-test: *$p<0.05$, **$p<0.01$ and ***$p<0.001$.

Figure 2: Validation of a newly generated MCT14 antibody. Renal homogenates were incubated with antibodies against MCT14 (A) and NaPi-IIa (B) in the presence and absence of the antigenic peptide as indicated. Lysates of *Xenopus laevis* oocytes injected with MCT14 cRNA and non-injected oocytes (n.i.) were incubated with the MCT14 antibody (C); renal homogenate was loaded in the last lane (+). Immunofluorescence was performed on kidney cryosections in the presence and absence of the antigenic peptide (E). Immunofluorescence in oocytes expressing MCT14 and corresponding non-injected oocytes (F).

Figure 3: MCT14 renal localization. Consecutive sections showing MCT14 and NaPi-IIa localization (A). Cortical (B) and outer medullary (C) staining patterns of MCT14 and NKCC2 on consecutive sections. Costainings performed with MCT14 and uromodulin (D) or NCC (E) on renal sections. MCT14 is shown in red, NaPi-IIa, NKCC2, uromodulin and NCC are represented in green and blue indicates nuclear fluorescence (DAPI).

Figure 4: Regulation of MCT14 protein abundance by dietary phosphate. Western blotting with MCT14 antibody was performed on renal homogenates from animals fed 14 hours (A) and 5 days (B) with either low (LPD) or high (HPD) phosphate. Expression levels were normalized to corresponding β-actin levels. MCT14 protein abundance was significantly increased in animals fed a HPD compared to LPD as indicated in the corresponding densitometric analysis. Statistical differences were calculated with t-test: *$p<0.05$ and ***$p<0.001$. Immunofluorescence staining against MCT14 was performed in kidneys of mice fed HPD or LPD for 5 days (C).

Figure 5: Uptake in *X. laevis* oocytes. Lactate transport was assessed in *Xenopus laevis* oocytes injected with cRNA of MCT14 and CD147, in oocytes injected with MCT14 or CD147 alone and non-injected oocytes (NI) (A). Oocytes expressing

MCT12 and CD147, MCT14, MCT14 and CD147 and non-expressing oocytes (N.I.) were used to perform creatine uptake (B). Transport of the indicated amino acids into oocytes expressing MCT14 is given in relation of uptakes into non-injected oocytes (NI) (C). Each experiment was performed with at least n = 7-10 oocytes.

Table 1: Transport studies in *Xenopus laevis* oocytes [pmol/10min]

Substrate	**MCT14**	**Non injected**	
Lactate	7.593 ± 0.600	7.174 ± 1.620	
Pyruvate	0.300 ± 0.063	1.177 ± 0.169	*
Alanine	4.430 ± 0.702	5.135 ± 2.803	
Methionine	4.784 ± 0.906	4.863 ± 1.789	
Cysteine	0.635 ± 0.177	0.489 ± 0.076	
Cystine	6.601 ± 1.419	7.866 ± 0.962	
Glutamine	2.676 ± 0.274	6.053 ± 2.502	*
Serine	12.29 ± 7.19	7.52 ± 4.49	
Tyrosine	11.44 ± 1.05	12.69 ± 1.32	
Glutamate	0.882 ± 0.685	0.628 ± 0.278	
Aspartate	1.770 ± 0.327	1.625 ± 0.176	
Isoleucine	4.955 ± 6.238	1.997 ± 2.152	
Valine	25.70 ± 1.97	24.70 ± 3.23	
Tryptophane	90.97 ± 14.58	100.93 ± 8.41	
Phenylalanine	81.18 ± 23.12	86.28 ± 15.39	
Phosphate	1.384 ± 0.479	1.376 ± 0.377	
Urate	0.0039 ± 0.0015	0.0087 ± 0.0039	*
Citrate	6.442 ± 3.022	5.452 ± 0.462	

References

1. Hattenhauer O, Traebert M, Murer H, Biber J (1999) Regulation of small intestinal Na-P(i) type IIb cotransporter by dietary phosphate intake. Am J Physiol 277: G756-762.
2. Murer H, Forster I, Hernando N, Lambert G, Traebert M, et al. (1999) Posttranscriptional regulation of the proximal tubule NaPi-II transporter in response to PTH and dietary P(i). Am J Physiol 277: F676-684.
3. Shimada T, Kakitani M, Yamazaki Y, Hasegawa H, Takeuchi Y, et al. (2004) Targeted ablation of Fgf23 demonstrates an essential physiological role of FGF23 in phosphate and vitamin D metabolism. J Clin Invest 113: 561-568.
4. Scanni R, vonRotz M, Jehle S, Hulter HN, Krapf R (2014) The human response to acute enteral and parenteral phosphate loads. J Am Soc Nephrol 25: 2730-2739.
5. Thomas L, Bettoni C, Kno pfel T, Hernando N, Biber J, et al. (2016) Acute Adaption to Oral or Intravenous Phosphate Requires Parathyroid Hormone. Journal of the American Society of Nephrology.
6. Hu MC, Shiizaki K, Kuro-o M, Moe OW (2013) Fibroblast growth factor 23 and Klotho: physiology and pathophysiology of an endocrine network of mineral metabolism. Annu Rev Physiol 75: 503-533.
7. Shimada T, Hasegawa H, Yamazaki Y, Muto T, Hino R, et al. (2004) FGF-23 is a potent regulator of vitamin D metabolism and phosphate homeostasis. J Bone Miner Res 19: 429-435.
8. Xie W, Tran TL, Finegood DT, van de Werve G (2000) Dietary P(i) deprivation in rats affects liver cAMP, glycogen, key steps of gluconeogenesis and glucose production. Biochem J 352 Pt 1: 227-232.
9. Halestrap AP (2012) The monocarboxylate transporter family--Structure and functional characterization. IUBMB Life 64: 1-9.
10. Kirk P, Wilson MC, Heddle C, Brown MH, Barclay AN, et al. (2000) CD147 is tightly associated with lactate transporters MCT1 and MCT4 and facilitates their cell surface expression. EMBO J 19: 3896-3904.
11. Castorino JJ, Deborde S, Deora A, Schreiner R, Gallagher-Colombo SM, et al. (2011) Basolateral sorting signals regulating tissue-specific polarity of heteromeric monocarboxylate transporters in epithelia. Traffic 12: 483-498.
12. Becker HM, Mohebbi N, Perna A, Ganapathy V, Capasso G, et al. (2010) Localization of members of MCT monocarboxylate transporter family Slc16 in the kidney and regulation during metabolic acidosis. Am J Physiol Renal Physiol 299: F141-154.
13. Eladari D, Chambrey R, Irinopoulou T, Leviel F, Pezy F, et al. (1999) Polarized expression of different monocarboxylate transporters in rat medullary thick limbs of Henle. J Biol Chem 274: 28420-28426.
14. Friesema EC, Ganguly S, Abdalla A, Manning Fox JE, Halestrap AP, et al. (2003) Identification of monocarboxylate transporter 8 as a specific thyroid hormone transporter. J Biol Chem 278: 40128-40135.
15. Friesema EC, Grueters A, Biebermann H, Krude H, von Moers A, et al. (2004) Association between mutations in a thyroid hormone transporter and severe X-linked psychomotor retardation. Lancet 364: 1435-1437.
16. Kim DK, Kanai Y, Chairoungdua A, Matsuo H, Cha SH, et al. (2001) Expression cloning of a Na+-independent aromatic amino acid transporter with structural similarity to H+/monocarboxylate transporters. J Biol Chem 276: 17221-17228.

17. Abplanalp J, Laczko E, Philp NJ, Neidhardt J, Zuercher J, et al. (2013) The cataract and glucosuria associated monocarboxylate transporter MCT12 is a new creatine transporter. Hum Mol Genet 22: 3218-3226.
18. Dhayat N, Simonin A, Anderegg M, Pathare G, Luscher BP, et al. (2016) Mutation in the Monocarboxylate Transporter 12 Gene Affects Guanidinoacetate Excretion but Does Not Cause Glucosuria. J Am Soc Nephrol 27: 1426-1436.
19. Murakami Y, Kohyama N, Kobayashi Y, Ohbayashi M, Ohtani H, et al. (2005) Functional characterization of human monocarboxylate transporter 6 (SLC16A5). Drug Metab Dispos 33: 1845-1851.
20. Nowik M, Lecca MR, Velic A, Rehrauer H, Brandli AW, et al. (2008) Genome-wide gene expression profiling reveals renal genes regulated during metabolic acidosis. Physiol Genomics 32: 322-334.
21. Park SY, Kim JK, Kim IJ, Choi BK, Jung KY, et al. (2005) Reabsorption of neutral amino acids mediated by amino acid transporter LAT2 and TAT1 in the basolateral membrane of proximal tubule. Arch Pharm Res 28: 421-432.
22. Kirat D, Sallam KI, Kato S (2013) Expression and cellular localization of monocarboxylate transporters (MCT2, MCT7, and MCT8) along the cattle gastrointestinal tract. Cell Tissue Res 352: 585-598.
23. Kirat D, Kato S (2009) Monocarboxylate transporter genes in the mammary gland of lactating cows. Histochem Cell Biol 132: 447-455.
24. Roshanbin S, Lindberg FA, Lekholm E, Eriksson MM, Perland E, et al. (2016) Histological characterization of orphan transporter MCT14 (SLC16A14) shows abundant expression in mouse CNS and kidney. BMC Neurosci 17: 43.
25. Wagner CA, Loffing-Cueni D, Yan Q, Schulz N, Fakitsas P, et al. (2008) Mouse model of type II Bartter's syndrome. II. Altered expression of renal sodium- and water-transporting proteins. Am J Physiol Renal Physiol 294: F1373-1380.
26. Bernascone I, Janas S, Ikehata M, Trudu M, Corbelli A, et al. (2010) A transgenic mouse model for uromodulin-associated kidney diseases shows specific tubulo-interstitial damage, urinary concentrating defect and renal failure. Hum Mol Genet 19: 2998-3010.
27. Loffing J, Vallon V, Loffing-Cueni D, Aregger F, Richter K, et al. (2004) Altered renal distal tubule structure and renal Na(+) and Ca(2+) handling in a mouse model for Gitelman's syndrome. J Am Soc Nephrol 15: 2276-2288.
28. Custer M, Lotscher M, Biber J, Murer H, Kaissling B (1994) Expression of Na-P(i) cotransport in rat kidney: localization by RT-PCR and immunohistochemistry. Am J Physiol 266: F767-774.
29. Biber J, Gisler SM, Hernando N, Wagner CA, Murer H (2004) PDZ interactions and proximal tubular phosphate reabsorption. Am J Physiol Renal Physiol 287: F871-875.
30. Bourgeois S, Capuano P, Stange G, Muhlemann R, Murer H, et al. (2013) The phosphate transporter NaPi-IIa determines the rapid renal adaptation to dietary phosphate intake in mouse irrespective of persistently high FGF23 levels. Pflugers Arch 465: 1557-1572.
31. Zhang MYH, Wang XM, Wang JT, Compagnone NA, Mellon SH, et al. (2002) Dietary phosphorus transcriptionally regulates 25-hydroxyvitamin D-1 alpha-hydroxylase gene expression in the proximal renal tubule. Endocrinology 143: 587-595.
32. Halestrap AP, Price NT (1999) The proton-linked monocarboxylate transporter (MCT) family: structure, function and regulation. Biochem J 343 Pt 2: 281-299.

33. Poole RC, Sansom CE, Halestrap AP (1996) Studies of the membrane topology of the rat erythrocyte H+/lactate cotransporter (MCT1). Biochem J 320 (Pt 3): 817-824.
34. Greger R (1985) Ion transport mechanisms in thick ascending limb of Henle's loop of mammalian nephron. Physiol Rev 65: 760-797.
35. Rampoldi L, Scolari F, Amoroso A, Ghiggeri G, Devuyst O (2011) The rediscovery of uromodulin (Tamm-Horsfall protein): from tubulointerstitial nephropathy to chronic kidney disease. Kidney Int 80: 338-347.
36. Plotkin MD, Kaplan MR, Verlander JW, Lee WS, Brown D, et al. (1996) Localization of the thiazide sensitive Na-Cl cotransporter, rTSC1 in the rat kidney. Kidney Int 50: 174-183.

Figure 1

A) Renal NaPi-IIa

B) Renal NaPi-IIa

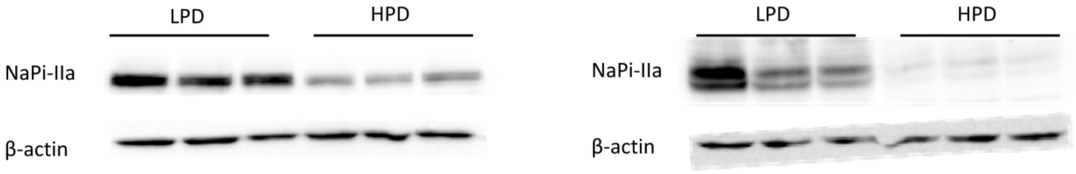

C) Renal Cyp27b1 mRNA

D) Renal Cyp27b1 mRNA

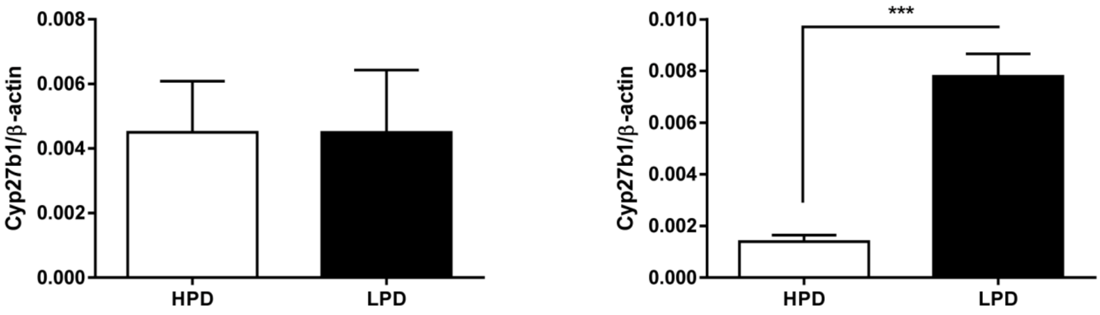

E) Renal MCT14 mRNA

F) Renal MCT14 mRNA

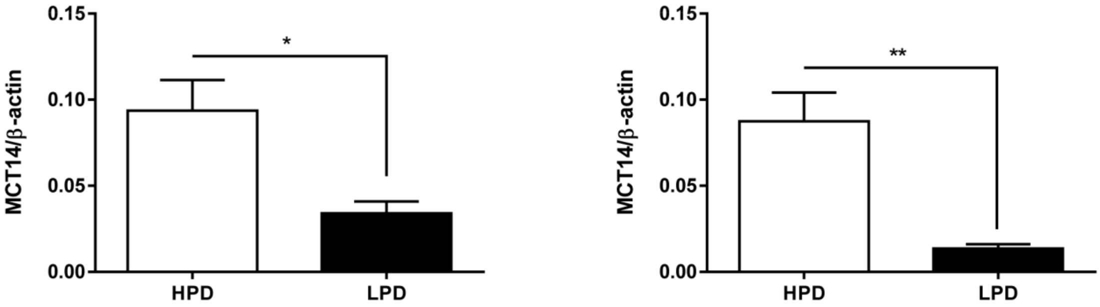

Figure 2

A) Renal MCT14

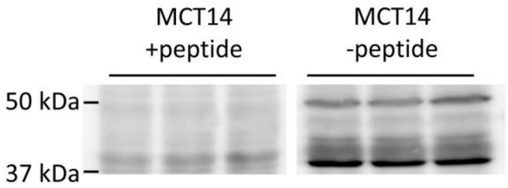

B) Renal NaPi-IIa

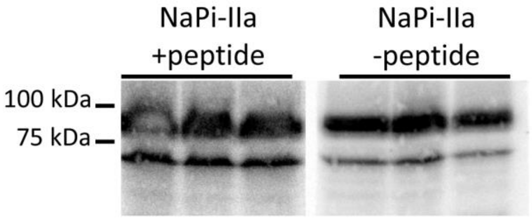

C) *Xenopus leavis* oocytes expressing MCT14

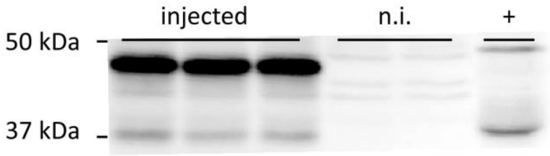

D) Renal MCT14

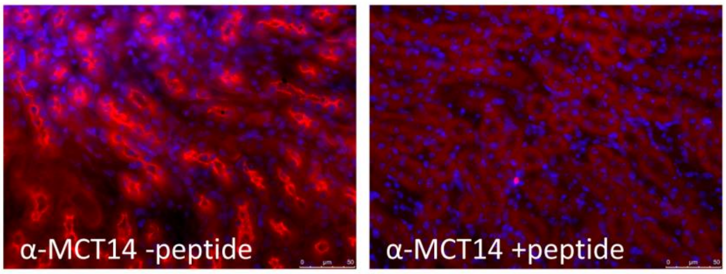

E) Oocytes expressing MCT14

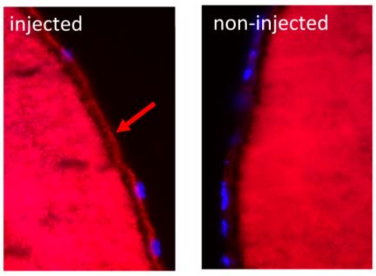

Figure 3

A) Renal MCT14 and NaPi-IIa

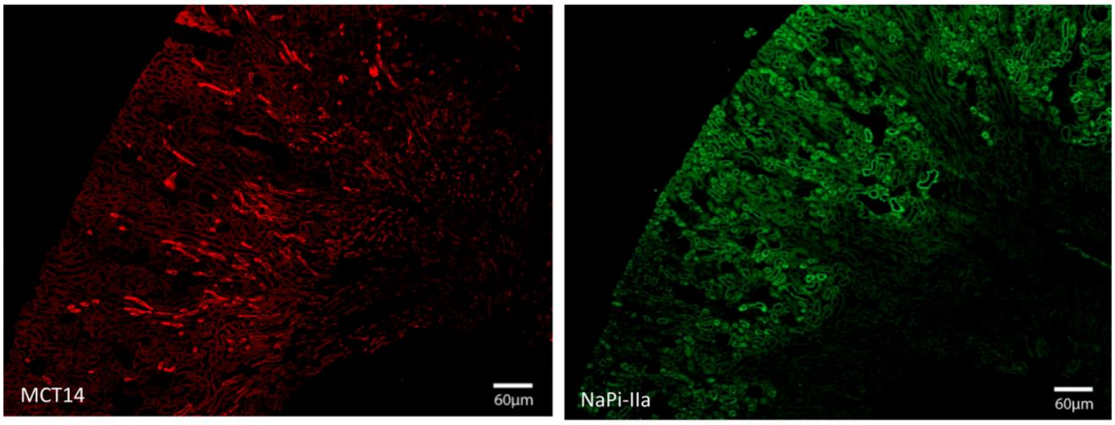

B) Renal MCT14 and NKCC2

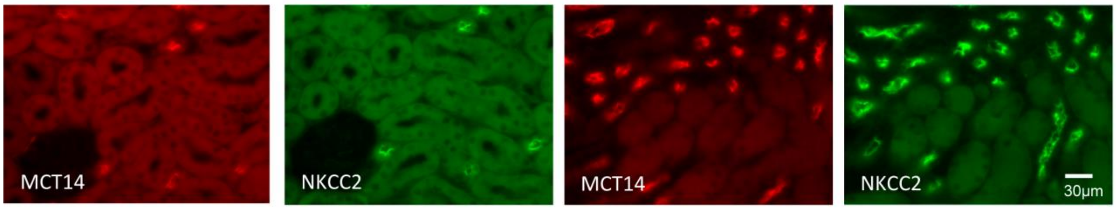

C) Renal MCT14 and Uromodulin

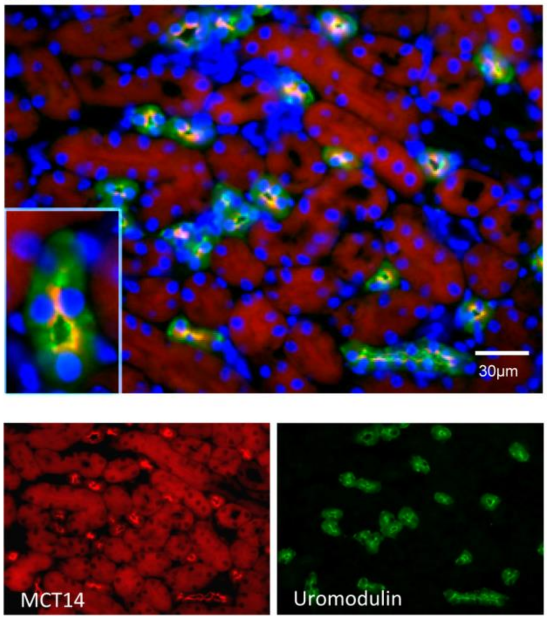

D) Renal MCT14 and NCC

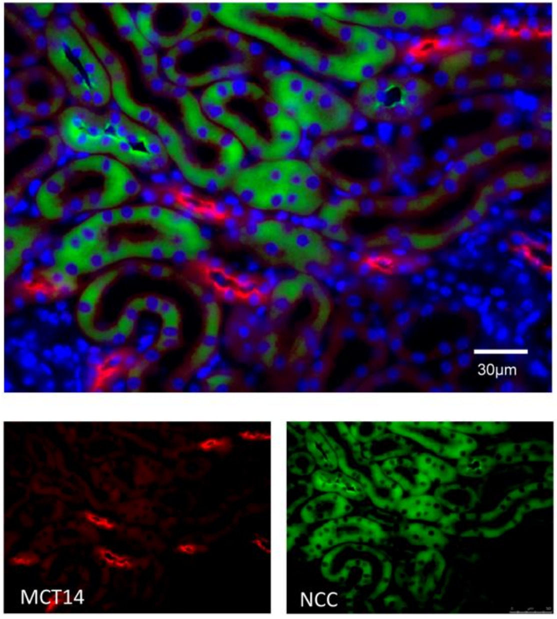

Figure 4

A) Renal MCT14: 14h LPD vs HPD

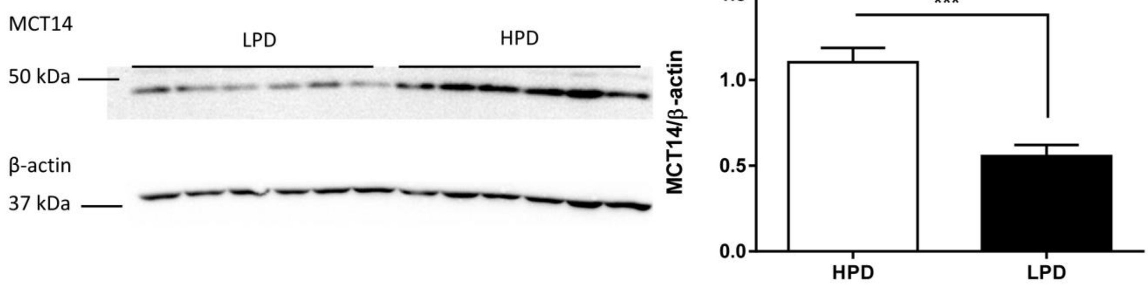

B) Renal MCT14: 5d LPD vs HPD

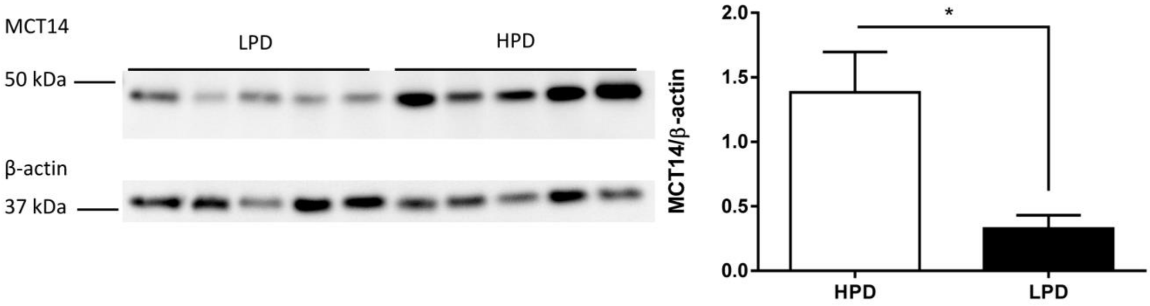

C) Renal MCT14: 5d LPD vs HPD

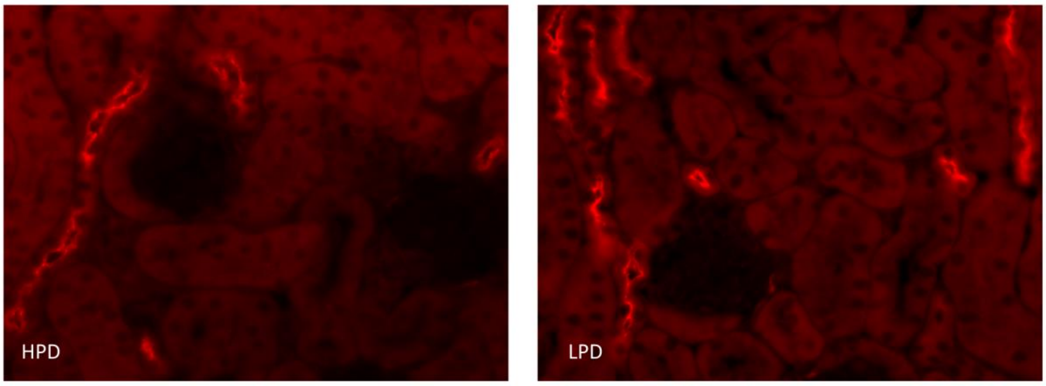

Figure 5

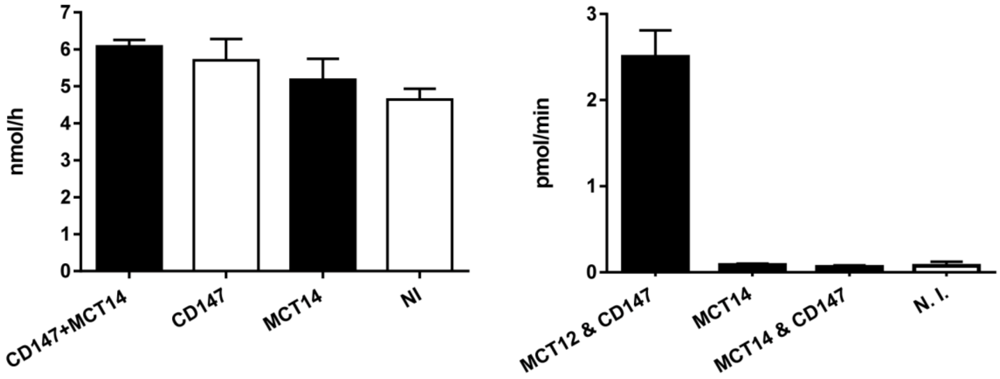

A) Lactate uptake

B) Creatine uptake

C) Amino acid uptake

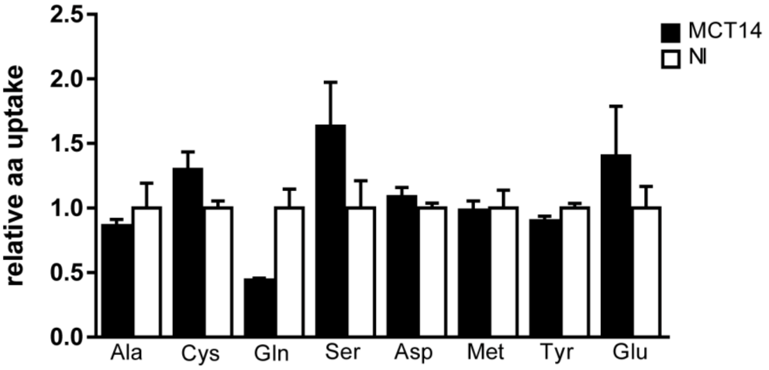

Chapter 4

4. Discussion

Pi is an essential nutrient and the maintenance of its homeostasis is vital for several biological functions in the mammalian body. The impact of dietary Pi content has been granted little attention until recently, when Pi was associated with premature aging, vascular calcifications, cardiovascular mortality, risk for renal failure, and bone damage [210,211]. Therefore it is of importance to get a better understanding of the mechanisms underlying intestinal Pi absorption. Especially since some novel therapeutic approaches to decrease pathologically high Pi levels in CKD patients involve intestinal NaPi-IIb inhibition. Though animal models suggest that NaPi-IIb is the major if not only transporter for transcellular Pi transport in the intestine [43,52], the relative contribution of transcellular versus paracellular absorption of Pi is not clear yet.

NaPi-IIb deficient animals fed normal chow show a rather mild phenotype regarding Pi homeostasis. Whereas intestinal ablation of NaPi-IIb abolishes Pi uptake into ileal BBMV, the associated increase in fecal Pi excretion is very moderate. As a compensatory mechanism the expression of the renal NaPi-IIa is upregulated, which is reflected by increased Pi uptakes into renal BBMV. Consistently NaPi-IIb deficient mice excrete less Pi in urine. The reduced intestinal absorption seems to be fully compensated by the concomitantly reduced renal excretion of Pi, since plasma levels of Pi and its regulatory hormones remain constant in those animals [43]. Those findings were similar in intestinal specific as well as in inducible NaPi-IIb deficient mouse models [43,52]. Furthermore, this moderate contribution of NaPi-IIb may also apply to patients suffering from pulmonary alveolar microlithiasis, caused by mutations in NaPi-IIb [44]. Despite calcifications in lung no impact on Pi homeostasis is reported, and, if mentioned, plasma levels of Pi are normal [44]. Together, the above observations strongly suggest an alternative pathway for Pi across the intestinal epithelia. Since uptake into BBMV from ileum [43] and transport studies in everted gut sacs [52] showed an abolished transcellular transport of Pi in mice lacking NaPi-IIb, it may be hypothesized that the paracellular pathway plays an important role in those animals, and possibly even in non-mutated mammals. Of note, the transport studies in everted gut sacs were performed with equimolar Pi concentrations on both sides of the epithelium, neglecting any possible contribution of the paracellular pathway, since paracellular transport requires a concentration gradient [52]. In fact Pi concentrations in the intestinal lumen exceed plasma levels of Pi more than tenfold [53]. Additionally, upon Pi depletion the absorptive rate is about 50% higher in WT animals than in NaPi-IIb deficient animals [52], suggesting a contribution of NaPi-IIb in the same margin. Instead nothing is known about the molecules allowing for paracellular Pi transport and possible adaptive mechanisms. Since NaPi-IIb is upregulated upon dietary Pi restriction, this rather highlights the maximal contribution of NaPi-IIb, than reflecting the physiological relevance under normal dietary conditions.

Upon dietary Pi restriction a strong increase of intestinal NaPi-IIb abundance is observed [212], consistent with higher uptakes into ileal BBMV. Furthermore NaPi-IIb has an apparent K_m >10µM [16], thus it is a high affinity transporter that is expected to be saturated already at very low luminal Pi concentrations. This might suggest that the role of NaPi-IIb is critical once dietary Pi supply is low. In order to investigate this hypothesis we challenged NaPi-IIb deficient animals with either high or low Pi diets. We found that similarly to WT mice, NaPi-IIb deficient mice also increase urinary and fecal Pi excretion when fed with a high Pi diet. On the contrary, dietary Pi restriction decreased fecal and urinary Pi excretion in both groups. Though urinary excretion was decreased under low dietary Pi conditions, it does not seem to be sufficient to match the lack of intestinal absorption in NaPi-IIb deficient mice, resulting in a transient hypophosphatemia. Considering that in response to low Pi WT animals increase their renal Pi reabsorption to a point where almost no Pi is excreted (after 14 days), it is not surprising that NaPi-IIb deficient mice are unable to further adapt through renal Pi transport rates. Interestingly, the circulating levels of vitamin D_3, PTH and FGF23 are comparable in both groups, even when intestinal ablation of NaPi-IIb leads to a transient hypophosphatemia during low dietary supply of Pi. However, upon prolonged Pi deprivation NaPi-IIb deficient mice show increased urinary levels of deoxypyridinoline (DPD), a marker for bone resorption, indicating that mutant mice release Pi from bones to maintain its circulating levels constant. The concomitant mobilization of Ca^{2+} from bones is refleceted by the increased amount of Ca^{2+} excreted in urine. NaPi-IIb deficient mice also show higher urinary excretion of corticosterone and two of its metabolites 5α-dihydrocorticosterone and 11-

dehydrocorticosterone, which together reflect higher plasma levels of corticosterone. Glucocorticoids have been shown to be potent stimulators of bone catabolism and osteoclast activity [154], which is consistent with the observed Ca^{2+} loss and elevated DPD in urine, thus supporting the hypothesis of the bone as a source of Pi of NaPi-IIb deficient mice under Pi depletion. As a consequence, we found that bone mineral density under low Pi diet was decreased in NaPi-IIb deficient mice. Thus, NaPi-IIb mediated Pi absorption during low Pi availability is important to protect bone from demineralization and to maintain systemic Pi balance.

Our observations in dilution potential measurements in intestinal and renal cell culture models suggest that the tight junctions are permeable to Pi. Because under physiological conditions Pi is present in monovalent and divalent forms and claudins are charge and size selective, experiments were initially performed at pH 6 and pH 8.4, to investigate if claudins discriminate between the two Pi species. Additionally, claudins form pores that facilitate diffusion selectively, and their transport is supposed to be symmetric, unlike transcellular transport. Therefore experiments were performed with apical and basolateral application of Pi and permeability was normalized to that of Na^+. In intestinal cell culture models we observed a strong preference of the paracellular pathway for monovalent Pi, with a relative permeability of about 40% versus a maximal permeability of 20% for divalent Pi. The relative permeability to Cl^-, was unaffected by pH, suggesting that the differences observed are truly due to Pi species selectivity. Moreover, permeabilities were symmetric, indicating that potential changes were indeed due to ion flux through the paracellular pathway. Overexpression of either claudin 17 (cldn17) or tricellulin in MDCK cells had no effect on Pi permeability, whereas as expected cldn17 strongly increased the paracellular permeability to Cl^-. This suggests that the anion selective cldn17 [209] is not involved in mediating Pi passage through the tight junctions. Similar experiments were also performed in different segments of rat and mouse intestine. Duodenum (done only in mice), Jejunum, ileum and colon all conducted Pi across their epithelium, with the small intestine having a higher absolute permeability than the colon, due to higher transepithelial resistance. The same was true for Na^+ and Cl^-. Following Ohm's law ($I=V/R$), the higher the resistance of the tissue the lower is the flux of ions (current) observed across the epithelium. As for the cell culture models the tight junctions of the intestine also show a preference for monovalent Pi, though the effect of pH was not as strong as observed in cultured cell. Again pH did not affect transport of Na^+ or Cl^-. The permeability for Pi was symmetric and about half of the permeability of Na^+ and Cl^-. In our experimental setup the colon paracellular pathway is permeable to Pi. Moreover, hyperphospatemia develops after enemas containing Pi concentrations exceeding blood levels, highlighting the capacity of the colon to absorb Pi [31]. However, the role of the colon in intestinal Pi absorption might be minor, due to increasing solidity of the content. Paracellular Pi permeability in NaPi-IIb deficient mice fed a normal diet is comparable to the one observed in WT mice. These findings strongly support the hypothesis that the paracellular transport is involved in intestinal Pi absorption and is sufficient to provide enough Pi to maintain Pi homeostasis in NaPi-IIb deficient mice (and eventually PAM patients) under normal dietary Pi supply.

The confirmation of paracellular Pi transport in intestine might also help to explain the observations in NaPi-IIb deficient mice adapted to different dietary Pi content. Assuming that the luminal Pi content somehow reflects the dietary content, the higher the dietary Pi content the higher the amount of Pi absorbed through paracellular diffusion. Thus the urinary Pi excretion in NaPi-IIb deficient animals should reflect the efficiency of this concentration dependent mechanism. In the absence of an active transport mechanism, NaPi-IIb mice excrete higher levels of Pi with increasing amount of Pi in the diet, and even under normal dietary conditions more Pi is absorbed than necessary since there is still a large proportion excreted in urine. Only when dietary Pi is restricted and presumably the concentration gradient is not high enough to drive passive diffusion, NaPi-IIb deficiency proofs to be critical. These findings suggest that active transport mediated by NaPi-IIb is there to cope with low luminal Pi concentrations, while under normal dietary conditions paracellular transport may be the major component. Also from an energetic point of view, it would make sense to utilize a passive diffusion gradient for absorption, because every Pi imported via NaPi-IIb requires one ATP since the Na^+/K^+-ATPase to remove the three imported sodium.

Hyperphosphatemia promotes secondary hyperparathyroidism and is a risk factor for cardiovascular disease, soft tissue calcification and is the major cardiovascular risk factor in CKD patients, increasing cardiovascular morbidity [1]. Still, daily intake of Pi exceeds recommended amounts. For instance a daily intake of 1500 mg Pi is reported for American males, whereas 700 mg is recommended [213]. The increased dietary intake of Pi is partially attributed to the consumption of processed food and soft drinks. Preservatives in these products contain a high amount of Pi salts. In contrast to Pi naturally present in the food, these additives have a much higher availability for absorption [214]. This high amount of Pi in our nutrition is expected to provide a strong diffusion gradient across the intestinal epithelium, triggering the passive absorption of Pi, which does not show any saturation and linearly increases with luminal Pi content. Luminal Pi concentration in human jejunum has been reported to be between 0.7 and 12.7mM [215] depending on dietary conditions, thus NaPi-IIb might transport already close to the maximal capacity considering its K_M or may even be downregulated. Therefore the excessive amount of Pi causing adverse effects, including renal damage and vascular calcification might be eventually attributed to the passive absorption in the intestine. Thus our dietary habits might be reflected by the experiments presented in this study, in which mice were fed high Pi diet: even in the absence of NaPi-IIb, Pi supply was excessive and led to phosphaturia.

Hyperphosphatemia is observed in CKD patients due to renal failure and worsens the patients` outcome. Dietary Pi restriction, the inhibition of intestinal NaPi-IIb, or the use of Pi binders have been suggested as an approach to treat hyperphosphatemia in CKD patients. However, a combination of at least two might be necessary, since NaPi-IIb independent mechanisms, i.e. paracellular transport may be sufficient to drive the intestinal absorption of dietary Pi supply. Furthermore NaPi-IIb might already be down regulated due to hyperphosphatemia and its relative contribution already blunted. In contrast, lowering luminal Pi concentrations by Pi binders might induce NaPi-IIb upregulation. Indeed experiments in mice with adenine induced CKD show that administration of sevelamer (a Pi binder) stimulates the expression of NaPi-IIb, despite high levels of serum Pi in adenine treated and untreated mice [216]. Thus sevelamer was not able to correct hyperphosphatemia in this CKD mouse model. NaPi-IIb deficiency alone decreased serum Pi levels in adenine induced CKD, but was not able to completely correct the hyperphosphatemia. However sevelamer was able to reduce serum Pi levels to normal values in adenine treated NaPi-IIb deficient mice, supporting the notion that both pathways contribute to intestinal absorption of Pi [216].

In summary we could show that under normal and high dietary Pi conditions the ablation of intestinal NaPi-IIb can be compensated by the kidney and does not alter overall Pi homeostasis. Pi seems to be sufficiently/excessively supplied by the paracellular pathway. However the role of NaPi-IIb appears to be crucial as soon as dietary Pi is restricted. In this case NaPi-IIb deficient mice compensate impaired intestinal Pi absorption by resorbing bone to release Pi. Furthermore we demonstrate that the tight junctions in the intestine are permeable to Pi, providing the requirements for paracellular diffusion of Pi.

Additionally, we showed that the renal abundance of MCT14, an orphan member of the monocarboxylate transporter family, is highly regulated by the dietary content of Pi and that its expression in kidney is restricted to the luminal side of the TAL. However, MCT14 seems to transport neither Pi nor several other substrates of different members of the MCT family.

Chapter 5

5. Outlook

1. The permeability of the intestinal paracellular pathway to Pi, assessed by dilution potential measurements in Ussing chambers, needs to be confirmed, for example with radioactive flux experiments. Furthermore the responsiveness of the paracellular pathway for Pi to alterations in dietary Pi content or other regulators of Pi homeostasis like vitamin D_3, PTH and FGF23 should be addressed. Of interest some claudins are regulated by vitamin D_3. Moreover, it was reported that passive Pi transport in small intestine was stimulated by the glucocorticoid cortisone [217]. The increase in glucocorticoids observed in NaPi-IIb deficient mice might not only be involved in increased bone resorption, but also provide another mechanism to increase intestinal reabsorption.
2. Comparing possible regulatory mechanisms with transcriptome data on Pi regulated transcripts in intestine might give insight into the molecular mechanism behind paracellular Pi permeability. So far there is no association of any tight junction component and intestinal Pi absorption. Preliminary results indicate that the anion selective claudin 17 and tricellulin are not participating in this gating of Pi.
3. Final aspect to be addressed is the relative contribution of active and passive transport in the intestine to understand the relevance of each pathway. From an energetic point of view this would be of interest, because for active transport intestinal cells have to spend ATP through the Na^+/K^+-ATPase, to maintain the membrane potential and the Na^+ gradient for secondary active transport. Also from an evolutionary point of view it would not make sense to spend energy as long as there is a passive pathway providing the body with Pi.

Chapter 6

6. Publications that did not contribute to the thesis

The papers listed here were published during the PhD period but do not contribute to the thesis

- **Structural Fold and Binding Sites of the Human Na^+-Phosphate Cotransporter NaPi-II**

  Cristina Fenollar-Ferrer, Monica Patti, Thomas Knöpfel, Andreas Werner, Ian C. Forster, and Lucy R. Forrest

  Published in:

  Biophysical Journal. 2014 Mar 18;106(6):1268-79. doi:10.1016/j.bpj.2014.01.043

- **Identification of the First Sodium Binding Site of the Phosphate Cotransporter NaPi-IIa (SLC34A1)**

  Cristina Fenollar-Ferrer, Ian C. Forster, Monica Patti, Thomas Knoepfel, Andreas Werner, and Lucy R. Forrest

  Published in:

  Biophysical Journal. 2015 May 19;108(10):2465-80. doi: 10.1016/j.bpj.2015.03.054.

- **Acute Adaption to Oral or Intravenous Phosphate Requires Parathyroid Hormone**

  Linto Thomas, Carla Bettoni, Thomas Knöpfel, Nati Hernando, Jürg Biber, and Carsten A. Wagner

  Published online before print October 6, 2016, doi: 10.1681/ASN.2016010082

1268 Biophysical Journal Volume 106 March 2014 1268–1279

Structural Fold and Binding Sites of the Human Na^+-Phosphate Cotransporter NaPi-II

Cristina Fenollar-Ferrer,[†] Monica Patti,[‡] Thomas Knöpfel,[‡] Andreas Werner,[§*] Ian C. Forster,[‡*]
and Lucy R. Forrest[†*]
[†]Computational Structural Biology Group, Max Planck Institute of Biophysics, Frankfurt am Main, Germany; [‡]Institute of Physiology and Zurich Center for Integrative Human Physiology, University of Zurich, Zürich, Switzerland; and [§]Epithelial Research Group, Institute for Cell and Molecular Biosciences, Newcastle University, Newcastle upon Tyne, United Kingdom

ABSTRACT Phosphate plays essential biological roles and its plasma level in humans requires tight control to avoid bone loss (insufficiency) or vascular calcification (excess). Intestinal absorption and renal reabsorption of phosphate are mediated by members of the SLC34 family of sodium-coupled transporters (NaPi-IIa,b,c) whose membrane expression is regulated by various hormones, circulating proteins, and phosphate itself. Consequently, NaPi-II proteins are also potentially important pharmaceutical targets for controlling phosphate levels. Their crucial role in P_i homeostasis is underscored by pathologies resulting from naturally occurring SLC34 mutations and SLC34 knockout animals. SLC34 isoforms have been extensively studied with respect to transport mechanism and structure-function relationships; however, the three-dimensional structure is unknown. All SLC34 transporters share a duplicated motif comprising a glutamine followed by a stretch of threonine or serine residues, suggesting the presence of structural repeats as found in other transporter families. Nevertheless, standard bioinformatic approaches fail to clearly identify a suitable template for molecular modeling. Here, we used hydrophobicity profiles and hidden Markov models to define a structural repeat common to all SLC34 isoforms. Similar approaches identify a relationship with the core regions in a crystal structure of *Vibrio cholerae* Na^+-dicarboxylate transporter VcINDY, from which we generated a homology model of human NaPi-IIa. The aforementioned SLC34 motifs in each repeat localize to the center of the model, and were predicted to form Na^+ and P_i coordination sites. Functional relevance of key amino acids was confirmed by biochemical and electrophysiological analysis of expressed, mutated transporters. Moreover, the validity of the predicted architecture is corroborated by extensive published structure-function studies. The model provides key information for elucidating the transport mechanism and predicts candidate substrate binding sites.

INTRODUCTION

Cells depend on inorganic phosphate (P_i) to ensure growth and structural integrity, maintain energy balance, and communicate with their environment. In mammals, P_i transport across the cell membrane is mediated by secondary active transporter proteins that use the free energy from the Na^+ gradient and transmembrane (TM) electrical potential to catalyze uphill P_i transport. Multicellular organisms, especially vertebrates, face a particular challenge in maintaining whole body P_i homeostasis: the solubility of P_i is limited in the presence of divalent cations, especially calcium, and excess of P_i in bodily fluids promotes Ca-P_i precipitation. This is of particular concern in patients with chronic kidney disease who tend to retain excessive levels of P_i (hyperphosphatemia), which leads to vascular calcification (1).

A family of Na^+-coupled P_i transporters belonging to the solute carrier family SLC34 (NaPi-II), is central to maintaining whole body P_i homeostasis (2). All vertebrates express up to three isoforms of NaPi-II in organs that contribute to maintaining P_i balance. Mammals express NaPi-IIb (SLC34A2) in the intestine to mediate dietary P_i absorption and express NaPi-IIa (SLC34A1) together with NaPi-IIc (SLC34A3) in the renal proximal tubule to mediate reabsorption of P_i from the glomerular filtrate (2–4). The central role of NaPi-II proteins emerged when hormones and metabolic factors known to influence body P_i levels, such as parathyroid hormone, calcitonin, growth hormones, or P_i availability, were found to regulate NaPi-II membrane expression (reviewed in (5,6)). Their homeostatic role was further corroborated by NaPi-II knockout mice, which displayed organ-specific perturbations of P_i handling (7). Of importance, in humans, dysfunction in renal P_i handling can be attributed to naturally occurring mutations in NaPi-IIa (8,9); NaPi-IIc (10), and to P_i-related pathologies for NaPi-IIb in lung and testes (11), further underscoring the importance of these proteins.

Functional analyses of wild-type (WT) and mutant transporters expressed in *Xenopus laevis* oocytes have allowed a detailed characterization of each isoform. The NaPi-II proteins transport one divalent P_i ion with an apparent affinity ($K_{0.5}^{Pi}$) of 10–70 μM, together with two (NaPi-IIc) or three

---

Submitted November 1, 2013, and accepted for publication January 29, 2014.

*Correspondence: lucy.forrest@nih.gov or iforster@access.uzh.ch or andreas.werner@newcastle.ac.uk

Cristina Fenollar-Ferrer and Lucy R. Forrest's present address is Computational Structural Biology Section, Porter Neuroscience Research Center, National Institutes of Neurological Disorders and Stroke, National Institutes of Health, Bethesda, MD 20892.

Cristina Fenollar-Ferrer and Monica Patti share equal first authorship.

Editor: Joseph Mindell.

0006-3495/14/03/1268/12 $2.00

http://dx.doi.org/10.1016/j.bpj.2014.01.043

Na^+ ions (NaPi-IIa and NaPi-IIb) with an apparent affinity ($K_{0.5}{}^{Na}$) of 25–50 mM (reviewed in (12)). The experimental evidence supports the notion that NaPi-II proteins mediate transport according to the canonical alternating access mechanism (13–15). In the normal transport cycle (Fig. 1 *A*), substrate binding at the external side is ordered, with 2 Na^+ ions binding before P_i. These cation interactions, together with intrinsic mobile charges that are postulated to alter the empty carrier orientation between inward and outward facing conformations (*states* 0 and 1, Fig. 1 *A*), effectively couple membrane potential to the NaPi-IIa/b transport cycle to act as a transport driving force (12). In contrast, the electroneutral NaPi-IIc cycle is insensitive to membrane voltage and only one of the Na^+ ions preceding P_i binding is translocated. However, for all three isoforms, binding of the last Na^+ is a rate-determining partial reaction (Fig. 1 *A*, *transition* 4 → 5) (16,17) and moreover, the similarity of apparent substrate affinities suggests that they share the same substrate recognition and translocation structural unit.

All vertebrate NaPi-II homologs identified and studied to date are assumed to have identical TM topologies (12) (Fig. 1 *B*). Specifically, the protein contains two sets of TM helices, each containing a copy of a conserved sequence motif, separated by a large extracellular loop. Epitope tagging and cysteine scanning mutagenesis experiments suggest that these repeated units have inverted TM topologies and that both termini are cytosolic (12,18). However, a three-dimensional structural model of NaPi-II proteins that integrates these functional and structural data is still lacking, preventing further understanding of the transport mechanism and limiting the interpretation of structure-function data.

The inverted-topology repeat architecture represents a common structural *leitmotif* displayed by a number of

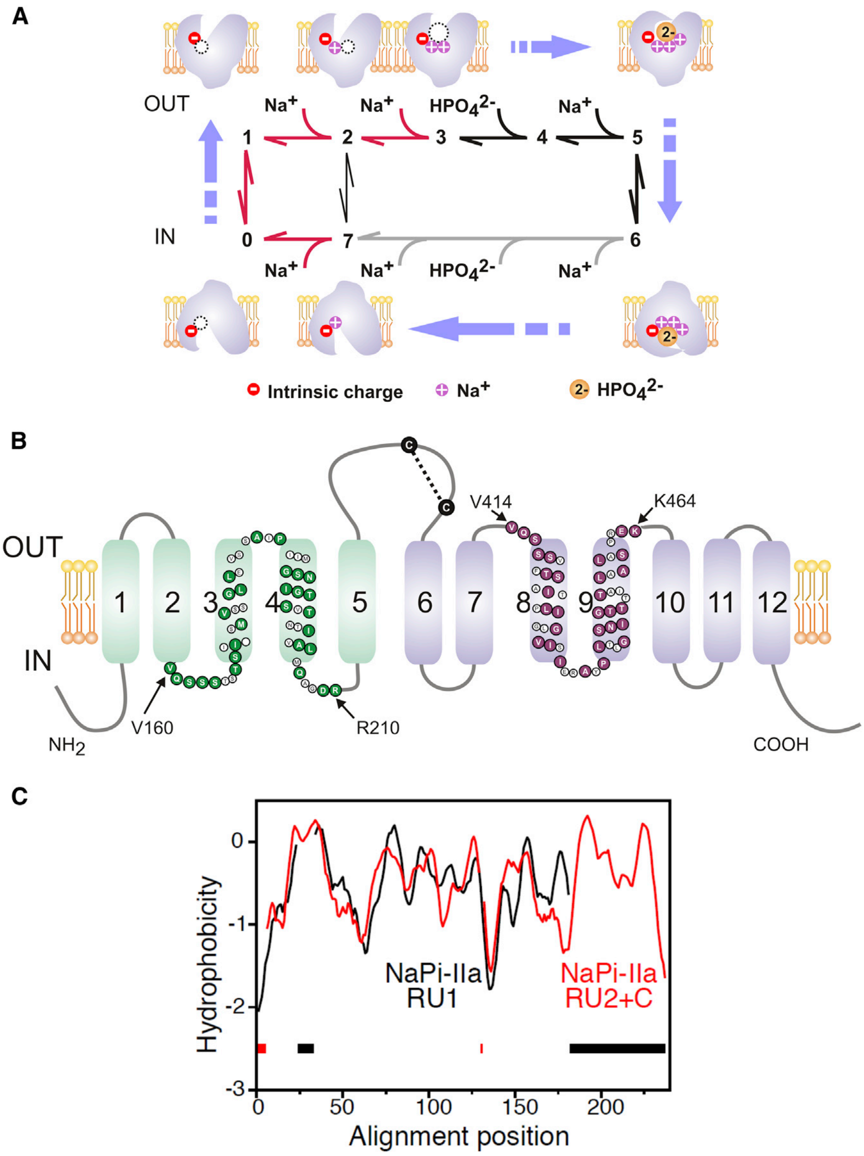

FIGURE 1 Kinetic and structural features of NaPi-IIa. (*A*) The transport cycle is depicted as a sequence of partial reactions between conformational states, numbered 0–7 (reviewed in (12)). Cartoons illustrate the ordered nature of protein-substrate interaction based on experimental evidence. Partial reactions on the cytosolic side have not been explicitly identified except the last Na^+ release (*transition* 7 → 0) (68). Red arrows: electrogenic partial reactions (involving charge movement); black arrows: electroneutral partial reactions. In the absence of external P_i, Na^+ ions can also translocate via a leak transition (2 ↔ 7) (66). For the electroneutral cycle (of NaPi-IIc), all transitions are electroneutral and the first Na^+ ion to bind (*transition* 1 → 2) is hypothesized not to translocate (58). (*B*) Secondary topology of NaPi-IIa based on previous experimental evidence and bioinformatic predictions (12). The assumed boundaries of repeat regions (*rat sequence*) are indicated (52); colored symbols indicate identical or conserved residues in each repeat. A disulfide bridge links the two halves of the protein in the large extracellular loop. (*C*) Hydropathy plots of the regions predicted to contain the structural repeats in NaPi-II, averaged over a set of sequence homologs and aligned using AlignMe. Region 1, containing residues 86–256 of the human NaPi-IIa (RU1, *black*) is aligned to region 2 plus C-terminus consisting of residues 335–564 (RU2+C, *red*). Gaps in the alignment are indicated by dashes along the base of the plot. To see this figure in color, go online.

secondary active transporters for which crystal structures have been determined recently (see e.g. (13,19,20).). Such repeats provide a pseudosymmetry to the fold that has a number of important implications for function. For example, these transporters frequently harbor a central substrate binding site at the axis of pseudosymmetry. This site is then accessed alternately via two pseudosymmetric pathways, each constructed from equivalent elements from the two repeats (21,22). Interestingly, binding sites for sodium ions have also been identified by studying pseudosymmetric positions in structures of a sodium-coupled transporter, BetP (23). Thus, although many transporters have evolved significant breaks in this pseudosymmetry, presumably as a means to introduce specificity and variety, consideration of the repeats and their symmetry can be a useful starting point for structure-function studies of secondary transporters.

The recognition of the conserved inverted-topology sequence repeat in NaPi-II prompted us to search for a suitable template among the crystal structures of solute transporters reported to date, from which a homology model could be generated, compared with a wealth of experimental evidence, and used to predict putative binding site regions.

METHODS

Computational methods

Full details of the computational procedures are provided in the Supporting Material. A brief description follows. Sequences of NaPi-II transporters were identified using HMMER (24) from the National Center for Biotechnology Information (NCBI) nonredundant (*nr*) database, clustered using UCLUST (25), and aligned with MSAProbs (26). Segments of the multiple sequence alignments were converted to averaged hydropathy profiles and aligned with the AlignMe web server (27). Hidden Markov-models (HMMs) of the same segments were constructed after identifying homologs from the NCBI *nr*20 database using HHblits (28). HMMs were aligned using HHalign (29).

Template structures were searched for using PSI-BLAST (30), Phyre2 (31), COMA (32), and HHpred (29). Template-target alignments of either full-length proteins or individual repeats were generated with either Profile+Secondary-Structure (AlignMePS) or +Transmembrane (AlignMePST) modes on the AlignMe server (27), or with HHalign.

A homology model was constructed using Modeler (33) based on the structure of VcINDY (PDB identifier 4F35). After refinement and guided by conservation patterns from the ConSurf server (34), the percentage of identical residues between VcINDY and NaPi-II was ~15% in repeat unit 1 (RU1) and 11% in repeat unit 2 (RU2). A single model was selected after 2000 Modeler attempts, with two sodium ions and a phosphate molecule modeled in putative binding sites. The model was evaluated using ProQM (35) and PROCHECK (36).

Functional expression in oocytes and transport assays

Reagents and solutions

Oocytes were incubated in Modified Barth's solution that contained (in mM): 88 NaCl, 1 KCl, 0.41 $CaCl_2$, 0.82 $MgSO_4$, 2.5 $NaHCO_3$, 2 $Ca(NO_3)_2$, 7.5 HEPES, adjusted to pH 7.5 with TRIS and supplemented with antibiotics doxycyclin and gentamicin (5 mg/l). The solution compositions were as follows: Control superfusate (100 Na) (in mM): 100 NaCl, 2 KCl, 1.8 $CaCl_2$, 1 $MgCl_2$, 10 HEPES, adjusted to pH 7.4 using TRIS. Choline solution (100 Ch): as for 100 Na with isosmotic substitution of 100 mM choline chloride. P_i was added to the required substrate concentration from 1 M K_2HPO_4 and KH_2PO_4 stocks premixed to give the required pH (7.4).

Molecular biology and single point mutations

cDNA encoding WT human NaPi-IIa was subcloned into a vector containing the 5′ and 3′ UTRs from *Xenopus* β-globin to improve its expression in oocytes. Mutations were introduced using the Quickchange site-directed mutagenesis kit (Stratagene, La Jolla, CA). The sequence was verified by sequencing (Microsynth, AG, Balgach, Switzerland), plasmids were linearized with XbaI and cRNA was synthesized in presence of Cap analog using the T3 Message Machine kit (Ambion, Austin, TX).

Functional expression and transport assays

X. laevis frogs were purchased from *Xenopus* Express France (Vernassal, France). Ovarian lobes were surgically removed and the oocytes isolated following standard protocols (e.g. (37)). Animal procedures were performed according to Swiss Cantonal and Federal legislation. Injected oocytes (50 nl of cRNA (0.2 μg/μl)) were incubated for 3–5 days in modified Barth's solution. Radioisotope uptake assays were performed using standard procedures as described elsewhere (e.g. (38)) using 100 Na solution and 1 mM cold P_i to which $^{32}P_i$ (specific activity 10 mCi/mmol P_i) was added. Standard two-electrode voltage clamp hardware was used for electrophysiology (GeneClamp, model 500, Molecular Devices, Sunnyvale, CA) and controlled using pClamp 8-9 software (Molecular Devices). Clampfit (Molecular Devices) was used for postacquisition analysis.

Immunostaining

After 3 days of expression, oocytes were fixed according to standard procedures (e.g. (39)). Further details are given in the Supporting Material.

RESULTS

Identifying the repeated elements and peripheral TM helices in NaPi-IIa

Modeling the structure of a protein is aided by knowledge of the conserved and repeated structural elements within its fold. Although it was clear from earlier studies, and from the presence of a repeated conserved motif (Fig. S1), that NaPi-II transporters contain a structural repeat with inverted topology, it was not obvious where the boundaries of the repeat units lay, or was it clear whether their overall fold had an equivalent already reported. Aligning family-averaged hydropathy profiles of different fragments of the sequence clearly shows that the structure comprises two repeat units (RU1, RU2) plus a C-terminal extension of two additional TM helices (Fig. 1 *C*). These segments correspond to TMs 1–5, TMs 6–10 and TMs 11–12, respectively, of the published topology (Fig. 1 *B*).

A similar result was obtained by aligning HHalign hidden HMMs of region 1 with region 2 or with region 2+C (see Methods; Fig. S1, Fig. S2). This confirmed that regions 1 and 2 have similar secondary structures and further indicated that they have ~27% identical residues. We concluded that RU1 and RU2 in NaPi-II comprise residues 86–256 and

335–489, respectively, and residues 504–564 form peripheral TM helices that are not part of the core fold.

Identifying a structural homolog of NaPi-IIa

To identify whether any available structure would be a suitable template for NaPi-IIa, several approaches were attempted (see Methods), of which HHpred provided the most promising clue. Specifically, among the top five hits was a Na^+-coupled dicarboxylate transporter from *Vibrio cholera* (VcINDY) (40), also known as NaDC, a member of the Divalent Anion:Na^+ Symporter (DASS, 2.A.47) (41) or SLC13 family (42), which also includes Na^+-coupled inorganic anion (sulfate and phosphate) transporters (41). The VcINDY structural fold belongs to the ST[3] class (43) and contains an inverted-topology repeat fold (40). The E-values of the top 10 hits were rather large ($>2 \times 10^2$), indicative of low confidence levels. Among those top 10 were three aquaporins, a GlpG protease, a KQT potassium channel, and a disulphide reductase, DsbD, as well as three water-soluble proteins. Pairwise alignments of NaPi-IIa with four of the five highest-scoring membrane proteins (aquaporin-4, GlpG protease, AQY1 aquaporin, and VcINDY) using AlignMe in PS mode indicated that the template with the greatest fold similarity among these hits was VcINDY, with 62% sequence coverage and 7% identical residues, compared to $\leq$40% coverage and $\leq$4% identity for the other four proteins. (The other HHpred hit in the top five, the KQT potassium channel was excluded because the region matched to NaPi-II comprised unconserved residues.)

The high E-value and small percentage of identical residues in VcINDY and NaPi-II suggested significant differences between their sequences, though these properties do not preclude them from sharing a common core fold given that structure is much more conserved during evolution than sequence. Indeed, the two repeats in inverted-topology membrane proteins can contain $<$10% identical residues, despite being structurally related (14,40,44). In the aforementioned search, HHpred matched the conserved QSSS NaPi-II motif to a SNT motif that contributes to Na^+ and dicarboxylate binding in VcINDY (Fig. S4 *B*), which suggested that the binding site regions at least are conserved. To assess whether the similarities between VcINDY and NaPi-II extend beyond function, the presence of inverted repeats and hydrophilic binding motifs, we used a number of other bioinformatic approaches (see Methods) culminating in homology modeling and comparison with experimental data.

An important factor complicating the detection of distant sequence relationships between transporter proteins has been the presence of additional structurally-peripheral TM helices that confound the alignment algorithms. A case in point is the BCCT and NSS families (14,20,40,44,45), which contain two additional TM helices either before or after, respectively, the core inverted-topology fold. The structural similarity between these families is clear using hydropathy profile alignments, especially after separating out the repeats of each protein, because that reduces the chances of core helices aligning to peripheral helices (46).

In a family-averaged hydropathy profile alignment of full-length NaPi-IIa and VcINDY, RU1 of NaPi-IIa was aligned with several helices in the first repeat of VcINDY (Fig. S4 *A*, *green dashed box*). That segment of the alignment resembled the NaPi-II repeat alignment (Fig. 1 *B*), suggesting a relationship between the two proteins. However, RU2 was not aligned to the second repeat of VcINDY in this global alignment, due to a shift of one TM segment (Fig. S4 *A*, *orange dashed box*). Therefore, to identify putative corresponding helices in both VcINDY and NaPi-II repeats, we separately aligned hydropathy profiles of RU1 or RU2 from the two proteins (Fig. 2 *A*), as well as HMMs of these repeat units (Fig. S4 *C* and *D*). These alignments from both methods, as well as alignments obtained using AlignMe in PST mode, clearly indicated that the first two TMs of each of the repeats of VcINDY (Fig. S3 *A*) has no equivalent in NaPi-IIa.

In VcINDY, these additional helices (TMs 2, 3, 7, and 8) are located at the periphery of the VcINDY monomer (Fig. S3 *A*), and therefore could be omitted from the NaPi-IIa model without affecting the integrity of the core transport unit. Indeed, in the case of citrate carrier (CitS), which was recently shown to share a similar architecture with VcINDY, substrate-activated structural changes observed in electron microscopy projection maps include no conformational changes in these helices. This indicated that they act as a stator with little or no functional role (47). The fact that both NaPi-IIa repeats align to the equivalent structurally repeated regions in VcINDY (i.e., the C-terminal segment of each repeat, Fig. 2 *A*) gave support to the proposed relationship between the two proteins. At the same time, the significant number of additional helices in VcINDY compared to NaPi-IIa, before, between, and after the repeats (Fig. S3 *A*) indicated why the alignments of the full-length sequences were poor and the scores were low.

According to HHalign and AlignMePST alignments of the individual repeats the proposed Na^+ and substrate binding site residues of both RU1 and RU2 of VcINDY were aligned to the most conserved regions of NaPi-IIa (Fig. 2 *B*, Fig. S4 *B*, and Fig. S4 *C*). This matching of conserved residues, the consistency of the alignments using three different alignment methodologies, i.e., AlignMePST, HHalign, and hydropathy profile alignment, and the equivalency of the matched helices in both repeats, together provided support for the choice of VcINDY as a template for NaPi-II transporters.

A structural model of human NaPi-IIa

Although the expected accuracy of a model with this level of sequence similarity is modest, it should suffice for

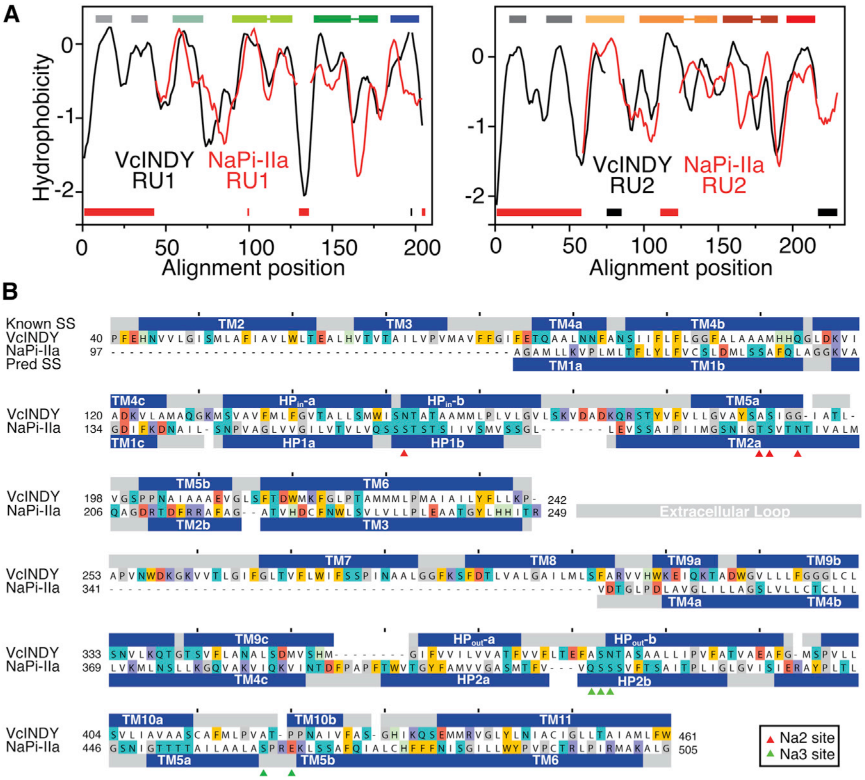

FIGURE 2 Comparison of repeat units in NaPi-II and the sodium-carboxylate transporter VcINDY suggests that they share a common fold. (*A*) Hydrophobicity profiles of the two repeat units in NaPi-II (*red line*) and VcINDY (*black line*). Hydropathy plots averaged over a set of sequence homologs of human NaPi-IIa or of VcINDY were aligned using AlignMe for repeat unit 1 (*left*) and repeat unit 2 (*right*). (*B*) Sequence alignment between VcINDY and the core region of human NaPi-IIa used for modeling. The helices assigned from the structure of VcINDY (*Known SS*) and the PSIPRED predictions for helices in NaPi-IIa (*Pred SS*) are shown as blue bars above and below the sequences, respectively. Residues whose side chains contribute to site Na2 (*red triangles*) or Na3 (*green triangles*) are indicated. To see this figure in color, go online.

comparison with topological and accessibility data even if individual TM segments are misaligned by one or two helical turns (48). An initial model of human NaPi-IIa comprising residues 97–249 (RU1) and 341–505 (RU2) was constructed (Fig. 3 and Fig. 4, *A–C*), whose topology differs in some aspects from earlier proposals (Fig. 1 *B*). The earlier, simpler proposal, based on the assumption of membrane-spanning segments, agrees with the present model on the nature of TMs 1 and 3 (previously 1 and 5) and TMs 4 and 6 (previously 6 and 10). In addition, the overall topology, in the sense of the accessibility of the loops, is unchanged. However, in its oversimplicity, the earlier model did not satisfactorily explain the unusual hydropathic nature of the segments between TMs 1 and 3, and between TMs 4 and 6 (Figs. 2 *B*, 3 *A*, and 4 *C*). Because these segments in VcINDY consist of helical hairpins that do not fully span the membrane, as well as long nonhelical elements within TM segments, the model based on VcINDY therefore makes sense of the hydropathy plots. At the same time, the updated topology based on VcINDY agrees well with results from studies using in vitro glycosylation (49) and cysteine scanning mutagenesis and accessibility measurements (SCAM -substituted cysteine accessibility method (50)), e.g. (51–55).), as shown mapped onto the model (Fig. 3 *B*, Fig. 4 *C*).

First, SCAM in the linker between TM1 and TM2 of RU1 (see Fig. 3 *B*) established that this region is accessible to the external medium (56), consistent with its position at the exposed external surface of our model (*helix* 1c, Fig. 4 *C*).

Second, SCAM in RU2 identified an externally accessible region in loop L5ab between TM5a and TM5b (Fig. 3 *B*) (53). In our model (Fig. 4 *C*), this linker is now localized at the same depth as the proposed substrate coordination sites (see below). Nevertheless, it should be accessible to cysteine modifiers via the same aqueous pathway as that of the substrates. Our original topology (Fig. 1 *B*) also implied that helix 1c should be more accessible from the external medium than loop L5ab, whereas SCAM studies (56) indicate that both regions have similar apparent accessibilities, which is in better agreement with their positioning relative to the external medium depicted in our three-dimensional model (Fig. 4 *C*). Finally, a cysteine at position S424, which was considered accessible based on the original topology, did not give resolvable fluorescence upon attempts to label the equivalent site in the flounder isoform (57). In better agreement with that data, the updated model (Figs. 3 and 4 *C*) places this residue deeper in the structure within HP2b.

Third, thiol modification from the external medium of a Cys substituted at S183 in NaPi-IIa or at the equivalent site in flounder NaPi-IIb (S155) at the top of helix 2a in RU1 (Fig. 3 *B*) is possible, with minimal functional consequences (49,57,58). These findings are consistent with the relatively exposed position of this site, far from the central binding region in the new fold (Fig. 4 *C*).

Fourth, SCAM revealed four sites that are accessible only from the cytosol: N199 at the end of TM2a, together with V202, A203, and M205 from L2ab (49,52,57,58)

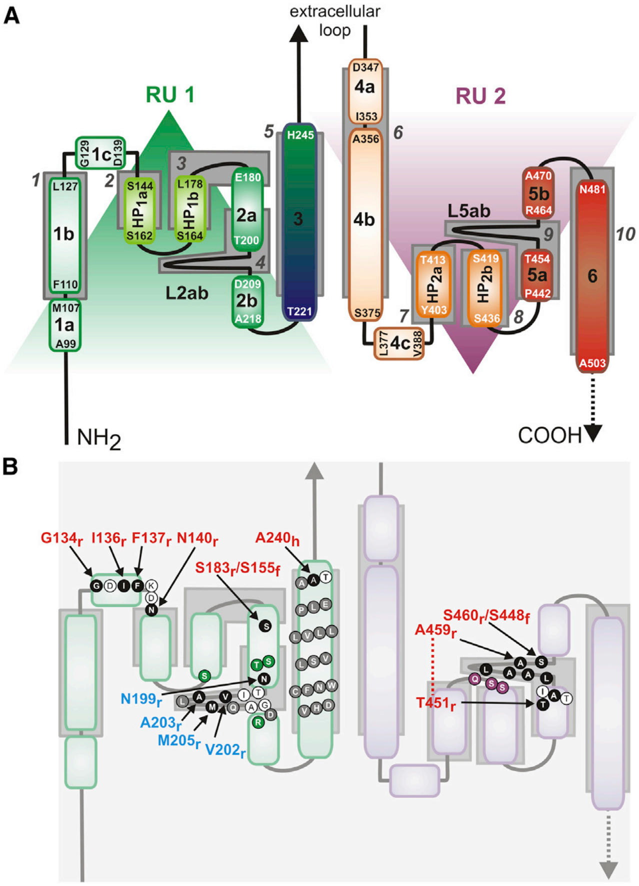

FIGURE 3 Schematics of refined topology of NaPi-IIa. (*A*) Topological elements are colored shades of green for RU1 and shades of red for RU2, and the structural repeats (RU1, RU2) are indicated (*shaded triangles*). Approximate positions of helical domains according to an earlier, simplified topology (*gray boxes*) are numbered according to the scheme in Fig. 1 *B* for the human NaPi-IIa sequence. (*B*) Comparison with published experimental data. The position of key residues is indicated. Residues that are accessible based on cysteine scanning (SCAM) studies (*black solid circles*); residues that are inaccessible based on SCAM (*gray solid circles*) are highlighted. Sites accessible from the external milieu (*red*) or accessible only from the internal milieu (*blue*) are labeled according to the organism: flounder NaPi-IIb (f), human (h) or rat (r) NaPi-IIa. Positions on the topology of residues mutated in this study are also shown (*green and violet solid circles* for RU1 and RU2, respectively). To see this figure in color, go online.

(Fig. 3 *B*). By contrast, the model suggests that these sites are buried. However, it should be noted that our model corresponds to an outward-open state, in which only the extracellular pathway should be accessible. Transporters containing pseudosymmetric repeats typically have pseudosymmetric pathways, which become exposed in a given state, whereas their counterparts in the other repeat are not (13,14). In NaPi-II, residues from TM5a and loop L5ab—the symmetry equivalents of TM2a and L2ab—are accessible in the modeled outward-open state (Fig. 4), and so it is plausible that L2ab and TM2a are accessible from the internal medium in cytosolic-open conformers of the protein. However, we cannot completely rule out an error in the choice of template or sequence alignment used for the modeling.

Fifth, SCAM in TM3 of human NaPi-IIa indicated that this helix was inaccessible from the external medium, with the exception of A240 at its extracellular end (55) (Fig. 3 *B*). This pattern fits well with our model, wherein TM3 acts as a buried scaffold with A240 exposed at the extracellular side (Fig. 3 *C*).

We note that the proposed NaPi-IIa model has the opposite TM topology from the core of VcINDY (Fig. S3), with the first helix of RU1 in NaPi-II originating in the cytoplasm (54). As a consequence, our NaPi-IIa model corresponds to an extracellular-facing state.

Predicting substrate coordination sites

As indicated previously, the Na^+ and citrate coordinating residues located in the loops of the hairpins (HP_{in} and HP_{out}) in VcINDY have conserved polar counterparts in hairpins HP1 and HP2 of the NaPi-IIa model (Figs. 2 *B* and 4 *C*). In addition, after comparing the structures, we observed that the Cα atom of N199 from TM2a of NaPi-IIa (Fig. 4 *D*) is located ~5 Å from the Cα atom of the Na^+-binding residue N151 in VcINDY (40) even though they originate from different helices. Although the accuracy of the binding-site region in the model (Fig. 4 *D*) is highly dependent on the correctness of the sequence alignment, we considered the possibility that residue N199 in NaPi-II plays a similar role to N151 in VcINDY; this possibility would be consistent with an earlier finding that Cys substitution of N199 in NaPi-IIa reduces the apparent Na^+ affinity 40-fold (52). We therefore reasoned that other residues in this region might coordinate the substrates or cosubstrates. To identify such residues, we tentatively modeled an ion into this region (see Methods), designated the Na2 site. We observed that three other highly conserved hydroxyl-containing residues lay nearby (Cα atoms within 6 Å of the ion), namely S164 from HP1b, and T195 and S196 from TM2a (Fig. 4 *D*), which could provide suitable sodium coordinating residues.

Assuming direct coupling between the substrate and Na^+, as observed in LeuT (20) and in VcINDY (Fig. S3 *B*), a P_i ion was tentatively placed at a position equivalent to that of bound citrate (Fig. 4 *D*). The citrate density was observed at the axis of the twofold pseudosymmetry between the structural repeats, a common position for transporter substrate binding sites (13). During the modeling, we imposed coordination of the P_i by S164 and N199, such that they each coordinate the ion at Na2 and the P_i (Fig. 4 *D*, see also Fig S5 for coordination in the final model). This reflects the observation that the nature of the side chain at site 199 is a critical determinant of the mode of transport: small polar and nonpolar residues do not alter the coupling mode, albeit while causing a large increase in apparent sodium affinity (see above), whereas large polar and charged residues at

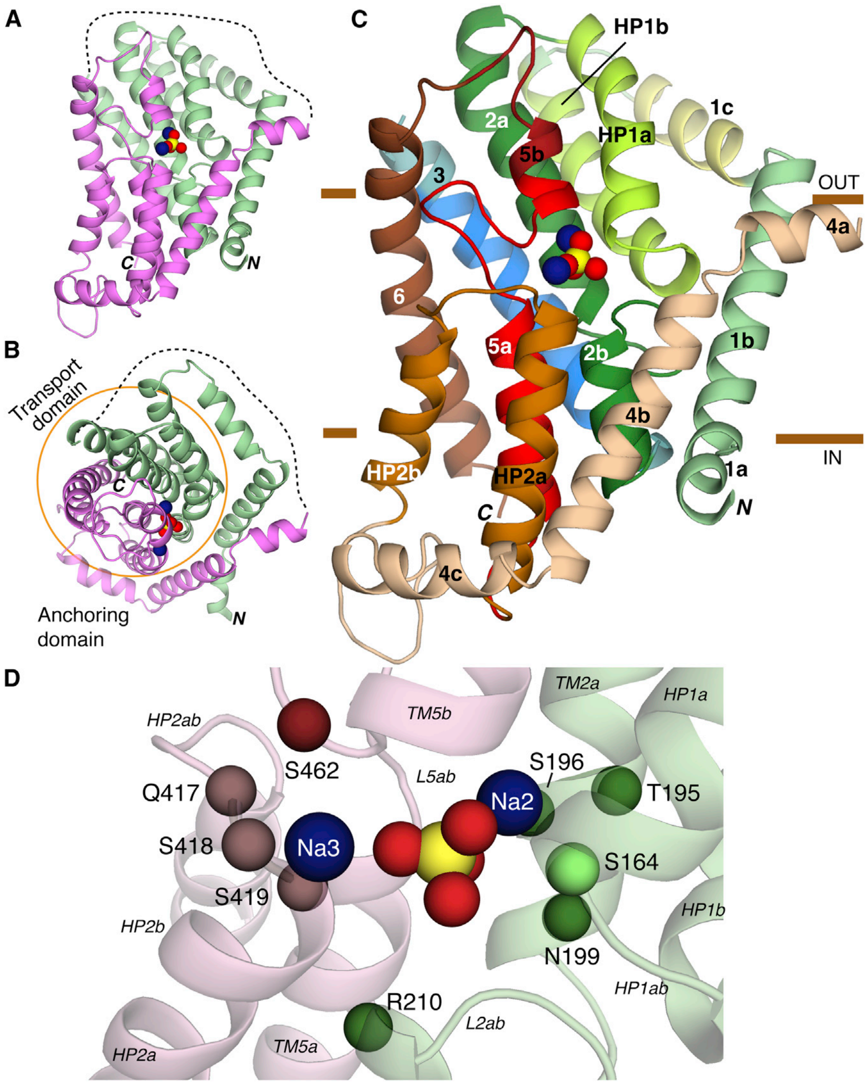

FIGURE 4 Structural model of human NaPi-IIa based on VcINDY. (*A–C*) Overview of the predicted fold of the NaPi-IIa model represented by cartoon helices. Two sodium ions (*blue*) and P_i (*yellow, red*) are shown as spheres. The model is viewed (*A* and *C*) from within the plane of the membrane, or (*B*) from the extracellular side. (*A* and *B*) Location of the structural repeats RU1 (*green*) and RU2 (*pink*), and the connecting long extracellular loop (*dashed lines*). The transport domain is highlighted by an orange circle, in *B*. In *C*, individual helices are colored according to Fig. 3 *A*. Regions for which experimental data relating to the topology are highlighted: residues accessible to the extracellular side (*yellow*) or buried (*blue*) in helix 1c and 3, respectively; and residues expected to be helical in TM5a, TM5b, and the 5ab loop (*red*). The approximate extents of the membrane are indicated by brown bars. (*D*) The predicted binding site region in the model of NaPi-IIa. The Cα-atoms of conserved and polar residues close to the putative binding site are highlighted, as are bound P_i and sodium ions (*spheres*). Residues N199 and S462 have previously been implicated in substrate binding. Residues S164, T195, S196, R210, Q417, S418, S419 are investigated in this study. To see this figure in color, go online.

this position lead to only the uncoupled leak mode being observed (*transition* 2 ↔ 7, Fig. 1 *A*) (52). Although we cannot rule out a more indirect role for these mutations, such an ability to affect the mode of coupling would be consistent with a direct coordination of both substrates (Fig. 4 *D*, Fig. S5).

In the model, residue S164 (at the start of HP1b) has a symmetry equivalent position, namely S419 at the start of HP2b, and so we speculated that S419 may also coordinate P_i. Finally, beneath the binding site we identified a positively charged residue, R210 from TM2b, whose Cα atom is ~8 Å from the substrate (Fig. 4 *D*), suitable for P_i coordination by the arginine side chain. R210 was therefore tested as a putative P_i coordinating residue.

A second Na^+ site, pseudosymmetric to that described previously, could be hypothesized from our model—this site would also involve direct coordination by the substrate P_i. Assuming this pseudosymmetry predicts that other residues in HP2ab and L4ab might coordinate an ion in that site. In particular, according to the current model, S462 lies at the start of TM5b, which after mutation to Cys in flounder NaPi-IIb (S448) and in NaPi-IIc (S437), can be modified by a thiol reagent and this modification abolishes transport (17,60,61). Under these conditions, Na^+ and P_i can still bind (partial reactions 1 ↔ 2, 2 ↔ 3, and 3 ↔ 4, Fig. 1 *A*) (17,39,58,60), but either the final Na^+ binding step or the translocation step has been compromised, consistent with the notion that S462 contributes to the third Na^+ binding site, hereafter designated Na3.

Two other positions predicted to be in L5ab, corresponding to A455 and L457 of NaPi-IIa, have been previously mutated to Cys and subjected to thiol modification. Under these conditions, not only was cotransport function compromised, but the uncoupled leak (*transition* 2 ↔ 7, Fig. 1 *A*) significantly increased (53), which provided further confirmation of the importance of this loop in substrate translocation and cosubstrate coupling.

Finally, according to their proximity in the model (the Cα atoms are within 6 Å of the ions), we identified residues Q417 and S418 as potentially coordinating this ion in addition to S419 and S462.

Testing predictions by functional studies of NaPi-IIa mutants

As mentioned previously, the minimal sequence identity between VcINDY and NaPi-IIa limits the certainty with which we can assign specific residues to the binding sites. Therefore, to attempt to refine the structure of these sites in atomic detail, for example using molecular dynamics simulations, would not necessarily be informative. However, the predicted involvement of these residues in substrate coordination requires experimental validation. We therefore mutated S164, T195, S196, R210, Q417, S418, and S419 to Ala or Cys, expressed the mutant constructs in *Xenopus* oocytes, and performed standard radiotracer and voltage clamp assays to compare their functional behavior with that of WT NaPi-IIa (Table 1 and Fig. 5). For constructs that displayed no measurable functional behavior (namely S196C), we confirmed membrane expression by immunohistochemistry (Fig. S6). Furthermore, we used presteady-state charge relaxation measurements to ascertain if the mutagenesis had affected partial reactions involving charge displacement arising from the empty carrier and the movement of Na$^+$ ions to and from their binding sites (Fig. 1 *A*) (12).

TABLE 1 Functional properties of mutants

Repeat unit	Construct	^{32}P uptake	Presteady-state 100Na	Activation index[a] P_i[a]	 Na[a]
	WT	+	+	0.61	0.63
RU1	S164A	−	+	n.a.	n.a.
	S164C	−	+	n.a.	n.a.
	T195C	−	+	n.a.	n.a.
	S196C	−	−	n.a.	n.a.
	N199C[b]	+	n.d.	0.10	0.03
	R210C	+	+	0.60	0.65
RU2	Q417C	+	+	0.46	0.39
	S418C	−	+	n.a.	n.a.
	S419A	−	+	n.a.	n.a.
	S419C	−	+	n.a.	n.a.

n.a.: not applicable; n.d.: not determined; −: not detected; +: detected.

Presteady-state relaxations suppressed (−) or left unchanged (+) by 1 mM P_i.

Bold entries indicate constructs used for immunohistological confirmation of membrane expression (Fig S6).

[a] Activation indices were defined as follows: the P_i index was the ratio of P_i-induced current with 0.1 mM P_i to that with 1 mM P_i in 100 mM Na$^+$ and the Na$^+$ index was the ratio of the response to 1 mM P_i with 50 mM Na$^+$ to that with 100 mM Na$^+$. Both indices were determined at −50 mV. These ratios give an approximate indication of shifts in the apparent substrate affinity for screening purposes (e.g., (56)).

[b] From (52) for rat NaPi-IIa isoform, equivalent to N199 in human NaPi-IIa.

Two constructs (R210C and Q417C) displayed significant ^{32}P uptake (Fig. 5 *A*), P_i-induced currents (data not shown) and WT-like, resolvable charge relaxations in response to voltage steps in the absence of P_i (Fig. 5 *B*). However, the uptake levels of these two mutants were significantly smaller than for the WT (Fig. 5 *A*). Because the uptake assay was performed at only one P_i concentration (1 mM), the lower transport rates could be ascribed to either altered kinetics (apparent substrate affinity, reduced maximum transport rate), or compromised membrane expression, or a combination of both. Given the low transport activity of R210C and Q417C and associated data uncertainties, we did not perform standard dose dependence assays. Instead, to assess whether the mutations had significantly altered the apparent substrate affinities for Na$^+$ and P_i, we determined activation indices defined as the ratio of P_i-induced currents under defined conditions in which either Na$^+$ or P_i concentration was altered (see *legend*, Table 1) (56). For R210C, the Na$^+$ and P_i activation indices were both close to those of the WT, whereas Q417C showed significantly reduced indices (Table 1). These findings indicated that transport and binding were unaffected by the R210C mutation, but that the Gln-Cys substitution in the predicted Na3 site (Fig. 4 *D*) reduced the apparent substrate affinities. Nevertheless, for R210C, we noted that the presteady-state relaxations showed a clear asymmetry compared with the WT and other mutants (more charge movement for the hyperpolarizing step compared to the depolarizing step) (Fig. 5 *B*). This indicated that removal of this charge had affected the voltage-dependent kinetics.

The replacement of S196 in RU1 with Cys did not prevent surface expression (Fig. S6), but was considered lethal, as the oocyte membranes became leaky after 2 days, preventing further functional investigation. Nevertheless, this behavior underscored the potentially critical role played by this residue predicted to be at the Na2 site (Fig. 4 *D*).

The remaining six constructs (S164A, S164C, T195C, S418C, S419A, and S419C) gave resolvable presteady-state relaxations (Fig. 5 *B*), but insignificant ^{32}P uptake or P_i-induced current under voltage clamp (Table 1). The presence of presteady-state relaxations that are superimposed on the background linear capacitive charge current of the oocyte membrane (Fig. 5 *B*) provided strong experimental evidence that, in the absence of P_i, one or more Na$^+$ ions could still interact with these six mutants, in agreement with our kinetic scheme for the WT (Fig. 1 *A*). However, subsequent partial reactions required for cotransport, such as association of P_i or the last Na$^+$ ion, were compromised by these conservative, and yet apparently deleterious, substitutions.

As described previously, the model predicts that S164 of the first QSSS motif coordinates Na2 and/or P_i and that T195 and S196 of TM2b contribute to the Na2 binding site. The observation of presteady currents, combined with the lack of uptake for both S164A and S164C supports the

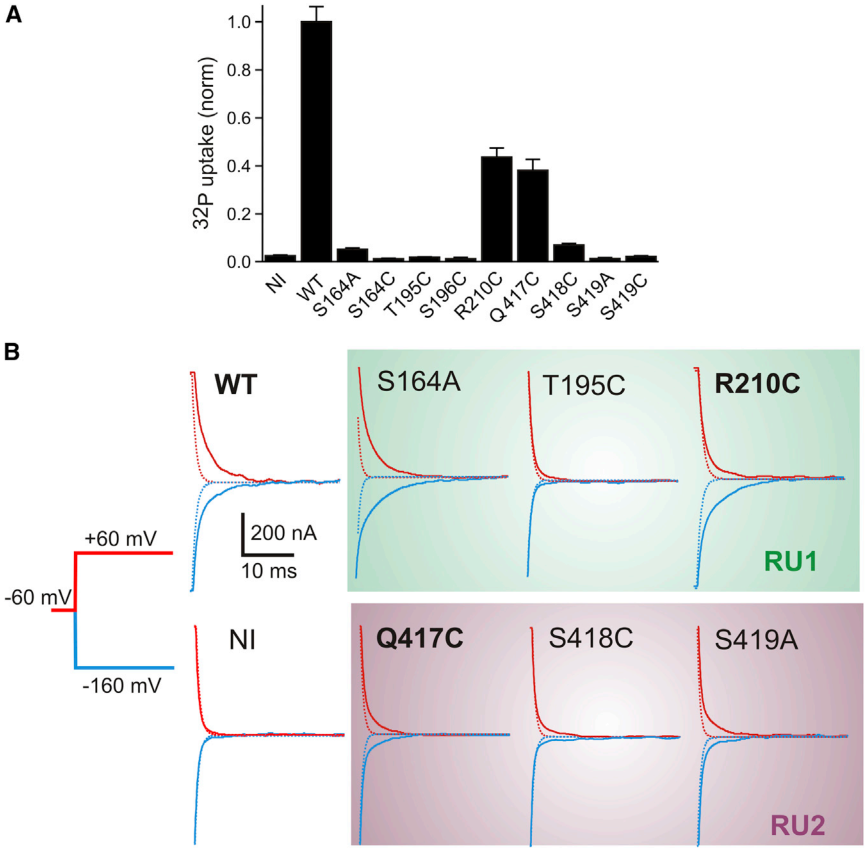

FIGURE 5 Effect of site-specific mutations on transport and substrate interactions in human NaPi-IIa. (*A*) Tracer uptake (^{32}P) data normalized to WT for the mutants and noninjected (NI) oocytes as control. Each data set is the mean ± SE of data from two batches of oocytes (4–5 oocytes per batch). (*B*) Presteady-state relaxations recorded from representative oocytes expressing selected constructs in RU1 and RU2, together with WT and NI as controls superfused in 100 mM Na$^+$. Bold label indicates active P$_i$ transport was also measured. Transient currents shown in response to voltage steps as indicated, from a holding potential = –60 mV to two test potentials: –160 (*blue*) and +60 mV (*red*). Traces were baseline corrected and are shown with the same ±500 nA range. Each relaxation was fit with a double exponential function. Dotted traces is the fitted fast component (relaxation time constant <1ms) corresponding to endogenous membrane charging and are comparable to the NI data in all cases. For all mutants shown there was charge movement in excess of the endogenous component. To see this figure in color, go online.

proposal that S164 is critically required for later steps of transport, consistent with a role in coordinating Na2 and/or P$_i$.. Similar observations for T195C are consistent with the proposal that it contributes to the Na2 binding site, whereas the lethality of S196C indicates an important, albeit less clearly defined, role for S196.

The model also predicts that Q417, S418, and S419 of the second QSSS motif coordinate Na3, with the latter also possibly coordinating P$_i$. The ~50% reduction in Na$^+$ and P$_i$ activation indices of Q417C (Table 1) indicates a reduction in the apparent substrate affinities for both substrates after modification, which is consistent with the proposed role of Q417. Cys substitutions at neighboring sites (S418, S419) resulted in similar properties to the S164 and T195 mutants described above, i.e., the mutants exhibited presteady-state currents while uptake was abolished, consistent with a critical role in later steps in the transport mechanism, most likely in Na$^+$ and P$_i$ coordination. Finally, based on the WT-like behavior of R210C with respect to substrate activation, it is likely that R210 does not contribute to substrate coordination. Nevertheless, the asymmetry of the presteady-state relaxations compared with the WT (Fig. 5 *B*) suggests that R210 may play a critical role in defining the voltage dependence of the cotransport cycle and therefore may be proximal to the binding sites.

DISCUSSION

The structural repeat has emerged as a common architectural *leitmotif* in all reported structures of secondary transporters (e.g. (13,22), and in a majority of those, the repeats have inverted TM topologies. The pseudosymmetries introduced by these repeats have functional implications that can include the location of binding sites and the equivalency of repeated elements in defining pathways or gating elements. In NaPi-IIa the repeated sequence of the QSSS motif is particularly prominent and biochemical studies suggested that these were accessible from opposite sides of the membrane, consistent with the repeats exhibiting inverted topologies (52,53). Inspired by the number of new structures available, we used both statistical (using, e.g., HHpred) and qualitative (using hydropathy profile alignments) approaches to search for a putative template. Notably, there is no similarity with the structure of a recently reported fungal proton-dependent P$_i$ transporter (62), which is a member of the major facilitator superfamily of transporters, with its characteristic fold of two lobes, each containing 6 TM helices.

Hydropathy analysis was previously used to predict fold similarity in the ST[3] class to which VcINDY belongs (43). Biochemical topology analysis (63) and two-dimensional crystallography (47) have since confirmed that, e.g., the 2HCT family that includes CitS and the AIT family that includes VcINDY adopt similar architectures, providing support for the use of hydropathy profiles to classify members of this 5TM+hairpin repeat fold.

In NaPi-II, the repeat has fewer TM helices, but that repeat contains a reentrant hairpin before the last helix, as in the ST[3] fold, giving a 3TM+hairpin repeat. The truncated helices contribute to a stator domain (47) and therefore may have minimal effect on transport. Indeed, a variety of lengths are observed in the ST[3] class, including a truncation to a 4-TM helix repeat (63).

The low-resolution electron microscopy-based structure of CitS hints that rearrangements of helices are possible within the context of the same fold (47). We therefore questioned whether a model of NaPi-II could be improved by using CitS as a guiding template. However, comparison of the hydropathy plots of the repeats of CitS with those of NaPi-IIa showed significant differences in the region of the re-entrant hairpins and broken helices (Fig. S7). These were reminiscent of differences between profiles of VcINDY and CitS (Fig. S7). In contrast, the hydropathy profiles of NaPi-IIa and VcINDY share more characteristics (Fig. 2 *A*). We therefore conclude that, although the three protein families appear to share a common core fold, VcINDY provides the most suitable available template. Moreover, these comparisons (Fig. S7) provide support for the proposal that a homology model based on VcINDY, despite its modest resolution, provides an important step forward in predicting the architecture and approximate binding regions of NaPi-IIa.

We note that hydropathy profile comparisons are statistically poorly defined, therefore the final sequence alignments were made with quantitative techniques in which detailed sequence and secondary structure profiles represent each repeat. The two strategies converged in their matching of TM segments, and placed conserved residues from NaPi-II at the binding region of VcINDY.

The QSSS repeats are hallmarks of all NaPi-II isoforms from bacteria to human (64) and, according to this model, help coordinate P_i, Na2, and Na3. When we mutated residues that contribute to these predicted coordination sites in RU1 (S164, T195, S196) and RU2 (Q417, S418, and S419), even using very conservative substitutions, transport was either markedly affected or abolished completely. These data, combined with previous evidence implicating N199 (52) and S462 (54), provide strong support for their involvement in substrate coordination. The Cys substitution at S462 in RU2 is well tolerated in all NaPi-II isoforms, however when subjected to thiol modification, cotransport function is inhibited, although cation and P_i binding remain (17,54,61). One scenario to explain this would be that binding of the last Na^+ ion is restricted by having a bulky MTS moiety at this site. In contrast, Cys substitution at N199 in RU1 leads to a >10-fold reduction in the estimated apparent substrate affinities (52), which is consistent with its proposed proximity to both P_i and Na2. The effect of Cys substitution at Q417 in RU2 was much less dramatic (equivalent to ~threefold and twofold increases in $K_{0.5}{}^{Pi}$ and $K_{0.5}{}^{Na}$, respectively; see Fig. 5 in (56)). This smaller deviation from the WT behavior may reflect Q417's proposed proximity to Na3 only (Fig. 4). The possibility of the substrate itself being directly coordinated in part by the cosubstrate, as in the proposed coordination of Na2, Na3, and P_i, and as observed previously for LeuT (20), underscores the notion of strictly coupled transport and offers a molecular basis for the experimentally observed dependence of the apparent affinity constants on the invariant substrate (16,65).

Currently, there is insufficient evidence to locate the binding site of the first Na^+ ion, designated Na1, (*partial reaction* 1 ↔ 2, Fig. 1 *A*). In the electroneutral isoform this ion is hypothesized to interact allosterically with NaPi-IIc and contribute to the overall cooperativity of Na^+ activation, but not to be translocated (17). In contrast, for the electrogenic isoforms (NaPi-IIa and NaPi-IIb) the binding of a Na^+ ion to Na1 to the outward facing conformation (state 1) is critical for conferring electrogenicity to the transport cycle; moreover, in the absence of P_i, this ion is assumed to contribute to the uncoupled leak (66). Our model proposes that P_i is tightly coordinated with 2 Na^+ ions (at sites Na2 and Na3), and together these would constitute the translocated, and effectively electroneutral, complex for both electroneutral and electrogenic isoforms.

The detection of presteady-state charge movements in the absence of external P_i provides indirect evidence that conformational changes occur in response to changes in membrane potential. For six of the seven mutants whose cotransport function was compromised (Table 1, Fig. 5 *A*), we were able to resolve such presteady-state relaxations in the presence of 100 mM Na^+. The detection of these relaxation currents supported the notion that intrinsic charge movements (analogous to gating currents in ion channels (e.g. (67).) and displacement charge associated with the interaction of a Na^+ ion at the postulated Na1 site, most likely still occurred in the mutated constructs. The lack of transport function is therefore consistent with these mutations drastically affecting Na2, Na3, or P_i coordination, events that are common to both electroneutral and electrogenic NaPi-II isoforms. Unfortunately, the small magnitude of the presteady-state relaxations for these dysfunctional mutants precluded more detailed analysis to ascertain whether cation interactions had been altered specifically at Na2 or Na3. Nevertheless, these observations will serve as a basis for more detailed structure-function studies of SLC34 proteins.

In conclusion, we propose a structural model for the architecture of the human, Na^+-coupled phosphate transport protein NaPi-II. Because the predictions of the substrate coordination sites (Fig. 4) are based on a homology model at low sequence similarity, they should be considered hypotheses that will help to guide experiments until more detailed structural data for the SLC34 protein family can be obtained. To our knowledge, the strategy used to define equivalent regions in the template by identifying and separating out the structural repeats is novel and may be applied to model other transporters of as yet unknown architecture. As the proposed model is relevant for all members of the SLC34 family it should also provide an important step in structure-function studies of all SLC34 proteins.

SUPPORTING MATERIAL

Seven figures, supporting data, and references (69–70) are available at http://www.biophysj.org/biophysj/supplemental/S0006-3495(14)00175-1.

Financial support was given by The Dunhill Medical Trust (A.W.), Swiss National Science Foundation (I.C.F.), and the Intramural Research Program of the NIH, NINDS (L.R.F.). We thank Eva Hänsenberger for oocyte preparation.

Author contributions: C.F.F., L.R.F.: bioinformatics, modeling, data analysis; M.P.: bioinformatics, molecular biology, transport assays, data analysis; I.C.F.: data analysis; T.K.: oocyte assays, immunohistochemistry; L.R.F., A.W., and I.C.F.: designed experiments and wrote the paper.

REFERENCES

1. Shroff, R., D. A. Long, and C. Shanahan. 2013. Mechanistic insights into vascular calcification in CKD. *J. Am. Soc. Nephrol.* 24:179–189.
2. Biber, J., N. Hernando, and I. Forster. 2013. Phosphate transporters and their function. *Annu. Rev. Physiol.* 75:535–550.
3. Forster, I. C., N. Hernando, …, H. Murer. 2013. Phosphate transporters of the SLC20 and SLC34 families. *Mol. Aspects Med.* 34:386–395.
4. Sabbagh, Y., H. Giral, …, S. C. Schiavi. 2011. Intestinal phosphate transport. *Adv. Chronic Kidney Dis.* 18:85–90.
5. Biber, J., N. Hernando, …, H. Murer. 2009. Regulation of phosphate transport in proximal tubules. *Pflugers Arch.* 458:39–52.
6. Forster, I., N. Hernando, …, A. Werner. 2011. Phosphate transporters in renal, gastrointestinal, and other tissues. *Adv. Chronic Kidney Dis.* 18:63–76.
7. Beck, L., A. C. Karaplis, …, H. S. Tenenhouse. 1998. Targeted inactivation of Npt2 in mice leads to severe renal phosphate wasting, hypercalciuria, and skeletal abnormalities. *Proc. Natl. Acad. Sci. USA.* 95:5372–5377.
8. Kenny, J., M. M. Lees, …, D. Bockenhauer. 2011. Sotos syndrome, infantile hypercalcemia, and nephrocalcinosis: a contiguous gene syndrome. *Pediatr. Nephrol.* 26:1331–1334.
9. Magen, D., L. Berger, …, K. Skorecki. 2010. A loss-of-function mutation in NaPi-IIa and renal Fanconi's syndrome. *N. Engl. J. Med.* 362:1102–1109.
10. Bergwitz, C., N. M. Roslin, …, H. Juppner. 2006. SLC34A3 mutations in patients with hereditary hypophosphatemic rickets with hypercalciuria predict a key role for the sodium-phosphate cotransporter NaPi-IIc in maintaining phosphate homeostasis. *Am. J. Hum. Genet.* 78:179–192.
11. Corut, A., A. Senyigit, …, A. Tolun. 2006. Mutations in SLC34A2 cause pulmonary alveolar microlithiasis and are possibly associated with testicular microlithiasis. *Am. J. Hum. Genet.* 79:650–656.
12. Forster, I. C., N. Hernando, …, H. Murer. 2012. Phosphate transport kinetics and structure-function relationships of SLC34 and SLC20 proteins. *Curr. Top. Membr.* 70:313–356.
13. Forrest, L. R., R. Krämer, and C. Ziegler. 2011. The structural basis of secondary active transport mechanisms. *Biochim. Biophys. Acta.* 1807:167–188.
14. Forrest, L. R., Y. W. Zhang, …, G. Rudnick. 2008. Mechanism for alternating access in neurotransmitter transporters. *Proc. Natl. Acad. Sci. USA.* 105:10338–10343.
15. Jardetzky, O. 1966. Simple allosteric model for membrane pumps. *Nature.* 211:969–970.
16. Forster, I., N. Hernando, …, H. Murer. 1998. The voltage dependence of a cloned mammalian renal type II Na^+/P_i cotransporter (NaPi-2). *J. Gen. Physiol.* 112:1–18.
17. Ghezzi, C., H. Murer, and I. C. Forster. 2009. Substrate interactions of the electroneutral Na+-coupled inorganic phosphate cotransporter (NaPi-IIc). *J. Physiol.* 587:4293–4307.
18. Forster, I. C., K. Köhler, …, H. Murer. 2002. Forging the link between structure and function of electrogenic cotransporters: the renal type IIa Na^+/P_i cotransporter as a case study. *Prog. Biophys. Mol. Biol.* 80:69–108.
19. Abramson, J., and E. M. Wright. 2009. Structure and function of Na(+)-symporters with inverted repeats. *Curr. Opin. Struct. Biol.* 19:425–432.
20. Yamashita, A., S. K. Singh, …, E. Gouaux. 2005. Crystal structure of a bacterial homologue of Na+/Cl-dependent neurotransmitter transporters. *Nature.* 437:215–223.
21. Forrest, L. R. 2013. Structural biology. (Pseudo-)symmetrical transport. *Science.* 339:399–401.
22. Forrest, L. R., and G. Rudnick. 2009. The rocking bundle: a mechanism for ion-coupled solute flux by symmetrical transporters. *Physiology (Bethesda).* 24:377–386.
23. Khafizov, K., C. Perez, …, L. R. Forrest. 2012. Investigation of the sodium-binding sites in the sodium-coupled betaine transporter BetP. *Proc. Natl. Acad. Sci. USA.* 109:E3035–E3044.
24. Finn, R. D., J. Clements, and S. R. Eddy. 2011. HMMER web server: interactive sequence similarity searching. *Nucleic Acids Res.* 39 (Web Server issue):W29–W37.
25. Edgar, R. C. 2010. Search and clustering orders of magnitude faster than BLAST. *Bioinformatics.* 26:2460–2461.
26. Liu, Y., B. Schmidt, and D. L. Maskell. 2010. MSAProbs: multiple sequence alignment based on pair hidden Markov models and partition function posterior probabilities. *Bioinformatics.* 26:1958–1964.
27. Stamm, M., R. Staritzbichler, …, L. R. Forrest. 2013. Alignment of helical membrane protein sequences using AlignMe. *PLoS ONE.* 8:e57731.
28. Remmert, M., A. Biegert, …, J. Soding. 2011. HHblits: lightning-fast iterative protein sequence searching by HMM-HMM alignment. *Nat. Methods.* 9:173–175.
29. Söding, J. 2005. Protein homology detection by HMM-HMM comparison. *Bioinformatics.* 21:951–960.
30. Altschul, S. F., T. L. Madden, …, D. J. Lipman. 1997. Gapped BLAST and PSI-BLAST: a new generation of protein database search programs. *Nucleic Acids Res.* 25:3389–3402.
31. Kelley, L. A., and M. J. Sternberg. 2009. Protein structure prediction on the Web: a case study using the Phyre server. *Nat. Protoc.* 4:363–371.
32. Margelevicius, M., M. Laganeckas, and C. Venclovas. 2010. COMA server for protein distant homology search. *Bioinformatics.* 26:1905–1906.
33. Šali, A., and T. L. Blundell. 1993. Comparative protein modelling by satisfaction of spatial restraints. *J. Mol. Biol.* 234:779–815.
34. Ashkenazy, H., E. Erez, …, N. Ben-Tal. 2010. ConSurf 2010: calculating evolutionary conservation in sequence and structure of proteins and nucleic acids. *Nucleic Acids Res.* 38 (Web Server issue):W529–W533.
35. Ray, A., E. Lindahl, and B. Wallner. 2010. Model quality assessment for membrane proteins. *Bioinformatics.* 26:3067–3074.

36. Laskowski, R. A., M. W. Macarthur, …, J. M. Thornton. 1993. PROCHECK - a program to check the stereochemical quality of protein structures. *J. Appl. Cryst.* 26:283–291.

37. Bossi, E., M. S. Fabbrini, and A. Ceriotti. 2007. Exogenous protein expression in *Xenopus* oocytes: basic procedures. *Methods Mol. Biol.* 375:107–131.

38. Andrini, O., A. K. Meinild, …, I. C. Forster. 2012. Lithium interactions with Na+-coupled inorganic phosphate cotransporters: insights into the mechanism of sequential cation binding. *Am. J. Physiol. Cell Physiol.* 302:C539–C554.

39. Köhler, K., I. C. Forster, …, H. Murer. 2002. Transport function of the renal type IIa $Na^{+}/P_{(i)}$ cotransporter is codetermined by residues in two opposing linker regions. *J. Gen. Physiol.* 120:693–705.

40. Mancusso, R., G. G. Gregorio, …, D. N. Wang. 2012. Structure and mechanism of a bacterial sodium-dependent dicarboxylate transporter. *Nature.* 491:622–626.

41. Saier, Jr., M. H., and I. T. Paulsen. 2000. Whole genome analyses of transporters in spirochetes: *Borrelia burgdorferi* and *Treponema pallidum. J. Mol. Microbiol. Biotechnol.* 2:393–399.

42. Bergeron, M. J., B. Clémençon, …, D. Markovich. 2013. SLC13 family of Na^{+}-coupled di- and tri-carboxylate/sulfate transporters. *Mol. Aspects Med.* 34:299–312.

43. Lolkema, J. S., and D. J. Slotboom. 2003. Classification of 29 families of secondary transport proteins into a single structural class using hydropathy profile analysis. *J. Mol. Biol.* 327:901–909.

44. Crisman, T. J., S. Qu, …, L. R. Forrest. 2009. Inward-facing conformation of glutamate transporters as revealed by their inverted-topology structural repeats. *Proc. Natl. Acad. Sci. USA.* 106:20752–20757.

45. Ressl, S., A. C. Terwisscha van Scheltinga, …, C. Ziegler. 2009. Molecular basis of transport and regulation in the Na(+)/betaine symporter BetP. *Nature.* 458:47–52.

46. Khafizov, K., R. Staritzbichler, …, L. R. Forrest. 2010. A study of the evolution of inverted-topology repeats from LeuT-fold transporters using AlignMe. *Biochemistry.* 49:10702–10713.

47. Kebbel, F., M. Kurz, …, H. Stahlberg. 2013. Structure and substrate-induced conformational changes of the secondary citrate/sodium symporter CitS revealed by electron crystallography. *Structure.* 21:1243–1250.

48. Faraldo-Gómez, J. D., and L. R. Forrest. 2011. Modeling and simulation of ion-coupled and ATP-driven membrane proteins. *Curr. Opin. Struct. Biol.* 21:173–179.

49. Radanovic, T., S. M. Gisler, …, H. Murer. 2006. Topology of the type IIa Na+/P(i) cotransporter. *J. Membr. Biol.* 212:41–49.

50. Karlin, A., and M. H. Akabas. 1998. Substituted-cysteine accessibility method. *Methods Enzymol.* 293:123–145.

51. Ehnes, C., I. C. Forster, …, H. Murer. 2004. Structure-function relations of the first and fourth extracellular linkers of the type IIa Na^{+}/P_{i} cotransporter: II. Substrate interaction and voltage dependency of two functionally important sites. *J. Gen. Physiol.* 124:489–503.

52. Köhler, K., I. C. Forster, …, H. Murer. 2002. Identification of functionally important sites in the first intracellular loop of the NaPi-IIa cotransporter. *Am. J. Physiol. Renal Physiol.* 282:F687–F696.

53. Lambert, G., I. C. Forster, …, H. Murer. 2001. Cysteine mutagenesis reveals novel structure-function features within the predicted third extracellular loop of the type IIa $Na^{(+)}/P_{(i)}$ cotransporter. *J. Gen. Physiol.* 117:533–546.

54. Lambert, G., M. Traebert, …, H. Murer. 1999. Studies on the topology of the renal type II NaPi-cotransporter. *Pflugers Arch.* 437:972–978.

55. Virkki, L. V., I. C. Forster, …, H. Murer. 2005. Functionally important residues in the predicted $3^{(rd)}$ transmembrane domain of the type IIa sodium-phosphate co-transporter (NaPi-IIa). *J. Membr. Biol.* 206:227–238.

56. Ehnes, C., I. C. Forster, …, H. Murer. 2004. Structure-function relations of the first and fourth predicted extracellular linkers of the type IIa Na^{+}/Pi cotransporter: I. Cysteine scanning mutagenesis. *J. Gen. Physiol.* 124:475–488.

57. Virkki, L. V., H. Murer, and I. C. Forster. 2006. Mapping conformational changes of a type IIb Na+/Pi cotransporter by voltage clamp fluorometry. *J. Biol. Chem.* 281:28837–28849.

58. Ghezzi, C., A. K. Meinild, …, I. C. Forster. 2011. Voltage- and substrate-dependent interactions between sites in putative re-entrant domains of a Na(+)-coupled phosphate cotransporter. *Pflugers Arch.* 461:645–663.

59. Reference deleted in proof.

60. Lambert, G., I. C. Forster, …, H. Murer. 1999. Properties of the mutant Ser-460-Cys implicate this site in a functionally important region of the type IIa $Na^{(+)}/P_{(i)}$ cotransporter protein. *J. Gen. Physiol.* 114:637–652.

61. Virkki, L. V., H. Murer, and I. C. Forster. 2006. Voltage clamp fluorometric measurements on a type II Na^{+}-coupled P_{i} cotransporter: shedding light on substrate binding order. *J. Gen. Physiol.* 127:539–555.

62. Pedersen, B. P., H. Kumar, …, R. M. Stroud. 2013. Crystal structure of a eukaryotic phosphate transporter. *Nature.* 496:533–536.

63. ter Horst, R., and J. S. Lolkema. 2012. Membrane topology screen of secondary transport proteins in structural class ST[3] of the MemGen classification. Confirmation and structural diversity. *Biochim. Biophys. Acta.* 1818:72–81.

64. Werner, A., and R. K. Kinne. 2001. Evolution of the Na-P_{i} cotransport systems. *Am. J. Physiol.* 280:R301–R312.

65. Virkki, L. V., I. C. Forster, …, H. Murer. 2005. Substrate interactions in the human type IIa sodium-phosphate cotransporter (NaPi-IIa). *Am. J. Physiol. Renal Physiol.* 288:F969–F981.

66. Andrini, O., C. Ghezzi, …, I. C. Forster. 2008. The leak mode of type II Na(+)-P(i) cotransporters. *Channels (Austin).* 2:346–357.

67. Bezanilla, F. 2008. How membrane proteins sense voltage. *Nat. Rev. Mol. Cell Biol.* 9:323–332.

68. Patti, M., C. Ghezzi, and I. C. Forster. 2013. Conferring electrogenicity to the electroneutral phosphate cotransporter NaPi-IIc (SLC34A3) reveals an internal cation release step. *Pflugers Arch.* 465:1261–1279.

69. Hessa, T., H. Kim, …, G. von Heijne. 2005. Recognition of transmembrane helices by the endoplasmic reticulum translocon. *Nature.* 433:377–381.

70. Custer, M., M. Lotscher, …, B. Kaissling. 1994. Expression of Na-P(i) cotransport in rat kidney: localization by RT-PCR and immunohistochemistry. *Am. J. Physiol.* 266:F767–F774.

Biophysical Journal Volume 108 May 2015 2465–2480

Article

Identification of the First Sodium Binding Site of the Phosphate Cotransporter NaPi-IIa (SLC34A1)

Cristina Fenollar-Ferrer,[1] Ian C. Forster,[2,*] Monica Patti,[2] Thomas Knoepfel,[2] Andreas Werner,[3,*] and Lucy R. Forrest[1,*]

[1]Computational Structural Biology Section, Porter Neuroscience Research Center, National Institute of Neurological Disorders and Stroke, National Institutes of Health, Bethesda, Maryland; [2]Institute of Physiology and Zurich Center for Integrative Human Physiology, University of Zürich, Zürich, Switzerland; and [3]Institute for Cell and Molecular Biosciences, Epithelial Research Group, University of Newcastle upon Tyne, Newcastle upon Tyne, United Kingdom

ABSTRACT Transporters of the SLC34 family (NaPi-IIa,b,c) catalyze uptake of inorganic phosphate (P_i) in renal and intestinal epithelia. The transport cycle requires three Na^+ ions and one divalent P_i to bind before a conformational change enables translocation, intracellular release of the substrates, and reorientation of the empty carrier. The electrogenic interaction of the first Na^+ ion with NaPi-IIa/b at a postulated Na1 site is accompanied by charge displacement, and Na1 occupancy subsequently facilitates binding of a second Na^+ ion at Na2. The voltage dependence of cotransport and presteady-state charge displacements (in the absence of a complete transport cycle) are directly related to the molecular architecture of the Na1 site. The fact that Li^+ ions substitute for Na^+ at Na1, but not at the other sites (Na2 and Na3), provides an additional tool for investigating Na1 site-specific events. We recently proposed a three-dimensional model of human SLC34a1 (NaPi-IIa) including the binding sites Na2, Na3, and P_i based on the crystal structure of the dicarboxylate transporter VcINDY. Here, we propose nine residues in transmembrane helices (TM2, TM3, and TM5) that potentially contribute to Na1. To verify their roles experimentally, we made single alanine substitutions in the human NaPi-IIa isoform and investigated the kinetic properties of the mutants by voltage clamp and ^{32}P uptake. Substitutions at five positions in TM2 and one in TM5 resulted in relatively small changes in the substrate apparent affinities, yet at several of these positions, we observed significant hyperpolarizing shifts in the voltage dependence. Importantly, the ability of Li^+ ions to substitute for Na^+ ions was increased compared with the wild-type. Based on these findings, we adjusted the regions containing Na1 and Na3, resulting in a refined NaPi-IIa model in which five positions (T200, Q206, D209, N227, and S447) contribute directly to cation coordination at Na1.

INTRODUCTION

Inorganic phosphate (P_i) levels in humans are tightly regulated to enable growth and metabolism and to prevent pathologies related to vascular calcification. Na^+-coupled P_i transporters of the SLC34 solute carrier family (NaPi-II) are responsible for maintaining whole-body P_i homeostasis and mediate epithelial transport of P_i in intestine and kidney (1–3). Three isoforms catalyze the uphill transport of divalent phosphate (HPO_4^{2-}) in the presence of a downhill Na^+ electrochemical gradient. Electrogenic isoforms (NaPi-IIa and NaPi-IIb) are characterized by a transport stoichiometry (Na^+:HPO_4^{2-}) of 3:1 and show voltage-dependent cotransport rates, with one net positive charge translocated per cycle. In contrast, the stoichiometry of the electroneutral isoform (NaPi-IIc) is 2:1, its transport kinetics show no voltage dependence, and no net charge is translocated. This functional difference is postulated to arise because NaPi-IIc does not release the first-bound Na^+ ion to the intracellular medium (4).

The interaction of one Na^+ ion with the empty carrier is thought to be the critical step in initiating the transport cycle for both electrogenic and electroneutral isoforms (4,5). This leads to the cooperative binding of a second Na^+ ion, followed by HPO_4^{2-} and a third Na^+ ion before translocation occurs (Fig. 1). For the electrogenic NaPi-IIa/b transporters, the voltage dependence of the overall transport kinetics can be satisfactorily explained by assuming that only the empty carrier reorientation (partial reaction $0 \leftrightarrow 1$; Fig. 1), and the cation-carrier interactions between the first Na^+ ion and the Na1 site are voltage dependent (partial reactions $1 \leftrightarrow 2$, $0 \leftrightarrow 6$; Fig. 1). By implication, these partial reactions must therefore involve charge displacements that are sensitive to the transmembrane (TM) electric field. Indeed, when rapid changes in membrane potential are applied to a membrane containing a large population of NaPi-IIa/b, charge movements manifesting as so-called presteady-state relaxations are readily detected. In the absence of external cations, these presteady-state relaxations, which are analogous to the gating charges observed in ion channel electrophysiology,

---

Submitted December 23, 2014, and accepted for publication March 17, 2015.

*Correspondence: lucy.forrest@nih.gov or iforster@access.uzh.ch or andreas.werner@newcastle.ac.uk

Cristina Fenollar-Ferrer and Ian C. Forster contributed equally to this work.

Andreas Werner and Lucy R. Forrest contributed equally to this work.

Editor: Joseph Mindell.

0006-3495/15/05/2465/16 $2.00

http://dx.doi.org/10.1016/j.bpj.2015.03.054

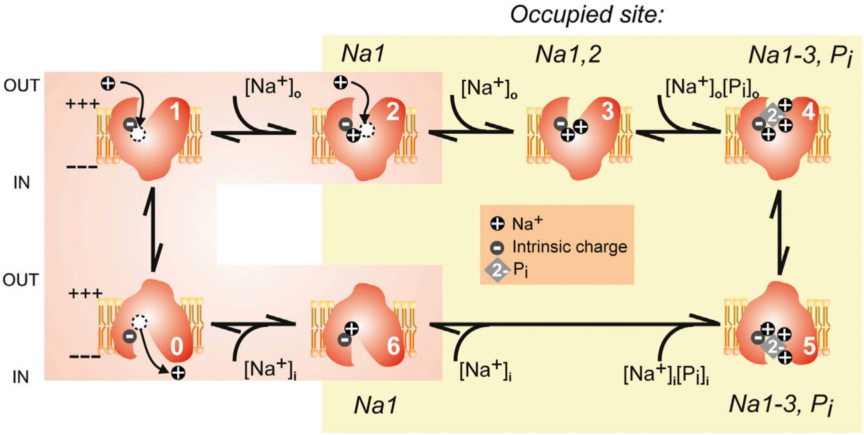

FIGURE 1 Kinetic scheme for the electrogenic NaPi-IIa/b isoforms. Schematics represent the conformational states identified by previous functional analyses to show the occupancy of the proposed substrate-binding sites. The physiologically relevant cotransport cycle (clockwise, starting from state 0) involves a voltage-dependent reorientation of the unloaded carrier (state 0) to state 1 (assuming a hyperpolarized membrane potential), and movement of a single Na^+ ion to the proposed Na1 site (state 2), followed by the cooperative interaction of a second Na^+ ion before divalent P_i and a final Na^+ ion, resulting in occupancy of the Na2-P_i-Na3 sites (state 4). A major translocation event then occurs (transition 4–5) and substrates can be released to the cytosol (transition 5–6). The last Na^+ unbinding event (transition 6–0) effectively frees the empty carrier intrinsic charge to allow reorientation of the empty carrier to state 1 under the influence of a hyperpolarizing TM potential, in readiness for the next cycle. For the electroneutral NaPi-IIc, the empty carrier reorientation is voltage independent and no detectable charge displacement is associated with any of the partial reactions.

arise from charges intrinsic to the protein, and additional charge is detected when cations are present (5).

For the electroneutral NaPi-IIc transporter, the order of substrate interactions remains the same, with two Na^+ ions proposed to interact before P_i. However, it is thought that the first Na^+ ion is not translocated and thus does not contribute to the transport stoichiometry. Moreover, unlike NaPi-IIa/b, the binding of the first Na^+ ion to NaPi-IIc is not electrogenic, meaning that it does not lead to detectable presteady-state relaxations, yet a cooperative interaction of two Na^+ ions still occurs (4). However, if a charged aspartic acid residue that is found in all electrogenic isoforms (D224 in hNaPi-IIa) is replaced by a glycine at the equivalent site in the electroneutral NaPi-IIc, the P_i cotransport becomes electroneutral (6). The converse substitution in NaPi-IIc restores electrogenic behavior, including presteady-state relaxations (7). This behavior implicates D224 in conferring voltage dependence to the transport cycle and potentially coordinating a Na^+ ion at Na1. Moreover, kinetic studies of the electroneutral construct with restored electrogenicity (AAD-IIc) (8) established that whereas cation interactions originating from the external medium remained electroneutral, electrogenicity appeared to arise from the empty carrier and from cytosolic Na^+ ion interactions (partial reactions 6↔0 and 0↔1; Fig. 1). Thus, D224 appears to be intimately associated with occupancy of Na1 from either side of the membrane.

Taking into account the highly conserved inverted repeat symmetry of all NaPi-II isoforms, we recently identified similar repeats in the x-ray crystallographic structure of a Na^+-dicarboxylate transporter, VcINDY (9), which allowed us to generate a homology model of the human NaPi-IIa protein based on VcINDY in an outward-facing conformation (10). Only one Na^+ ion site was identified in the 3.2 Å VcINDY crystal structure, and a second ion position was proposed based on pseudo-symmetry considerations (9), although, like NaPi-IIa/b, transport mediated by VcINDY is electrogenic, and the Na^+/citrate stoichiometry is most likely 3:1 (11). Our structural model predicts sites for P_i and two Na^+ ions similar to those in VcINDY, and when these are occupied, the model therefore corresponds to state 4 in the NaPi-IIa transport cycle without considering Na1 occupancy (Fig. 1). Importantly, mutations at the proposed Na2, Na3, and P_i sites abolished cotransport function, and the observation of Na^+-dependent, presteady-state relaxations suggested that the hypothesized Na1 interaction still occurred (10).

Here, we investigate the Na1-binding site, whose position in the published structural model was not previously considered (10). We focus on eight residues close to D224, which, as mentioned above, has been identified as a critical determinant of electrogenicity and transport stoichiometry (6–8,12). We noted that in the model, D224 is located at the cytoplasmic end of TM3, i.e., deeper in the protein than the previously identified Na2-P_i-Na3 substrate site. This deep position would be consistent with a site that could allow cation interactions also from the cytosol and would be similar to the position of the Na1 site in the Na^+-dependent aspartate transporter Glt_{Ph} (13). Although it is not conclusively involved, this region appeared to be a reasonable starting point for identifying Na1-binding-site residues. Site-directed mutagenesis and functional analysis, including pre-steady state kinetics and Li^+ substitution experiments, confirmed the functional relevance of four of the eight proposed amino acids in contributing to the Na1 site in NaPi-II transporters. Refinements to the model based on these data indicate how they may be arranged to form the site.

MATERIALS AND METHODS

Molecular biology

Mutations causing single amino acid changes were introduced into human NaPi-IIa cDNA cloned into an oocyte expression vector using the

QuikChange Lightning Site-Directed Mutagenesis Kit (Agilent Technologies). Downscaled reactions were run according to the supplier's instructions and primers were purchased from IDT Biotech (Integrated DNA Technologies). All mutations were confirmed by Sanger sequencing (Genevision, Newcastle, UK). The plasmids were linearized using *Xba*I, and RNA was transcribed using T3 RNA polymerase and the Message Machine kit (Ambion/ Life Technologies). The RNA was assessed by agarose gel electrophoresis and quantified by UV spectroscopy.

Oocytes

Oocytes were harvested from *Xenopus laevis* frogs (*Xenopus* Express France, Vernassal, France) following standard procedures according to Swiss Cantonal and Federal legislation. Defolliculated cells were incubated in modified Barth's solution containing (in mM) 88 NaCl, 1 KCl, 0.41 $CaCl_2$, 0.82 $MgSO_4$, 2.5 $NaHCO_3$, 2 $Ca(NO_3)_2$, and 7.5 HEPES, adjusted to pH 7.5 with TRIS, and supplemented with antibiotics (doxycycline and gentamicin, 5 mg/l). Oocytes were injected with 50 nl of RNA (0.2 μg/μl) and kept in modified Barth's solution at 18°C for 3–5 days before analysis.

Solutions

The superfusing solutions contained (in mM) 100Na (100 NaCl, 2 KCl, 1.8 $CaCl_2$, 1 $MgCl_2$, 10 HEPES, pH 7.4 adjusted with TRIS) or 100Ch (the same as for the 100 Na solution but with equimolar replacement of NaCl with choline Cl). For intermediate Na^+ concentrations, 100Na and 100Ch were appropriately mixed to maintain the same osmolarity. For the lithium-containing solutions (100Li and 50Na50Li), NaCl was replaced equimolarly with LiCl to give the required concentration. Inorganic phosphate (P_i) was added to the superfusate from 1 M K_2HPO_4 and KH_2PO_4 stocks that were mixed to give pH 7.4, and further diluted in H_2O to give the required test concentration. All standard reagents were obtained from either Sigma-Aldrich or Fluka (Buchs, Switzerland).

Functional assays

Radioisotope uptake assays were performed according to standard procedures as described elsewhere (14) using 100Na solution and 1 mM cold P_i to which $^{32}P_i$ (specific activity 10 mCi/mmol P_i) was added. Standard two-electrode voltage-clamp (TEVC) hardware was used for electrophysiology (Turbo TEC-10CX; NPI, Tamm, Germany) and controlled using pClamp 10 software (Molecular Devices, Sunnyvale, CA). Clampfit (Molecular Devices, Sunnyvale, CA) and Prism version 3.0, 5.0 (Graphpad Software, San Diego, CA) were used for postacquisition analysis. The protocol for determining the steady-state P_i activation used voltage steps from the standard holding potential ($V_h = -60$ mV) to voltages in the range of -160 mV to $+40$ mV. Presteady-state current relaxations were typically quantified for voltages in the range of $-180 \text{ mV} \le V \le 80$ mV with four signal averages. Current relaxations were typically fitted with a multiple exponential function. The fastest component represented the linear capacitive charging of the oocyte membrane (typically 0.35–0.6 ms, depending on the oocyte). The slower component (typically >3 ms) was extrapolated to the peak of the capacitive transient, at which time we assumed the membrane was $>90\%$ charged, and numerically integrated to obtain the charge moved (Q) for a step from the holding potential to the test potential. The charge-voltage (Q-V) data were fitted with a Boltzmann function of the form given by Eq. 1:

$$Q = Q_{hyp} + Q_{\max}\big/\left(1 + \exp(z\,e(V_{0.5} - V)/kT)\right), \quad (1)$$

where $V_{0.5}$ is the voltage at which the charge is distributed equally between two hypothetical states, z is the apparent valency of an equivalent charge that moves through the whole of the membrane field, $Q_{\max}$ is the total mobile charge available, Q_{hyp} is the charge of the hyperpolarizing limit and is a function of V_h, and e, k, and T have their usual meanings.

Western blotting and immunocytochemistry

Oocytes were fixed in 3% paraformaldehyde and sections were blocked in 1% BSA/PBS for 15 min at room temperature. NaPi-IIa antibody raised against a COOH-terminal peptide was diluted 1/400 in 0.02% Na-azide/ PBS and slides were incubated overnight at 4°C. Sections were washed twice with hypertonic PBS (PBS with additional 18 g NaCl/L) and once in PBS for 5 min. Sections were incubated with secondary donkey anti-rabbit Alexa-488 antibody (Invitrogen) for 1 h, washed with PBS, and mounted with Glycergel (DAKO). Fluorescence was detected using a fluorescence microscope (Leica CTR600).

Bioinformatics

Sequences of NaPi-II transporters were identified from the NCBI nr20 database (dated February 22, 2013) using HHblits (15). Sequence conservation among the top 50 nonredundant sequences was analyzed using the Weblogo v3 webserver (16).

Structural modeling

In our previous work, we built a homology model of human NaPi-IIa (10) using a structure of VcINDY (9) (PDB ID: 4F35) as a template. In that work, we identified VcINDY as a possible template, albeit with a low confidence, using the HHpred server. We obtained further evidence of their fold similarity by comparing the individual repeats of VcINDY and NaPi-IIa using HHalign and AlignMe (either in PST or PS mode), indicating similarities with the region of the binding site of VcINDY, which was aligned to the conserved QSSS motif of NaPi-IIa (10). We obtained the same result when we aligned the family-averaged hydropathy profiles of the individual repeats using AlignMe (10). Here, the published homology model of human NaPi-IIa was refined in two stages, involving first TM2b and then TM5-6. In each stage, the alignment between NaPi-II and VcINDY was adjusted in regions with low scores according to ProQM analysis (see below) and/ or to be consistent with the experimental evidence. In addition, helical constraints were introduced according to secondary structure predictions (10) for residues 202–205 (TM2b), 217–223 (TM3), 440–444, 448–452 (TM5a), 455–456, 461–462 (TM5b), and 493–505 (TM6).

The human NaPi-IIa model containing residues 97–249 and 346–505 (excluding the long extracellular loop, TM7, TM8, and both cytoplasmic terminal domains) was built using Modeller v9.12 (17), alignments were manipulated using Jalview (18), and models were assessed using Procheck (19) as a measure of the chemical fidelity of bonds and angles. ProQM (20) was used to quantify the agreement of the structural model with sequence conservation, secondary structure predictions, and TM predictions for individual residues, the entire model, and the template.

First, to position the side chains of residues Q206, D209, R210, and N227 in or close to the Na1-binding site according to the experimental data, we progressively adjusted the alignment of residues 202–214 in TM2b relative to the VcINDY template by one position at a time. We monitored agreement with the experiments by using the distance between the Cα atom of N227 and the Cα atom of Q206, D209, or R210, as well as the angle between the Cα atom of N227 and the C$\alpha-$Cδ bond of Q206, the C$\alpha-$Cγ bond of D209, or the C$\alpha-$Cζ bond of R210. A shift of five residues relative to the initial model resulted in the optimal arrangement of these residues to form the putative Na1 site (Table S1 in the Supporting Material).

Second, we adjusted the alignment of TM5 and TM6 progressively until we obtained a configuration that optimally positioned S447 proximal to and oriented toward Q206, and at the same time positioned T451 close to S417 near the Na2-P_i-Na3 site (Table S2). We monitored this adjustment using two C$\alpha-$Cα distances (i.e., between S417 and T451, and between S447 and Q206) and two angles (i.e., between the Cα atom of S419 and the Cα−Cδ bond of T451, and between the Cα atom of S447 and the Cα−Cγ bond of Q206).

In the refined alignment, the percentage of identical residues between the template and model was ~14% in repeat unit 1 (RU1) and ~8% in repeat unit 2 (RU2). The expected accuracy of a homology model with this level of sequence identity to the template is 1.5–4 Å in the Cα positions, assuming the correct alignment (21). In a final modeling stage, three Na$^+$ ions and a P$_i$ substrate were included. Harmonic upper-bound distance restraints of 3.3 Å were imposed between the Na$^+$ ion at Na1 and side-chain O atoms of residues T200, Q206, D209, N227, and S447; the Na$^+$ ion at Na2 and side-chain O atoms of residues S164, T195, S196, N199, and substrate P$_i$; the Na$^+$ ion at Na3 and side-chain O atoms of residues Q417, S418, S419, T451, and T454; and the O atoms of P$_i$ and side-chain O atom of residue S164, or side-chain N atom of N199. We selected the model with the lowest Modeller probability distribution function (Molpdf) score out of a set of 2000 models, i.e., the model that was in best agreement with all of the input constraints. In this model, only 0.7% of the residues are in disallowed regions (I142 and L143), 1.8% are in generously allowed regions of the Ramachandran plot, and all of these residues are located in loop regions away from the binding sites and helix packing interfaces. The total ProQM score increased from 0.555 in the published model (10) to 0.572 after the refinements in TM2 and TM5-6. ProQM scores can range from 0 to 1, with 1 being the most membrane-protein like, although typical structures have ProQM scores of ~0.7 and the truncated template structure has a ProQM score of 0.643. The refined model is provided in the Supporting Material as Model S1.

RESULTS

A putative Na1-binding region close to D224 in TM3

The universe of possible binding sites for Na$^+$ in NaPi-IIa is large because the core of the protein is littered with serine, threonine, asparagine, and glutamine residues that are good candidates for cation coordination (22). Therefore, to identify Na1, we narrowed down the options by focusing on the region near D224 (see above) (6–8,12). Additional support for the importance of this region comes from the reported role of a position one turn away on TM3, namely, N227, mutations of which led to impaired substrate affinities that could be attributable to altered Na1 interactions (6) (Fig. 2).

The most reliable aspects of the published NaPi-IIa model are its overall fold, the positioning of the residues in TM3, and the regions around the Na2, Na3, and P$_i$ sites, especially the helical hairpins (HP1 and HP2), all of which agree well with various experimental data (10). However, because of the low sequence identity between NaPi-IIa and its template, VcINDY (~10%), other predicted regions that to date have not been validated in detail experimentally, such as the more peripheral helices, may be less reliable. Relatively minor adjustments to the underlying sequence alignment between NaPi-IIa and VcINDY could shift the orientation and vertical positioning of specific residues in the model while still maintaining the overall fold. Therefore, we broadened our search for putative Na1-site residues to any position along the cytoplasmic halves of the two helices that are adjacent to TM3 in the published model, i.e., TM2b and TM5a (10) (Fig. 2). This strategy identified nine hydroxylic, carboxylic, or amide-containing residues that could potentially contribute to Na1, namely, T200, Q206, D209, and T211 in TM2; N227 in TM3; and S447, N448, T451, and T454 in TM5 (Fig. 2). We then individually mutated these residues to alanine or to less severe substitutions (Q206N, D209E, and N227Q), to examine their impact on transport function (Table 1). Furthermore, we also included R210 from TM2 in our mutagenesis study because as a positively charged residue in a putative cation-binding region, it may play a critical functional role, as suggested by previous work (10).

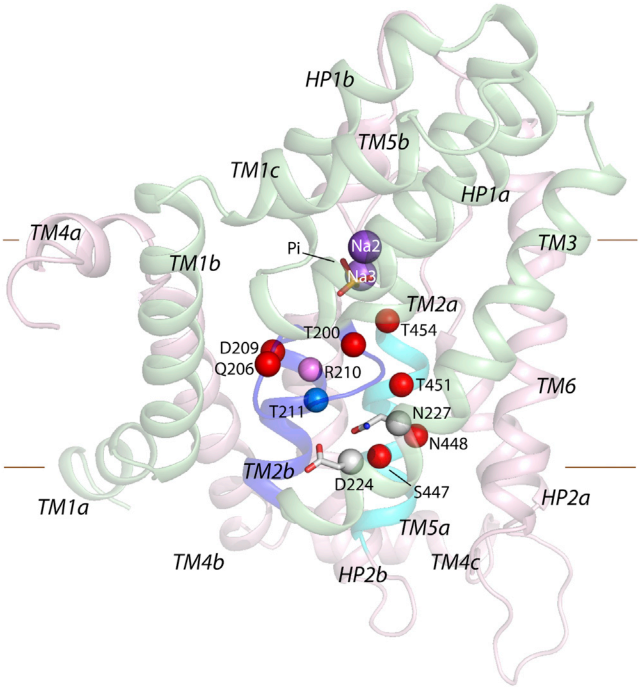

FIGURE 2 Candidate Na1-binding-site residues in a published structural model of human NaPi-IIa based on VcINDY. The model included two Na$^+$ ions (*purple spheres*) and one P$_i$ anion (*yellow* and *red sticks*), and was generated using the alignment described previously (10). The protein backbone is represented as cartoon helices with RU1 colored green and RU2 in pink, and is viewed from along the plane of the membrane from the face furthermost from the dimer interface in the template. TM2b and TM5a are colored blue and cyan, respectively. Candidate Na1-binding-site residues are represented as spheres at their Cα positions. Residues whose mutation had an effect on transport activity, apparent affinities for substrate or ions, or steady-state currents are colored red or pink. The residue whose mutation did not alter any of these parameters (T211) is colored blue. Residues D224 and N227 are colored gray, and their side chain and Cα atoms are represented as sticks and spheres, respectively.

Functional characterization: steady-state response to P$_i$

We expressed the mutated transporters in *Xenopus laevis* oocytes and first screened them for electrogenic function using a TEVC. Seven constructs with mutations in TM2 and one in TM5 (Table 1) gave detectable responses to test applications of 1 mM P$_i$ (in the presence of 100 mM Na$^+$ (100Na

TABLE 1 Overview of human NaPi-IIa constructs

		Expression		Transport Function		Kinetics	
	Construct	WB	IC	$^{32}P_i$	TEVC	Steady State	Pre-Steady State
Transmembrane Segment	WT	+	+	+	1.0	+	+
TM2	T200A	+	+	+	0.14 ± 0.02	+	−
	Q206A	ND	ND	ND	0.35 ± 0.05	+	+
	Q206N	ND	ND	ND	0.79 ± 0.09	+	+
	D209A	ND	ND	ND	0.35 ± 0.05	+	+
	D209E	ND	ND	ND	1.11 ± 0.14	+	+
	R210A	ND	ND	+	0.37 ± 0.04	+	+
	T211A	ND	ND	ND	1.14 ± 0.01	+	+
TM3	N227A	+	+	ND	ND	−	ND
	N227Q[a]	+	ND	+	+	+	ND
TM5	S447A	+	+	+	0.58 ± 0.13	+	+
	N448A	+	+	−	−	−	−
	T451A	+	+	−	−	−	+
	T454A	+	+	−	−	−	+

For TEVC transport function, values indicate mean ± SE fraction of P_i-induced current at -60 mV relative to WT for $n > 5$ cells per construct. WB, western blot (total oocyte lysate); IC, immunocytochemistry; +, experimental verification; −, undetected/unresolved; ND, not done.

[a] See Virkki et al. (6).

solution)) in the form of an inwardly directed change in the holding current (typically with absolute P_i-induced currents in the range of -20 nA to -150 nA) when voltage clamped at -50 mV. The response to 1 mM P_i (at -60 mV) relative to the wild-type (WT) response varied among constructs (Table 1) and the largest deviation was documented for T200A, which displayed only 14% of the WT response. These changes in the magnitude of the response could result from reduced surface expression, altered kinetics, or both. In the case of T200A, the membrane staining was comparable to that observed for the other constructs, suggesting that membrane expression was not compromised (Fig. S1). Oocytes injected with the cRNA coding for N227A (TM3) developed leaky membranes 2–3 days after injection, which precluded a detailed functional analysis. Three mutants with substitutions in TM5 (N448A, T451A, and T454A) showed no P_i-induced inward currents and were further assayed for ^{32}P uptake (to test for the possibility of electroneutral transport) and subjected to presteady-state assays (to detect charge displacements associated with the empty carrier and cation movements), western blotting, and immunocytochemistry (Table 1). For these constructs, immunocytochemistry confirmed that in each case the protein was expressed in the membrane (Fig. S1), although the uptake data for these mutants were indistinguishable from those obtained for noninjected control oocytes (Fig. S2).

We further characterized the functional mutants by measuring the P_i-dependent change in holding current (I_{Pi}) as a function of membrane potential under four different superfusing conditions (100Na + 1 mM P_i, 100Na + 0.1 mM P_i, 50Na + 1 mM P_i, and 50Na50Li + 1 mM P_i) and compared their behavior with that of the WT (Figs. 3 and 4). Mutations affecting the architecture of Na1 were expected to have significant consequences for the current-voltage (*I-V*) relation and/or the sensitivity to Li^+, and the superfusion conditions were chosen to best highlight deviations in these properties from WT behavior. Data were normalized to the response to 1 mM P_i in 100Na at -100 mV for each construct to aid comparison. For the WT, I_{Pi} with 100Na + 0.1 mM P_i, 50 Na^+1 mM P_i, and 50Na50Li + 1 mM P_i was ~50% of the response in 100Na + 1 mM P_i at all membrane potentials in the test range (-160 mV to +40 mV; Fig. 3, *upper left*) and similar behavior was found for mutant T211A (Fig. 3, *lower center*), which suggested that this position is not a critical determinant of the kinetic profile.

In contrast, all other functional mutants showed deviations from the WT profile (i.e., altered voltage dependence and relative changes in I_{Pi} for the different superfusion conditions), and these deviations were unique for each mutation position. Moreover, the form of the changed *I-V* profiles depended on the type of substitution, as can be readily seen by comparing Q206A with Q206N, or D209A with D209E. Whereas the alanine substitution at Q206 resulted in a marginal change in the response to 100Na + 1 mM P_i, the more conservative Q→N substitution significantly altered the voltage dependence, which became more curvilinear, and concomitantly increased the response when Li^+ ions were substituted for 50% of the external Na^+. In contrast, the alanine substitution of D209 caused comparable changes to Q206N, whereas the conservative D→E substitution at 209 had a less dramatic effect on the electrogenic profile. Interestingly, like D209A and Q206N in TM2, the only mutant in TM5 (S447A) that showed cotransport (I_{Pi}; Fig. 3) and ^{32}P uptake (Fig. S2) also showed a curvilinear relationship in response to 1 mM P_i. However, for the other superfusing conditions, especially 50Na50Li, its response pattern was dissimilar to that of D209A and Q206N.

These qualitative comparisons between the WT and mutant *I-V* profiles revealed that the mutagenesis had

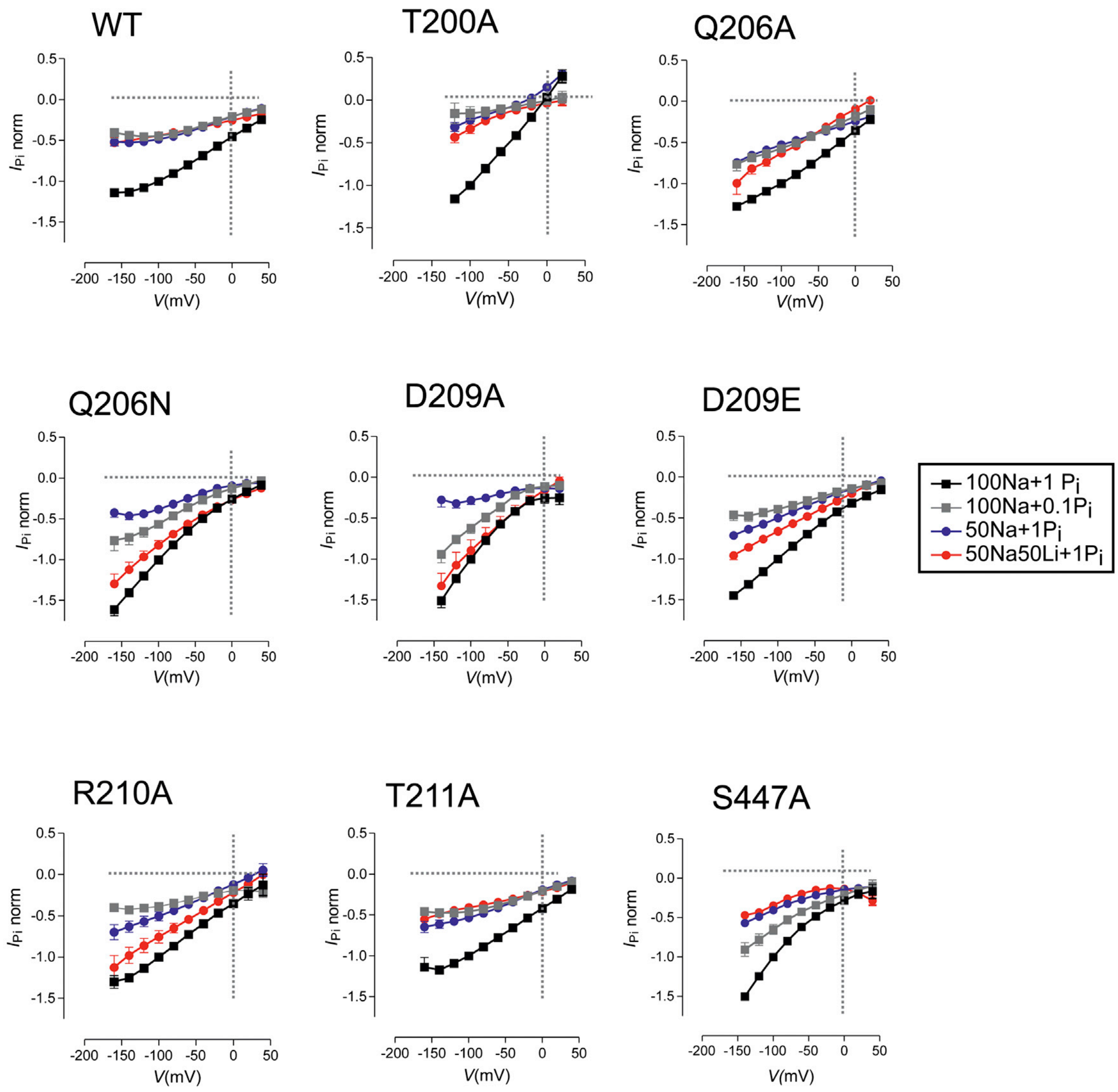

FIGURE 3 Current-voltage (*I-V*) data for the WT and functional mutants with substitutions at sites in TM2. Each panel shows the normalized P_i-dependent current (I_{Pi}) under four superfusion conditions: 100Na + 1 mM P_i (*black squares*); 100Na + 0.1 mM P_i (*gray squares*), 50Na + 1 mM P_i (*blue circles*), and 50Na50Li + 1 mM P_i (*red circles*). Data were pooled from more than three batches of oocytes and each point represents the mean ± SE of $n > 10$ oocytes. Data for each oocyte were normalized to the control response to 1 mM P_i in 100Na at -100 mV. Data points are joined for graphical clarity.

resulted in both common changes to their profiles (voltage dependence) and unique differences that we might expect given their unique structural disposition. In particular, they provided the first indication that the introduced changes at 206, 209, and 447 had possibly affected Na1. To analyze these electrogenic profiles in more detail and gain insight into their role in the Na1 interactions, we next focused on specific features of voltage dependence, apparent substrate affinities, and cation substitution by extracting relevant data from the *I-V* profiles.

Steady-state voltage dependence

Superposition of the *I-V* data, normalized to -100 mV in response to 100Na + 1 mM P_i (i.e., close to saturation for both substrates for the WT (23)), revealed that substitutions in TM2 (206, 209, and 210) and TM5 (447) caused variable hyperpolarizing shifts relative to the WT data (Fig. 4 *A*). These data are depicted separately for mutants in which either a polar residue (*left panel*) or charged residue (*right panel*) was replaced, and the WT data are shown in each case for comparison. The normalized *I-V* data for T211A were similar to those for the WT, indicating that this site was not critical for defining the steady-state voltage dependence, as already noted. Mutant T200A showed a significant outward component of current at depolarizing potentials, whereas the *I-V* relations for the other constructs showed only inward currents over the range of potentials tested. Replacement of external Cl^- by MES reduced this outward component, which suggested that it was in part due to an

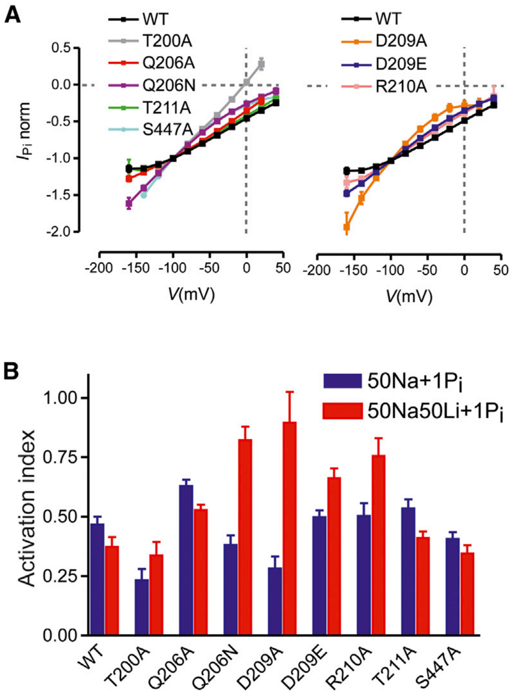

FIGURE 4 Steady-state properties of TM2 mutants. (*A*) Normalized *I-V* data for WT and mutants. Each data set is the I_{Pi} for 1 mM P_i in 100 Na normalized to the response at -100 mV. (*Left*) WT and mutants involving substitution of polar residues. (*Right*) WT and mutants involving substitution of acidic or basic residues. Data points have been joined for graphical clarity. (*B*) The effect of cation replacement at -100 mV is depicted as the ratio of I_{Pi} with 1 mM P_i superfusion of either 50Na + 1 mM P_i (*blue bars*) or 50Na50Li + 1 mM P_i to the control response in 100 Na^+ 1 P_i (*red bars*). Each bar shows the mean ratio ± SE for $n > 5$ oocytes expressing the indicated construct.

inward Cl^- flux in T200A similar to that reported previously, which may arise from a response of endogenous channels to P_i (24). The hyperpolarizing shifts were most pronounced for D209A and weaker for Q206N, D209E, R210A, and S447A. Given that the voltage dependence of NaPi-IIa arises from the partial reactions associated with the empty carrier and the first Na^+ ion interaction, these data suggested that the mutagenesis at 206, 209, 210, and 447 had altered the kinetics of one or more partial reactions that link states 6, 0, 1, 2, and 3 (Fig. 1). However, from these data alone we were unable to discriminate between changes to the empty carrier kinetics and/or Na^+ interactions.

Apparent affinities for P_i and Na^+ at -100 mV

We applied a two-point screening assay to determine whether a mutation had significantly altered the apparent affinity for P_i ($K_{0.5}{}^{Pi}$), by defining a P_i activation index (see Supporting Results, Fig. S3, and Table S3) as the ratio of I_{Pi} induced by 0.1 mM P_i to that induced by 1 mM P_i, always in the presence of 100 mM Na (100Na solution; Fig. S3 *C*) (25). For the WT voltage clamped at -100 mV, this ratio lies typically in the range of 0.4–0.5, consistent with the reported $K_{0.5}{}^{Pi}$ of ~0.1 mM (6,23). An increase or decrease in this ratio compared with the WT value would indicate that in the presence of 100 mM Na^+, $K_{0.5}{}^{Pi}$ had decreased or increased, respectively. Similarly, we defined a Na^+ activation index as the ratio of the response to 1 mM P_i in the presence of 50 mM Na (50Na solution) to that in the presence of 100 mM Na^+ (see Supporting Results). For the WT at -100 mV, this ratio was found to be ~0.5, consistent with the reported $K_{0.5}{}^{Na}$ of ~50 mM (6,23). This ratio also reflects how the maximum transport rate depends on external $[Na^+]$ under saturating $[P_i]$.

For mutants Q206A, Q206N, D209A, and S447A, the P_i activation indices were larger than the WT value (Fig. S3 *C*). According to our two-point screening assay, the altered activation indices would correspond to an ~25% decrease in the apparent $K_{0.5}{}^{Pi}$, and therefore indicated that the mutagenesis had resulted in a marginal effect on the apparent P_i affinities. In contrast, T200A showed a significantly reduced P_i-activation index, which suggested that its apparent $K_{0.5}{}^{Pi}$ had increased by ~8-fold. For the Na^+-activation assay, T200A also showed a significantly reduced activation index, whereas for D209E, R210A, and S447A, the indices were closer to the WT value (23,26).

We concluded that, with the exception of T200A, only marginal changes in apparent substrate affinities resulted from the mutagenesis at 447 and at the other sites in TM2.

Cation selectivity

In the final steady-state assays, we examined the response of the mutants to 1 mM P_i when 50% of the external Na^+ was replaced with Li^+ (50Na50Li solution). Li^+ is proposed to substitute for the first Na^+ ion, but not for Na^+ bound to Na2 and Na3 (14). Thus, mutations that affect Na1 might be expected to show altered electrogenic behavior in the presence of Li^+. For the WT, we observed a small decrease in the relative activity when we compared the P_i responses in 50Na and 50Na50Li solutions, and the response to 1 mM P_i was ~50% of that observed in 100Na (Fig. 4 *B*), consistent with previous findings for WT human NaPi-IIa (I.C.F. and C. Ghezzi, unpublished data). In contrast, the ratio of the response to 1 mM P_i in 50Na50Li relative to 100Na revealed that the mutagenesis at positions 206, 209, and 210 resulted in a significantly increased electrogenic response compared with the same ratio measured for 50Na (Q206N, D209A, and R201A; Fig. 4 *B*). The ratio reflects the ability of Li^+ to substitute for Na^+ at a given membrane potential (-100 mV); thus, if Li^+ substituted fully for Na^+, the ratio would be unity. Given that Li^+ is hypothesized to interact with NaPi-IIa at the Na1 site, our data directly implicate positions 206 and 209 in coordinating a cation at Na1. Since R210 is positively charged, it is extremely unlikely to coordinate the Na^+ ion directly. Nevertheless, these data suggest that position 210 is close enough that the R→A mutation affects either the electrostatics or sterics of Na1. It should be noted, however, that when Li^+ fully replaced Na^+ as the cosubstrate (100Li solution), no significant P_i-induced change in the holding current was observed for the mutants, which confirmed that Na^+ was still required to complete the transport cycle (data not shown), as previously reported for the WT (27).

Functional characterization: presteady-state responses

Presteady-state analysis allowed us to quantify the charge displacements associated with conformational state changes between states 6 and 2 (Fig. 1) in the absence of external P_i, i.e., transitions between states associated with the empty carrier and cation interactions preceding P_i binding, as well as transitions following its cytosolic release (transition $6 \leftrightarrow 0$). We resolved presteady-state relaxation currents induced by voltage steps for six mutants with substitutions in TM2 and three mutants with substitutions in TM5 (Table 1). The activity of T200A was too small for reliable presteady-state analysis, and for N448A we were unable to resolve relaxations that could be separated from the capacitive charging transient, even though the protein was detected at the membrane (Table 1; Fig. S1). Integration of the relaxation currents after baseline correction and exclusion of the capacitive component yielded presteady-state *Q-V* distributions that we fit with a single Boltzmann function (Eq. 1, Materials and Methods) to obtain an estimate of the maximum moveable charge (Q_{max}), the mid-point voltage ($V_{0.5}$), and the apparent valence (z). Both Q_{max} and $V_{0.5}$ were used as indicators of possible changes to the occupancies of the states relevant to cation interactions.

Representative presteady-state relaxation currents evoked by voltage steps in the range of −180 mV to +80 mV from the −60 mV holding potential (V_h) are depicted in Fig. 5 *A* for the WT and for two mutants that showed very different phenotypes (D209E and T454A). Quantification of the relaxation currents is shown as *Q-V* relationships for each construct for superfusion in the absence of Na^+ ions (0Na) and with 100 mM Na^+ (100Na). No relaxations were detected in the typical noninjected (NI) control oocyte for either of the superfusates (shown here for 100Na; Fig. 5 *A*). For the WT NaPi-IIa, presteady-state relaxation currents were detected under both superfusing conditions, as previously reported (23), and with 0Na the charge movements were approximately symmetrically distributed for equal positive and negative steps around V_h. With 100 mM Na^+ present, the distribution became more asymmetrical with respect to the baseline record at V_h, such that more charge movement was evoked with depolarizing steps, reflecting the release of Na^+ back into the external medium.

The behavior was very different for mutant D209E, which showed a more asymmetrically distributed charge movement in 0Na, with more charge evoked by hyperpolarizing steps from V_h. Moreover, like the WT, in the presence of 100Na, additional charge movement was evoked, although in contrast to the WT, the charge increase for

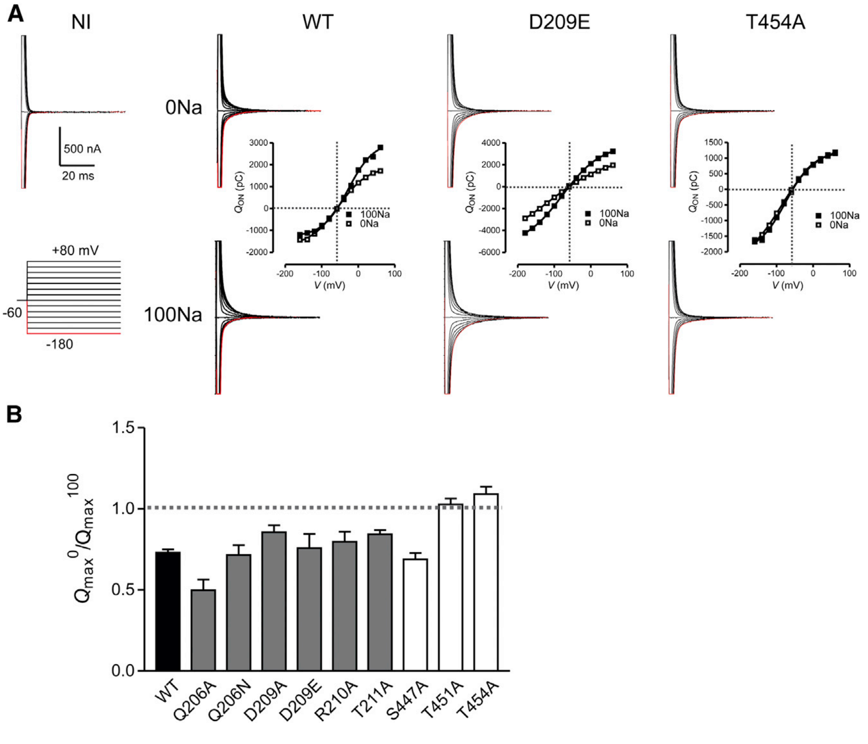

FIGURE 5 Presteady-state relaxations. (*A*) Representative examples of presteady-state relaxations evoked by voltage steps in the range of −180 mV to +80 mV from a −60 mV holding potential for a typical noninjected (NI) oocyte, the WT, and mutants D209E and T454A. Upper data traces correspond to superfusion in 0 Na solution, and lower traces correspond to superfusion in 100Na solution. For each construct, *Q-V* data are shown for the two superfusates. Gray dashed lines help to visualize the charge distribution about the holding potential. Continuous lines are fits to a single Boltzmann function (Eq. 1). The parameters for the fits for the individual cells shown are summarized in Table S4. (*B*) Ratio of the estimated total charge predicted from the Boltzmann equation fit to data obtained by superfusion with 0Na to that obtained by superfusion with 100Na ($Q_{max}{}^{0}/Q_{max}{}^{100}$) for each construct. Data are shown as mean ± SE for $n > 5$ cells. Black, WT; gray, mutants in TM2; white, mutants in TM5.

D209E was detected for both hyper- and hypopolarizing steps relative to V_h. Mutant T454A also showed a significant asymmetry of charge movement with respect to V_h; however, there was little difference in the magnitude of the charge evoked, whether or not Na^+ was present, apart from a small depolarizing shift in the Q-V in 100Na (see below).

To quantify these findings further, we first considered the effect of the mutation on the Boltzmann fit parameters Q_{max} and $V_{0.5}$ when changing from 0Na to 100Na solutions. For the WT, superfusion with 100Na increases Q_{max} by ~30% (23) (Fig. 5 *A*), and we quantified this as the ratio of Q_{max} in 0Na to Q_{max} in 100Na ($Q_{max}{}^0/Q_{max}{}^{100}$) (Fig. 5 *B*). This ratio was used as an indication of whether the mutagenesis had altered the electrogenic properties of the apparent Na^+ ion interaction with the TM electric field before P_i binding. Such alterations may reflect changes in the ability of Na^+ to bind in its site or changes in the ability of the protein to respond to Na^+ binding. Like the WT, all mutants with substitutions in TM2, as well as S447A in TM5, showed an increase in total charge movement when the superfusate was 100Na, although the relative increase varied according to the site and substituted residue type. In contrast, T451A and T454A in TM5 showed little difference in Q_{max} whether external Na^+ ions were present or not, and therefore exhibited distinct behavior from the other mutants (see Fig. 5 *A*).

Significant shifts in the $V_{0.5}$ were observed in the pooled data for the mutants relative to the WT, and these shifts also depended on the superfusion conditions (Fig. 6 *A*). As expected from the steady-state analysis, T211A behaved similarly to the WT. Four of the mutants with substitutions in TM2 (Q206A, Q206N, D209A, and D209E) and one mutant in TM5 (S447A) that showed obvious hyperpolarizing shifts in their steady-state I-V relations (Fig. 4 *A*) also displayed significant hyperpolarizing shifts in $V_{0.5}$ when superfused with 100Na. In the absence of external Na^+ (0Na), we also found significant deviations of $V_{0.5}$ from the WT value (Q206N, D209E, R210A, and S447A), which indicated that the mutagenesis had altered the distribution of occupancies among states 0, 1, and 6 (Fig. 1). This was particularly obvious for mutants R210A and S447A, for which we determined $V_{0.5}$ values approaching -100 mV for each construct (c.f. WT: -65 ± 7 mV). As noted above, we also observed a small Na^+-dependent depolarizing shift in $V_{0.5}$ for the two TM5 mutants (T451A and T454A) when Na^+ ions were present, even though $Q_{max}{}^0/Q_{max}{}^{100}$ was close to unity (Fig. 5, *A* and *B*). Their behavior suggested that Na^+ ions still interact with the protein, but only weakly with the TM electric field (see Discussion).

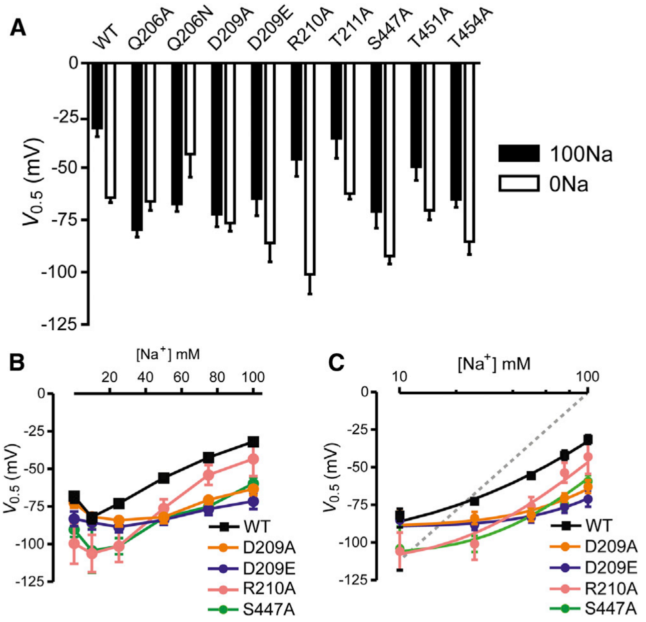

FIGURE 6 Quantification of midpoint voltage ($V_{0.5}$) for WT and mutants. (*A*) Comparison of $V_{0.5}$ for superfusion in 100Na (*solid bars*) and 0Na (*open bars*) for each construct. Each bar represents the mean ± SE for $n \geq 4$ cells from at least two donor animals. (*B*) Dependence of $V_{0.5}$ on external [Na^+] for mutants of two neighboring charged sites (D209 and R210) in TM2. Data points are joined by lines. (*C*) The same data as in (*B*) plotted on a semilog scale. The continuous lines are best fits to the data points predicted by a four-state model that accounts for the empty carrier and sequential Na^+ binding partial reactions (see Discussion). The dashed line represents the theoretical limiting slope of 116 mV/decade expected at high [Na^+].

Based on the altered steady-state voltage dependence of I_{Pi} (Fig. 3), we hypothesized that the three mutants in TM2 (D209A, D209E, and R210A) involving removal or modification of the existing charged residues, and S447A in TM5, which showed a similar curvilinear I_{Pi}-V relationship, should also show correspondingly altered Na^+ interactions in a presteady-state analysis. Therefore, we investigated the dependence of $V_{0.5}$ on external [Na^+] in detail for these mutants (Fig. 6 *B*). Previous studies have shown that with high external [Na^+], there is a near linear relationship between $V_{0.5}$ and $\log_{10}$[Na^+], the slope of which reflects the cooperativity of interaction between Na^+ ions and the empty carrier (5,14,23). This slope approaches ~116 mV/decade for two Na^+ ions interacting with the empty carrier (5,28). When the $V_{0.5}$ versus [Na^+] data were replotted on a semi-log scale (Fig. 6 *C*), it was obvious that the limiting slope behavior was severely compromised for D209A/E and S447A. In contrast, although R210A had a strongly hyperpolarized $V_{0.5}$ in 0Na, its $V_{0.5}$ approached that of the WT as [Na^+] increased. This suggested that a direct involvement in Na1 coordination is less likely for this position.

In summary, the presteady-state assays corroborate the steady-state findings and provide further support for the association of sites Q206, D209, and S447 with cation interactions at Na1. The removal of charge at position 210 affected the empty carrier equilibrium; however, at a sufficiently high [Na^+] the WT state distribution was almost reached, suggesting that R210 is not directly associated with Na1 in NaPi-IIa.

Refinement of the structural model of human NaPi-IIa

Unlike Q206, D209, and S447, which are strongly implicated in contributing to the Na1 site, T211 can be excluded from Na1 (Figs. 3 and 4), consistent with the weak sequence conservation of threonine at this position (Fig. S4). The T200A mutation, on the other hand, caused significant changes in the apparent affinity for both Na^+ and P_i (Figs. 4 *B* and S3 *C*), consistent with the strong sequence conservation of this position (Fig. S4). Moreover, although the signal was too small to allow presteady-state currents to be analyzed, the voltage dependence of phosphate-induced currents was also altered by T200A, especially in the form of outward currents at depolarizing potentials (Fig. 4 *A*), reminiscent of previous observations for N227Q (23). The origin of these outward currents is not clear. An inward chloride leak has been ruled out in the case of N227Q (23), whereas in chloride-free solution, the phosphate-induced outward currents were suppressed for T200A. In any case, the similarity of the phenotypes of N227Q and T200A suggests that these two residues play a similar role in the voltage-dependent steps of transport, and therefore may be proximal in the protein structure.

Given the high confidence in the positioning of TM3 in the structural model of NaPi-IIa based on the agreement with accessibility measurements, it is reasonable to assume that D224 and N227 are indeed >10 Å from the Na2-P_i-Na3-binding regions, i.e., the tips of HP1 and HP2 (Fig. 2). Taking this assumption and all of the above data into account, we refined the structural model of human NaPi-IIa so that Q206 and D209 are on the same face of TM2b and point toward TM3, while T211 is farther away (see Materials and Methods; Fig. 7 *B*; Table S1). In this model, T200 remains midway across the membrane near the cytoplasmic end of TM2a, just before L2ab, with its backbone carbonyl pointing into the Na1 site, and its side chain can potentially orient either downward to Na1 or upward toward the Na2-P_i-Na3 cluster.

The refinement of TM2b involved adjusting the sequence alignment of NaPi-IIa with VcINDY by five positions (Table S1; Fig. S5), which shortened the previously rather long loop L2ab between TM2a and TM2b (cf. Figs. 2 and 7). These adjustments resulted in other improvements. For example, several evolutionarily variable, ionizable residues, including D212, R214, and R215 (Fig. S4), were repositioned into the cytoplasmic loop (cf. Fig. S6, *A* and *C*), while R210 was moved away from the P_i-binding site (Fig. 7), consistent with the lack of effect of an R210A mutation on the P_i apparent affinity (10). The model quality score (ProQM) in the region of TM2b decreased somewhat after the refinement (Fig. S7), indicating a slightly worse model. This may be because conserved residues in the cytoplasmic end of TM3 now point away from the core of the protein (Fig. S6), which is atypical. Nevertheless, a comparison with VcINDY suggests that in the complete protein these residues will pack against the peripheral helices TM7 and TM8, which are not modeled due to the absence of a reliable template (Fig. S8). To test the effect of removing peripheral helices on the ProQM score of the remaining core helices, we compared the ProQM scores of the full-length structure of VcINDY with the scores obtained for the segments used as a template, i.e., after removing TM1-3, TM7-8, and the other protomer (Fig. S9). Significant reductions in the ProQM scores at TM5, TM9, and HP2b in the truncated structure of VcINDY (Fig. S9 *A*) reflect the removal of packing interactions with TM7, the other protomer, and TM3, respectively (Fig. S9, *B* and *C*). Therefore, a similar effect may explain the reduction in the ProQM profiles for TM2b/TM3 of the new NaPi-IIa model, in which those residues are more exposed (Fig. S8). Importantly, in the refined model, the residues from TM2 and TM3, which were

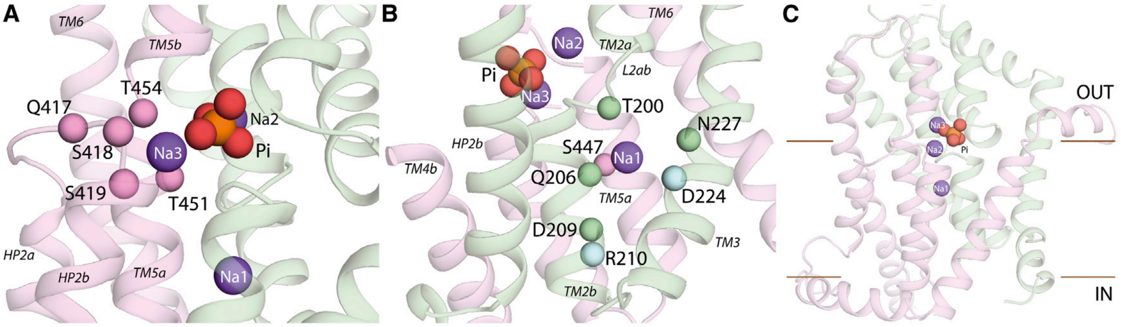

FIGURE 7 Refined structural model of human NaPi-IIa bound to three Na^+ ions and one P_i anion. The Na^+ ions are shown as purple spheres and the P_i is shown as orange and red spheres. Residues comprising RU1 and RU2 are colored in green and pink, respectively. (*A*) Close-up of the Na3-binding site, viewed from the extracellular side of the membrane into the binding site. The Cα atoms of several residues predicted to form the Na3 site or to coordinate P_i are highlighted (*spheres*). (*B*) Predicted Na1-binding site. The Cα atoms of the residues whose side chain and/or backbone atoms are predicted to form the Na1 site are shown as green spheres. The Cα atoms belonging to residues R210 and D224 are highlighted as light blue spheres. (*C*) Overview of the human NaPi-IIa model represented as cartoon helices, viewed from along the plane of the membrane.

implicated experimentally in Na1 binding, are clustered together. Moreover, without imposing specific constraints on their orientation, the side chain of R210 can readily contact D224 (Fig. 7 *B*), consistent with their similar phenotypes in altering the voltage dependence of the empty carrier, as well as their likely involvement in either the return step (Fig. 1, 0 → 1) of the empty transporter or release of the Na1 into the cytoplasm.

Informed by the functional and biochemical characterization of mutants S447, N448, T451, and T454, we also modified the alignment in the region of TM5 and TM6 (Fig. S5), placing T451 and T454 farther to the extracellular side and closer to the predicted Na3 site, and placing S447 closer to the other putative Na1-binding residues (Fig. 7 *A*; Table S2). The resultant structural model has a dramatically improved ProQM quality score in this region (Fig. S7 *B*), in part due to the repositioning of three arginines into the cytosol instead of facing the hydrophobic core of the membrane in TM6 (cf. Fig. S6, *B* and *D*). In accordance with PSIPRED secondary structure predictions (Fig. S5) and the strong helical conservation pattern (Fig. S6 *D*), this arginine-rich segment was modeled as a helix. Note that in the model, this helix extends into the cytoplasm because there are no additional constraints to fix its relative orientation (Fig. S6 *D*), although its strong amphipathic character (Fig. S5) suggests that in reality this segment will form a helix that lies parallel to the membrane plane along the lipid headgroups.

In summary, the experimentally guided refinements led to a structurally reasonable model of the core of human NaPi-IIa in which the overall fold is maintained (Supporting Model S1). Compared with the earlier model, TM2 and TM5-6 change by >5 Å, and the loops L2ab and L5ab are significantly shorter (Fig. S10). This new model illustrates how T451 and T454 from TM5 may contribute to the predicted Na3- or P_i-binding sites (Fig. 7 *A*) together with Q417, S418, and S419 from the HP2ab loop, whereas the binding site for Na1 would be formed by T200, Q206, D209, N227, and S447 (Fig. 7 *B*). Moreover, the model predicts that R210 and D224 point toward each other and are located on the cytoplasmic side of the Na1 site (Fig. 7, *B* and *C*).

DISCUSSION

In this work, we improved upon our previous homology model of the human isoform of NaPi-IIa (SLC34A1) (10) to incorporate the first Na^+ ion-binding site (Na1). The binding of Na^+ at Na1 is the initiator of all subsequent steps in the transport cycle, and the kinetics of binding are a critical determinant of the overall transport rate and the electrogenic properties. Our strategy for defining the coordinating residues for Na1 involved bioinformatic prediction of candidate positions based on the existing structural model, functional investigation of the effects of single point substitutions at the predicted positions, and further model refinement in the light of the functional data. In addition to using conventional criteria for selecting potential Na^+ coordinating residues (serine, threonine, asparagine, glutamine, aspartate, and glutamate), as seen in available Na^+-coupled transporter structures (29–31), we also took into account two salient functional properties of NaPi-II proteins.

First, previous functional studies on both WT and mutated constructs have revealed the importance of the Na1-cation interaction in determining the electrogenic properties of the NaPi-II transport cycle. The aspartic acid at 224, which is conserved in all electrogenic isoforms, is a key requirement for the 3:1 stoichiometry and transport electrogenicity, and, by implication, the translocation of the first Na^+ ion through the protein (4,6–8). Therefore, D224 became the focal point for identifying other side chains in close proximity. Second, previous kinetic studies have highlighted the involvement of the Na1 interaction with an uncoupled leak, and proposed that in the absence of substrate (P_i), Na^+ ions participate in a uniport mode that involves cycling between states 0 and 6 (Fig. 1) (23,24,26,32,33). This phenomenon is only observed for the electrogenic isoforms. Although they were not functionally explored in this study because of their small magnitude, the existence of uncoupled leak currents also implies that the Na1 site must allow accessibility from either side of the membrane with minimal rearrangements, and we also used this feature as a criterion for selecting the initial binding region.

Once we had proposed the positions, the goals of the functional assays were twofold. First, we aimed to distinguish between mutations at positions that were more likely to be involved with Na1 and those that contributed to the Na2-P_i-Na3-binding region, as well as those with little functional significance, by comparison with the WT. Second, for the Na1-related mutations, we aimed to further distinguish between effects on the empty carrier kinetics and those on the Na^+ interactions, and thereby gain more insight into the structure-function basis for electrogenicity, by using presteady-state assays. We then used the interpretation of the functional data for the final model refinement.

Discrimination between Na1 and Na2-P_i-Na3 sites using steady-state assays

In our previous study (10), Ala or Cys substitutions at three positions in TM2 and HP1 (S164, T195, and S196) and two positions in HP2 (S418 and S419), which we associate with Na2-P_i-Na3 coordination, caused a total loss of cotransport function, yet evidence for cation interactions at Na1 was still detected in the form of presteady-state relaxations in the presence of 100 mM Na^+. In contrast, the mutagenesis in the study presented here was well tolerated by the transporter, as evidenced by the complete cotransport cycle remaining intact in most cases (Table 1). Notable exceptions were three positions in TM5 (N448, T451, and T454), for which we detected no transport activity from the respective mutants. In the case of T451 and T454, presteady-state relaxations were also resolved (see below), suggesting that those side chains were more likely to be associated with the Na2-P_i-Na3-binding region. The basis for the lack of any functional activity for N448A, which was expressed in the oocyte membrane, is unclear. In all, only one mutant showed WT-like behavior (T211A), and this was taken into account in subsequent model refinement (see below).

In the steady-state cotransport mode, the kinetics of the transport cycle for WT NaPi-IIa (Fig. 1) have been extensively described in terms of macroscopic phenomenological parameters, such as apparent substrate affinities derived from standard TEVC assays (23,26). These parameters are a function of the rate constants associated with all of the hypothesized partial reactions in the transport cycle (Fig. 1), and therefore deviations from the WT macroscopic kinetic profile resulting from mutagenesis might be caused by changes in the rates associated with more than one partial reaction, leading to ambiguous interpretations. Thus, with three partial reactions involving external Na^+ interactions for the cotransport cycle, any one or all of them might be involved in determining $K_{0.5}^{Na}$ and $K_{0.5}^{Pi}$.

With the exception of T200A, the two-point assay for substrate activation (Fig. S3) indicated that the mutagenesis at all considered positions did not cause large changes in the apparent substrate affinities (Fig. S3 *C*). Nevertheless, small but significant deviations were observed that would require a more detailed analysis, beyond the scope of this study, to identify the partial reactions affected. For example, in the P_i-activation assay (Fig. S3 *C*), Q206A/N, D209A, and S447A all showed increased activation indices, consistent with an increased $K_{0.5}^{Pi}$. This increase could arise indirectly from changes to the Na^+ interactions preceding P_i binding, the P_i binding step, or a combination thereof. Indeed, for Q206A the Na^+ activation index was also increased, consistent with an altered Na^+ interaction involving partial reactions (1↔2 and 2↔3; Fig. 1), whereas for Q206N, D209A, and S447A, the Na^+ activation index was not markedly altered compared with the WT. Because deviations from WT behavior for the activation indices might be attributable to changes in more than one partial reaction in the overall cotransport cycle, we were careful to avoid overinterpreting these data. This was particularly true for the Na^+-inactivation data, which reflect the combined effect of all five cation- and substrate-dependent partial reactions (Fig. 1), including cation and substrate release to the cytosol. Of all the mutants investigated, T200A showed the largest deviation from WT behavior. Its very low functional activity allowed us to perform only basic steady-state assays, from which we concluded that $K_{0.5}^{Na}$ and $K_{0.5}^{Pi}$ were significantly reduced based on the smaller activation indices (Fig. S3). Similar effects were also reported for the N→C substitution at 199 (32) and the N→Q substitution at 227 located on TM3 (6). Given the limited kinetic analysis, we are unable assign this phenotype to either a direct effect on Na1 interactions or more global effects involving the Na2-P_i-Na3 site. As positions 199 and 200 are located between the proposed Na1- and Na2-P_i-Na3-binding regions, with N227 close by (Fig. 7, *A* and *B*), we speculate that these positions may play a critical role in the coupling between the two regions, specifically in the observed apparent cooperativity of Na2 occupancy. Furthermore, the fact that the N→A substitution at position 227 was not tolerated by the oocytes suggests a critical role for the side chain at 227 and corroborates the previous finding that only a N→Q substitution yielded functional activity (6).

Despite the potential limitations of steady-state assays for resolving effects unique to a specific partial reaction, the *I-V* data (Fig. 3) revealed two significant deviations from WT behavior that implicated the involvement of positions 206, 209, and 210 from TM2, and 447 from TM5 in coordinating a cation at Na1.

First, alanine substitution at 209, 210, and 447 resulted in the same qualitative hyperpolarizing shift in the voltage dependence of I_{Pi} as observed for the more conservative Q→N substitution at 206. This result is consistent with the first Na^+ interaction being a strong determinant of voltage dependence, and also underscores how elements of both structural repeats (RU1 and RU2) are involved in cation coordination. Similar shifts in the steady-state voltage dependence were reported in two structure-function studies on the rat NaPi-IIa (34) and flounder NaPi-IIb (12). In the former study, Cys was substituted at two conserved sites (corresponding to I449 and A461 in TM5 of hNaPi-IIa) (34). In the latter study, an A→C substitution was also made at site 175 (corresponding to 203 in TM2 of hNaPi-IIa) (12), and simulations of the A175C kinetics could readily account for the observed shift in voltage dependence by effectively increasing the dissociation constant for the first Na^+ binding partial reaction (1↔2; Fig. 1) (12). In our structural model, these conserved positions are involved in the packing of helices TM2 and TM5 with their neighbors, suggesting unspecified indirect effects of these mutations and supporting the notion that the molecular determinants of the steady-state voltage dependence are shared between functionally important elements of the symmetry-equivalent repeat units.

Second, Li^+ is proposed to bind only at Na1, where it competes with Na^+ ions for occupancy when both are present in the external medium (14). This is a useful property because it allowed us to discriminate between Na1 interactions and those involving Na1 and Na2 when only Na^+ was present. Simulations based on an extensive kinetic analysis of the flounder NaPi-IIb isoform predict that the dissociation constant associated with partial reaction 2↔3 (Fig. 1)—leading to occupancy of Na2 by a Na^+ ion—is significantly reduced when Na1 is occupied by Li^+. Moreover, Li^+ occupancy of Na1 was predicted to reduce the inward translocation rate of the fully loaded carrier to account for the smaller $I_{\mathrm{Pi}}^{\max}$ of the WT at hyperpolarizing potentials (see Fig. 3 *C*) (14). In this study, superfusion with the 50Na50Li solution increased the response to 1 mM $\mathrm{P_i}$ for Q206N, D209A/E, R210A, and S447A, exceeding the response with 50Na. In contrast, for the WT there was only a marginal change in I_{Pi} over a wide voltage range when superfusing with either solution (Fig. 3). This behavior established that Li^+ ions interact with the mutated constructs and are more readily tolerated as a driving cation compared with the WT. Although our data were consistent with the notion that mutagenesis directly impacts only the Na1 site, and 100% replacement of Na^+ with Li^+ resulted in no electrogenic activity or $^{32}\mathrm{P}$ uptake (data not shown) (14), we cannot exclude the possibility that for the mutants, both Na1 and Na2 sites might bind Li^+ and result in an overall cotransport stoichiometry of 2 Li^+:1 $\mathrm{HPO_4}^{2-}$:1 Na^+.

Presteady-state assays focus on Na1 and the empty carrier

The presteady-state assays performed in the absence of external $\mathrm{P_i}$ allowed us to restrict the number of occupied conformational states and obtain additional insights into the functional consequences of the mutagenesis. Voltage steps applied to the membrane move the transporters between state 6 (extreme depolarizing potentials) and state 1 (0Na) or 3 (100Na) (extreme hyperpolarizing potentials), with a distribution between the possible states at intermediate potentials that depends on the kinetics of the partial reactions. The *Q-V* data were fit with a single Boltzmann function, which is strictly valid only for a two-state system (35). Here, data resolution limitations and fit uncertainties precluded fitting with a more complex function; however, despite this limitation, two parameters from the single Boltzmann fit analysis ($Q_{\max}$ and $V_{0.5}$; Eq. 1) provided useful indicators of the effects of mutagenesis.

For all mutants assayed, except for T451A and T454A, there was an increase in estimated total displaceable charge ($Q_{\max}$) when external Na^+ was present, with the $Q_{\max}{}^{0}/Q_{\max}{}^{100}$ ratio being comparable to the WT estimate (Fig. 5 *B*). Therefore, we can conclude that the mutagenesis did not alter the amount of charge displacement attributable to Na^+ ions under the influence of the TM electric field. In this context, it should be noted that $Q_{\max}{}^{100}$ describes both the movement of the empty carrier and the additional charge due to Na^+ ion displacement. Constructs T451A and T454A, for which we detected no cotransport activity, also showed no significant dependence of $Q_{\max}$ on Na^+. This result indicated that Na^+ movements to the Na1 and Na2 sites were severely compromised, consistent with the lack of transport activity, although we cannot exclude the possibility that the charge movement attributable to Na^+ ions remained undetected due to the resolution limitations of the system. We note that the molecular rearrangements that accompany the Na^+ interaction with Na1 remain unresolved and will require knowledge about the structure of NaPi-IIa (or homologs thereof) in states other than the equivalent of state 4 (Fig. 1).

The hyperpolarizing shift in the steady-state voltage dependence of I_{Pi} was reflected in corresponding changes in the presteady-state charge distributions of the mutants (i.e., a hyperpolarizing shift of the midpoint voltage, $V_{0.5}$; Fig. 6 *A*) when 100 mM Na^+ was present externally (Q206A/N, D209A/E, and S447A). This was in accord with the notion that the kinetics of transitions between states associated with the empty carrier (states 0 and 1) and when Na1 (states 2 and 6) or Na2 (state 3) is occupied (Fig. 1) are the main determinants of the voltage dependence of the overall cotransport cycle. In the absence of external Na^+, there was more variation in the empty carrier equilibrium potential ($V_{0.5}$) among the constructs, which suggested that the mutagenesis had also affected the distribution between states 6, 0, and 1, to an extent that depended on the site mutated. Mutants D209E and R210A (TM2), and S447A (TM5) showed significant hyperpolarizing shifts in $V_{0.5}$ when no external Na^+ was present. This indicated that at the −60 mV holding potential, at which the WT would be equally likely to be in state 0 or 1, the inward orientation of the empty carrier (state 0) was more favored for these mutants (Fig. 1). It should be noted that since we had no direct access to the oocyte cytosol to manipulate the intracellular [Na^+], we cannot fully exclude the possible occupancy of Na^+ bound from the inside (state 6), although indirect evidence from kinetic simulations and the low internal [Na^+] for typical oocytes (<10 mM (36)) would be consistent with a low occupancy of state 6 for the WT.

For the two nontransporting mutants in TM5 (T451A and T454A), charge movement was detected in the absence of external Na^+. This indicated that the conformational change accompanying the empty carrier reorientation ($0 \leftrightarrow 1$; Fig. 1) in response to changes in the TM field still occurred, although for T454A, $V_{0.5}$ was further shifted in the hyperpolarizing direction relative to the WT, consistent with an inward facing orientation of the empty carrier being favored, as also found for D209E, R210A, and S447A. When Na^+ was present in the external medium, the ~+20 mV depolarizing shift of $V_{0.5}$ seen for both T451A and T454A could be explained by an electroneutral, or weakly electrogenic, interaction of Na^+ with Na1. Given the profound effect on function that mutagenesis had at these sites, we propose that the side chains at 451 and 454 are critical for coupling the Na1 occupancy to the subsequent binding at Na2 rather than directly participating in cation coordination at Na1. Indeed, their general phenotype was consistent with that of mutations at other sites in TM5 that we propose to be nearer the Na2-$\mathrm{P_i}$-Na3-binding region (10).

Two of the positions explored in this study were charged (D209 and R210), and the finding that electrogenic activity remained after charge removal indicates that the charge per se at these positions was not critical for overall function and might argue against their direct involvement at Na1. This contrasts with the removal of negative charge at 224, which results in electroneutral cotransport (6,7). Nevertheless, since the alanine substitution at each position, or merely changing the side-chain length (D209E), significantly altered the electrogenic properties of the mutants, we explored their presteady-state kinetics in more detail by determining the dependence of $V_{0.5}$ on external [Na^+]. This dependence has been used to investigate the apparent affinities of the Na1- and Na2-binding sites in the Na^+-dependent sugar transporter SGLT1 (28). Similar to what was found for SGLT1, analysis of presteady-state data from WT NaPi-IIa and NaPi-IIb yields a relationship between $V_{0.5}$ and $\log_{10}$[Na^+] that is consistent with a sequential binding model for Na^+. At high [Na^+], this relationship is linear and approaches a maximum slope of ~116 mV/decade (5,14,23,28). Over the range of external [Na^+] used in our assays, the data for D209A and D209E showed no evidence of limiting slope behavior, which suggested that the Na^+ interactions had been compromised by mutagenesis at position 209. For R210A, the empty carrier $V_{0.5}$ was also shifted in the hyperpolarizing direction relative to the WT; however, its $V_{0.5}$ value tended to approach that of the WT at high [Na^+]. Based on this behavior, we concluded that R210 was not critical for Na1 coordination, but that the charge at this site was important for defining the equilibrium between the empty carrier states. Interestingly, the polar-to-nonpolar substitution at 447 also resulted in a comparable hyperpolarizing shift to that of R210A for the 0Na superfusion condition. However, this mutant showed a weaker depolarizing shift in $V_{0.5}$ when Na^+ was present that lay between the WT and D209A/E values, suggesting an intermediate effect on Na1 interactions.

We attempted to gain further insight into the significance of these data by fitting them with the implicit function obtained by modeling a four-state sequential binding scheme describing the dependence of $V_{0.5}$ on [Na^+] (corresponding to transitions between states 0, 1, 2, and 3; Fig. 1). The variables in this model comprise the ratio of forward and backward zero voltage rates for each partial reaction and associated apparent valences (14,28) (Supporting Results). Although our ability to discriminate between effects only at Na1 or only at Na2 was limited by having only five nonzero [Na^+] data points and a maximum [Na^+] $=$ 100 mM, the fit parameters were nevertheless consistent with significantly increased dissociation constants for the first Na^+ binding partial reaction compared with the WT for D209A/E and S447A, whereas for R210A the change was less dramatic. These findings further confirmed the likely participation of D209 and S447 in cation coordination at Na1. Changes were also observed for the dissociation constant associated with the Na2 occupancy partial reaction that would suggest that the mutagenesis had also impacted the cooperativity of Na^+ interaction.

Taken together, the steady-state and presteady-state functional data strongly implicated Q206, D209, D224, and S447 as likely candidates for coordinating Na^+ at Na1. The positive charge at 210 appeared to be a critical determinant of the kinetics of the $0 \leftrightarrow 1$ transition after cytosolic release of Na^+ and coupling to the Na2 site.

A structural model of human NaPi-IIa including all four binding sites

The low sequence identity between human NaPi-IIa and its only available template structure, VcINDY, means that although the overall fold is likely to be correct, key regions should be optimized with the guidance of specific experimental data. Preliminary data implicated D224 from TM3 in the role of Na1, and, helpfully, the vertical positioning of the residues in this TM helix was one of the most reliable aspects in the published model (10) because of the clear agreement with the TM prediction from OCTOPUS (residues 224–244) and experimental accessibility data (6). That Na1 is likely to be fairly close to the cytoplasmic surface can be inferred from the leak mode observed in the absence of substrate for the electrogenic forms of SLC34. Therefore, we focused our efforts on residues close to D224 and on the cytoplasmic halves of TM2 and TM5, i.e., the only two helices contacting TM3 in this fold. This strategy allowed us to identify nine candidate positions for the Na1 site, only three to five of which are likely to be directly involved. Remarkably, the experimental data described above delineates the roles of most of the nine tested residues.

For the available template, only one alignment of TM2b between NaPi-IIa and VcINDY was compatible with a Na1 site in which D206 and N209 coordinate the ion, but T211 does not. This adjustment had the added advantage that a conspicuously long loop in the membrane (L2ab), which previously could not be unambiguously modeled, was significantly shortened, and several charged residues could be repositioned into a more suitable aqueous environment (Fig. S6). The distinct behavior of mutations at T451 and T454 was reminiscent of previous results for residues in the Na2-P_i-Na3-binding region of NaPi-IIa. Although the published data do not delineate which residues contribute to the Na2, Na3, or Pi sites in NaPi-IIa, they nevertheless provide strong support for the involvement of several residues in HP1 (S164, T195, and S196), HP2 (Q417, S418, and S419), and TM2 (N199) in contributing to this binding region (10). The similar data for T451A and T454A suggest that these two residues in TM5 also contribute to this binding region, so we positioned T451 and T454 close to the tip of HP2 by adjusting the alignment of TM5, shortening the L5ab loop, and improving the model of TM6.

We note that S462, which we previously concluded might be part of the Na2-P_i-Na3-binding region, and might coordinate Na3, is now moved farther to the periplasmic end of TM5b. Our earlier proposal was based on the observation that P_i transport by an S462C mutant of rat NaPi-IIa was inhibited by an MTS reagent (34). However, it should be noted that similar observations have been made for positions remote from binding sites (e.g., the helical hairpin HP2 in glutamate transporters) if the repacking of that segment is required for transport (37). Therefore, we propose that an alternative role should be assigned to S462, and that T451 and T454 may be positioned close to the Na2-P_i-Na3 cluster.

As described above, the type of side chain at 224 plays a critical role in determining charge translocation and electrogenicity by NaPi-II family members (6–8,12). After refinement, the NaP-IIa model predicts a possible salt-bridge between R210 (TM2) and D224 (TM3), with both residues close to the Na1 site, but on the cytoplasmic side thereof. Although a clear structural interpretation of the electrophysiological data is difficult, we speculate that when D224 is a Gly, as in NaPi-IIc, R210 does not interact with TM3, reducing the repulsion of R210 to the Na1 ion and allowing the ion to remain bound during the $0 \leftrightarrow 1$ transition (Fig. 1). In addition, in NaPi-IIa/b, formation of the salt-bridge by D224 may be voltage dependent; thus, breaking of this bridge could provide a pathway for the ion to leak in the absence of P_i (24). Whatever the mechanism, it is clear that these two residues are involved in distinguishing between the electrogenic and electroneutral isoforms. Therefore, it will be essential to examine in further detail how those positions and their valency relate to the voltage dependence of transport.

In conclusion, the fact that residues from three distinct TM segments (TM2, TM3, and TM5) come together to form the Na1 site, as predicted by our models, provides strong support for the predicted fold of NaPi-II transporters and the choice of VcINDY as a template. Moreover, the refinements of TM2, TM5, and TM6 in this structural model and the identification of the Na1 site residues provide a firmer foundation for the future design of experiments to define functionally critical aspects of transport by the SLC34 family of proteins, as well as of VcINDY homologs from the SLC13 family such as NaDC1 and NaDC3 (Fig. S11).

SUPPORTING MATERIAL

Supporting Results, eleven figures, four tables, and one structural model are available at http://www.biophysj.org/biophysj/supplemental/S0006-3495(15)00342-2.

AUTHOR CONTRIBUTIONS

C.F.-F.: bioinformatics and modeling. L.R.F.: analysis of computational data. A.W.: molecular biology. M.P.: molecular biology, electrophysiology, and data analysis. I.C.F.: electrophysiology and data analysis. T.K.: tracer assays and immunohistochemistry. L.R.F., A.W., and I.C.F.: experimental design and writing of the manuscript.

ACKNOWLEDGMENTS

We thank Eva Hänsenberger for oocyte preparation, Mehdi Taslimifar (Interface Group, Institute of Physiology, University of Zürich) for valuable assistance in MATLAB modeling, and members of the Theoretical Molecular Biophysics Unit of the National Heart, Lung and Blood Institute for useful discussions.

This work was supported by The Dunhill Medical Trust (AW SA10/0210), the Swiss National Science Foundation (I.C.F.), the Hartmann Müller Foundation (I.C.F.), and the Intramural Research Program of the NIH, National Institute of Neurological Disorders and Stroke (L.R.F.).

REFERENCES

1. Biber, J., N. Hernando, and I. Forster. 2013. Phosphate transporters and their function. *Annu. Rev. Physiol.* 75:535–550.
2. Forster, I. C., N. Hernando, …, H. Murer. 2013. Phosphate transporters of the SLC20 and SLC34 families. *Mol. Aspects Med.* 34:386–395.
3. Lederer, E. 2014. Renal phosphate transporters. *Curr. Opin. Nephrol. Hypertens.* 23:502–506.
4. Ghezzi, C., H. Murer, and I. C. Forster. 2009. Substrate interactions of the electroneutral Na^+-coupled inorganic phosphate cotransporter (NaPi-IIc). *J. Physiol.* 587:4293–4307.
5. Forster, I. C., N. Hernando, …, H. Murer. 2012. Phosphate transport kinetics and structure-function relationships of SLC34 and SLC20 proteins. *Curr. Top. Membr.* 70:313–356.
6. Virkki, L. V., I. C. Forster, …, H. Murer. 2005. Functionally important residues in the predicted $3^{(rd)}$ transmembrane domain of the type IIa sodium-phosphate co-transporter (NaPi-IIa). *J. Membr. Biol.* 206:227–238.
7. Bacconi, A., L. V. Virkki, …, I. C. Forster. 2005. Renouncing electroneutrality is not free of charge: switching on electrogenicity in a Na^+-coupled phosphate cotransporter. *Proc. Natl. Acad. Sci. USA.* 102:12606–12611.
8. Patti, M., C. Ghezzi, and I. C. Forster. 2013. Conferring electrogenicity to the electroneutral phosphate cotransporter NaPi-IIc (SLC34A3) reveals an internal cation release step. *Pflugers Arch.* 465:1261–1279.
9. Mancusso, R., G. G. Gregorio, …, D. N. Wang. 2012. Structure and mechanism of a bacterial sodium-dependent dicarboxylate transporter. *Nature.* 491:622–626.
10. Fenollar-Ferrer, C., M. Patti, …, L. R. Forrest. 2014. Structural fold and binding sites of the human Na^+-phosphate cotransporter NaPi-II. *Biophys. J.* 106:1268–1279.
11. Mulligan, C., G. A. Fitzgerald, …, J. A. Mindell. 2014. Functional characterization of a Na^+-dependent dicarboxylate transporter from *Vibrio cholerae*. *J. Gen. Physiol.* 143:745–759.
12. Ghezzi, C., A. K. Meinild, …, I. C. Forster. 2011. Voltage- and substrate-dependent interactions between sites in putative re-entrant domains of a Na(+)-coupled phosphate cotransporter. *Pflugers Arch.* 461:645–663.
13. Yernool, D., O. Boudker, …, E. Gouaux. 2004. Structure of a glutamate transporter homologue from *Pyrococcus horikoshii*. *Nature.* 431:811–818.
14. Andrini, O., A. K. Meinild, …, I. C. Forster. 2012. Lithium interactions with Na^+-coupled inorganic phosphate cotransporters: insights into the mechanism of sequential cation binding. *Am. J. Physiol. Cell Physiol.* 302:C539–C554.

15. Remmert, M., A. Biegert, …, J. Söding. 2012. HHblits: lightning-fast iterative protein sequence searching by HMM-HMM alignment. *Nat. Methods.* 9:173–175.

16. Crooks, G. E., G. Hon, …, S. E. Brenner. 2004. WebLogo: a sequence logo generator. *Genome Res.* 14:1188–1190.

17. Šali, A., and T. L. Blundell. 1993. Comparative protein modelling by satisfaction of spatial restraints. *J. Mol. Biol.* 234:779–815.

18. Waterhouse, A. M., J. B. Procter, …, G. J. Barton. 2009. Jalview Version 2—a multiple sequence alignment editor and analysis workbench. *Bioinformatics.* 25:1189–1191.

19. Laskowski, R. A., M. W. Macarthur, …, J. M. Thornton. 1993. PROCHECK—a program to check the stereochemical quality of protein structures. *J. Appl. Cryst.* 26:283–291.

20. Ray, A., E. Lindahl, and B. Wallner. 2010. Model quality assessment for membrane proteins. *Bioinformatics.* 26:3067–3074.

21. Forrest, L. R., C. L. Tang, and B. Honig. 2006. On the accuracy of homology modeling and sequence alignment methods applied to membrane proteins. *Biophys. J.* 91:508–517.

22. Harding, M. M. 2004. The architecture of metal coordination groups in proteins. *Acta Crystallogr. D Biol. Crystallogr.* 60:849–859.

23. Virkki, L. V., I. C. Forster, …, H. Murer. 2005. Substrate interactions in the human type IIa sodium-phosphate cotransporter (NaPi-IIa). *Am. J. Physiol. Renal Physiol.* 288:F969–F981.

24. Andrini, O., C. Ghezzi, …, I. C. Forster. 2008. The leak mode of type II Na(+)-P(i) cotransporters. *Channels (Austin).* 2:346–357.

25. Ehnes, C., I. C. Forster, …, H. Murer. 2004. Structure-function relations of the first and fourth extracellular linkers of the type IIa Na^+/P_i cotransporter: II. Substrate interaction and voltage dependency of two functionally important sites. *J. Gen. Physiol.* 124:489–503.

26. Forster, I., N. Hernando, …, H. Murer. 1998. The voltage dependence of a cloned mammalian renal type II Na^+/P_i cotransporter (NaPi-2). *J. Gen. Physiol.* 112:1–18.

27. Virkki, L. V., J. Biber, …, I. C. Forster. 2007. Phosphate transporters: a tale of two solute carrier families. *Am. J. Physiol. Renal Physiol.* 293:F643–F654.

28. Loo, D. D., X. Jiang, …, E. M. Wright. 2013. Functional identification and characterization of sodium binding sites in Na symporters. *Proc. Natl. Acad. Sci. USA.* 110:E4557–E4566.

29. Yamashita, A., S. K. Singh, …, E. Gouaux. 2005. Crystal structure of a bacterial homologue of Na^+/Cl^--dependent neurotransmitter transporters. *Nature.* 437:215–223.

30. Verdon, G., S. Oh, …, O. Boudker. 2014. Coupled ion binding and structural transitions along the transport cycle of glutamate transporters. *eLife.* 3:e02283.

31. Zdravkovic, I., C. Zhao, …, S. Y. Noskov. 2012. Atomistic models of ion and solute transport by the sodium-dependent secondary active transporters. *Biochim. Biophys. Acta.* 1818:337–347.

32. Köhler, K., I. C. Forster, …, H. Murer. 2002. Identification of functionally important sites in the first intracellular loop of the NaPi-IIa cotransporter. *Am. J. Physiol. Renal Physiol.* 282:F687–F696.

33. Köhler, K., I. C. Forster, …, H. Murer. 2002. Transport function of the renal type IIa Na^+/P(i) cotransporter is codetermined by residues in two opposing linker regions. *J. Gen. Physiol.* 120:693–705.

34. Lambert, G., I. C. Forster, …, H. Murer. 2001. Cysteine mutagenesis reveals novel structure-function features within the predicted third extracellular loop of the type IIa Na(+)/P(i) cotransporter. *J. Gen. Physiol.* 117:533–546.

35. Bezanilla, F., and C. A. Villalba-Galea. 2013. The gating charge should not be estimated by fitting a two-state model to a Q-V curve. *J. Gen. Physiol.* 142:575–578.

36. Sciortino, C. M., and M. F. Romero. 1999. Cation and voltage dependence of rat kidney electrogenic Na(+)-HCO(−)(3) cotransporter, rkNBC, expressed in oocytes. *Am. J. Physiol.* 277:F611–F623.

37. Qu, S., and B. I. Kanner. 2008. Substrates and non-transportable analogues induce structural rearrangements at the extracellular entrance of the glial glutamate transporter GLT-1/EAAT2. *J. Biol. Chem.* 283:26391–26400.

BASIC RESEARCH www.jasn.org

Acute Adaption to Oral or Intravenous Phosphate Requires Parathyroid Hormone

Linto Thomas, Carla Bettoni, Thomas Knöpfel, Nati Hernando, Jürg Biber, and Carsten A. Wagner

Institute of Physiology, University of Zurich, Zurich, Switzerland; and National Centre for Competence in Research, Zurich, Switzerland

ABSTRACT

Phosphate (Pi) homeostasis is regulated by renal, intestinal, and endocrine mechanisms through which Pi intake stimulates parathyroid hormone (PTH) and fibroblast growth factor-23 secretion, increasing phosphaturia. Mechanisms underlying the early adaptive phase and the role of the intestine, however, remain ill defined. We investigated mineral, endocrine, and renal responses during the first 4 hours after intravenous and intragastric Pi loading in rats. Intravenous Pi loading (0.5 mmol) caused a transient rise in plasma Pi levels and creatinine clearance and an increase in phosphaturia within 10 minutes. Plasma calcium levels fell and PTH levels increased within 10 minutes and remained low or high, respectively. Fibroblast growth factor-23, 1,25-(OH)$_2$-vitamin D$_3$, and insulin concentrations did not respond, but plasma dopamine levels increased by 4 hours. In comparison, gastric Pi loading elicited similar but delayed phosphaturia and endocrine responses but did not affect plasma mineral levels. Either intravenous or gastric loading led to decreased expression and activity of renal Pi transporters after 4 hours. In parathyroidectomized rats, however, only intravenous Pi loading caused phosphaturia, which was blunted and transient compared with that in intact rats. Intravenous but not gastric Pi loading in parathyroidectomized rats also led to higher creatinine clearance and lower plasma calcium levels but did not reduce the expression or activity of Pi transporters. This evidence suggests that an intravenous or intestinal Pi bolus causes rapid phosphaturia through mechanisms requiring PTH and downregulation of renal Pi transporters but does not support a role of the intestine in stimulating renal clearance of Pi.

J Am Soc Nephrol 28: ●●●–●●●, 2016. doi: 10.1681/ASN.2016010082

Phosphate (Pi) homeostasis is achieved by the balanced actions of intestinal absorption, renal reabsorption, and bone mineralization/demineralization. Intestinal absorption and renal reabsorption of Pi are mostly mediated by Na$^+$–dependent phosphate (NaPi) cotransporters from the SLC34 family of solute carriers, consisting of the renal NaPi-IIa and NaPi-IIc, and the intestinal NaPi-IIb transporters.[1] The activity and expression of these transporters are downregulated in response to increased dietary Pi intake, whereas Pi deficiency promotes their upregulation.[1,2] The adaptive regulation of renal and intestinal Pi transport is at least in part mediated by several hormones, including fibroblast growth factor-23 (FGF23), 1,25-dihydroxy-vitamin D$_3$ [1,25-(OH)$_2$-vitamin D$_3$], parathyroid hormone (PTH), insulin, and dopamine.[2–6] PTH and FGF23 rise in response to Pi intake and alone or together downregulate renal Pi transporters, increasing phosphaturia.[3,5] Similarly, dopamine stimulates renal Pi excretion by reducing renal Pi transporter activity and expression.[7–9] 1,25-(OH)$_2$-vitamin D$_3$ levels increase during Pi deficiency and enhance renal and intestinal Pi absorption.[3,10–12] Also, insulin stimulates expression of renal Pi transporters and reduces phosphaturia.[13]

Received January 21, 2016. Accepted August 22, 2016.

Correspondence: Prof. Carsten A. Wagner, Institute of Physiology, University of Zurich, Winterthurerstrasse 190, CH-8057 Zurich, Switzerland. Email: Wagnerca@access.uzh.ch

The actions of FGF23, PTH, and 1,25-(OH)$_2$-vitamin D$_3$ are coupled through multiple negative and positive feedback loops.[3,5,14]

However, the exact roles of these hormones in the acute and chronic response to changes in Pi intake are not fully defined. Moreover, the existence and role of additional factors and mediators in the control of Pi homeostasis have been proposed.[15,16] Klotho, a cofactor for FGF23 signaling, also exerts direct effects on renal Pi and calcium transporters independent from FGF23.[5,17,18] MEPE and sFRP4 may act on renal and extrarenal targets to lower plasma Pi.[19–21] Also, the existence of a putative intestinal phosphaturic factor has been postulated on the basis of the rapid phosphaturic effect of duodenal Pi infusion; the absence of changes in plasma Pi, PTH, and FGF23; its independence from renal innervation; and the phosphaturic effect of duodenal extracts from Pi-infused rats.[22] However, in humans, acute enteral and parenteral Pi loads cause dose-dependent changes in phosphaturia only on changes in plasma Pi and PTH, and a similar phosphaturic response is observed with both routes of Pi administration. Thus, in contrast to rodents, the human data are not consistent with the presence of an intestinal Pi sensor.[23] Local Pi sensing mechanisms in kidney and other organs may be involved in sensing changes in dietary Pi intake and may mediate or modulate some of the effects on renal Pi handling. Evidence for Pi sensing has been obtained from isolated parathyroid gland cells *in vitro*,[24,25] the opossum kidney–derived OK cell line,[26,27] bone, and vascular cells[28–30]

The aim of this study was to investigate the endocrine, mineral, and renal responses to acute Pi loading in rats and test for evidence for a role of the intestine in determining the adaptive response by administering Pi either intravenously or intragastrically.

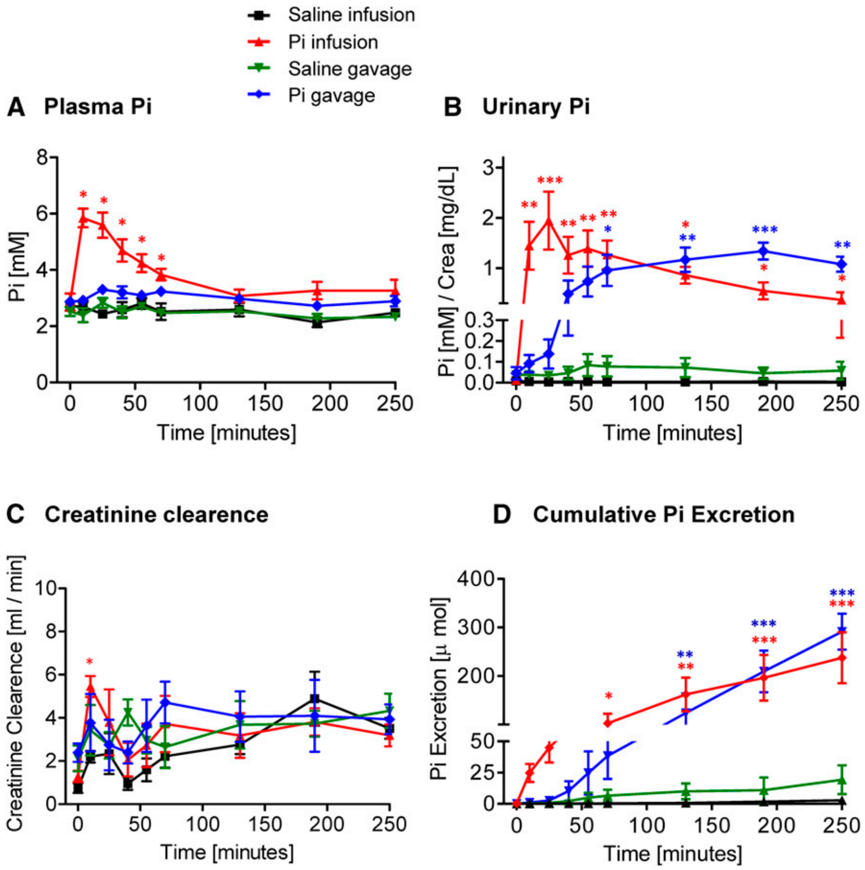

Figure 1. Effect of intravenous and intragastric administration of Pi on body Pi distribution and renal excretion in intact rats. Rats were loaded with 500 μmol Pi or saline intravenously or orally. (A) Plasma Pi, (B) urinary Pi/creatinine, (C) creatinine clearance, and (D) cumulative Pi excretion. Four profiles are shown: saline intravenous infusion (black), Pi intravenous infusion (red), saline intragastric gavage (green), and Pi intragastric gavage (blue). Data are presented as the means±SEM. ANOVA test; *n*=5–9 per group and time point. **P*<0.05 versus time 0; ***P*<0.01 versus time 0; ****P*<0.001 versus time 0.

RESULTS

Pi Loading Rapidly Elicits Phosphaturia

Intravenous infusion of a Pi bolus (500 μmol Pi) caused a rapid and transient increase in plasma Pi concentration in intact rats (Figure 1A), with a peak after 10 minutes. Two hours after infusion, plasma Pi had returned to baseline values. A significant, although blunted, increase in plasma Pi was observed after 10 minutes on infusion of 150 μmol Pi but not with 50 μmol Pi (Supplemental Figure 1A). In contrast, plasma Pi did not change in rats gavaged with 500 μmol Pi (Figure 1A). The concentration of plasma Pi remained normal after intravenous or intragastric administration of 500 or 150 μmol NaCl (Figure 1A, Supplemental Figure 2A).

Intravenous infusion of 500 μmol Pi rapidly and strongly increased urinary Pi excretion within 10 minutes. Although phosphaturia tended to decrease after 30 minutes, it remained high over 4 hours after administration (Figure 1B). Infusions of 150 and 50 μmol Pi failed to induce any significant phosphaturic response (Supplemental Figure 1B). Intragastric administration of 500 μmol Pi increased urinary excretion of Pi to a similar extent as intravenous administration; however, the onset of phosphaturia was delayed compared with infusion, reaching significance only 60 minutes after the Pi bolus (Figure 1B). Phosphaturia remained high over 4 hours postgavage (Figure 1B). Changes in the fractional excretion of Pi after the Pi bolus paralleled urinary Pi concentration (Supplemental Figure 3A). Neither intravenous infusion nor gavage of 500 or 150 μmol NaCl affected the urinary excretion of Pi (Figure 1B, Supplemental Figure 2B).

Creatinine clearance significantly increased within 10 minutes after intravenous application of 500 μmol Pi and thereafter, rapidly normalized (Figure 1C). Intragastric loading with 500 μmol Pi did not alter creatinine clearance (Figure 1C). Similarly, administration of 500 or 150 μmol NaCl by infusion or gavage had no effect (Figure 1C) (data not shown).

The cumulative urinary excretion of Pi showed a similar level after 4 hours of the oral or intravenous bolus (Figure 1D). Although a delay was observed in the gavage group, both groups had excreted comparable amounts of Pi 4 hours post-application, with mean values of around 230 and 280 μmol Pi, respectively, representing about 50%–60% of the initial Pi load (500 μmol).

To examine possible organ storage of the nonexcreted Pi, we assessed the Pi content in femurs, liver, and skeletal muscle in tissues from rats infused and gavaged with Pi or NaCl. As expected, the concentration of Pi in femurs was higher (10–20 times) than in the other two organs (Supplemental Figure 4). However, in all three tissues, similar levels of Pi were measured in samples from control and Pi-loaded rats.

The concentration of total Ca^{2+} in plasma slightly but significantly decreased on intravenous infusion of 500 μmol Pi (Figure 2A). The reduction was already detectable 10 minutes after the Pi bolus, and although it tended to normalize at the latest time points, plasma Ca^{2+} remained low until the end of the experiment (4 hours). Similar changes were observed on Pi infusion with 150 μmol Pi but not observed with 50 μmol Pi (Supplemental Figure 1C). In contrast, total plasma Ca^{2+} did not change significantly after intragastric administration of 500 μmol Pi (Figure 2A). Infusion or gavage with either 500 or 150 μmol NaCl did not alter total plasma Ca^{2+} (Figure 2A, Supplemental Figure 2C).

The urinary excretion of Ca^{2+} remained unchanged after intravenous or intragastric Pi or NaCl application (Figure 2B, Supplemental Figures 1D and 2D). However, infusion with Pi or NaCl caused a small, nonsignificant, and transient increase in urinary Ca^{2+} excretion, possibly reflecting an acute volume load (Figure 2B).

Pi Loading Causes an Immediate PTH Rise

In intact animals, intravenous infusion of 500 μmol Pi increased plasma intact PTH levels sixfold within 10 minutes, whereas in gavaged rats, a twofold increase was detected after 25 minutes, paralleling or even preceding the increase in urinary Pi excretion (Figure 3A). In both cases, PTH remained high 4 hours after Pi administration (Figure 3A). No changes in the plasma levels of intact FGF23 (Figure 3B), 1,25-$(OH)_2$-vitamin D_3 (Figure 3C), and insulin (Figure 3D) were observed in rats after Pi administration. Plasma dopamine significantly increased at 4 hours after 500 μmol Pi infusion but not gavage (Figure 3E), whereas urine dopamine was not altered (Figure 3F). Infusion and gavage with saline had no effect on the hormones analyzed.

The Pi Load Reduces Renal Pi Transporter Activity and Expression

Flux measurements of ^{32}Pi and ^{3}H-D-glucose were performed in brush border membrane vesicles (BBMVs) isolated from kidneys collected 40 minutes and 4 hours after 500 μmol Pi or saline application to assess proximal tubular luminal Pi transporter activity. In BBMVs from kidneys extracted 40 minutes after application, all ^{32}Pi uptake components were similar in Pi-loaded and control samples (Figure 4, A and B). Similarly, no differences were detected for the Na^+-dependent uptake of D-glucose (Figure 4E). In contrast, the total Na^+–dependent as well as SLC34–mediated ^{32}Pi transport activities were reduced in kidneys 4 hours after infusion with 500 μmol Pi (Figure 4C). ^{32}Pi fluxes also decreased, although nonsignificantly, in the Pi-gavaged animals after 4 hours (Figure 4D). The Na^+-dependent uptake of D-glucose remained unaffected for 4 hours in Pi-infused or -gavaged animals (Figure 4F).

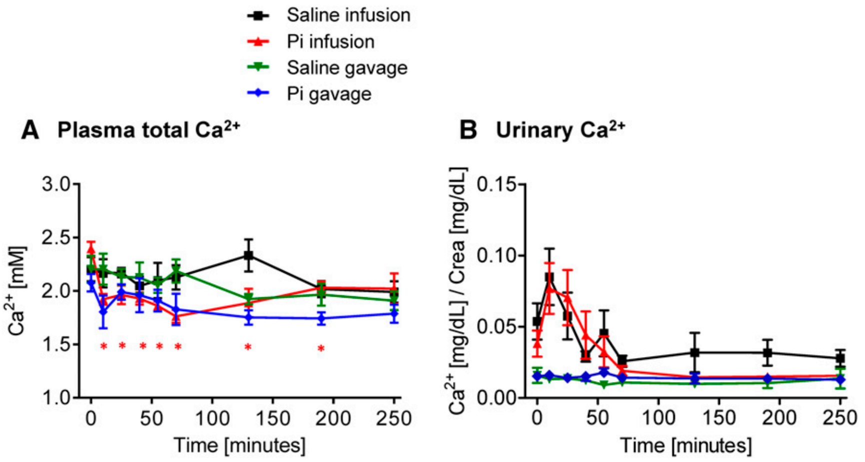

Figure 2. Effect of intravenous and intragastric administration of Pi on Ca^{2+} plasma levels and urinary excretion in intact rats. Rats were loaded with 500 μmol Pi or saline intravenously or orally. (A) Plasma Ca^{2+} and (B) urinary Ca^{2+}/creatinine. Four profiles are shown: saline intravenous infusion (black), Pi intravenous infusion (red), saline intragastric gavage (green), and Pi intragastric gavage (blue). Data are presented as the means±SEM. ANOVA test; n=5–9 per group and time point. *$P<0.05$ versus time 0.

The abundance of the major renal Pi transporters NaPi-IIa and NaPi-IIc in renal BBMVs isolated 40 minutes after infusion or gavage with Pi or saline was unchanged (Figure 5, A and B). The abundance of both cotransporters was significantly reduced in kidneys collected 4 hours after infusion

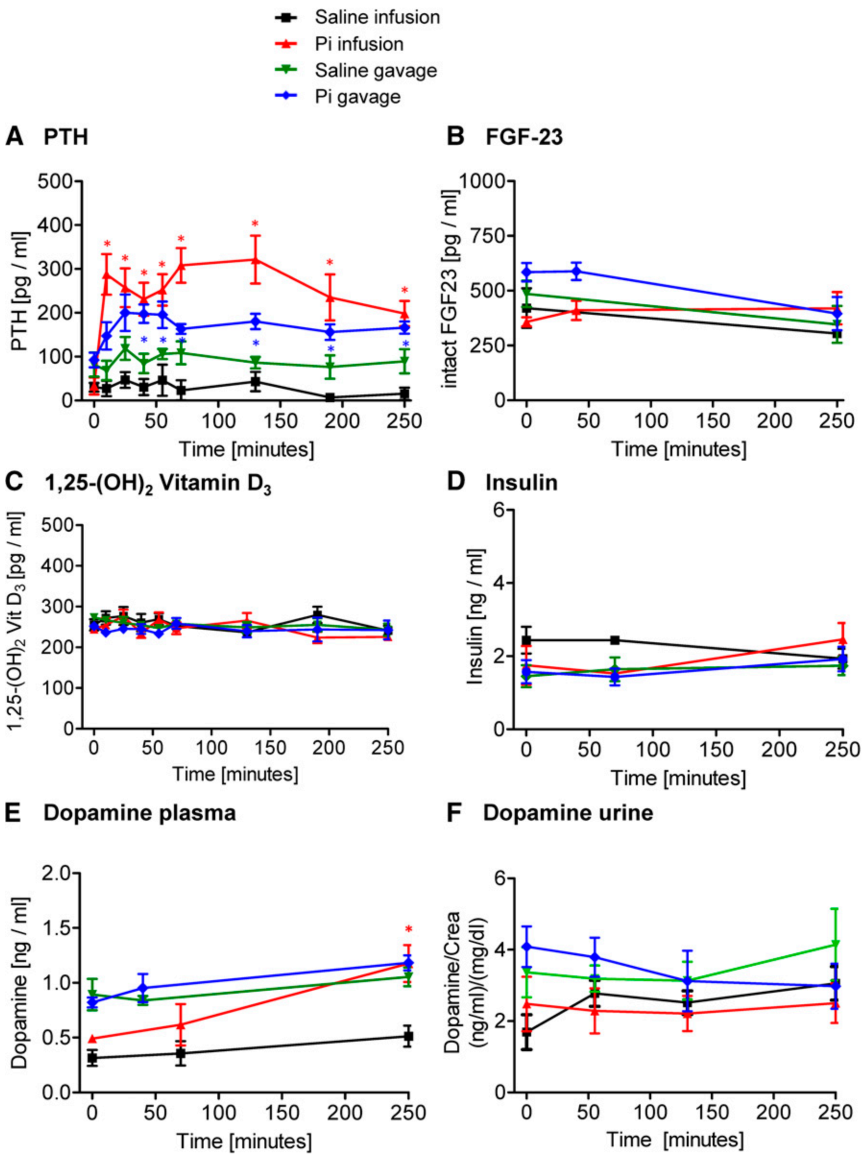

Figure 3. Effect of intravenous and intragastric administration of Pi on hormonal levels in intact rats. Rats were loaded with 500 μmol Pi or saline intravenously or orally. (A) Plasma intact PTH, (B) plasma intact FGF23, (C) plasma 1,25-(OH)$_2$-vitamin D$_3$, (D) plasma insulin, (E) plasma dopamine, and (F) urine dopamine. Four profiles are shown: saline intravenous infusion (black), Pi intravenous infusion (red), saline intragastric gavage (green), and Pi intragastric gavage (blue). Data are presented as the means±SEM. ANOVA test; *n*=5–9 per group and time point. *$P<0.05$ versus time 0.

with 500 μmol Pi (Figure 5C), whereas the expression of NaPi-IIa but not NaPi-IIc was diminished 4 hours after intragastric loading (Figure 5D).

PTH Is Required to Clear the Acute Phosphate Load

Because PTH increased very rapidly on Pi loading and paralleled or even preceded phosphaturia, we tested the role of PTH in the adaptive response in parathyroidectomized (PTX) rats. Infusion of 500 μmol Pi caused a rapid increase in plasma Pi in PTX rats (Figure 6A), peaking after 10 minutes and decreasing thereafter. However, whereas the levels of Pi fully normalized within 2 hours postinfusion in intact rats, Pi levels remained elevated until the end of the experiment in PTX animals (Figure 6A). Gavage of 500 μmol Pi in PTX rats induced a slow rise in plasma Pi (Figure 6A) in contrast with the lack of effect of the Pi gavage in intact animals (Figure 1A). Administration of saline to PTX rats by infusion or gavage did not alter plasma Pi (Figure 6A).

Infusion with 500 μmol Pi induced a fast but small increase in urinary excretion of Pi in PTX rats (Figure 6B). Maximal phosphaturia was detected 10 minutes postinfusion, similar to in intact animals (Figure 1B). However, phosphaturia returned to baseline within 2 hours after infusion in PTX rats, despite elevated plasma Pi levels (Figure 6B). Moreover, gavage of Pi in PTX rats failed to elicit any significant phosphaturia (Figure 6B). Neither infusion nor gavage with saline affected urinary Pi (Figure 6B).

In PTX rats, creatinine clearance increased within 10 minutes of 500 μmol Pi infusion and rapidly normalized thereafter, whereas it was not altered with either Pi gavage or saline administration (Figure 6C).

The cumulative urinary excretion of Pi over 4 hours in PTX rats infused with 500 μmol Pi was of about 30 μmol (Figure 6D), equivalent to about 6% of the Pi load. The cumulative urinary excretion of Pi over 4 hours in PTX rats receiving Pi by gavage was about 3 μmol (Figure 6D), representing $<1\%$ of the Pi load.

The content of Pi was higher in femurs than liver and muscle in PTX animals, and no differences were found between organs extracted from saline-treated and Pi-loaded rats (Supplemental Figure 5).

Plasma total Ca^{2+} decreased slightly within 10 minutes on 500 μmol Pi infusion in PTX rats (Figure 7A) and remained low until the end of the experiment. In contrast, plasma total Ca^{2+} did not change significantly in Pi–gavaged PTX rats (Figure 7A). Administration of 150 μmol NaCl by infusion or gavage did not alter plasma Ca^{2+}.

Urinary excretion of Ca^{2+} in PTX showed no significant changes after administration of Pi or saline (Figure 7B).

As expected, plasma PTH was undetectable in PTX rats under all conditions (Figure 8A). In contrast to intact rats, FGF23 was elevated in PTX animals 4 hours after oral or intravenous Pi loading (Figure 8B). The plasma concentrations of 1,25-(OH)$_2$-vitamin D$_3$ (Figure 8C), insulin (Figure 8D), and

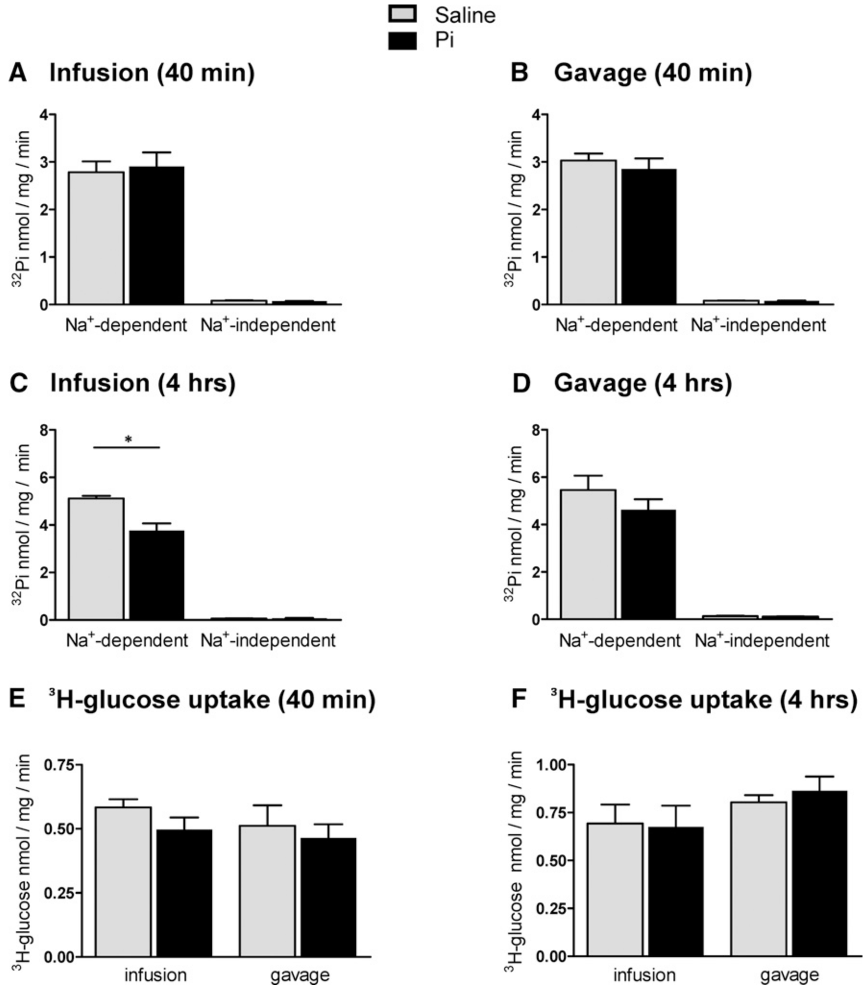

Figure 4. Effect of intravenous and intragastric administration of Pi on Pi and glucose transport activities in renal BBMVs from intact rats. Rats were loaded with 500 μmol Pi or saline intravenously or orally. Kidneys were extracted 40 minutes or 4 hours after infusion or gavage, and Na$^+$–dependent and –independent Pi and glucose transport activities were measured. Pi transport was assayed in the presence or absence of the SLC34 transport inhibitor phosphonoformic acid. (A) ^{32}P uptakes 40 minutes after intravenous infusion of saline (gray bars) and Pi (black bars). (B) ^{32}P uptakes 40 minutes after intragastric administration of saline (gray bars) and Pi (black bars). (C) ^{32}P uptakes 4 hours after intravenous infusion of saline (gray bars) and Pi (black bars). (D) ^{32}P uptakes 4 hours after intragastric administration of saline (gray bars) and Pi (black bars). (E) ^{3}H-D-glucose uptakes 40 minutes after intravenous and intragastric administration of saline (gray bars) and Pi (black bars). (F) ^{3}H-D-glucose uptakes 4 hours after intravenous and intragastric administration of saline (gray bars) and Pi (black bars). Data are presented as the means±SEM. Unpaired *t* test; *n*=5–9 per group and time point. **P*<0.05 versus saline group.

dopamine (Figure 8E) as well as urine dopamine (Figure 8F) remained unchanged under all conditions.

PTH Downregulates Renal Pi Transporters in Response to Acute Pi Loading

Flux measurements of ^{32}Pi and ^{3}H-D-glucose in BBMVs from PTX rat kidneys collected 4 hours postloading were similar in samples from Pi-loaded rats and controls (Figure 9). The protein abundances of NaPi-IIa and NaPi-IIc in PTX rats were similar in the Pi-loaded and saline-treated animals 4 hours postadministration (Figure 10).

DISCUSSION

Acute and chronic changes in plasma Pi elicit adaptive responses in several hormones that regulate renal and intestinal epithelia–(re)absorbing Pi.[1–3] High dietary Pi increases the phosphaturic hormones PTH, FGF23, and dopamine while decreasing the levels of 1,25-$(OH)_2$-vitamin D_3,[6–7,31] resulting in reduced expression and activity of NaPi cotransporters in renal and intestinal epithelia, blunting intestinal Pi absorption, and increasing urinary excretion. However, there are conflicting data regarding the sequence of events triggered by high dietary Pi as well as the nature of the trigger itself. PTH may have a key role in the acute renal response, with other hormones coming into play only later on,[23,32–34] but the presence of yet–unidentified intestinal factor(s) stimulating renal Pi excretion independent from PTH has been proposed.[22] Here, we administered a Pi load to rats both intravenously (to bypass the gastrointestinal tract) and intragastrically and compared the acute responses in intact and PTX animals.

Our data show that, compared with equimolar NaCl infusions and the time point 0, the acute infusion of Pi elicited a dose-dependent response that consisted at the highest dose of (*1*) an immediate but transient rise in plasma Pi, (*2*) an early and transient increase in creatinine clearance, (*3*) a rapid phosphaturic response, (*4*) a fall in plasma total calcium, (*5*) a rapid and sustained phosphaturia, and (*6*) a reduced expression and activity of renal Pi transporters. Intragastric application of Pi caused a qualitatively similar response in the cumulative Pi excretion without a significant change in creatinine clearance and with no obvious hyperphosphatemia, a lower and delayed rise in PTH, a nonsignificant reduction in renal Pi transporter activity and lower expression of only NaPi-IIa but not NaPi-IIc, and a slower onset in phosphaturia. Infusion or gavage of NaCl had no effects.

Several points are of major interest: the onset of phosphaturia is paralleled by a rise in PTH in infused and gavaged

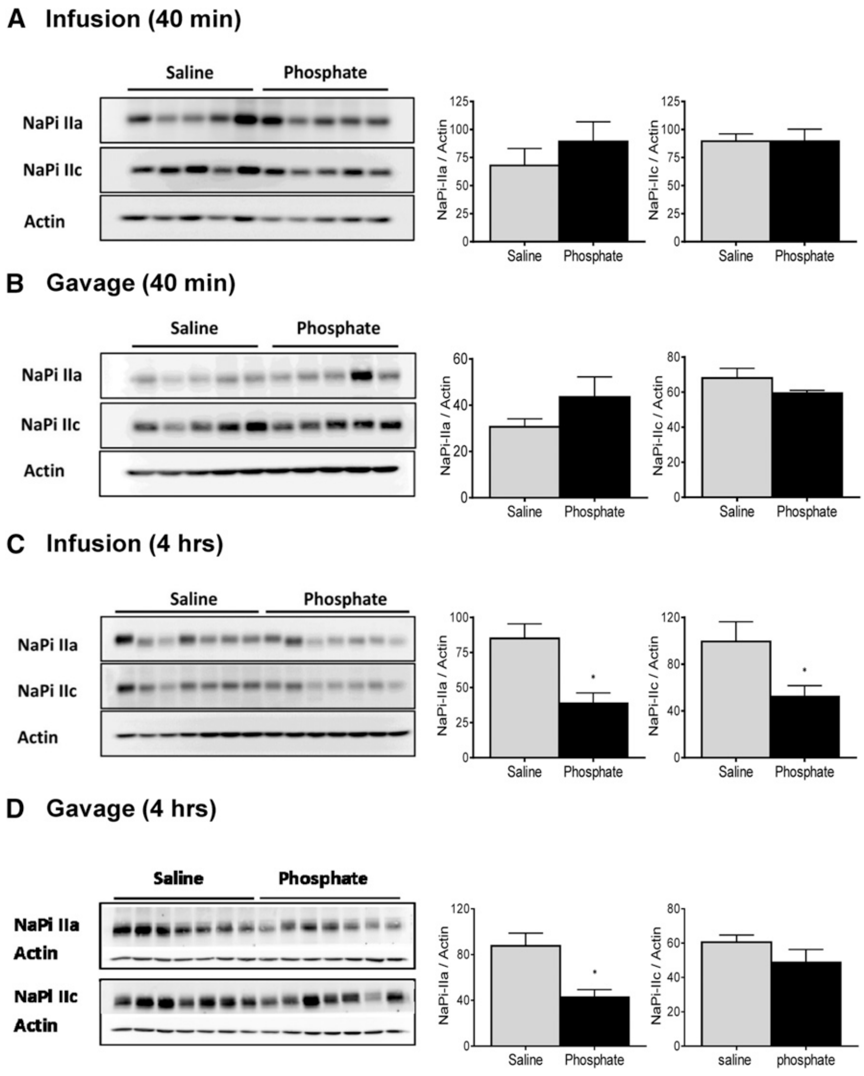

A Infusion (40 min)

B Gavage (40 min)

C Infusion (4 hrs)

D Gavage (4 hrs)

Figure 5. Effect of intravenous and intragastric administration of Pi on the expression of renal NaPi cotransporters in intact rats. Rats were loaded with 500 μmol Pi or saline intravenously or orally. Kidneys were extracted 40 minutes or 4 hours postadministration, and the abundance of NaPi-IIa and NaPi-IIc in brush border membranes was determined by Western blot. Expression of cotransporters (A) 40 minutes after intravenous infusion of saline (gray bars) and Pi (black bars), (B) 40 minutes after intragastric administration of saline (gray bars) and Pi (black bars), (C) 4 hours after intravenous infusion of saline (gray bars) and Pi (black bars), and (D) 4 hours after intragastric administration of saline (gray bars) and Pi (black bars). Unpaired *t* test; *n*=5–9 per group and time point. $^*P<0.05$ versus saline group.

animals and precedes changes in plasma dopamine, whereas levels of 1,25-$(OH)_2$-vitamin D_3, FGF23, insulin, and urine dopamine were not altered, suggesting an important role of PTH. Early phosphaturia (40 minutes) occurred in infused animals without obvious changes in the activity or abundance of renal Pi transporters expressed in the brush border membrane of the proximal tubule, which may be explained at least in part by a higher tubular load in the infused animals, because creatinine clearance had more than doubled and plasma Pi levels were elevated. However, we noted also a partial dissociation between the degree of phosphaturia, Pi transport activities in BBMVs, and the abundance of the NaPi-IIa and NaPi-IIc transporters as most evident in the Pi-gavaged group after 4 hours. Activity of NaPi-IIa transporters in the brush border membrane is influenced by lipid composition of the plasma membrane and *in situ* cleavage by klotho and possibly, regulated association with and dissociation from NHERF1 through phosphorylation of NHERF1 stimulated by PTH or dopamine.[17,35–37] We did not obtain evidence for cleavage of NaPi-IIa as evident from immunoblotting, but changes in lipid composition or NHERF1 phosphorylation were not tested and may contribute to the dissociation of transport activity and NaPi-IIa abundance.

Plasma PTH rises *in vivo* and *in vitro* in response to a fall in ionized calcium or an increase in Pi concentrations. Whether the response to Pi is independent from calcium has remained unclear, because Pi retains its ability to stimulate PTH secretion, even in the absence of a measurable fall in ionized or total calcium.[23–25,33,38] Along the same line, *in vitro* incubation of human parathyroid glands with escalating concentrations of Pi while keeping ionized calcium constant stimulated PTH secretion.[24,38] However, inhibitors of calcium–stimulated receptor–mediated PTH secretion (calcimimetics) have been shown to suppress Pi–induced PTH secretion *in vivo*, suggesting a role of the calcium-stimulated receptor, even in the absence of changes of ionized calcium levels.[25] Here, plasma total calcium decreased in parallel with the rise in PTH, allowing no clear distinction between a calcium-dependent or -independent mechanism. However, infusion of 150 μmol Pi caused a similar fall in plasma total calcium as 500 μmol Pi, but the rise in PTH was blunted and detected only 10 minutes postadministration, suggesting that Pi may stimulate PTH release synergistically or independently. The early response of PTH found in our animal model is consistent with experiments in humans and other rodent models.[23,32,33]

PTH is critical for the early response to Pi, independent from the route of application. In PTX rats, massive and sustained hyperphosphatemia developed with a more pronounced fall in plasma total calcium than in intact rats. There was a small and transient increase in renal Pi excretion in the Pi–infused PTX group that is most likely attributable to the

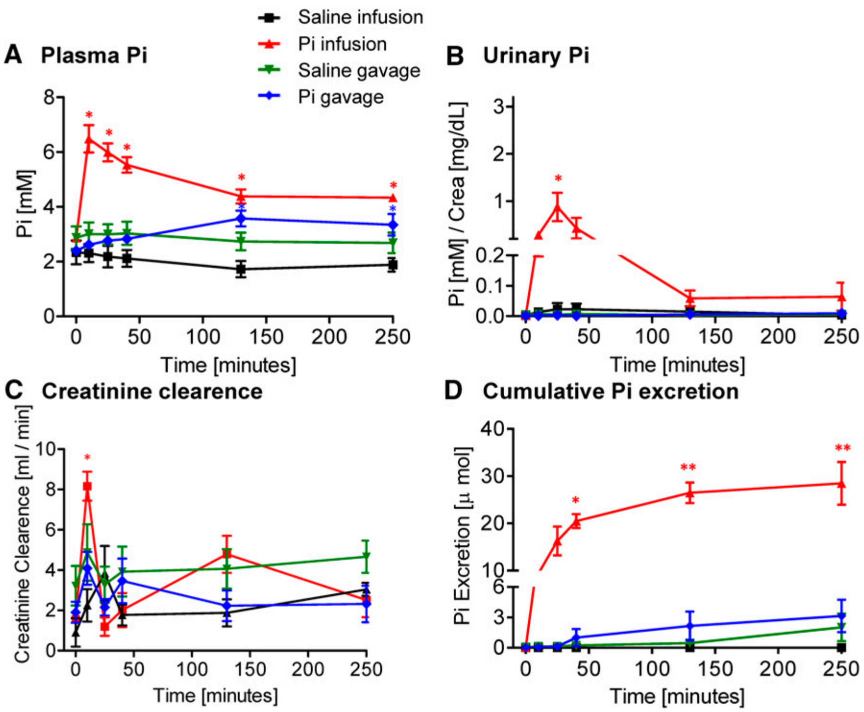

Figure 6. Effect of intravenous and intragastric administration of Pi on renal excretion in PTX rats. PTX rats were loaded with 500 μmol Pi or saline intravenously or orally. (A) Plasma Pi, (B) urinary Pi/creatinine, (C) creatinine clearance, and (D) cumulative Pi excretion. Four profiles are shown: saline intravenous infusion (black), Pi intravenous infusion (red), saline intragastric gavage (green), and Pi intragastric gavage (blue). Data are presented as the means±SEM. ANOVA test; n=4–6 per group and time point. *$P<0.05$ versus time 0; **$P<0.01$ versus time 0.

combination of hyperphosphatemia and elevated GFR (as indicated by higher creatinine clearance). Phosphaturia ceased after normalization of creatinine clearance and the fall of plasma Pi below about 5 mM. The transient increase in creatinine clearance in the Pi-infused animals is independent from PTH and may involve other Pi–sensitive mechanisms. The rise in plasma Pi and/or the fall in plasma calcium may be (in)direct triggers affecting factors controlling glomerular filtration, such as vascular tone of afferent and/or efferent arterioles, where calcium channels play an important role.[39] PTH is also required for the downregulation of renal Pi transporters after 4 hours, because this response was also blunted in PTX rats. Thus, our results show that PTH is required for the early response to high Pi intake.

We detected only small or no changes in FGF23, 1,25-(OH)$_2$-vitamin D$_3$, insulin, and dopamine. The increase in dopamine or FGF23 was found only at the latest time point and is probably not responsible for the massive phosphaturia at earlier time points. In Pi–infused intact rats, the late rise in plasma dopamine (but not in urine) may enhance PTH-induced phosphaturia. Dopamine acts *via* D$_1$ receptors to downregulate NaPi-IIa in proximal tubules.[7–9] The increase in FGF23 in PTX rats occurs between 50 and 240 minutes after the Pi bolus (because of the small volumes of blood that could be collected, only a few FGF23 determinations were possible). This finding suggests first that, in the absence of PTH, FGF23 levels adapt more acutely to the Pi overload and second, that systemic Pi can regulate FGF23 production and/or stability independently of PTH. Interestingly, FGF23 production by osteocytes is not directly regulated by Pi[40] and instead, requires previous production of PTH and activation of protein kinase A and Wnt pathways by PTHR1[23,41,42]

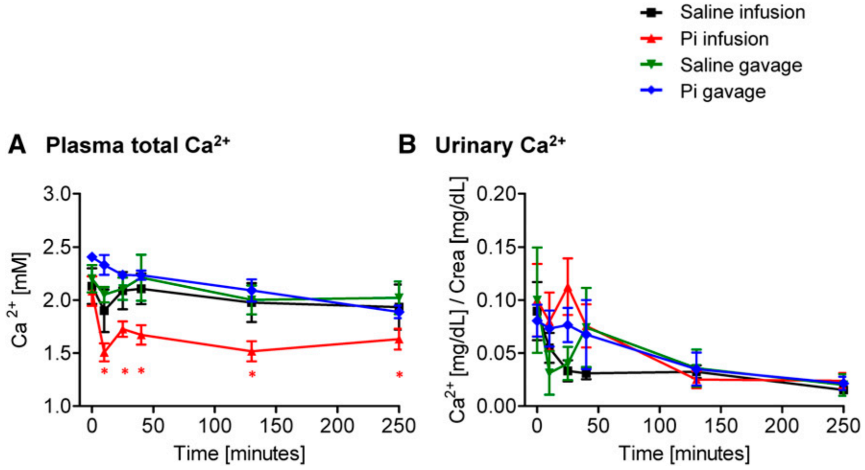

Figure 7. Effect of intravenous and intragastric administration of Pi on Ca^{2+} plasma levels and urinary excretion in PTX rats. PTX rats were loaded with 500 μmol Pi or saline intravenously or orally. (A) Plasma Ca^{2+} and (B) urinary Ca^{2+}/creatinine. Four profiles are shown: saline intravenous infusion (black), Pi intravenous infusion (red), saline intragastric gavage (green), and Pi intragastric gavage (blue). Data are presented as the means±SEM. ANOVA test; n=4–6 per group and time point. *$P<0.05$ versus time 0.

Intestinal Pi sensors and an intestine–derived phosphaturic factor had been postulated on the basis of experiments with rats infused with Pi into duodenum. This mechanism would allow for a rapid crosstalk between intestine and kidney and provide a feedforward mechanism preventing a potentially detrimental hyperphosphatemia.[22] The existence of such feedforward mechanisms has been shown for potassium and salt.[43–46] However, Scanni *et al.*[23] had found, in healthy humans, that the rate of elimination and overall quantity of Pi excretion did not depend

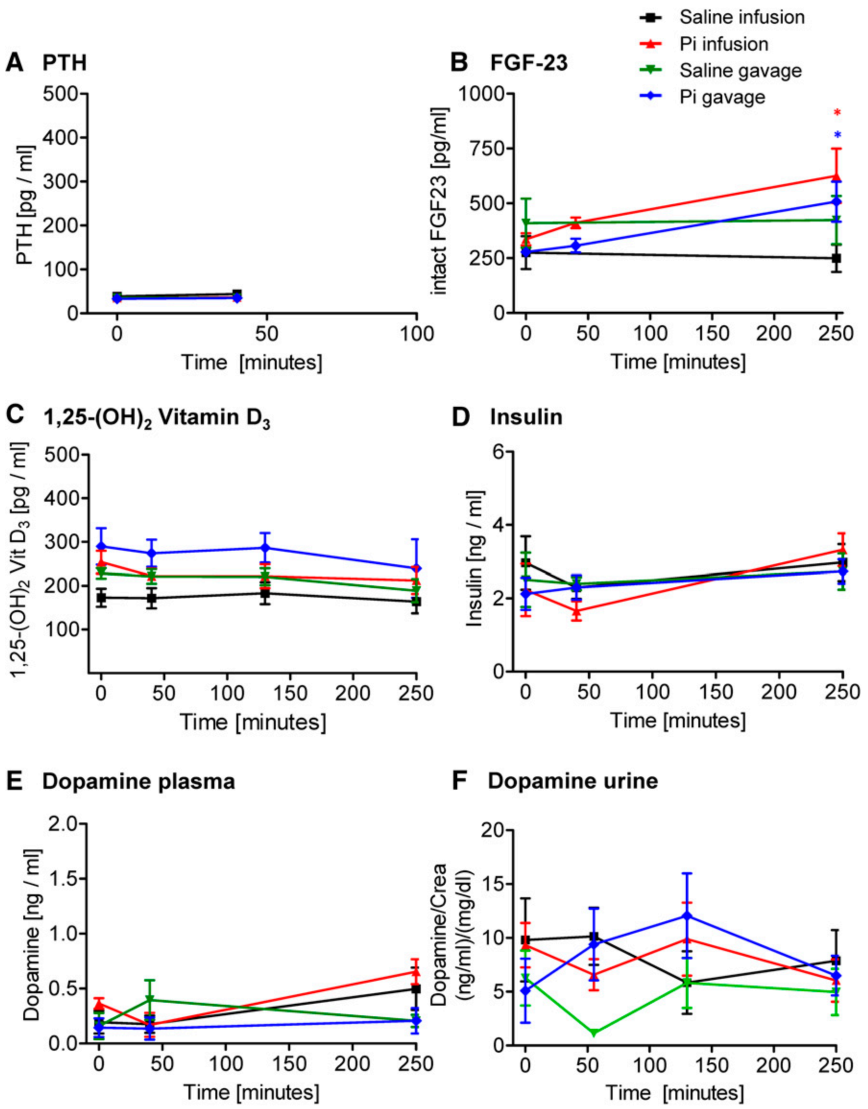

Figure 8. Effect of intravenous and intragastric administration of Pi on hormonal levels in PTX rats. PTX rats were loaded with 500 μmol Pi or saline intravenously or orally. (A) Plasma intact PTH, (B) plasma intact FGF23, (C) plasma 1,25-(OH)$_2$-vitamin D$_3$, (D) plasma insulin, (E) plasma dopamine, and (F) urine dopamine. Four profiles are shown: saline intravenous infusion (black), Pi intravenous infusion (red), saline intragastric gavage (green), and Pi intragastric gavage (blue). Data are presented as the means±SEM. ANOVA test; *n*=4–6 per group and time point. *$P<0.05$ versus time 0.

on the route of application (intravenous versus intraduodenal infusion). Consistently, our data do not provide any evidence for a role of the intestine in promoting phosphaturia. Moreover, in the absence of PTH, no phosphaturia could be elicited by intragastric Pi infusions.

The cumulative urinary elimination of the Pi bolus reached only about 50%–60% after 4 hours in intact animals, whereas normophosphatemia was achieved much faster, suggesting that a large amount of Pi had been eliminated by other routes (*i.e.*, intestinal tract), extravasated and accumulated in tissues, or complexed in blood into a pool that is not measurable by the Fiske–Subbarow method. Scanni *et al.*[23] showed that urinary excretion of Pi accounted for 100% of the intravenous Pi overload in humans, but full elimination required 120 hours; the authors rule out a contribution of the gastrointestinal tract in the elimination of Pi. We quantified the Pi content in femurs as well as liver and skeletal muscle. Pi content in bones is much higher than in the other two organs, and the measured values were so high that a rough estimation of the total amount of Pi stored in the skeleton (assuming a 10% contribution to body weight and a comparable composition of all bones) suggests that, even if all of the nonexcreted Pi would have been accumulated in bones, this would only result in a small change of content (approximately 0.5%), nondetectable with the Fiske–Subbarow method. Although similar estimations predicted that partial accumulation of Pi in liver and skeletal muscle could be detectable, we failed to observe any changes. Thus, other approaches should be used to identify the organs responsible for a transient accumulation of a large excess of Pi.

In summary, our data indicate that (*1*) normophosphatemia is rapidly re-established after intravenous and intragastric Pi loading by mechanisms largely depending on the ability of the kidneys to excrete Pi; (*2*) an efficient phosphaturic response requires increased levels of PTH and reduced expression of renal Pi transporters; (*3*) these compensatory responses are, to a major extent, similar, regardless of whether Pi bypasses the gastrointestinal tract; and (*4*) reduced plasma Ca^{2+} together with elevated Pi may trigger the secretion of PTH in intravenously loaded animals. Our findings leave two major issues unresolved, namely the identity of the compartment responsible for the rapid quenching of a large fraction of the loaded Pi and the nature of the signal that triggers the stimulation of PTH release.

CONCISE METHODS

Animal Experimental Protocol

Male Wistar rats (Charles River Laboratories, Wilmington, MA) weighing 250–350 g were adapted to a low-Pi diet (0.1%) for 5 days. After an overnight fast in metabolic cages with free access to water, animals were anesthetized with 3% isoflurane/air and placed on a heated pad to maintain body temperature at 37°C–38°C. Rats inhaled

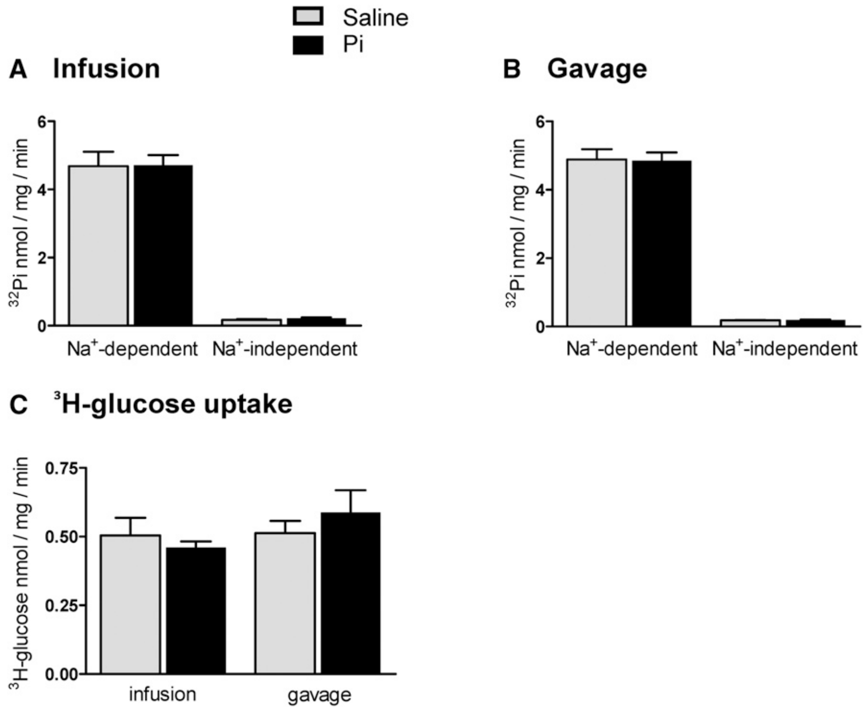

Figure 9. Effect of intravenous and intragastric administration of Pi on Pi and glucose transport activities in renal BBMVs from PTX rats. PTX rats were loaded with 500 μmol Pi or saline intravenously or orally. Kidneys were extracted 4 hours after infusion or gavage, and Na^{+}–dependent and –independent Pi and glucose transport activities in isolated BBMVs were measured. Pi transport was assayed in the presence or absence of the SLC34 transport inhibitor phosphonoformic acid. (A) ^{32}P uptakes 4 hours after intravenous infusion of saline (gray bars) and Pi (black bars), (B) ^{32}P uptakes 4 hours after intragastric administration of saline (gray bars) and Pi (black bars), and (C) ^{3}H-D-glucose uptakes 4 hours after intravenous and intragastric administration of saline (gray bars) and Pi (black bars). Data are presented as the means±SEM. Unpaired test; *n*=4–6 per group and time point.

constantly a low dose of anesthesia (1%–2% isoflurane/air) until the end of the experiment. Catheters (BPE-T 50; Instech) were placed into the femoral vein, femoral artery, and urinary bladder (for infusion of solutions and collection of blood and urine, respectively). A Ringer solution (116 mM NaCl, 1.2 mM KCl, 1 mM $CaCl_2$, and 2.7 mM $NaHCO_3$) containing 5% glucose was infused continuously at a rate of 3.0 ml/h until the end of the experiment. To determine baseline values, blood and urine samples were collected over a period of 30 minutes after the start of the Ringer infusion. In the infusion protocol, 1 ml either Na_2HPO_4/NaH_2PO_4 (500, 150, or 50 mM; pH 7.4) or NaCl (500 or 150 mM; pH 7.4) was infused immediately after the baseline sampling within 2–3 minutes. For gavage, 1 ml either 500 mM NaH_2PO_4/Na_2HPO_4 (pH 5) or NaCl (500 or 150 mM; pH 5) was administered directly into the stomach by using a gavage tube (FTP-15–100; Instech). Blood and urine samples were collected at different time intervals postinfusion or postgavage. At the end of sample collections (40 minutes or 4 hours), the animals were euthanized, and blood, kidneys, intestine (duodenum, jejunum, and ileum), liver, muscle, and femur were harvested. Blood samples (both from intermediate time points and at termination) were centrifuged immediately on collection, and plasma was aliquoted. Plasma and organs were store at −80°C until further used.

In addition, an identical experimental protocol to the one described above was performed in 350–450 g PTX male rats (Charles River Laboratories) receiving 1% calcium gluconate in drinking water.

All animal experiments were according to Swiss and international laws of animal protection, and all protocols were approved by the appropriate local veterinary authority (Kantonales Veterinäramt Zürich).

General Analytic Measurements

The concentration of Pi in plasma and urine was determined according to the Fiske–Subbarow method (Randox). Plasma and urinary levels of calcium were measured using a Quantichrom Calcium Kit from Bioassay System. The concentration of creatinine in plasma was enzymatically measured using a peroxidase-antiperoxidase-creatinine kit (Biomed), whereas urinary creatinine was measured according to the Jaffe method. Fractional excretion of Pi was calculated using the formula: [urine Pi × plasma creatinine]×100/[plasma Pi × urine creatinine]. The creatinine clearance was estimated from plasma and urinary creatinine concentrations and urine volume.

The concentration of glucose in plasma was measured by using Accu-Chek (Roche, Basel, Switzerland). ELISA kits were used to measure the concentrations in plasma and/or of intact PTH (Immutopic), intact FGF23 (Kainos), insulin (Crystal Chem Inc.), and dopamine (LDN). Plasma 1,25-$(OH)_2$-vitamin D_3 was determined with an RIA kit from IDS. Protein concentrations in renal brush border membranes were determined with the Bio-Rad Protein Assay (Bio-Rad, Hercules, CA).

Isolation of Renal BBMVs and Flux Measurements of ^{32}Pi and ^{3}H-Glucose

Kidney cortex and medulla were dissected from frozen kidneys and homogenized in a buffer containing 300 mM mannitol, 5 EGTA, and 12 Tris-HCl, pH 7.1; BBMVs were isolated according to the Mg^{2+} precipitation method as described in detail.[47] Uptake of ^{32}Pi and ^{3}H-glucose was measured in three different solutions, all three containing 300 mM mannitol plus 20 mM HEPES-Tris, pH 7.4 and 125 mM NaCl, 125 mM KCl, or 125 mM NaCl. The uptake solutions contained either 0.125 μM K_2HPO4/KH_2PO_4, pH 7.4 as cold substrate and ^{32}Pi as a tracer or 0.125 μM D-glucose as cold substrate and ^{3}H-D-glucose as tracer. To measure the incorporation of ^{32}Pi/^{3}H-glucose, 10 μl freshly prepared BBMVs were incubated for 1 minute or 2 hours with 40 μl different uptake solutions. The 1-minute time point was chosen, because ^{32}Pi/^{3}H-glucose uptake was in the linear phase of

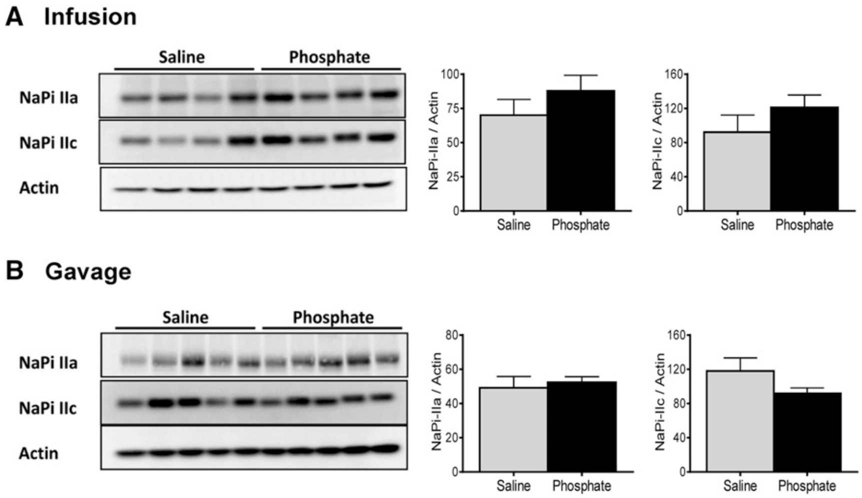

Figure 10. Effect of intravenous and intragastric administration of Pi on the expression of renal NaPi cotransporters in PTX rats. PTX rats were loaded with 500 μmol Pi or saline intravenously or orally. Kidneys were extracted 4 hours postadministration, and the abundance of NaPi-IIa and NaPi-IIc in brush border membranes was determined by Western blot. Expression of cotransporters (A) 4 hours after intravenous infusion of saline (gray bars) and Pi (black bars) and (B) 4 hours after intragastric administration of saline (gray bars) and Pi (black bars). Unpaired *t* test; *n*=4–6 per group and time point.

the maximal transport rate as determined earlier.[47] After the indicated incubation time, uptakes were stopped by transferring 20 μl sample to 1 ml ice cold stop solution (100 mM mannitol, 5 mM Tris-HCl, 150 mM NaCl, 5 mM Pi, and 5 mM glucose). The resulting suspension was then spotted onto a filter and vacuum washed with 10 ml ice cold stop solution. Filters were finally transferred into plastic vials, and on addition of 3 ml scintillation medium (PerkinElmer, Waltham, MA), the retained radioactivity was measured on a β-counter (TRI-CARB 2900TR; Packard). All measurements were carried out in triplicate. The Na^+-dependent uptakes were calculated by subtracting the uptake values obtained in the K^+ medium from those measured in the Na^+ medium (total uptake). Because phosphonoformic acid is a competitive inhibitor of SLC34 cotransporters (NaPi-IIa and NaPi-IIc), SLC34-mediated uptake was determined by subtracting the uptake values obtained in the presence of phosphonoformic acid from the Na^+-dependent values. The remaining BBMVs that were not used in the uptake experiments were stored immediately at −80°C for further experiments.

Immunoblotting

The protein expression levels of NaPi-IIa and NaPi-IIc in renal brush border membranes were quantified by immunoblotting. To this end, 20 μg brush border membranes were solubilized in Laemmli buffer and separated on 10% SDS-PAGE, and then, they were transferred to polyvinylidene difluoride membranes (EMD Millipore, Billerica, MA). After blocking nonspecific binding with 5% milk powder in Tris-buffered saline containing 0.1% Tween-20 for 40 minutes, the blots were incubated overnight at 4°C with primary antibodies against NaPi-IIa (1:4000),[48] NaPi-IIc (1:2500),[49,50] and β-Actin (1:10,000; Sigma-Aldrich, St. Louis, MO). After washing and further blocking, blots were incubated with appropriate secondary antibodies for 2 hours at room temperature. Finally, membranes were exposed to chemiluminescent substrate for 5 minutes, and protein signals were detected on an LAS-4000 Luminescent Image Analyzer (Fujifilm, Tokyo, Japan). All of the images were quantified with Advanced Image Data Analyzer (Raytest). The expression of both cotransporters was normalized to the abundance of β-Actin.

Determination of Pi in Tissues

Tissues (liver, skeletal muscle, and femur) collected from intact and PTX rats 4 hours after infusion or gavage were dried in an oven at 70°C for 24 hours. Samples were weighed, transferred into a silica crucible, and burned to ashes in an electric furnace at 700°C for 12 hours; 1 N HCl was used to dissolve the Pi present in ashes, and after centrifugation, supernatants were collected for Pi determination by the above–mentioned Fiske–Subbarow method.

Statistical Analyses

Statistical significances were calculated by *t* test or one-way ANOVA (Bonferroni) as indicated. $P<0.05$ was considered significant. Results are presented as means±SEM.

ACKNOWLEDGMENTS

The authors acknowledge the technical support by Udo Schnitzbauer as well as the Zurich Integrative Rodent Physiology Core Facility for Rodent Phenotyping.

The study was supported by a grant from the National Center for Competence in Research (NCCR Kidney.CH; to J.B. and C.A.W.).

DISCLOSURES

The authors declare that they have no competing financial interests. N.H. and C.A.W. received financial research support from AstraZeneca Pharmaceuticals (Wilmington, DE) unrelated to this project.

REFERENCES

1. Wagner CA, Hernando N, Forster IC, Biber J: The SLC34 family of sodium-dependent phosphate transporters. *Pflugers Arch* 466: 139–153, 2014
2. Biber J, Hernando N, Forster I: Phosphate transporters and their function. *Annu Rev Physiol* 75: 535–550, 2013
3. Bergwitz C, Jüppner H: Regulation of phosphate homeostasis by PTH, vitamin D, and FGF23. *Annu Rev Med* 61: 91–104, 2010
4. Berndt T, Kumar R: Novel mechanisms in the regulation of phosphorus homeostasis. *Physiology (Bethesda)* 24: 17–25, 2009
5. Hu MC, Shiizaki K, Kuro-o M, Moe OW: Fibroblast growth factor 23 and Klotho: Physiology and pathophysiology of an endocrine network of mineral metabolism. *Annu Rev Physiol* 75: 503–533, 2013

6. Martin A, David V, Quarles LD: Regulation and function of the FGF23/klotho endocrine pathways. *Physiol Rev* 92: 131–155, 2012
7. Weinman EJ, Biswas R, Steplock D, Wang P, Lau YS, Desir GV, Shenolikar S: Increased renal dopamine and acute renal adaptation to a high-phosphate diet. *Am J Physiol Renal Physiol* 300: F1123–F1129, 2011
8. Bacic D, Capuano P, Baum M, Zhang J, Stange G, Biber J, Kaissling B, Moe OW, Wagner CA, Murer H: Activation of dopamine D1-like receptors induces acute internalization of the renal Na+/phosphate cotransporter NaPi-IIa in mouse kidney and OK cells. *Am J Physiol Renal Physiol* 288: F740–F747, 2005
9. Isaac J, Berndt TJ, Chinnow SL, Tyce GM, Dousa TP, Knox FG: Dopamine enhances the phosphaturic response to parathyroid hormone in phosphate-deprived rats. *J Am Soc Nephrol* 2: 1423–1429, 1992
10. Capuano P, Radanovic T, Wagner CA, Bacic D, Kato S, Uchiyama Y, St-Arnoud R, Murer H, Biber J: Intestinal and renal adaptation to a low-Pi diet of type II NaPi cotransporters in vitamin D receptor- and 1alphaOHase-deficient mice. *Am J Physiol Cell Physiol* 288: C429–C434, 2005
11. Marks J, Debnam ES, Unwin RJ: Phosphate homeostasis and the renal-gastrointestinal axis. *Am J Physiol Renal Physiol* 299: F285–F296, 2010
12. Marks J, Srai SK, Biber J, Murer H, Unwin RJ, Debnam ES: Intestinal phosphate absorption and the effect of vitamin D: A comparison of rats with mice. *Exp Physiol* 91: 531–537, 2006
13. Allon M, Rodriguez M, Llach F: Insulin in the acute renal adaptation to dietary phosphate restriction in the rat. *Kidney Int* 37: 14–20, 1990
14. Torres PA, De Brauwere DP: Three feedback loops precisely regulating serum phosphate concentration. *Kidney Int* 80: 443–445, 2011
15. Blaine J, Chonchol M, Levi M: Renal control of calcium, phosphate, and magnesium homeostasis. *Clin J Am Soc Nephrol* 10: 1257–1272, 2015
16. Rowe PS: A unified model for bone-renal mineral and energy metabolism. *Curr Opin Pharmacol* 22: 64–71, 2015
17. Hu MC, Shi M, Zhang J, Pastor J, Nakatani T, Lanske B, Razzaque MS, Rosenblatt KP, Baum MG, Kuro-o M, Moe OW: Klotho: A novel phosphaturic substance acting as an autocrine enzyme in the renal proximal tubule. *FASEB J* 24: 3438–3450, 2010
18. Chang Q, Hoefs S, van der Kemp AW, Topala CN, Bindels RJ, Hoenderop JG: The beta-glucuronidase klotho hydrolyzes and activates the TRPV5 channel. *Science* 310: 490–493, 2005
19. Berndt TJ, Bielesz B, Craig TA, Tebben PJ, Bacic D, Wagner CA, O'Brien S, Schiavi S, Biber J, Murer H, Kumar R: Secreted frizzled-related protein-4 reduces sodium-phosphate co-transporter abundance and activity in proximal tubule cells. *Pflugers Arch* 451: 579–587, 2006
20. Marks J, Churchill LJ, Debnam ES, Unwin RJ: Matrix extracellular phosphoglycoprotein inhibits phosphate transport. *J Am Soc Nephrol* 19: 2313–2320, 2008
21. David V, Martin A, Hedge AM, Rowe PS: Matrix extracellular phosphoglycoprotein (MEPE) is a new bone renal hormone and vascularization modulator. *Endocrinology* 150: 4012–4023, 2009
22. Berndt T, Thomas LF, Craig TA, Sommer S, Li X, Bergstralh EJ, Kumar R: Evidence for a signaling axis by which intestinal phosphate rapidly modulates renal phosphate reabsorption. *Proc Natl Acad Sci U S A* 104: 11085–11090, 2007
23. Scanni R, vonRotz M, Jehle S, Hulter HN, Krapf R: The human response to acute enteral and parenteral phosphate loads. *J Am Soc Nephrol* 25: 2730–2739, 2014
24. Almaden Y, Hernandez A, Torregrosa V, Canalejo A, Sabate L, Fernandez Cruz L, Campistol JM, Torres A, Rodriguez M: High phosphate level directly stimulates parathyroid hormone secretion and synthesis by human parathyroid tissue in vitro. *J Am Soc Nephrol* 9: 1845–1852, 1998
25. Almaden Y, Rodriguez-Ortiz ME, Canalejo A, Cañadillas S, Canalejo R, Martin D, Aguilera-Tejero E, Rodríguez M: Calcimimetics normalize the phosphate-induced stimulation of PTH secretion in vivo and in vitro. *J Nephrol* 22: 281–288, 2009
26. Hansch E, Forgo J, Murer H, Biber J: Role of microtubules in the adaptive response to low phosphate of Na/Pi cotransport in opossum kidney cells. *Pflugers Arch* 422: 516–522, 1993
27. Reshkin SJ, Forgo J, Biber J, Murer H: Functional asymmetry of phosphate transport and its regulation in opossum kidney cells: Phosphate "adaptation." *Pflugers Arch* 419: 256–262, 1991
28. Camalier CE, Yi M, Yu LR, Hood BL, Conrads KA, Lee YJ, Lin Y, Garneys LM, Bouloux GF, Young MR, Veenstra TD, Stephens RM, Colburn NH, Conrads TP, Beck GR Jr.: An integrated understanding of the physiological response to elevated extracellular phosphate. *J Cell Physiol* 228: 1536–1550, 2013
29. Khoshniat S, Bourgine A, Julien M, Weiss P, Guicheux J, Beck L: The emergence of phosphate as a specific signaling molecule in bone and other cell types in mammals. *Cell Mol Life Sci* 68: 205–218, 2011
30. Michigami T: Extracellular phosphate as a signaling molecule. *Contrib Nephrol* 180: 14–24, 2013
31. Cuche JL, Marchand GR, Greger RF, Lang RC, Knox FG: Phosphaturic effect of dopamine in dogs. Possible role of intrarenally produced dopamine in phosphate regulation. *J Clin Invest* 58: 71–76, 1976
32. Nishida Y, Taketani Y, Yamanaka-Okumura H, Imamura F, Taniguchi A, Sato T, Shuto E, Nashiki K, Arai H, Yamamoto H, Takeda E: Acute effect of oral phosphate loading on serum fibroblast growth factor 23 levels in healthy men. *Kidney Int* 70: 2141–2147, 2006
33. Martin DR, Ritter CS, Slatopolsky E, Brown AJ: Acute regulation of parathyroid hormone by dietary phosphate. *Am J Physiol Endocrinol Metab* 289: E729–E734, 2005
34. Bourgeois S, Capuano P, Stange G, Mühlemann R, Murer H, Biber J, Wagner CA: The phosphate transporter NaPi-IIa determines the rapid renal adaptation to dietary phosphate intake in mouse irrespective of persistently high FGF23 levels. *Pflugers Arch* 465: 1557–1572, 2013
35. Zajicek HK, Wang H, Puttaparthi K, Halaihel N, Markovich D, Shayman J, Béliveau R, Wilson P, Rogers T, Levi M: Glycosphingolipids modulate renal phosphate transport in potassium deficiency. *Kidney Int* 60: 694–704, 2001
36. Weinman EJ, Biswas R, Steplock D, Douglass TS, Cunningham R, Shenolikar S: Sodium-hydrogen exchanger regulatory factor 1 (NHERF-1) transduces signals that mediate dopamine inhibition of sodium-phosphate co-transport in mouse kidney. *J Biol Chem* 285: 13454–13460, 2010
37. Weinman EJ, Biswas RS, Peng G, Shen L, Turner CL, e X, Steplock D, Shenolikar S, Cunningham R: Parathyroid hormone inhibits renal phosphate transport by phosphorylation of serine 77 of sodium-hydrogen exchanger regulatory factor-1. *J Clin Invest* 117: 3412–3420, 2007
38. Almaden Y, Canalejo A, Hernandez A, Ballesteros E, Garcia-Navarro S, Torres A, Rodriguez M: Direct effect of phosphorus on PTH secretion from whole rat parathyroid glands in vitro. *J Bone Miner Res* 11: 970–976, 1996
39. Hansen PB: Functional and pharmacological consequences of the distribution of voltage-gated calcium channels in the renal blood vessels. *Acta Physiol (Oxf)* 207: 690–699, 2013
40. Liu S, Zhou J, Tang W, Jiang X, Rowe DW, Quarles LD: Pathogenic role of Fgf23 in Hyp mice. *Am J Physiol Endocrinol Metab* 291: E38–E49, 2006
41. Lavi-Moshayoff V, Wasserman G, Meir T, Silver J, Naveh-Many T: PTH increases FGF23 gene expression and mediates the high-FGF23 levels of experimental kidney failure: A bone parathyroid feedback loop. *Am J Physiol Renal Physiol* 299: F882–F889, 2010
42. Rhee Y, Allen MR, Condon K, Lezcano V, Ronda AC, Galli C, Olivos N, Passeri G, O'Brien CA, Bivi N, Plotkin LI, Bellido T: PTH receptor signaling in osteocytes governs periosteal bone formation and intracortical remodeling. *J Bone Miner Res* 26: 1035–1046, 2011
43. Youn JH, McDonough AA: Recent advances in understanding integrative control of potassium homeostasis. *Annu Rev Physiol* 71: 381–401, 2009

44. Preston RA, Afshartous D, Rodco R, Alonso AB, Garg D: Evidence for a gastrointestinal-renal kaliuretic signaling axis in humans. *Kidney Int* 88: 1383–1391, 2015
45. Mueller T, Dieplinger B: The guanylin peptide family and the proposed gastrointestinal-renal natriuretic signaling axis. *Kidney Int* 82: 1253–1255, 2012
46. Michell AR, Debnam ES, Unwin RJ: Regulation of renal function by the gastrointestinal tract: Potential role of gut-derived peptides and hormones. *Annu Rev Physiol* 70: 379–403, 2008
47. Biber J, Stieger B, Stange G, Murer H: Isolation of renal proximal tubular brush-border membranes. *Nat Protoc* 2: 1356–1359, 2007
48. Custer M, Lötscher M, Biber J, Murer H, Kaissling B: Expression of Na-P($_i$) cotransport in rat kidney: Localization by RT-PCR and immunohistochemistry. *Am J Physiol* 266: F767–F774, 1994
49. Nowik M, Picard N, Stange G, Capuano P, Tenenhouse HS, Biber J, Murer H, Wagner CA: Renal phosphaturia during metabolic acidosis revisited: Molecular mechanisms for decreased renal phosphate reabsorption. *Pflugers Arch* 457: 539–549, 2008
50. Hernando N, Myakala K, Simona F, Knöpfel T, Thomas L, Murer H, Wagner CA, Biber J: Intestinal depletion of NaPi-IIb/Slc34a2 in mice: Renal and hormonal adaptation. *J Bone Miner Res* 30: 1925–1937, 2015

This article contains supplemental material online at http://jasn.asnjournals.org/lookup/suppl/doi:10.1681/ASN.2016010082/-/DCSupplemental.

Acknowledgments

I would like to express my gratitude to Carsten Wagner my supervisor for accepting me as his PhD student and coaching me through these four years. Particularly when things initially did not turn out as expected, he had a plan B up his sleeve. I want to thank him especially for giving me the opportunity to go to Berlin and Kiel to learn the secrets of the Ussing chambers, and that he trusted me to bring this technique to Zurich. A very special thanks goes to Nati Hernando, who was supervising and teaching me during all the time I spent in the institute. Without her efforts and support I would never have managed to get thus far. A lot of what I learned during my master and PhD studies was taught by her, but no only scientifically but also moral support she provided when I had my doubts and frustrations, and our fresh air breaks contributed a lot to that. I also want to express my gratitude to Jürg Biber for being my mentor during my master thesis and the beginning of my PhD. In fact it was the course BIO411, taught by Jürg, Nati, Gerti, Soline, Ian and Bruno, that made me apply for the master project in the institute. And through Jürgs and Natis and also Carstens coaching I considered science and continued after my master.

I also want to express my gratitude to the members of my thesis committee Bruno Stieger and Gerhard Burckhardt for their scientific input and concerns during the committee meetings to guide my projects towards a good direction. Especially I want to thank Bruno, who even took his time outside our regular meetings to offer his advice. Here I also want to thank Ian Forster for teaching the basics of electrophysiology and for giving me the opportunity to contribute to his projects.

Further I want to thank Dorothee Günzel, Markus Bleich und Nina Himmerkus for welcoming me to their labs and teaching me how to set up and handle the Ussing chambers and the electrophysiology behind, thus far a black box for me. I had a great time in Berlin and Kiel, also outside the lab!

A very big “Thank you!” goes to my great colleagues and friends Linto Thomas, Marta Figueiredo, Pedro Imenez Silva and Eva Maria Pastor particularly for their non-scientific input, making the time in the lab a lot of fun! Further I want to thank Eva and Udo Schnitzbauer for performing several measurements for me, with precision I could only dream of. My thanks go to the whole Wagner group and J-floor of the Institute for providing an environment, which was very pleasant to work in.

Moreover, I am very grateful for my friends, who had to bear with this nerd and helped me getting distance from work and free my mind.

Ganz speziell möchte ich auch meiner Familie danken! Vorallem meinen Eltern, die es mir ermöglicht haben zu studieren und mich während der ganzen Zeit unterstützt haben.

Very importantly, I want to thank Emilia Boiadjieva for all the support and love throughout the entire time. You encouraged me when I failed; you cheered me up when I was lacking motivation; but you were also there in the great moments making them even better! Thank you Emi!

References

1. Hruska KA, Mathew S, Lund R, Qiu P, Pratt R (2008) Hyperphosphatemia of chronic kidney disease. Kidney Int 74: 148-157.
2. Biber J, Hernando N, Forster I (2013) Phosphate Transporters and Their Function. Annual Review of Physiology, Vol 75 75: 535-550.
3. Forster IC, Loo DDF, Eskandari S (1999) Stoichiometry and Na+ binding cooperativity of rat and flounder renal type II Na+-P-i cotransporters. American Journal of Physiology-Renal Physiology 276: F644-F649.
4. Bacconi A, Virkki LV, Biber J, Murer H, Forster IC (2005) Renouncing electroneutrality is not free of charge: Switching on electrogenicity in a Na+-coupled phosphate cotransporter. Proc Natl Acad Sci U S A 102: 12606-12611.
5. Segawa H, Kaneko I, Takahashi A, Kuwahata M, Ito M, et al. (2002) Growth-related renal type IINa/P-i cotransporter. Journal of Biological Chemistry 277: 19665-19672.
6. Ghezzi C, Murer H, Forster IC (2009) Substrate interactions of the electroneutral Na+-coupled inorganic phosphate cotransporter (NaPi-IIc). Journal of Physiology-London 587: 4293-4307.
7. Forster IC, Biber J, Murer H (2000) Proton-sensitive transitions of renal type IINa+-coupled phosphate cotransporter kinetics. Biophysical Journal 79: 215-230.
8. Custer M, Lotscher M, Biber J, Murer H, Kaissling B (1994) Expression of Na-P(i) cotransport in rat kidney: localization by RT-PCR and immunohistochemistry. Am J Physiol 266: F767-774.
9. Picard N, Capuano P, Stange G, Mihailova M, Kaissling B, et al. (2010) Acute parathyroid hormone differentially regulates renal brush border membrane phosphate cotransporters. Pflugers Arch 460: 677-687.
10. Beck L, Karaplis AC, Amizuka N, Hewson AS, Ozawa H, et al. (1998) Targeted inactivation of Npt2 in mice leads to severe renal phosphate wasting, hypercalciuria, and skeletal abnormalities. Proc Natl Acad Sci U S A 95: 5372-5377.
11. Myakala K, Motta S, Murer H, Wagner CA, Koesters R, et al. (2014) Renal-specific and inducible depletion of NaPi-IIc/Slc34a3, the cotransporter mutated in HHRH, does not affect phosphate or calcium homeostasis in mice. Am J Physiol Renal Physiol 306: F833-843.
12. Miyamoto KI, Haito-Sugino S, Kuwahara S, Ohi A, Nomura K, et al. (2011) Sodium-Dependent Phosphate Cotransporters: Lessons from Gene Knockout and Mutation Studies. Journal of Pharmaceutical Sciences 100: 3719-3730.
13. Hilfiker H, Hattenhauer O, Traebert M, Forster I, Murer H, et al. (1998) Characterization of a murine type II sodium-phosphate cotransporter expressed in mammalian small intestine. Proc Natl Acad Sci U S A 95: 14564-14569.
14. Radanovic T, Wagner CA, Murer H, Biber J (2005) Regulation of intestinal phosphate transport. I. Segmental expression and adaptation to low-P(i) diet of the type IIb Na(+)-P(i) cotransporter in mouse small intestine. Am J Physiol Gastrointest Liver Physiol 288: G496-500.
15. Forster IC, Hernando N, Biber J, Murer H (2012) Phosphate transport kinetics and structure-function relationships of SLC34 and SLC20 proteins. Curr Top Membr 70: 313-356.
16. Forster IC, Virkki L, Bossi E, Murer H, Biber J (2006) Electrogenic kinetics of a mammalian intestinal type IIb Na(+)/P(i) cotransporter. J Membr Biol 212: 177-190.
17. Forster IC, Kohler K, Biber J, Murer H (2002) Forging the link between structure and function of electrogenic cotransporters: the renal type IIa Na+/P-i cotransporter as a case study. Progress in Biophysics & Molecular Biology 80: 69-108.
18. Hernando N, Karim-Jimenez Z, Biber J, Murer H (2001) Molecular determinants for apical expression and regulatory membrane retrieval of the type IIa Na/Pi cotransporter. Kidney Int 60: 431-435.

19. Karim-Jimenez Z, Hernando N, Biber J, Murer H (2001) Molecular determinants for apical expression of the renal type IIa Na+/P-j-cotransporter. Pflugers Archiv-European Journal of Physiology 442: 782-790.
20. Fenollar-Ferrer C, Patti M, Werner A, Knoepfel T, Forster IC, et al. (2015) The Na1 Binding Site in the Human Sodium-Phosphate Cotransporter NaPi-IIa. Biophysical Journal 108: 29a-29a.
21. Fenollar-Ferrer MC, Patti M, Knoepfel T, Werner A, Forster IC, et al. (2014) Structural Model of the Human Sodium-Phosphate Cotransporter NaPi-II. Biophysical Journal 106: 228a-228a.
22. Ravera S, Virkki LV, Murer H, Forster IC (2007) Deciphering PiT transport kinetics and substrate specificity using electrophysiology and flux measurements. American Journal of Physiology-Cell Physiology 293: C606-C620.
23. Saliba KJ, Martin RE, Broer A, Henry RI, McCarthy CS, et al. (2006) Sodium-dependent uptake of inorganic phosphate by the intracellular malaria parasite. Nature 443: 582-585.
24. Wang C, Li YL, Shi L, Ren J, Patti M, et al. (2012) Mutations in SLC20A2 link familial idiopathic basal ganglia calcification with phosphate homeostasis. Nature Genetics 44: 254-256.
25. Bezerra DP, Oliveira JRM (2016) New Studies on Knockout Mouse for the SLC20A2 Gene Show Much More Than Brain Calcifications. Journal of Molecular Neuroscience 59: 565-566.
26. Giovannini D, Touhami J, Charnet P, Sitbon M, Battini JL (2013) Inorganic Phosphate Export by the Retrovirus Receptor XPR1 in Metazoans. Cell Reports 3: 1866-1873.
27. Wild R, Gerasimaite R, Jung JY, Truffault V, Pavlovic I, et al. (2016) Control of eukaryotic phosphate homeostasis by inositol polyphosphate sensor domains. Science 352: 986-990.
28. Schell MJ, Letcher AJ, Brearley CA, Biber J, Murer H, et al. (1999) PiUS (Pi uptake stimulator) is an inositol hexakisphosphate kinase. Febs Letters 461: 169-172.
29. Ansermet C, Moor MB, Centeno G, Auberson M, Hu DZ, et al. (2016) Renal Fanconi Syndrome and Hypophosphatemic Rickets in the Absence of Xenotropic and Polytropic Retroviral Receptor in the Nephron. J Am Soc Nephrol.
30. Cramer CF (1961) Progress and Rate of Absorption of Radiophosphorus through Intestinal Tract of Rats. Canadian Journal of Biochemistry and Physiology 39: 499-&.
31. Hu MS, Kayne LH, Jamgotchian N, Ward HJ, Lee DBN (1997) Paracellular phosphate absorption in rat colon: A mechanism for enema-induced hyperphosphatemia. Mineral and Electrolyte Metabolism 23: 7-12.
32. McHardy GJR, Parsons DS (1956) THE ABSORPTION OF INORGANIC PHOSPHATE FROM THE SMALL INTESTINE OF THE RAT. Quarterly Journal of Experimental Physiology and Cognate Medical Sciences 41: 398-409.
33. Taylor AN (1974) In-Vitro Phosphate Transport in Chick Ileum - Effect of Cholecalciferol, Calcium, Sodium and Metabolic-Inhibitors. Journal of Nutrition 104: 489-494.
34. Walling MW, Brautbar N, Coburn JW (1977) Jejunal Phosphate (Pi) Active-Transport - Effects of Phosphorus Depletion and Vitamin-D. Federation Proceedings 36: 1097-1097.
35. Walton J, Gray TK (1979) Absorption of Inorganic-Phosphate in the Human Small-Intestine. Clinical Science 56: 407-412.
36. Nordin BEC (1976) Calcium, Phosphate, and Magnesium Metabolism: Clinical Physiology and Diagnostic Procedures: Churchill Livingstone.
37. Giral H, Caldas Y, Sutherland E, Wilson P, Breusegem S, et al. (2009) Regulation of rat intestinal Na-dependent phosphate transporters by dietary phosphate. Am J Physiol Renal Physiol 297: F1466-1475.
38. Hattenhauer O, Traebert M, Murer H, Biber J (1999) Regulation of small intestinal Na-P(i) type IIb cotransporter by dietary phosphate intake. Am J Physiol 277: G756-762.
39. Virkki LV, Biber J, Murer H, Forster IC (2007) Phosphate transporters: a tale of two solute carrier families. Am J Physiol Renal Physiol 293: F643-654.
40. Reining SC, Liesegang A, Betz H, Biber J, Murer H, et al. (2010) Expression of renal and intestinal Na/Pi cotransporters in the absence of GABARAP. Pflugers Arch 460: 207-217.
41. Bai L, Collins JF, Ghishan FK (2000) Cloning and characterization of a type III Na-dependent phosphate cotransporter from mouse intestine. Am J Physiol Cell Physiol 279: C1135-1143.

42. Shibasaki Y, Etoh N, Hayasak M, Takahashi MO, Kakitani M, et al. (2009) Targeted deletion of the tybe IIb Na+-dependent Pi-co-transporter, NaPi-IIb, results in early embryonic lethality. Biochemical and Biophysical Research Communications 381: 482-486.
43. Hernando N, Myakala K, Simona F, Knopfel T, Thomas L, et al. (2015) Intestinal Depletion of NaPi-IIb/Slc34a2 in Mice: Renal and Hormonal Adaptation. J Bone Miner Res 30: 1925-1937.
44. Corut A, Senyigit A, Ugur SA, Altin S, Ozcelik U, et al. (2006) Mutations in SLC34A2 cause pulmonary alveolar microlithiasis and are possibly associated with testicular microlithiasis. American Journal of Human Genetics 79: 650-656.
45. Palmada M, Dieter M, Speil A, Bohmer C, Mack AF, et al. (2004) Regulation of intestinal phosphate cotransporter NaPi IIb by ubiquitin ligase Nedd4-2 and by serum- and glucocorticoid-dependent kinase 1. American Journal of Physiology-Gastrointestinal and Liver Physiology 287: G143-G150.
46. Katai K, Miyamoto K, Kishida S, Segawa H, Nii T, et al. (1999) Regulation of intestinal Na+-dependent phosphate co-transporters by a low-phosphate diet and 1,25-dihydroxyvitamin D-3. Biochemical Journal 343: 705-712.
47. Capuano P, Radanovic T, Wagner CA, Bacic D, Kato S, et al. (2005) Intestinal and renal adaptation to a low-Pi diet of type II NaPi cotransporters in vitamin D receptor- and 1alphaOHase-deficient mice. Am J Physiol Cell Physiol 288: C429-434.
48. Giral H, Cranston D, Lanzano L, Caldas Y, Sutherland E, et al. (2012) NHE3 regulatory factor 1 (NHERF1) modulates intestinal sodium-dependent phosphate transporter (NaPi-2b) expression in apical microvilli. J Biol Chem 287: 35047-35056.
49. Shenolikar S, Voltz JW, Minkoff CM, Wade JB, Weinman EJ (2002) Targeted disruption of the mouse NHERF-1 gene promotes internalization of proximal tubule sodium-phosphate cotransporter type IIa and renal phosphate wasting. Proc Natl Acad Sci U S A 99: 11470-11475.
50. Schroder B, Kappner H, Failing K, Pfeffer E, Breves G (1995) Mechanisms of intestinal phosphate transport in small ruminants. Br J Nutr 74: 635-648.
51. Candeal E, Caldas YA, Guillen N, Levi M, Sorribas V (2014) Na+-independent phosphate transport in Caco2BBE cells. Am J Physiol Cell Physiol 307: C1113-1122.
52. Sabbagh Y, O'Brien SP, Song W, Boulanger JH, Stockmann A, et al. (2009) Intestinal npt2b plays a major role in phosphate absorption and homeostasis. J Am Soc Nephrol 20: 2348-2358.
53. Marks J, Lee GJ, Nadaraja SP, Debnam ES, Unwin RJ (2015) Experimental and regional variations in Na+-dependent and Na+-independent phosphate transport along the rat small intestine and colon. Physiol Rep 3.
54. Gunzel D, Yu AS (2013) Claudins and the modulation of tight junction permeability. Physiol Rev 93: 525-569.
55. Furuse M, Fujita K, Hiiragi T, Fujimoto K, Tsukita S (1998) Claudin-1 and -2: Novel integral membrane proteins localizing at tight junctions with no sequence similarity to occludin. Journal of Cell Biology 141: 1539-1550.
56. Furuse M, Sasaki H, Tsukita S (1999) Manner of interaction of heterogeneous claudin species within and between tight junction strands. Journal of Cell Biology 147: 891-903.
57. Piontek J, Fritzsche S, Cording J, Richter S, Hartwig J, et al. (2011) Elucidating the principles of the molecular organization of heteropolymeric tight junction strands. Cellular and Molecular Life Sciences 68: 3903-3918.
58. Claude P, Goodenough DA (1973) Fracture Faces of Zonulae Occludentes from Tight and Leaky Epithelia. Journal of Cell Biology 58: 390-400.
59. Frizzell RA, Schultz SG (1972) Ionic conductances of extracellular shunt pathway in rabbit ileum. Influence of shunt on transmural sodium transport and electrical potential differences. J Gen Physiol 59: 318-346.
60. Greger R (1981) Cation selectivity of the isolated perfused cortical thick ascending limb of Henle's loop of rabbit kidney. Pflugers Arch 390: 30-37.

61. Amasheh S, Meiri N, Gitter AH, Schoneberg T, Mankertz J, et al. (2002) Claudin-2 expression induces cation-selective channels in tight junctions of epithelial cells. J Cell Sci 115: 4969-4976.
62. Zihni C, Mills C, Matter K, Balda MS (2016) Tight junctions: from simple barriers to multifunctional molecular gates. Nature Reviews Molecular Cell Biology 17: 564-580.
63. Biber J, Custer M, Magagnin S, Hayes G, Werner A, et al. (1996) Renal Na/Pi-cotransporters. Kidney Int 49: 981-985.
64. Jaeger P, Bonjour JP, Karlmark B, Stanton B, Kirk RG, et al. (1983) Influence of acute potassium loading on renal phosphate transport in the rat kidney. Am J Physiol 245: F601-605.
65. Jaeger P, Karlmark B, Stanton B, Kirk RG, Duplinsky T, et al. (1980) Micropuncture study of distal tubular activation of phosphate reabsorption in the rat. Adv Exp Med Biol 128: 77-82.
66. Wagner CA, Hernando N, Forster IC, Biber J (2014) The SLC34 family of sodium-dependent phosphate transporters. Pflugers Arch 466: 139-153.
67. Custer M, Murer H, Biber J (1994) Nephron localization of Na/SO4(2-)-cotransport-related mRNA and protein. Pflugers Arch 429: 165-168.
68. Levi M, Lotscher M, Sorribas V, Custer M, Arar M, et al. (1994) Cellular mechanisms of acute and chronic adaptation of rat renal P(i) transporter to alterations in dietary P(i). Am J Physiol 267: F900-908.
69. Bourgeois S, Capuano P, Stange G, Muhlemann R, Murer H, et al. (2013) The phosphate transporter NaPi-IIa determines the rapid renal adaptation to dietary phosphate intake in mouse irrespective of persistently high FGF23 levels. Pflugers Arch 465: 1557-1572.
70. Bacic D, Lehir M, Biber J, Kaissling B, Murer H, et al. (2006) The renal Na+/phosphate cotransporter NaPi-IIa is internalized via the receptor-mediated endocytic route in response to parathyroid hormone. Kidney Int 69: 495-503.
71. Andrukhova O, Zeitz U, Goetz R, Mohammadi M, Lanske B, et al. (2012) FGF23 acts directly on renal proximal tubules to induce phosphaturia through activation of the ERK1/2-SGK1 signaling pathway. Bone 51: 621-628.
72. Gisler SM, Kittanakom S, Fuster D, Wong V, Bertic M, et al. (2008) Monitoring protein-protein interactions between the mammalian integral membrane transporters and PDZ-interacting partners using a modified split-ubiquitin membrane yeast two-hybrid system. Mol Cell Proteomics 7: 1362-1377.
73. Gisler SM, Stagljar I, Traebert M, Bacic D, Biber J, et al. (2001) Interaction of the type IIa Na/Pi cotransporter with PDZ proteins. J Biol Chem 276: 9206-9213.
74. Hernando N, Deliot N, Gisler SM, Lederer E, Weinman EJ, et al. (2002) PDZ-domain interactions and apical expression of type IIa Na/P(i) cotransporters. Proc Natl Acad Sci U S A 99: 11957-11962.
75. Hatano R, Fujii E, Segawa H, Mukaisho K, Matsubara M, et al. (2013) Ezrin, a membrane cytoskeletal cross-linker, is essential for the regulation of phosphate and calcium homeostasis. Kidney Int 83: 41-49.
76. Deliot N, Hernando N, Horst-Liu Z, Gisler SM, Capuano P, et al. (2005) Parathyroid hormone treatment induces dissociation of type IIa Na+-P(i) cotransporter-Na+/H+ exchanger regulatory factor-1 complexes. Am J Physiol Cell Physiol 289: C159-167.
77. Weinman EJ, Biswas RS, Peng G, Shen L, Turner CL, et al. (2007) Parathyroid hormone inhibits renal phosphate transport by phosphorylation of serine 77 of sodium-hydrogen exchanger regulatory factor-1. J Clin Invest 117: 3412-3420.
78. Weinman EJ, Steplock D, Shenolikar S, Biswas R (2011) Fibroblast growth factor-23-mediated inhibition of renal phosphate transport in mice requires sodium-hydrogen exchanger regulatory factor-1 (NHERF-1) and synergizes with parathyroid hormone. J Biol Chem 286: 37216-37221.
79. Keusch I, Traebert M, Lotscher M, Kaissling B, Murer H, et al. (1998) Parathyroid hormone and dietary phosphate provoke a lysosomal routing of the proximal tubular Na/Pi-cotransporter type II. Kidney Int 54: 1224-1232.

80. Karim Z, Gerard B, Bakouh N, Alili R, Leroy C, et al. (2008) NHERF1 mutations and responsiveness of renal parathyroid hormone. N Engl J Med 359: 1128-1135.
81. Giral H, Lanzano L, Caldas Y, Blaine J, Verlander JW, et al. (2011) Role of PDZK1 protein in apical membrane expression of renal sodium-coupled phosphate transporters. J Biol Chem 286: 15032-15042.
82. Bergwitz C, Juppner H (2010) Regulation of Phosphate Homeostasis by PTH, Vitamin D, and FGF23. Annu Rev Med 61: 91-104.
83. Shinkyo R, Sakaki T, Kamakura M, Ohta M, Inouye K (2004) Metabolism of vitamin D by human microsomal CYP2R1. Biochem Biophys Res Commun 324: 451-457.
84. Cheng JB, Motola DL, Mangelsdorf DJ, Russell DW (2003) De-orphanization of cytochrome P450 2R1: a microsomal vitamin D 25-hydroxilase. J Biol Chem 278: 38084-38093.
85. Kitanaka S, Takeyama K, Murayama A, Sato T, Okumura K, et al. (1998) Inactivating mutations in the 25-hydroxyvitamin D(3) 1 alpha-hydroxylase gene in patients with pseudovitamin D-deficiency rickets. New England Journal of Medicine 338: 653-661.
86. Ohyama Y, Hayashi S, Okuda K (1989) Purification of 25-Hydroxyvitamin D3 24-Hydroxylase from Rat-Kidney Mitochondria. Febs Letters 255: 405-408.
87. Ohyama Y, Okuda K (1991) Isolation and Characterization of a Cytochrome-P-450 from Rat-Kidney Mitochondria That Catalyzes the 24-Hydroxylation of 25-Hydroxyvitamin-D3. Journal of Biological Chemistry 266: 8690-8695.
88. Bai XY, Miao D, Goltzman D, Karaplis AC (2003) The autosomal dominant hypophosphatemic rickets R176Q mutation in fibroblast growth factor 23 resists proteolytic cleavage and enhances in vivo biological potency. J Biol Chem 278: 9843-9849.
89. Yu VC, Delsert C, Andersen B, Holloway JM, Devary OV, et al. (1991) Rxr-Beta - a Coregulator That Enhances Binding of Retinoic Acid, Thyroid-Hormone, and Vitamin-D Receptors to Their Cognate Response Elements. Cell 67: 1251-1266.
90. Kliewer SA, Umesono K, Mangelsdorf DJ, Evans RM (1992) Retinoid X-Receptor Interacts with Nuclear Receptors in Retinoic Acid, Thyroid-Hormone and Vitamin-D3 Signaling. Nature 355: 446-449.
91. Noda M, Vogel RL, Craig AM, Prahl J, Deluca HF, et al. (1990) Identification of a DNA-Sequence Responsible for Binding of the 1,25-Dihydroxyvitamin-D3 Receptor and 1,25-Dihydroxyvitamin-D3 Enhancement of Mouse Secreted Phosphoprotein-1 (Spp-1 or Osteopontin) Gene-Expression. Proc Natl Acad Sci U S A 87: 9995-9999.
92. Trochoutsou AI, Kloukina V, Samitas K, Xanthou G (2015) Vitamin-D in the Immune System: Genomic and Non-Genomic Actions. Mini Rev Med Chem 15: 953-963.
93. Yoshizawa T, Handa Y, Uematsu Y, Takeda S, Sekine K, et al. (1997) Mice lacking the vitamin D receptor exhibit impaired bone formation, uterine hypoplasia and growth retardation after weaning. Nature Genetics 16: 391-396.
94. Bouillon R, Van Cromphaut S, Carmeliet G (2003) Intestinal calcium absorption: Molecular vitamin D mediated mechanisms. Journal of Cellular Biochemistry 88: 332-339.
95. Moor MB, Bonny O (2016) Ways of calcium reabsorption in the kidney. American Journal of Physiology-Renal Physiology 310: F1337-F1350.
96. Katai K, Miyamoto K, Kishida S, Segawa H, Nii T, et al. (1999) Regulation of intestinal Na+-dependent phosphate co-transporters by a low-phosphate diet and 1,25-dihydroxyvitamin D3. Biochem J 343 Pt 3: 705-712.
97. Li YC, Pirro AE, Amling M, Delling G, Baron R, et al. (1997) Targeted ablation of the vitamin D receptor: an animal model of vitamin D-dependent rickets type II with alopecia. Proc Natl Acad Sci U S A 94: 9831-9835.
98. Panda DK, Miao D, Tremblay ML, Sirois J, Farookhi R, et al. (2001) Targeted ablation of the 25-hydroxyvitamin D 1alpha -hydroxylase enzyme: evidence for skeletal, reproductive, and immune dysfunction. Proc Natl Acad Sci U S A 98: 7498-7503.
99. Manolagas SC (2000) Birth and death of bone cells: basic regulatory mechanisms and implications for the pathogenesis and treatment of osteoporosis. Endocr Rev 21: 115-137.

100. Liu SG, Tang W, Zhou JP, Stubbs JR, Luo Q, et al. (2006) Fibroblast growth factor 23 is a counter-regulatory phosphaturic hormone for vitamin D. Journal of the American Society of Nephrology 17: 1305-1315.
101. Demay MB, Kiernan MS, Deluca HF, Kronenberg HM (1992) Sequences in the Human Parathyroid-Hormone Gene That Bind the 1,25-Dihydroxyvitamin-D3 Receptor and Mediate Transcriptional Repression in Response to 1,25-Dihydroxyvitamin-D3. Proc Natl Acad Sci U S A 89: 8097-8101.
102. Wettschureck N, Lee E, Libutti SK, Offermanns S, Robey PG, et al. (2007) Parathyroid-specific double knockout of G(q) and G(11) alpha-subunits leads to a phenotype resembling germline knockout of the extracellular Ca2+-sensing receptor. Mol Endocrinol 21: 274-280.
103. Kemper B, Habener JF, Rich A, Potts JT (1974) Parathyroid Secretion - Discovery of a Major Calcium-Dependent Protein. Science 184: 167-169.
104. Almaden Y, Canalejo A, Hernandez A, Ballesteros E, GarciaNavarro S, et al. (1996) Direct effect of phosphorus on PTH secretion from whole rat parathyroid glands in vitro. Journal of Bone and Mineral Research 11: 970-976.
105. Almaden Y, Canalejo A, Hernandez A, Ballesteros E, Garcia-Navarro S, et al. (1996) Direct effect of phosphorus on PTH secretion from whole rat parathyroid glands in vitro. J Bone Miner Res 11: 970-976.
106. Scanni R, vonRotz M, Jehle S, Hulter HN, Krapf R (2014) The human response to acute enteral and parenteral phosphate loads. J Am Soc Nephrol 25: 2730-2739.
107. Thomas L, Bettoni C, Kno pfel T, Hernando N, Biber J, et al. (2016) Acute Adaption to Oral or Intravenous Phosphate Requires Parathyroid Hormone. Journal of the American Society of Nephrology.
108. Segawa H, Yamanaka S, Onitsuka A, Tomoe Y, Kuwahata M, et al. (2007) Parathyroid hormone-dependent endocytosis of renal type IIc Na-Pi cotransporter. Am J Physiol Renal Physiol 292: F395-403.
109. Traebert M, Volkl H, Biber J, Murer H, Kaissling B (2000) Luminal and contraluminal action of 1-34 and 3-34 PTH peptides on renal type IIa Na-P-i cotransporter. American Journal of Physiology-Renal Physiology 278: F792-F798.
110. Guo J, Chung UI, Kondo H, Bringhurst FR, Kronenberg HM (2002) The PTH/PTHrP receptor can delay chondrocyte hypertrophy in vivo without activating phospholipase C. Dev Cell 3: 183-194.
111. Bourdeau JE, Burg MB (1980) Effect of PTH on calcium transport across the cortical thick ascending limb of Henle's loop. Am J Physiol 239: F121-126.
112. Kremer R, Goltzman D (1982) Parathyroid hormone stimulates mammalian renal 25-hydroxyvitamin D3-1 alpha-hydroxylase in vitro. Endocrinology 110: 294-296.
113. Ma YFL, Cain RL, Halladay DL, Yang XH, Zeng QQ, et al. (2001) Catabolic effects of continuous human PTH (1-38) in vivo is associated with sustained stimulation of RANKL and inhibition of osteoprotegerin and gene-associated bone formation. Endocrinology 142: 4047-4054.
114. Meir T, Durlacher K, Pan Z, Amir G, Richards WG, et al. (2014) Parathyroid hormone activates the orphan nuclear receptor Nurr1 to induce FGF23 transcription. Kidney Int 86: 1106-1115.
115. Martin A, David V, Quarles LD (2012) Regulation and function of the FGF23/klotho endocrine pathways. Physiol Rev 92: 131-155.
116. Miao DS, He B, Karaplis AC, Goltzman D (2002) Parathyroid hormone is essential for normal fetal bone formation. Journal of Clinical Investigation 109: 1173-1182.
117. Bai XY, Miao DS, Li JR, Goltzman D, Karaplis AC (2003) Early lethality in Hyp mice with targeted deletion of the Pth gene. Journal of Bone and Mineral Research 18: S170-S170.
118. Hu MC, Shiizaki K, Kuro-o M, Moe OW (2013) Fibroblast growth factor 23 and Klotho: physiology and pathophysiology of an endocrine network of mineral metabolism. Annu Rev Physiol 75: 503-533.
119. Mohammadi M, Olsen SK, Ibrahimi OA (2005) Structural basis for fibroblast growth factor receptor activation. Cytokine Growth Factor Rev 16: 107-137.

120. Itoh N, Ornitz DM (2008) Functional evolutionary history of the mouse Fgf gene family. Dev Dyn 237: 18-27.
121. Goetz R, Beenken A, Ibrahimi OA, Kalinina J, Olsen SK, et al. (2007) Molecular insights into the klotho-dependent, endocrine mode of action of fibroblast growth factor 19 subfamily members. Mol Cell Biol 27: 3417-3428.
122. Kurosu H, Ogawa Y, Miyoshi M, Yamamoto M, Nandi A, et al. (2006) Regulation of fibroblast growth factor-23 signaling by Klotho. Journal of Biological Chemistry 281: 6120-6123.
123. Grabner A, Amaral AP, Schramm K, Singh S, Sloan A, et al. (2015) Activation of Cardiac Fibroblast Growth Factor Receptor 4 Causes Left Ventricular Hypertrophy. Cell Metabolism 22: 1020-1032.
124. Yamashita T, Yoshioka M, Itoh N (2000) Identification of a novel fibroblast growth factor, FGF-23, preferentially expressed in the ventrolateral thalamic nucleus of the brain. Biochem Biophys Res Commun 277: 494-498.
125. Masuyama R, Stockmans I, Torrekens S, Van Looveren R, Maes C, et al. (2006) Vitamin D receptor in chondrocytes promotes osteoclastogenesis and regulates FGF23 production in osteoblasts. Journal of Clinical Investigation 116: 3150-3159.
126. Rhee Y, Bivi N, Farrow E, Lezcano V, Plotkin LI, et al. (2011) Parathyroid hormone receptor signaling in osteocytes increases the expression of fibroblast growth factor-23 in vitro and in vivo. Bone 49: 636-643.
127. Fon Tacer K, Bookout AL, Ding X, Kurosu H, John GB, et al. (2010) Research resource: Comprehensive expression atlas of the fibroblast growth factor system in adult mouse. Mol Endocrinol 24: 2050-2064.
128. Spichtig D, Zhang HB, Mohebbi N, Pavik I, Petzold K, et al. (2014) Renal expression of FGF23 and peripheral resistance to elevated FGF23 in rodent models of polycystic kidney disease. Kidney Int 85: 1340-1350.
129. Shimada T, Muto T, Urakawa I, Yoneya T, Yamazaki Y, et al. (2002) Mutant FGF-23 responsible for autosomal dominant hypophosphatemic rickets is resistant to proteolytic cleavage and causes hypophosphatemia in vivo. Endocrinology 143: 3179-3182.
130. Liu SG, Guo R, Simpson LG, Xiao ZS, Burnham CE, et al. (2003) Regulation of fibroblastic growth factor 23 expression but not degradation by PHEX. Journal of Biological Chemistry 278: 37419-37426.
131. Goetz R, Nakada Y, Hu MC, Kurosu H, Wang L, et al. (2010) Isolated C-terminal tail of FGF23 alleviates hypophosphatemia by inhibiting FGF23-FGFR-Klotho complex formation. Proc Natl Acad Sci U S A 107: 407-412.
132. Kato K, Jeanneau C, Tarp MA, Benet-Pages A, Lorenz-Depiereux B, et al. (2006) Polypeptide GalNAc-transferase T3 and familial tumoral calcinosis - Secretion of fibroblast growth factor 23 requires O-glycosylation. Journal of Biological Chemistry 281: 18370-18377.
133. Lopez I, Rodriguez-Ortiz ME, Almaden Y, Guerrero F, de Oca AM, et al. (2011) Direct and indirect effects of parathyroid hormone on circulating levels of fibroblast growth factor 23 in vivo. Kidney Int 80: 475-482.
134. Haussler MR, Whitfield GK, Kaneko I, Forster R, Saini R, et al. (2012) The role of vitamin D in the FGF23, klotho, and phosphate bone-kidney endocrine axis. Reviews in Endocrine & Metabolic Disorders 13: 57-69.
135. Rodriguez-Ortiz ME, Lopez I, Munoz-Castaneda JR, Martinez-Moreno JM, Ramirez AP, et al. (2012) Calcium Deficiency Reduces Circulating Levels of FGF23. Journal of the American Society of Nephrology 23: 1190-1197.
136. Chefetz I, Kohno K, Izumi H, Uitto J, Richard G, et al. (2009) GALNT3, a gene associated with hyperphosphatemic familial tumoral calcinosis, is transcriptionally regulated by extracellular phosphate and modulates matrix metalloproteinase activity. Biochimica Et Biophysica Acta-Molecular Basis of Disease 1792: 61-67.
137. Razzaque MS, Lanske B (2007) The emerging role of the fibroblast growth factor-23-klotho axis in renal regulation of phosphate homeostasis. Journal of Endocrinology 194: 1-10.

138. Gattineni J, Bates C, Twombley K, Dwarakanath V, Robinson ML, et al. (2009) FGF23 decreases renal NaPi-2a and NaPi-2c expression and induces hypophosphatemia in vivo predominantly via FGF receptor 1. Am J Physiol Renal Physiol 297: F282-291.
139. Perwad F, Zhang MY, Tenenhouse HS, Portale AA (2007) Fibroblast growth factor 23 impairs phosphorus and vitamin D metabolism in vivo and suppresses 25-hydroxyvitamin D-1alpha-hydroxylase expression in vitro. Am J Physiol Renal Physiol 293: F1577-1583.
140. Ranch D, Zhang MY, Portale AA, Perwad F (2011) Fibroblast growth factor 23 regulates renal 1,25-dihydroxyvitamin D and phosphate metabolism via the MAP kinase signaling pathway in Hyp mice. J Bone Miner Res 26: 1883-1890.
141. Zhang MY, Ranch D, Pereira RC, Armbrecht HJ, Portale AA, et al. (2012) Chronic inhibition of ERK1/2 signaling improves disordered bone and mineral metabolism in hypophosphatemic (Hyp) mice. Endocrinology 153: 1806-1816.
142. Miyamoto K, Ito M, Kuwahata M, Kato S, Segawa H (2005) Inhibition of intestinal sodium-dependent inorganic phosphate transport by fibroblast growth factor 23. Ther Apher Dial 9: 331-335.
143. Andrukhova O, Smorodchenko A, Egerbacher M, Streicher C, Zeitz U, et al. (2014) FGF23 promotes renal calcium reabsorption through the TRPV5 channel. EMBO J 33: 229-246.
144. Ben-Dov IZ, Galitzer H, Lavi-Moshayoff V, Goetz R, Kuro-o M, et al. (2007) The parathyroid is a target organ for FGF23 in rats. J Clin Invest 117: 4003-4008.
145. Canalejo R, Canalejo A, Martinez-Moreno JM, Rodriguez-Ortiz ME, Estepa JC, et al. (2010) FGF23 Fails to Inhibit Uremic Parathyroid Glands. Journal of the American Society of Nephrology 21: 1125-1135.
146. Roberts KE, Pitts RF (1953) The Effects of Cortisone and Desoxycorticosterone on the Renal Tubular Reabsorption of Phosphate and the Excretion of Titratable Acid and Potassium in Dogs. Endocrinology 52: 324-330.
147. Mills JN, Thomas S (1958) The Acute Effects of Cortisone and Cortisol Upon Renal Function in Man. Journal of Endocrinology 17: 41-53.
148. Laron Z, Crawford JD, Klein R (1957) Phosphaturic Effect of Cortisone in Normal and Parathyroidectomized Rats. Proceedings of the Society for Experimental Biology and Medicine 96: 649-651.
149. Anderson J, Foster JB (1959) The Effect of Cortisone on Urinary Phosphate Excretion in Man. Clinical Science 18: 437-439.
150. Freiberg JM, Kinsella J, Sacktor B (1982) Glucocorticoids Increase the Na+-H+ Exchange and Decrease the Na+ Gradient-Dependent Phosphate-Uptake Systems in Renal Brush-Border Membrane-Vesicles. Proceedings of the National Academy of Sciences of the United States of America-Biological Sciences 79: 4932-4936.
151. Levi M, Shayman JA, Abe A, Gross SK, Mccluer RH, et al. (1995) Dexamethasone Modulates Rat Renal Brush-Border Membrane Phosphate Transporter Messenger-Rna and Protein Abundance and Glycosphingolipid Composition. Journal of Clinical Investigation 96: 207-216.
152. Arima K, Hines ER, Kiela PR, Drees JB, Collins JF, et al. (2002) Glucocorticoid regulation and glycosylation of mouse intestinal type IIb Na-P-i cotransporter during ontogeny. American Journal of Physiology-Gastrointestinal and Liver Physiology 283: G426-G434.
153. Ishida Y, Heersche JNM (1998) Glucocorticoid-induced osteoporosis: Both in vivo and in vitro concentrations of glucocorticoids higher than physiological levels attenuate osteoblast differentiation. Journal of Bone and Mineral Research 13: 1822-1826.
154. Weinstein RS (2011) Glucocorticoid-Induced Bone Disease. New England Journal of Medicine 365: 62-70.
155. Lukert BP, Kipp D, Broy S (1997) Management of glucocorticoid-induced osteoporosis - first, do no harm: Comment on the American College of Rheumatology recommendations for the prevention and treatment of glucocorticoid-induced osteoporosis. Arthritis and Rheumatism 40: 1548-1548.

156. Lane NF, Lukert B (1999) Prevention and treatment of glucocorticoid-induced osteoporosis. Jcr-Journal of Clinical Rheumatology 5: S16-S22.
157. Rauch A, Seitz S, Baschant U, Schilling AF, Illing A, et al. (2010) Glucocorticoids Suppress Bone Formation by Attenuating Osteoblast Differentiation via the Monomeric Glucocorticoid Receptor. Cell Metabolism 11: 517-531.
158. Pereira RMR, de Carvalho JF, Canalis E (2010) Glucocorticoid-induced osteoporosis in rheumatic diseases. Clinics 65: 1197-1205.
159. Pereira RMR, Delany AM, Canalis E (2001) Cortisol inhibits the differentiation and apoptosis of osteoblasts in culture. Bone 28: 484-490.
160. Hofbauer LC, Gori F, Riggs BL, Lacey DL, Dunstan CR, et al. (1999) Stimulation of osteoprotegerin ligand and inhibition of osteoprotegerin production by glucocorticoids in human osteoblastic lineage cells: Potential paracrine mechanisms of glucocorticoid-induced osteoporosis. Endocrinology 140: 4382-4389.
161. Khosla S (2001) Minireview: The OPG/RANKL/RANK system. Endocrinology 142: 5050-5055.
162. Gennari C, Agnusdei D, Gonnelli S, Nardi P (1994) Differential Effect of Glucocorticoids on Calcium-Absorption and Bone Mass. Calcified Tissue International 54: 355-355.
163. Alizadeh Naderi AS, Reilly RF (2010) Hereditary disorders of renal phosphate wasting. Nat Rev Nephrol 6: 657-665.
164. Gaasbeek A, Meinders AE (2005) Hypophosphatemia: an update on its etiology and treatment. Am J Med 118: 1094-1101.
165. Prie D, Huart V, Bakouh N, Planelles G, Dellis O, et al. (2002) Nephrolithiasis and osteoporosis associated with hypophosphatemia caused by mutations in the type 2a sodium-phosphate cotransporter. N Engl J Med 347: 983-991.
166. Virkki LV, Forster IC, Hernando N, Biber J, Murer H (2003) Functional characterization of two naturally occurring mutations in the human sodium-phosphate cotransporter type IIa. J Bone Miner Res 18: 2135-2141.
167. Magen D, Berger L, Coady MJ, Ilivitzki A, Militianu D, et al. (2010) A loss-of-function mutation in NaPi-IIa and renal Fanconi's syndrome. N Engl J Med 362: 1102-1109.
168. Tieder M, Arie R, Modai D, Samuel R, Weissgarten J, et al. (1988) Elevated serum 1,25-dihydroxyvitamin D concentrations in siblings with primary Fanconi's syndrome. N Engl J Med 319: 845-849.
169. Schlingmann KP, Ruminska J, Kaufmann M, Dursun I, Patti M, et al. (2016) Autosomal-Recessive Mutations in SLC34A1 Encoding Sodium-Phosphate Cotransporter 2A Cause Idiopathic Infantile Hypercalcemia. J Am Soc Nephrol 27: 604-614.
170. Dinour D, Davidovits M, Ganon L, Ruminska J, Forster IC, et al. (2016) Loss of function of NaPiIIa causes nephrocalcinosis and possibly kidney insufficiency. Pediatric Nephrology.
171. Lorenz-Depiereux B, Benet-Pages A, Eckstein G, Tenenbaum-Rakover Y, Wagenstaller J, et al. (2006) Hereditary hypophosphatemic rickets with hypercalciuria is caused by mutations in the sodium-phosphate cotransporter gene SLC34A3. American Journal of Human Genetics 78: 193-201.
172. Bergwitz C, Roslin NM, Tieder M, Loredo-Osti JC, Bastepe M, et al. (2006) SLC34A3 mutations in patients with hereditary hypophosphatemic rickets with hypercalciuria predict a key role for the sodium-phosphate cotransporter NaPi-IIc in maintaining phosphate homeostasis. American Journal of Human Genetics 78: 179-192.
173. Traebert M, Hattenhauer O, Murer H, Kaissling B, Biber J (1999) Expression of type IINa-P-i cotransporter in alveolar type II cells. American Journal of Physiology-Lung Cellular and Molecular Physiology 277: L868-L873.
174. White KE, Evans WE, O'Riordan JLH, Speer MC, Econs MJ, et al. (2000) Autosomal dominant hypophosphataemic rickets is associated with mutations in FGF23. Nature Genetics 26: 345-348.

175. Du L, Desbarats M, Viel J, Glorieux FH, Cawthorn C, et al. (1996) cDNA cloning of the murine Pex gene implicated in X-linked hypophosphatemia and evidence for expression in bone. Genomics 36: 22-28.
176. Feng JQ, Ward LM, Liu SG, Lu YB, Xie YX, et al. (2006) Loss of DMP1 causes rickets and osteomalacia and identifies a role for osteocytes in mineral metabolism. Nature Genetics 38: 1310-1315.
177. Eicher EM, Southard JL, Scriver CR, Glorieux FH (1976) Hypophosphatemia - Mouse Model for Human Familial Hypophosphatemic (Vitamin-D-Resistant) Rickets. Proc Natl Acad Sci U S A 73: 4667-4671.
178. Liu SG, Zhou JP, Tang W, Jiang X, Rowe DW, et al. (2006) Pathogenic role of Fgf23 in Hyp mice. American Journal of Physiology-Endocrinology and Metabolism 291: E38-E49.
179. Martin A, Liu SG, David V, Li H, Karydis A, et al. (2011) Bone proteins PHEX and DMP1 regulate fibroblastic growth factor Fgf23 expression in osteocytes through a common pathway involving FGF receptor (FGFR) signaling. Faseb Journal 25: 2551-2562.
180. Martin A, David V, Li H, Dai B, Feng JQ, et al. (2012) Overexpression of the DMP1 C-Terminal Fragment Stimulates FGF23 and Exacerbates the Hypophosphatemic Rickets Phenotype in Hyp Mice. Mol Endocrinol 26: 1883-1895.
181. Halestrap AP (2012) The monocarboxylate transporter family--Structure and functional characterization. IUBMB Life 64: 1-9.
182. Hugo SE, Cruz-Garcia L, Karanth S, Anderson RM, Stainier DY, et al. (2012) A monocarboxylate transporter required for hepatocyte secretion of ketone bodies during fasting. Genes Dev 26: 282-293.
183. Friesema EC, Ganguly S, Abdalla A, Manning Fox JE, Halestrap AP, et al. (2003) Identification of monocarboxylate transporter 8 as a specific thyroid hormone transporter. J Biol Chem 278: 40128-40135.
184. Friesema EC, Grueters A, Biebermann H, Krude H, von Moers A, et al. (2004) Association between mutations in a thyroid hormone transporter and severe X-linked psychomotor retardation. Lancet 364: 1435-1437.
185. Park SY, Kim JK, Kim IJ, Choi BK, Jung KY, et al. (2005) Reabsorption of neutral amino acids mediated by amino acid transporter LAT2 and TAT1 in the basolateral membrane of proximal tubule. Arch Pharm Res 28: 421-432.
186. Abplanalp J, Laczko E, Philp NJ, Neidhardt J, Zuercher J, et al. (2013) The cataract and glucosuria associated monocarboxylate transporter MCT12 is a new creatine transporter. Hum Mol Genet 22: 3218-3226.
187. Suhre K, Shin SY, Petersen AK, Mohney RP, Meredith D, et al. (2011) Human metabolic individuality in biomedical and pharmaceutical research. Nature 477: 54-U60.
188. Poole RC, Sansom CE, Halestrap AP (1996) Studies of the membrane topology of the rat erythrocyte H+/lactate cotransporter (MCT1). Biochem J 320 (Pt 3): 817-824.
189. de Heredia FP, Wood IS, Trayhurn P (2010) Hypoxia stimulates lactate release and modulates monocarboxylate transporter (MCT1, MCT2, and MCT4) expression in human adipocytes. Pflugers Archiv-European Journal of Physiology 459: 509-518.
190. Halestrap AP (2013) Monocarboxylic Acid Transport. Comprehensive Physiology 3: 1611-1643.
191. Dimmer KS, Friedrich B, Lang F, Deitmer JW, Broer S (2000) The low-affinity monocarboxylate transporter MCT4 is adapted to the export of lactate in highly glycolytic cells. Biochemical Journal 350: 219-227.
192. Castorino JJ, Deborde S, Deora A, Schreiner R, Gallagher-Colombo SM, et al. (2011) Basolateral sorting signals regulating tissue-specific polarity of heteromeric monocarboxylate transporters in epithelia. Traffic 12: 483-498.
193. Kirk P, Wilson MC, Heddle C, Brown MH, Barclay AN, et al. (2000) CD147 is tightly associated with lactate transporters MCT1 and MCT4 and facilitates their cell surface expression. EMBO J 19: 3896-3904.

194. Fox JEM, Meredith D, Halestrap AP (2000) Characterisation of human monocarboxylate transporter 4 substantiates its role in lactic acid efflux from skeletal muscle. Journal of Physiology-London 529: 285-293.
195. Bergersen L, Waerhaug O, Helm J, Thomas M, Laake P, et al. (2001) A novel postsynaptic density protein: the monocarboxylate transporter MCT2 is co-localized with delta-glutamate receptors in postsynaptic densities of parallel fiber-Purkinje cell synapses. Experimental Brain Research 136: 523-534.
196. Pierre K, Pellerin L, Debernardi R, Riederer BM, Magistretti PJ (2000) Cell-specific localization of monocarboxylate transporters, MCT1 and MCT2, in the adult mouse brain revealed by double immunohistochemical labeling and confocal microscopy. Neuroscience 100: 617-627.
197. Nowik M, Lecca MR, Velic A, Rehrauer H, Brandli AW, et al. (2008) Genome-wide gene expression profiling reveals renal genes regulated during metabolic acidosis. Physiol Genomics 32: 322-334.
198. Gopal E, Umapathy NS, Martin PM, Ananth S, Gnana-Prakasam JP, et al. (2007) Cloning and functional characterization of human SMCT2 (SLC5A12) and expression pattern of the transporter in kidney. Biochimica Et Biophysica Acta-Biomembranes 1768: 2690-2697.
199. Thangaraju M, Ananth S, Martin PM, Roon P, Smith SB, et al. (2006) c/ebp delta null mouse as a model for the double knock-out of slc5a8 and slc5a12 in kidney. Journal of Biological Chemistry 281: 26769-26773.
200. Becker HM, Mohebbi N, Perna A, Ganapathy V, Capasso G, et al. (2010) Localization of members of MCT monocarboxylate transporter family Slc16 in the kidney and regulation during metabolic acidosis. Am J Physiol Renal Physiol 299: F141-154.
201. Halestrap AP, Meredith D (2004) The SLC16 gene family - from monocarboxylate transporters (MCTs) to aromatic amino acid transporters and beyond. Pflugers Archiv-European Journal of Physiology 447: 619-628.
202. Dhayat N, Simonin A, Anderegg M, Pathare G, Luscher BP, et al. (2016) Mutation in the Monocarboxylate Transporter 12 Gene Affects Guanidinoacetate Excretion but Does Not Cause Glucosuria. J Am Soc Nephrol 27: 1426-1436.
203. Lee WS, Berry MJ, Hediger MA, Larsen PR (1993) The type I iodothyronine 5'-deiodinase messenger ribonucleic acid is localized to the S3 segment of the rat kidney proximal tubule. Endocrinology 132: 2136-2140.
204. Kirat D, Kato S (2009) Monocarboxylate transporter genes in the mammary gland of lactating cows. Histochem Cell Biol 132: 447-455.
205. Kirat D, Sallam KI, Kato S (2013) Expression and cellular localization of monocarboxylate transporters (MCT2, MCT7, and MCT8) along the cattle gastrointestinal tract. Cell Tissue Res 352: 585-598.
206. Roshanbin S, Lindberg FA, Lekholm E, Eriksson MM, Perland E, et al. (2016) Histological characterization of orphan transporter MCT14 (SLC16A14) shows abundant expression in mouse CNS and kidney. BMC Neurosci 17: 43.
207. Rosenthal R, Gunzel D, Krug SM, Schulzke JD, Fromm M, et al. (2016) Claudin-2-mediated cation and water transport share a common pore. Acta Physiol (Oxf).
208. Lu Z, Ding L, Lu Q, Chen YH (2013) Claudins in intestines: Distribution and functional significance in health and diseases. Tissue Barriers 1: e24978.
209. Krug SM, Gunzel D, Conrad MP, Rosenthal R, Fromm A, et al. (2012) Claudin-17 forms tight junction channels with distinct anion selectivity. Cellular and Molecular Life Sciences 69: 2765-2778.
210. Razzaque MS (2011) Phosphate toxicity: new insights into an old problem. Clinical Science 120: 91-97.
211. Lien YHH (2013) Phosphorus: Another Devil in Our Diet? American Journal of Medicine 126: 280-281.

212. Hattenhauer O, Traebert M, Murer H, Biber J (1999) Regulation of small intestinal Na-P-i type IIb cotransporter by dietary phosphate intake. American Journal of Physiology-Gastrointestinal and Liver Physiology 277: G756-G762.
213. Calvo MS (2000) Dietary considerations to prevent loss of bone and renal function. Nutrition 16: 564-566.
214. Karp HJ, Vaihia KP, Karkkainen MUM, Niemisto MJ, Lamberg-Allardt CJE (2007) Acute effects of different phosphorus sources on calcium and bone metabolism in young women: A whole-foods approach. Calcified Tissue International 80: 251-258.
215. Davis GR, Zerwekh JE, Parker TF, Krejs GJ, Pak CYC, et al. (1983) Absorption of Phosphate in the Jejunum of Patients with Chronic-Renal-Failure before and after Correction of Vitamin-D Deficiency. Gastroenterology 85: 908-916.
216. Schiavi SC, Tang W, Bracken C, O'Brien SP, Song WP, et al. (2012) Npt2b Deletion Attenuates Hyperphosphatemia Associated with CKD. Journal of the American Society of Nephrology 23: 1691-1700.
217. Yeh JK, Aloia JF (1987) Effect of Glucocorticoids on the Passive Transport of Phosphate in Different Segments of the Intestine in the Rat. Bone and Mineral 2: 11-19.

Curriculum vitae

Surname: KNÖPFEL

Name: THOMAS

Date of Birth: 11. November 1987

Nationality: Swiss, Teufen AR

Education:

- November 2012 – present

  PhD Student at the Institute of Physiology, University of Zurich
  Mechanisms of Intestinal Phosphate Transport
  Supervisor: Prof. Carsten A. Wagner

- August 2011 – October 2012

  Master of Science UZH, Human Biology
  Master thesis at the Institute of Physiology, University of Zurich
  Renal localization and regulation of the monocarboxylate transporter MCT14
  Supervisor: Prof. Jürg Biber

- September 2007 – June 2011

  Bachelor of Science UZH, Biology

- August 2002 – July 2006

  Matura: Mathematisch Naturwissenschaftliches Profil, Chemie und Biologie
  Kantonsschule im Lee, Winterthur

List of Publications:

- Fenollar-Ferrer C, Patti M, Knöpfel T, Werner A, Forster IC, et al. (2014) Structural Fold and Binding Sites of the Human Na+-Phosphate Cotransporter NaPi-II. Biophysical Journal 106: 1268-1279.

- Hernando N, Myakala K, Simona F, Knöpfel T, Thomas L, et al. (2015) Intestinal Depletion of NaPi-IIb/Slc34a2 in Mice: Renal and Hormonal Adaptation. J Bone Miner Res 30: 1925-1937.

- Patti M, Fenollar-Ferrer C, Werner A, Knoepfel T, Forrest L, et al. (2015) Functional Identification of the Na1 Site of the Phosphate Cotransporter NaPi-IIa. Biophysical Journal 108: 29a-29a.

- Thomas L, Bettoni C, Knöpfel T, Hernando N, Biber J, et al. (2016) Acute Adaption to Oral or Intravenous Phosphate Requires Parathyroid Hormone. Journal of the American Society of Nephrology.

Abstracts:

- “Renal localization of monocarboxylate transporter family member SLC16A14 (MCT14)”
  91st Annual Meeting of the German Physiological Society, Dresden, March 2012 (Poster 197)

- “Identification of Phosphate Regulated Transcripts in Ileum and Renal Proximal Tubules”
  93rd Annual Meeting of the German Physiological Society, Mainz, March 2014 (Poster 274)

- “Renal Localization and Characterization of Monocarboxylate Transporter Family Member Slc16a14”
  Experimental Biology 2015, Boston (Poster 969.13)

- “Identification of Phosphate Regulated Transcripts in Ileum and Renal Proximal Tubules”
  Experimental Biology 2015, Boston (Poster 969.12)

- “Paracellular Phosphate Permeability in the Intestine”
  95th Annual Meeting of the German Physiological Society, Lübeck (Poster 194)

- “Dietary Adaptation to High and Low Phosphate in the Absence of the Intestinal Sodium Phosphate Symporter NaPi-IIb”
  95th Annual Meeting of the German Physiological Society, Lübeck (Poster 363)